Neutron Scattering from Disordered Antiferromagnetic Insulators

Mark Edward Hagen

Ph.D.

University of Edinburgh

1983

Abstract

The results of three projects are reported in this thesis. The first project was an experimental test of the hypothesis of Two Scale Factor Universality. This was achieved by measuring, using neutron diffraction, the intensities of the magnetic Bragg and critical scattering associated with the antiferromagnetic phase transition in Rb_2CoF_4. It is shown how, from these measurements, a value for a Universal combination of three critical amplitudes R_s, embodied in the hypothesis, was obtained. This value of R_s for Rb_2CoF_4 was compared with the value taken from the exact solution of the d = 2 Ising model and fair agreement was obtained.

The second project was an experimental study, by neutron diffraction, of the phase transition and magnetic ordering of the dilute antiferromagnets $Co_xZn_{1-x}F_2$ and $Mn_xZn_{1-x}F_2$ in an external magnetic field. The effect of the magnetic field was found to be drastic, destroying long range antiferromagnetic order for all the non-zero fields applied. A comparison of the results of these measurements with the theoretical predictions for the d = 3 Ising model in a random magnetic field, which is believed to be in the same Universality class, is given. The results reported disagree with the theoretical predictions for the magnetic order in d = 3 although a number of qualifications to this result are made.

The third project was a theoretical study, using a computer

simulation technique, of the spin wave spectrum of diluted and magnetically mixed compounds of $FeCl_2$. Of the two mixed compounds studied, one, $Fe_xCo_{1-x}Cl_2$, was also studied experimentally by inelastic neutron diffraction for a sample with x = 0.85. A comparison of the computational and experimental results shows that there exists in $Fe_{0.85}Co_{0.15}Cl_2$, a magnetic excitation which is inconsistent with a ground state of complete uniaxial order.

Declaration

I declare that, unless otherwise stated explicitly, the work presented in this thesis is my own and that the composition of this thesis has been my own work. Where the collaboration of others has played an important part in the performance of the experimental measurements reported in chapters two and three this has been acknowledged.

Signed

M. E. Hagen

Fundamental Constants and Units of Energy

A number of fundamental constants occur regularly in the following chapters and therefore the symbols used for these constants and their values are tabulated here.

$\hbar$	Planck's constant divided by 2π	1.054×10^{-34} Js
μ_B	Bohr magneton	9.274×10^{-24} J/T
μ_N	Nuclear magneton	5.051×10^{-27} J/T
m_N	Mass of the neutron	1.675×10^{-27} kg
γ_N	Gyromagnetic ratio of the neutron	-1.91
k_B	Boltzmann's constant	1.381×10^{-23} J/K

The units of energy used vary from chapter to chapter depending on which is the most suitable unit. The conversion factors between the three units used and the Joule are given below.

$$1 \text{ meV} = 1.6 \times 10^{-22} \text{ J}$$

$$1 \text{ THz} = 4.14 \text{ meV}$$

$$1 \text{ cm}^{-1} = 0.1241 \text{ meV}$$

Acknowledgements

Throughout the period of work for this thesis I have been financially supported by a. S.E.R.C. postgraduate studentship for which I am grateful. I have also benefitted from the award by the S.E.R.C. of financial support for travelling expenses in order to perform experiments and also to attend conferences.

I have benefitted from the provision of experimental facilities at the Institut Laue-Langevin, A.E.R.E. Harwell and Brookhaven National Laboratory. I would like to thank Dr. Gen Shirane and the other members of the neutron scattering group at B.N.L. for their help during my stay at B.N.L.

The computational work reported in the following chapters was performed using the ICL 2972, 2980 and 2988 computers of the Edinburgh Regional Computing Centre.

I would especially like to acknowledge and thank Professor Roger Cowley for his invaluable help and advice during my three years of research work at Edinburgh. Also I would like to acknowledge Dr. David Melville who first stimulated my interests in statistical mechanics and magnetism. Two other people to whom I am indebted for helping me through the initial hurdles of neutron scattering experiments and some of the theoretical aspects of phase transitions are Dr. David Bruce and Dr. Donald Paul.

I would also like to express my gratitude to Mrs. Moira Macdonald for her careful typing of the manuscript.

Finally, I dedicate this thesis to my mother and father, whose encouragement which now seems so many years ago, is not forgotten.

CONTENTS

Appendix A - Data Analysis Methods

CHAPTER ONE

Introductory Review

1.1 Introduction

The work reported in this thesis can be divided into three topics which, although there is some cross reference between them, were essentially independent projects. As a consequence only a very brief outline of each project will be given in this introduction and a more detailed background for each project will be given in the introduction sections of the relevant chapters. There are however two common features to these projects. Firstly, they have been investigated experimentally by neutron scattering methods and secondly the samples used in these experiments have all been antiferromagnetic insulators. The choice of antiferromagnetic insulators has been prompted both because they have relatively simple magnetic interactions whose form is known and because of the availability of good single crystal samples. The simplicity of the magnetic interactions therefore makes these materials excellent systems on which to test the predictions of theoretical models.

The first project considered is a test of the hypothesis of Two Scale Factor Universality (Stauffer et al (1972)). This hypothesis predicts that at a continuous phase transition there should be certain combinations of three critical amplitudes which should have the same Universality properties as the critical exponents for the transition. It has been shown by Bruce (1981) that one of these combinations of critical amplitudes could be measured in a neutron scattering experiment. Therefore in order to test the hypothesis of Two Scale Factor Universality a neutron scattering experiment has been performed to measure this combination

of amplitudes in the antiferromagnetic insulator Rb_2CoF_4. This project is reported in Chapter Two.

The second project reported is a study by neutron scattering of the phase transition and magnetic ordering of the dilute antiferromagnets $Co_xZn_{1-x}F_2$ and $Mn_xZn_{1-x}F_2$ in an external magnetic field. A dilute antiferromagnet in an external magnetic field is believed to be an experimental realisation of the so called random field problem (Fishman and Aharony (1979)). In recent years there has been a great deal of theoretical activity and controversy concerning the properties of random field systems. The results of these measurements are therefore interpreted in terms of the different theoretical predictions for random field systems. This project is reported in Chapter Three.

The third project is concerned with the calculation of the low temperature spin wave excitations in site disordered magnets. Calculations have been performed using the Alben and Thorpe (1975) 'Equation of Motion' computer simulation method for the diluted and mixed compounds of the magnetic insulator $FeCl_2$. In Chapter Four the method for these calculations and the results for the compounds $Fe_xMg_{1-x}Cl_2$ and $Fe_xMn_{1-x}Cl_2$ are presented. The calculations of the spin wave energies for the latter compound are compared with those measured by Bertrand et al (1981) using inelastic neutron scattering techniques.

In Chapter Five measurements of the spin wave spectrum for the compound $Fe_xCo_{1-x}Cl_2$ by inelastic neutron scattering are reported. This compound is an example of a system with random competing anisotropies (Wong et al (1980)). The measured spectrum is compared to the results of computer simulations performed using the techniques described in Chapter Four. These calculations were performed for a

model ground state of $Fe_xCo_{1-x}Cl_2$ proposed by Wiltshire (1981). The results are discussed in terms of the applicability of this ground state.

The measurements reported in Chapters Two and Three have involved a large amount of data analysis. The methods used for performing the various data analyses are given as an appendix. Included in this appendix are methods which have been devised to improve the efficiency and accuracy of data analysis computer programs.

Each of these four chapters and the appendix contains an introduction of its own explaining the background to that particular problem. The rest of this introductory chapter is taken up with brief descriptions of the 'common features'. In the following section a brief review of the origin of the magnetic interactions in magnetic insulators is given. The third and fourth sections of this chapter describe how measurements of the neutrons scattered by a magnetic insulator may be used to probe its magnetic properties. Of these two sections the first describes the theoretical aspects while the second describes how measurements are made in practice.

1.2 Magnetic Interactions in Magnetic Insulators

In this section it is intended to indicate the origins of the magnetic properties of the materials considered in Chapters Two to Five. These materials are the insulating compounds Rb_2CoF_4, CoF_2, FeF_2, MnF_2, $FeCl_2$ and $CoCl_2$. It is therefore the magnetic properties of the divalent transition metal ions Co^{2+}, Fe^{2+} and Mn^{2+} that are of interest. Calculations of the magnetic properties of ionic solids such as these, even though they may well be the simplest type of magnetic material, are still highly involved and occupy large chapters of books on magnetism (for example Zeiger and Pratt (1973)).

This section is therefore not intended to be a review of such calculations but merely an outline of the effects that occur.

The magnetic ground state of a free transition metal ion, ignoring the effects of spin-orbit coupling, can be found from Hund's rules (see for example, Mattis (1965) p. 94). These rules arise from minimising the coulomb and exchange energies between electrons on the ion and as a consequence the gap between the ground state and excited states is large. For the three ions given above the ground states given by Hund's rules are ^4F, ^5D and ^6S states respectively. Since the effects that arise for these ions by being part of a solid are small compared to the gap to the excited states, their effect is evaluated in perturbation theory using these free ion states as the starting point.

Schematically the perturbing part of the Hamiltonian for these transition metal ions in the compounds referred to above may be written as

$$\Delta\mathcal{H} = \mathcal{H}_{\substack{\text{CRYSTAL} \\ \text{FIELD}}} + \mathcal{H}_{\substack{\text{SPIN-ORBIT} \\ \text{COUPLING}}} + \mathcal{H}_{\text{EXCHANGE}} \qquad (1.2.1)$$

In this equation the effects are ordered from left to right in descending size. The effect that makes these compounds good models for the problems outlined in section (1) is the exchange effect. However, since it is the smallest of the perturbing terms for the Co^{2+} and Fe^{2+} ions its final form is strongly affected by the two preceding terms. For the Mn^{2+} ion these two preceding terms turn out to be zero to first order in perturbation theory.

The first term in equation (1.2.1) arises from the electrostatic interactions between the electrons on the magnetic ion sites and those on surrounding sites. The electrostatic potential at the magnetic ion site therefore has the symmetry of the surrounding

sites on the lattice. Since the interaction is electrostatic this crystal field term is a function of the components of the total orbital angular momentum only. First principles calculations of this term are not possible and it is usually constructed by group theory techniques using the method of operator equivalents (Zeiger and Pratt (1973) p. 142, Hutchings (1964)). This gives the dependence on the orbital angular momentum operators but does not give the absolute size of the effect which is left as a phenomenological parameter to be determined by experimental measurements. In the CoF_2, FeF_2, $FeCl_2$ and $CoCl_2$ compounds this crystal field effect is usually split into two terms. This is because in these compounds the ions surrounding the magnetic ions lead to an electrostatic potential which can be represented as the sum of the potentials due to a high symmetry structure plus a small distortion to that structure. The effect of the high symmetry term is larger than that due to the distortion term and the spin orbit coupling term and therefore the effect of this term on the free ion ground state is evaluated to first order in perturbation theory first.

The next step after evaluating the wavefunctions that result from the effect of the high symmetry crystal field is to evaluate the effect of the distortion to the crystal field and the spin orbit coupling as a perturbation to these levels. The form of the distortion term in terms of the components of the total angular momentum operator is given by group theory as before and the spin-orbit coupling term will be $-\lambda \hat{\underline{L}}.\hat{\underline{S}}$ where $\hat{\underline{L}}$ and $\hat{\underline{S}}$ are the total orbital and spin angular momenta and λ is a phenomenological parameter. These terms need to be evaluated at the same time since they are usually of the same size.

Hence it is possible to obtain the wavefunctions and energy levels of the single ions in terms of phenomenological parameters for the crystal field and spin-orbit coupling terms by successive applications of perturbation theory. The values of these parameters can then be found by experimental meaurement of the excitations between different levels.

In the following chapters it is only the very lowest levels of the magnetic ions which play any role in the observed phenomena. It is usual rather than to use a complicated superposition of orbital and spin angular mementum wavefunctions for these levels to associate them with the levels of a pseudo spin. Then by a suitable use of proportionality constants the matrix elements of true angular momentum operators within these levels can be represented by the matrix elements of the pseudo spin operator. If the pseudo spin operator is represented by a small $\hat{s}$, then this association leads to replacing the operators for the components of the orbital and spin angular momenta $\hat{L}^k$ and $\hat{S}^k$ and the magnetic moment $\hat{\mu}^k$ by:

$$\hat{L}^k = \alpha_L^k \, s^k \tag{1.2.2a}$$

$$\hat{S}^k = \alpha_s^k \, s^k \tag{1.2.2b}$$

$$\hat{\mu}^k = \mu_B(\hat{L}^k + 2\hat{S}^k) = g^k \, \mu_B \, \hat{s}^k \tag{1.2.2c}$$

where $g^k = \alpha_L^k + 2\alpha_s^k$.

So far the terms in equation (1.2.1) which have been discussed have been single ion terms applying only to the angular momentum operators on a single ion. The final term $\mathcal{H}_{\text{Exchange}}$ couples together angular momentum operators on different ions in the crystal. Its form can be written approximately as (Mattis (1965) p. 32):

$$\mathcal{H}_{\text{Exchange}} = -\sum_{ij} J_{ij}\, \hat{\underline{S}}_i . \hat{\underline{S}}_j \qquad (1.2.3)$$

where $\hat{\underline{S}}_i$ and $\hat{\underline{S}}_j$ are the true total spin angular momentum operators on the magnetic ions at positions $\underline{r}_i$ and $\underline{r}_j$. The origin of this term lies in the overlap of the electronic wavefunctions of the transition metal ions and the cations. This overlap leads to an electronic exchange effect between the electrons on the magnetic ion and the cation. The overlap of the cation wavefunctions with the wavefunctions of other ions will lead to an electronic exchange between these ions and so on until another magnetic ion is reached. There is therefore an indirect exchange between the total spin angular momenta of the two magnetic ions via the intermediate cations known as superexchange (Zeiger and Pratt (1973) p. 231). The factor J_{ij} therefore represents the overlap integrals of the electronic wavefunctions along the paths from the magnetic ions i to j. This factor cannot be calculated from first principles although there are empirical rules for estimating its size and sign (Zeiger and Pratt (1973) p. 244). In the compounds referred to earlier the superexchange only extends as far as at most the third nearest magnetic neighbour of a magnetic ion.

The importance of the exchange Hamiltonian is that it leads to co-operative phenomena. That is to say that instead of solving a Hamiltonian involving only one magnetic ion it is necessary to evaluate the properties of a many body problem, i.e. one that involves all of the magnetic ions in the crystal simultaneously. In the following chapters the temperatures at which measurements were performed and the energy of the incident neutrons is insufficient to appreciably excite any states other than the very lowest levels of these ions. Therefore it is the effect of the

exchange Hamiltonian within these levels that is of interest. For the Mn^{2+} ion equation (1.2.3) will retain its isotropic form since the lowest levels are eigenstates of the total real spin operators. However, this is not the case for the Co^{2+} and Fe^{2+} ions. The simplest way of representing the exchange Hamiltonian within the levels of these ions is to replace the components of the real spin by the components of the pseudo spin multiplied by the relevant proportionality constant. This is known on theoretical grounds to be incorrect (Elliott and Thorpe (1968)) but experiments (Buyers et al (1971)) have been unable to detect the difference between this simple prescription and more complicated procedures. In Chapter Five this point will be discussed again but until then this simple diagonal Hamiltonian will be assumed to give a very good reproduction of experimental results. Since in general the proportionality constants differ for different components of the pseudo spin the exchange Hamiltonian is an anisotropic function of the pseudo spin operators.

Thus the magnetic properties of these compounds provide an excellent test for the theoretical predictions on co-operative phenomena. The exchange interactions within the pseudo spin levels are short range, have a simple diagonal form and have a variety of symmetries for the different compounds. Further to this the size and form of the various parameters, crystal field, spin-orbit and exchange are well known from previous measurements on these compounds.

1.3 Neutron Scattering - Theoretical Aspects

In this section the basic formalism for the cross section of neutrons scattered from a magnetic sample is briefly reviewed. If

a monochromatic beam of neutrons with kinetic energy E and of unit flux is incident upon a target (i.e. the sample) then the number of neutrons scattered into a solid angle $d\Omega$ within the energy range E to dE is defined to be the partial differential cross section $\frac{\partial^2\sigma}{\partial\Omega\partial E}$. In the Born approximation the partial differential cross section is given by (Marshall and Lovesey (1971) p. 7):

$$\frac{\partial^2\sigma}{\partial\Omega\partial E} = \frac{|\underline{k}_f|}{|\underline{k}_i|}\left(\frac{m_N}{2\pi\hbar}\right)^2 \sum_{m\sigma_i}\sum_{n\sigma_f} P_m P_{\sigma_i} |\langle \underline{k}_f\sigma_f n |\hat{V}|\underline{k}_i\sigma_i\, m\rangle|^2 \times \delta(\hbar\omega + E_m - E_n) \qquad (1.3.1)$$

In equation (1.3.1) i and f refer to the incident and final states of the neutron, which are assumed to be plane wave states with wave-vector $\underline{k}$ and polarisation σ. The states $|m\rangle$ and $|n\rangle$ are the initial and final states of the sample, which have energies E_m and E_n. The frequency ω is related to the energy difference of the initial and final states of the neutron and is given by:

$$\hbar\omega = E_i - E_f = \frac{\hbar^2}{2m_N}(k_i^2 - k_f^2) \qquad (1.3.2)$$

An average over the initial state of the sample and the initial polarisation of the neutron is included in equation (1.3.1) by the probabilities P_m and P_{σ_i} of the sample and neutron being in these states. The operator $\hat{V}$ in equation (1.3.1) represents the interaction potential between the neutron and the sample and can be written as

$$\hat{V} = \sum_j \frac{2\pi\hbar^2}{m_N} b_j \delta(\underline{r} - \underline{R}_j) - \hat{\underline{\mu}}_N \cdot \hat{H}_{eff}(\underline{r}) \qquad (1.3.3)$$

The first term in equation (1.3.3) is the Fermi pseudo-potential (Marshall and Lovesey (1971) p. 8) which models the atomic nuclei at positions $\underline{R}_j$ as a delta function interaction with a strength

given by the scattering length b_j. Since in a crystal the atomic nuclei are arranged on a periodic lattice, including this term alone in equation (1.3.1) would give the partial differential cross section for the scattering from the lattice. This term will, however, be neglected for the rest of this section since it is the purpose to review the theoretical aspects of the use of neutron scattering as a probe of magnetic properties. The second term in equation (1.3.3) represents the interaction between the magnetic moment of the neutron $\hat{\underline{\mu}}_N$ and the effective magnetic field at a point $\underline{r}$ in the sample due to the unpaired electrons. The magnetic moment $\hat{\underline{\mu}}_N$ can be written as $\gamma_N \mu_N \hat{\underline{\sigma}}$ where γ_N is the gyromagnetic ratio of the neutron, μ_N is the nuclear magneton and the $\hat{\sigma}^\alpha$ which are the elements of the vector $\underline{\sigma}$ where α = x,y or z are the Pauli matrices. If the effective field is written as the sum of the fields due to the unpaired electrons then it can be shown after some algebra (Marshall and Lovesey (1971) pages 107 and 128) that the matrix element $\underline{H}_{eff}(r)$ between the states $|\underline{k}_i\rangle$ and $|\underline{k}_f\rangle$ is just

$$\langle \underline{k}_f | \hat{\underline{H}}_{eff}(\underline{r}) | \underline{k}_i \rangle = \int d^3r \, e^{i\underline{Q}.\underline{r}} \left\{ \hat{\underline{Q}} \times \left[\hat{\underline{M}}(r) \times \hat{\underline{Q}} \right] \right\} \qquad (1.3.4)$$

where $\underline{Q} = \underline{k}_f - \underline{k}_i$ is the wavevector transfer, $\hat{\underline{Q}} = \underline{Q}/|Q|$ and $\hat{\underline{M}}(\underline{r})$ is the magnetisation density operator. In a magnetic insulator the magnetic electrons are at the lattice sites and therefore if $|\underline{Q}|^{-1}$ is much greater than the mean radius of the electronic orbitals then the right hand side of equation (1.3.4) may be approximated by:

$$\int d^3r \, e^{i\underline{Q}.\underline{r}} \, \hat{\underline{Q}} \times \left[\hat{\underline{M}}(\underline{r}) \times \hat{\underline{Q}} \right] \simeq \sum_j e^{i\underline{Q}.\underline{R}_j} f_j(\underline{Q}) \, \hat{\underline{Q}} \times \left[\hat{\underline{\mu}}_j \times \hat{\underline{Q}} \right] \qquad (1.3.5)$$

In equation (1.3.5) it is assumed that the magnetisation around a magnetic ion may be replaced by the total magnetic moment operator $\hat{\underline{\mu}}_j$ for that ion multiplied by a form factor $f_j(\underline{Q})$. The form factor $f_j(\underline{Q})$

is the Fourier transform of the magnetic moment density on the ion. Substituting back through equations (1.3.5) to (1.3.3) and then into equation (1.3.1) gives the partial differential cross section for the magnetic scattering from localised magnetic ions as:

$$\frac{\partial^2\sigma}{\partial\Omega\partial E} = \frac{|\underline{k}_f|}{|\underline{k}_i|}\left(\frac{m_N}{2\pi\hbar}\right)^2 \gamma\mu_N \sum_{\hat{m}} P_m \sum_{\sigma_i\sigma_f} P_{\sigma_i} \Big| \sum_j e^{i\underline{Q}.\underline{R}_j} f_j(\underline{Q}) < m\,\sigma_f | \hat{\underline{\sigma}}.$$

$$(\tilde{\underline{Q}} \times [\hat{\underline{\mu}}_j \times \tilde{\underline{Q}}]) | m\sigma_i > |^2 \delta(\hbar\omega + E_m - E_n). \qquad (1.3.7)$$

If the dot and cross products within the matrix element of equation (1.3.7) are performed and the matrix element expanded then equation (1.3.7) can be rewritten as:

$$\frac{\partial^2\sigma}{\partial\Omega\partial E} = \frac{|\underline{k}_f|}{|\underline{k}_i|}\left(\frac{m_N}{2\pi\hbar}\right)^2 \gamma\mu_N \sum_{\alpha\beta} (\delta_{\alpha\beta} - \tilde{Q}_\alpha\tilde{Q}_\beta) \sum_{j\ell} e^{i\underline{Q}.(\underline{R}_j - \underline{R}_\ell)} f_j(\underline{Q}) f^*_\ell(\underline{Q})$$

$$\times \sum_{mn} P_m \; <m|\hat{\mu}^\alpha_j| \; n >< n| \; \hat{\mu}^\beta_\ell|m> \; \delta(\hbar\omega + E_m - E_n) \qquad (1.3.8)$$

In going from equation (1.3.7) to (1.3.8) use has been made of the result that $\sum_{\sigma_f} |\sigma_f >< \sigma_f|$ is a unit operator and that for unpolarised neutrons $\sum_{\sigma_i} P_{\sigma_i} < \sigma_i|\sigma^\alpha \sigma^\beta|\sigma_i> = \delta_{\alpha,\beta}$ where α and β are x,y,z, the cartesian components. The magnetic moment operators in equation (1.3.8) can be replaced by $g^\alpha\mu_B\hat{S}^\alpha$ where $\hat{S}^\alpha$ is the α^{th} component of the pseudo-spin operator. Equation (1.3.8) can be simplified further by noting that

$$<n|S^\beta_\ell|m> \delta(\hbar\omega + E_m - E_n) = \int dt\, e^{-i\omega t} < n|\hat{S}^\beta_\ell(t)|m > \qquad (1.3.9)$$

where $\hat{S}^\beta_\ell(t) = \exp(\frac{i\hat{\mathcal{H}}t}{\hbar})\, S^\beta_\ell \exp(\frac{-i\hat{\mathcal{H}}t}{\hbar})$ and $\hat{\mathcal{H}}$ is the Hamiltonian for the spins in the sample. The use of equation (1.3.9) means that the partial differential cross section may be written in the form:

$$\frac{\partial^2\sigma}{\partial\Omega\partial E} = \frac{|\underline{k}_f|}{|\underline{k}_i|} \left(\frac{m_N}{2\pi\hbar}\right)^2 \gamma\mu_N \, S(\underline{Q},\omega) \tag{1.3.10a}$$

$$\text{where } S(\underline{Q}, \omega) = \sum_{\alpha\beta} (\delta_{\alpha\beta} - \tilde{Q}_\alpha \tilde{Q}_\beta) S^{\alpha\beta}(\underline{Q}, \omega) \tag{1.3.10b}$$

$$\text{and } S^{\alpha\beta}(\underline{Q}, \omega) = \sum_{j\ell} g_j^\alpha \, g_\ell^\beta \, f_j(\underline{Q}) \, f_\ell^*(\underline{Q}) \, e^{i\underline{Q}\cdot(\underline{R}_j - \underline{R}_\ell)} \times \int dt \, e^{-i\omega t} \, \langle \hat{S}_j^\alpha(0) \hat{S}_\ell^\beta(t) \rangle \tag{1.3.10c}$$

where the angular brackets denote a thermal average which is equivalent to $\sum_m P_m \langle m| \ldots . |m\rangle$. The factor $S(\underline{Q}, \omega)$ is known as the dynamic structure factor and the $S^{\alpha\beta}(\underline{Q}, \omega)$ are partial dynamic structure factors. Equation (1.3.10c) is important because it relates the partial differential cross section to the spatial and temporal Fourier transforms of the spin-spin correlation function.

Although equation (1.3.10) contains $S^{\alpha\beta}(\underline{Q}, \omega)$ for uniaxial or isotropic magnets the number of partial dynamic structure factors is reduced by symmetry. In these cases $S(\underline{Q}, \omega)$ may be written as

$$S(\underline{Q},\omega) = (1 - \tilde{Q}_z^2) \, S^{zz}(\underline{Q}, \omega) + \left(\frac{1 + \tilde{Q}_z^2}{2}\right) \left[S^{xx}(\underline{Q}, \omega) + S^{yy}(\underline{Q}, \omega)\right] \tag{1.3.11}$$

where the z direction is now implicitly the direction of magnetic ordering. The first term in equation (1.3.11) the z-z dynamic structure factor measures the correlations of the magnetic order at different points in the system, while the second term measures the correlations between the components of the spins perpendicular to the ordering direction. The second term therefore measures the contribution to the cross section from spin waves. A further discussion of the $S^{zz}(\underline{Q}, \omega)$ is given in section (2) of Chapter Two and a discussion of the dynamic structure factor for the spin waves in section (3) of Chapter Four.

1.4 Neutron Scattering - Experimental Aspects

This section describes briefly how in practice a beam of neutrons is scattered from a sample and how the measured intensity of scattered neutrons relates to the partial differential cross section. It is intended that this section should essentially define terms that will be used repeatedly in the following chapters and is not intended as a general review.

A diagram of a triple axis spectrometer for neutron scattering is shown in figure (1.4.1). It is this type of spectrometer that has been used to perform the measurements reported in the later chapters. In general a triple axis spectrometer allows both the wavevector and energy transfers of the scattered neutrons to the sample to be measured. If the neutrons incident on the sample have a wavevector $\underline{k}_i$ and those scattered by the sample have a wavevector $\underline{k}_f$ then the wavevector transfer $\underline{Q}$ and energy transfer $\hbar\omega$ are defined by the equations:

$$\underline{Q} = \underline{k}_f - \underline{k}_i \qquad (1.4.1a)$$

$$\text{and} \quad \hbar\omega = \frac{\hbar^2}{2m_N}(\underline{k}_i^2 - \underline{k}_f^2) \qquad (1.4.1b)$$

Therefore the components of the spectrometer shown in figure (1.4.1) are arranged in such a way as to be able to define the wavevectors $\underline{k}_i$ and $\underline{k}_f$ before and after the sample.

The source of the neutrons is the moderator of a nuclear reactor. These neutrons have a Maxwell-Boltzmann distribution of energies corresponding to the temperature of the moderator, nominally room temperature. These neutrons pass through a collimator in order to limit the horizontal divergence of the neutron beam. A collimator consists of a series of parallel blades of steel coated with cadmium or mylar coated with gadolinium in a holder. Since cadmium or gadolinium absorb neutrons only those neutrons whose divergence from

Figure (1.4.1)

This figure shows the arrangement of the different components of a triple axis spectrometer

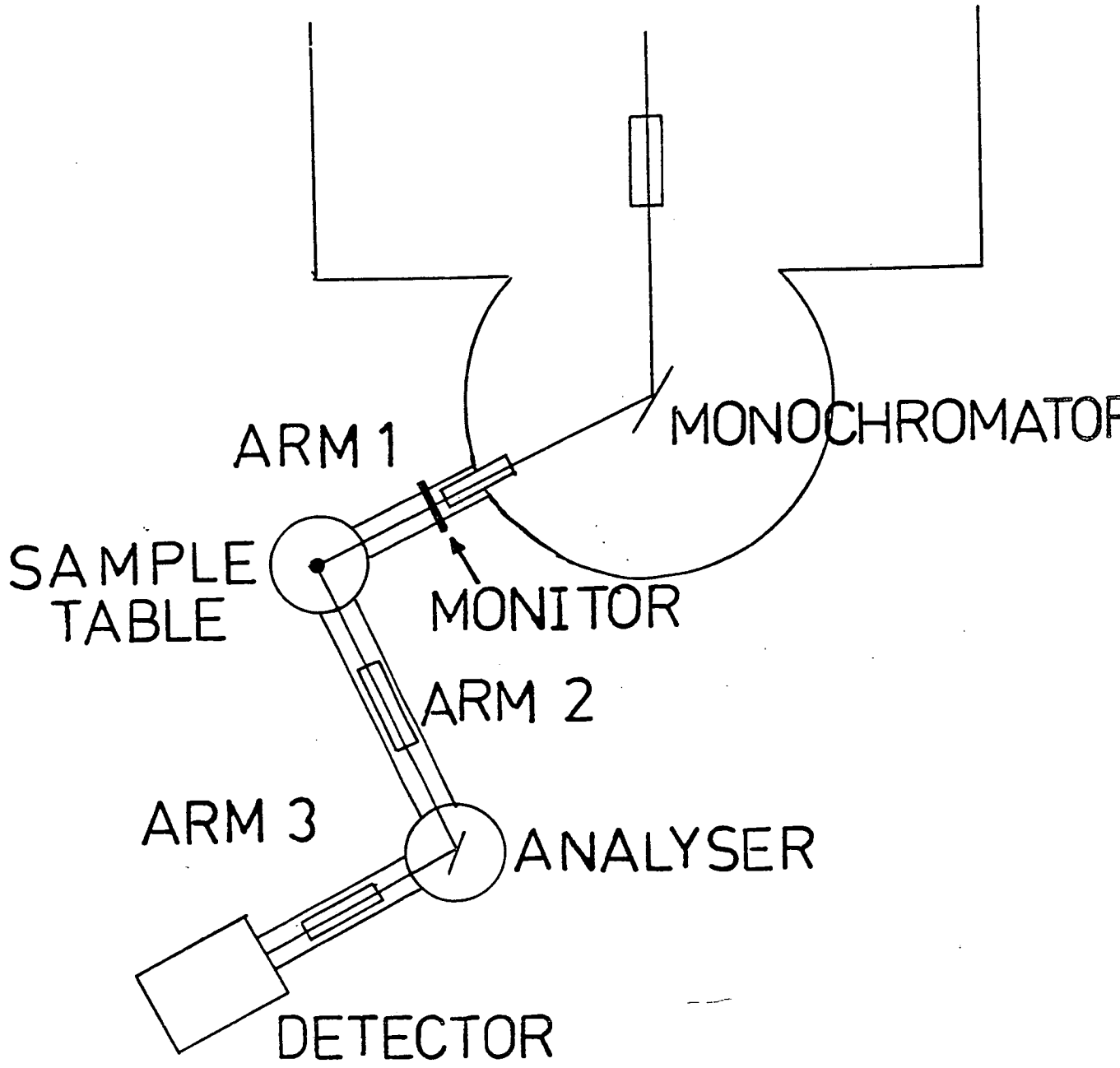
ARM 1
MONOCHROMATOR
SAMPLE TABLE
MONITOR
ARM 2
ARM 3
ANALYSER
DETECTOR

FIGURE(1.4.1)

the axis of the collimator is less than the spacing between the blades divided by the length of the collimator will, at least in principle, pass through.

A particular wavevector component $|\underline{k}_i|$ is selected out from this distribution of neutron energies by using a monochromator crystal (Bacon (1975) p. 5). This is done by utilising Bragg's law for the scattering of neutrons (or X-rays) from a solid. The arrangement for Bragg scattering is shown in figure (1.4.2) where $\underline{\tau}$ is a known reciprocal lattice vector of the monochromator, and $|\underline{k}|$ is the wavevector of the incident beam. The incident beam will only be scattered if $|\underline{k}|$ satisfied the condition:

$$|\underline{\tau}| = 2|\underline{k}| \sin\theta \qquad (1.4.2)$$

Hence when orientated at a given angle to the beam from the reactor the monochromator crystal will only scatter one wavevector component of the beam, given by equation (1.4.2). Different wavevector components can be selected out of the beam from the reactor by varying the orientation of the monochromator. The neutrons scattered from the monochromator then pass through another collimator on their way towards the sample. This collimator is mounted in a drum of shielding which surrounds the monochromator to protect against the radiation. The drum rotates with the monochromator in order to maintain the $\theta - 2\theta$ relation between incident and scattered beams shown in figure (1.4.2).

Before the neutrons are incident on the sample they pass through a monitor counter which measures the flux of the neutron beam. The monitor usually consists of a thin layer of ^{235}U in some suitable container and the flux is measured from the number of ^{235}U nuclei which undergo fission as the beam passes through. The efficiency of this type of monitor varies with wavevector as $|\underline{k}|^{-1}$.

Figure (1.4.2)

This figure shows the arrangement of the monochromator, the incident beam and the scattered beam for Bragg scattering

FIGURE(1.4.2)

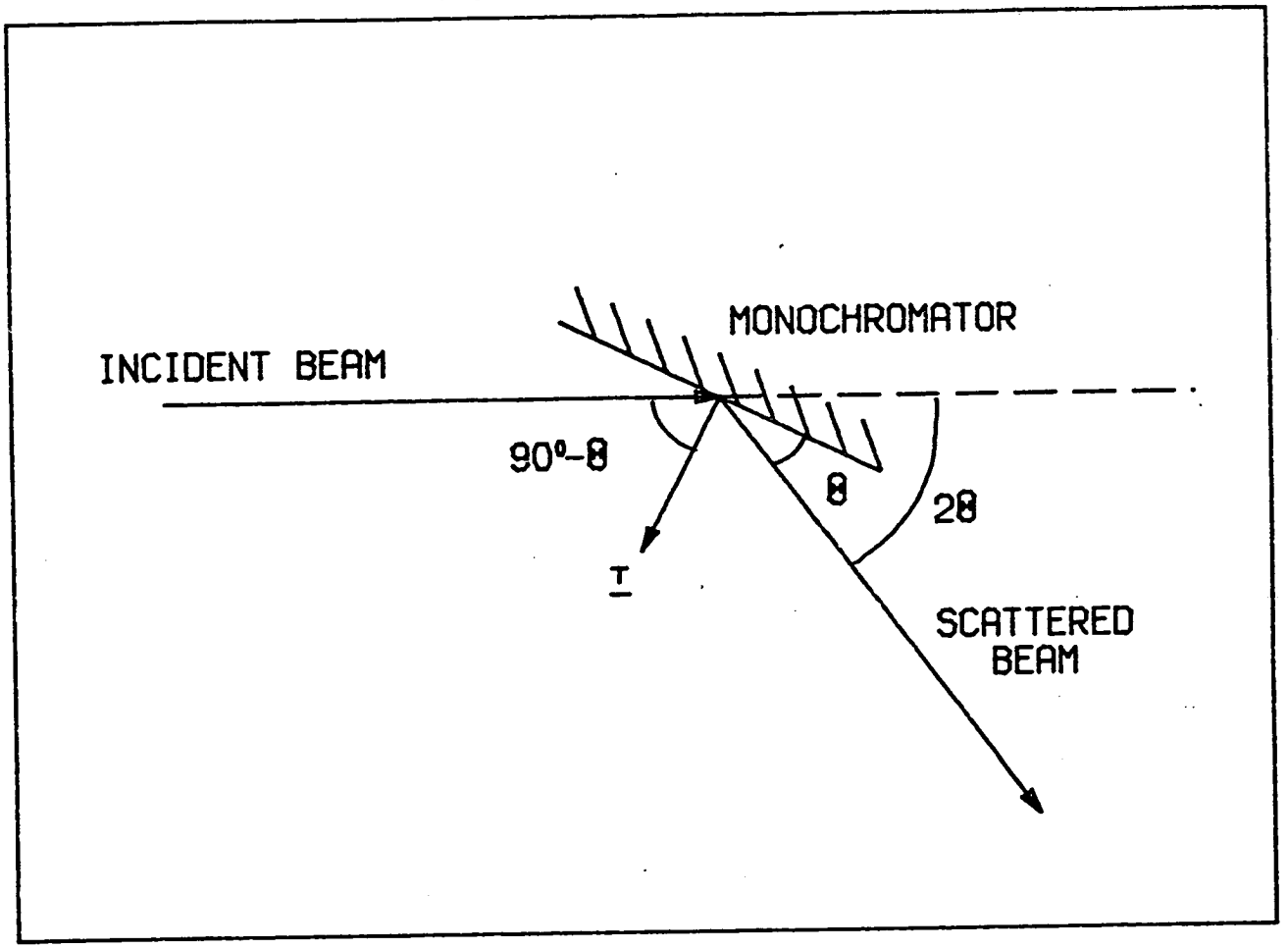

The sample is mounted on a table which can be rotated at the end of an arm, labelled arm 1 in figure (1.4.1) which is attached to the drum of shielding. Therefore once the positions of the crystallographic axes of the sample are known, it is possible to rotate the sample so that a chosen reciprocal lattice vector will be at some given angle to the incident wavevector $\underline{k}_i$.

In order to determine the number of neutrons scattered by a process in the sample with wavevector and energy transfers given by equations (1.4.1), it is necessary for the spectrometer to define the wavevector of the scattered neutrons, $\underline{k}_f$, that are measured. The direction of $\underline{k}_f$ is defined by the collimator on arm 2, shown in figure (1.4.1). In order to define the magntiude of $\underline{k}_f$ an analyser crystal is used. This crystal is used in the same way as the monochromator crystal. A known reciprocal lattice vector is oriented at a given angle to the scattered beam so that only neutrons of a particular wavevector will be scattered by the analyser. Those neutrons that are scattered then pass through a final collimator on arm 3 shown in figure (1.4.1) and then into the detector to be counted.

The operation of the spectrometer is controlled by a computer which runs the motors to position the arms and crystals. Once the computer has been given a set of crystallographic co-ordinates for the sample and a 'zero-angle' to relate these co-ordinates to the position of the sample table it can calculate the positions of the spectrometer components for $\underline{Q}$ and ω to correspond to a given scattering process in reciprocal space from equations (1.4.1). There is, however, an ambiguity in equations (1.4.1) since for a given $\underline{Q}$ and ω there are an infinite number of solutions for $\underline{k}_i$ and $\underline{k}_f$. In order to overcome this problem it is normal to fix the magnitude of either $\underline{k}_i$ or $\underline{k}_f$ to some chosen value. This leads to a unique solution of equations

(1.4.1).

The spectrometer is used to make measurements on the sample by measuring the intensity of neutrons scattered at a series of points along a path in $\underline{Q}$ and ω space. This scan then represents, up to intervening proportionality factors, a section through the dynamic structure factor $S(\underline{Q},\omega)$. There are two types of scan that are frequently used, the constant $\underline{Q}$ scan, where the value of $\underline{Q}$ is fixed and the value of ω is varied and the constant E where ω is fixed and $\underline{Q}$ is varied along some path in reciprocal space.

The proportionality factor between the measured intensity and $S(\underline{Q},\omega)$ depends on whether the spectrometer is operated with a fixed $|\underline{k}_i|$ or $|\underline{k}_f|$. The two cases will be considered in terms of equation (1.3.10a) which related the partial differential cross section $\frac{\partial^2\sigma}{\partial\Omega\partial E}$ to $S(\underline{Q}, \omega)$. In practice it is usual to measure the intensity for a given number of monitor counts. Since the monitor efficiency varies as $|\underline{k}_i|^{-1}$ the factor of $|\underline{k}_i|^{-1}$ in equation (1.3.10a) will be cancelled out in both cases. Therefore if the spectrometer has $|\underline{k}_f|$ fixed the measured intensity is directly proportional to $S(\underline{Q}, \omega)$. If however, $|\underline{k}_i|$ is fixed then instead of measuring $\frac{\partial^2\sigma}{\partial\Omega\partial E}$ the spectrometer actually measures $\frac{\partial^2\sigma}{\partial\Omega\partial\theta_A}$ where θ_A is the Bragg angle for the analyser. As a result, for $|\underline{k}_i|$ fixed the measured intensity is proportional to $k_F^3 \cot\theta_A S(\underline{Q},\omega)$.

Further to the above comments there is another intervening factor between the measured intensity and $S(Q, \omega)$. The spectrometer has so far been discussed only for neutrons with the preset wavevectors $\underline{k}_i$ and $\underline{k}_f$. Since the monochromator, analyser and sample are not ideal crystals and the collimators have a small but non-zero divergence neutrons with wavevectors only slightly different from $\underline{k}_i$ and $\underline{k}_f$

will have a finite probability of passing through the spectrometer and being counted. This finite resolution effect will not be described here since it is discussed in section (4) of Chapter Two where it plays an important role in the measurements. In inelastic measurements the resolution function plays an important role in deciding at what points to perform measurements due to 'focussing' effects (see for example Dolling (1975) p. 570).

CHAPTER TWO

An Experimental Test of Two Scale Factor Universality

2.1 Introduction

In this chapter the results of a neutron scattering experiment on the critical properties of the antiferromagnet Rb_2CoF_4 will be described and discussed. These experimental measurements were initiated following the suggestion of Bruce (1981, 1982) that data collected in a neutron or X-ray scattering experiment could be used to test the hypothesis of Two Scale Factor Universality (Stauffer et al (1972)). The general features of second order continuous phase transitions are now well known and are reviewed in detail in many texts (see for example Stanley (1971)). This introductory section will therefore not be a review of these features but instead will set out the notation for the rest of this chapter and will briefly describe the Universality hypothesis. The latter objective is itself divided into two parts, the first describes the Universality hypothesis as originally applied to critical exponents and the second to its extension to combinations of critical amplitudes via the hypothesis of Two Scale Factor Universality.

Since Rb_2CoF_4 is an antiferromagnet the critical temperature for the phase transition is the Néel temperature T_N. For temperatures close to the Néel temperature the thermodynamic quantities such as the sublattice magnetisation, staggered susceptibility and specific heat capacity are proportional to powers of the reduced temperature $\varepsilon = (T - T_N)/T_N$. These powers are known as critical exponents, and for the three quantities above the critical exponents β, γ and α, and also the critical amplitudes M_o, $\chi_o^{\pm}$ and $A_o^{\pm}$ are therefore defined by the equations:

$$M(\varepsilon) = \begin{cases} M_o\,(-\varepsilon)^{\beta}, & \varepsilon < 0 \\ 0, & \varepsilon > 0 \end{cases} \quad \text{(sublattice magnetisation)} \tag{2.1.1a}$$

$$k_B T\,\chi^{\pm}(\varepsilon) = \chi_o^{\pm}(\pm\varepsilon)^{-\gamma} \quad \text{(staggered susceptibility)} \tag{2.1.1b}$$

$$C^{\pm}(\varepsilon) = \frac{A_o^{\pm}}{\alpha}(\pm\varepsilon)^{-\alpha} \quad \text{(specific heat capacity)} \tag{2.1.1c}$$

The plus and minus signs refer to $\varepsilon > 0$ and $\varepsilon < 0$ respectively.

The critical exponents for the thermodynamic quantities are related to each other through the scaling hypothesis (Stanley (1971) p. 185). This hypothesis assumes that the part of the Helmholtz free energy that is singular at the phase transition may be written as a homogeneous function (see for example Stanley (1971) p. 175). The standard form for the singular part of the free energy is therefore given by:

$$F_s^{\pm}(\varepsilon, h) = \frac{\left[\pm \ell_\varepsilon\, \varepsilon\right]^{2-\alpha}}{\ell_h}\, f^{\pm}\left[\frac{\ell_h h}{(\pm \ell_\varepsilon\, \varepsilon)^{\beta+\gamma}}\right] \tag{2.1.2}$$

where ℓ_ε and ℓ_h are 'length scales' for the reduced temperature and magnetic field. For an antiferromagnet the magnetic field h is a staggered field which alternates from sublattice to sublattice. The length scales ℓ_ε and ℓ_h are such that by a suitable choice of their values the functions $f^{\pm}(x)$ will be universal. If equation (2.1.2) is differentiated in order to obtain the thermodynamic quantities in equation (2.1.1) then the critical amplitudes M_o, $\chi_o^{\pm}$ and $A_o^{\pm}$ will be given in terms of the lengths ℓ_ε and ℓ_h and the numerical values of the functions $f^{\pm}(x)$ and its derivatives at $x = 0$.

Apart from the thermodynamic quantities mentioned previously the function of most interest close to the phase transition is the correlation function. For an Ising system the correlation function

is defined as (Amit (1978) p. 20):

$$g(\underline{r}) = \sum_{\underline{h}} < S^z_{\underline{h}} S^z_{\underline{h}+\underline{r}} > - < S^z_{\underline{h}} >< S^z_{\underline{h}+\underline{r}} > \qquad (2.1.3)$$

The correlation function does not measure the degree of alignment of the spins but rather measures the correlation between the fluctuations of the spins from their expectation values. The correlation function is related to the susceptibility by the equation:

$$k_B T \ \chi(\varepsilon) = (g^z \mu_B)^2 \sum_{\underline{r}} g(r) \qquad (2.1.4)$$

where $g^z \mu_B$ relates the magnetic moment to the pseudo spin. It is, however, more frequent to consider the properties of the Fourier transform of $g(\underline{r})$ given by $G(\underline{q})$ rather than $g(\underline{r})$. This leads to a generalisation of equation (2.1.4) whereby the wavevector dependent susceptibility $\chi(\underline{q},\varepsilon)$ is given in terms of $G(\underline{q})$ by the relation:

$$k_B T \ \chi(\underline{q},\varepsilon) = (g^z \mu_B)^2 \ G(\underline{q}) \qquad (2.1.5)$$

The correlation length $\xi(\varepsilon)$ is defined from the correlation function by the relation (Amit (1978) p. 27):

$$\xi^2(\varepsilon) = \frac{1}{2d} \frac{\int r^2 g(r) \ d^d r}{\int g(r) \ d^d r} = - \frac{d^2 G(q)}{dq^2} \Bigg|_{q=0} \Big/ G(q=0) \qquad (2.1.6)$$

As with the thermodynamic quantities, close to the Néel temperature, the correlation length is proportional to a power of the reduced temperature. Therefore the critical exponent ν and the critical amplitudes $\xi_o^{\pm}$ are defined by the equation:

$$\xi^{\pm}(\varepsilon) = \xi_o^{\pm} (\pm \varepsilon)^{-\nu} \qquad (2.1.7)$$

From equation (2.1.7) it can be seen that at the Néel temperature the correlation length is infinite. The properties of the correlation function at the Néel temperature were considered by Fisher (1964)

who showed that G(q) would be proportional to $q^{-(2-\eta)}$ which serves as a definition of the critical exponent η.

A generalisation of the scaling hypothesis to the wavevector dependent susceptibility leads to the relation (Fisher and Aharony (1974))that:

$$k_B T \chi(\underline{q}, \varepsilon) = \chi_o^{\pm} (\pm\varepsilon)^{-\gamma} D^{\pm}(q\xi) \qquad (2.1.8)$$

where the functions $D^{\pm}(x)$ are Universal. The introduction of the wavevector q leads to the need for a third length scale ℓ_q. Therefore if the functions $D^{\pm}(x)$ are to be Universal the amplitude $\xi_o^{\pm}$ must be equal to the product of $\ell_q(\ell_\varepsilon)^{-\nu}$ and a Universal constant. This constant will be different for the two critical amplitudes since the functions $D^{+}(x)$ and $D^{-}(x)$ will not be the same.

The Universality hypothesis is an important feature of the modern theory of the critical phenomena associated with second order continuous phase transitions. In the Universality hypothesis systems are grouped into Universality classes. The hypothesis then states that for a given Universality class, Universal quantities such as the critical exponents and the functions $f^{\pm}(x)$ and $D^{\pm}(x)$ are the same for all systems within that Universality class. The values of the critical exponents and the forms of the functions $f^{\pm}(x)$ and $D^{\pm}(x)$ are therefore irrespective of the details of the Hamiltonian for the system and should only depend on those factors which determine the Universality class. Unfortunately there is no 'set of rules' which determine the members of a Universality class which apply in absolutely all cases. However, Kogut (1979) has listed three rules which apply for nearly all cases, certainly to this chapter and chapter three. These rules are that the Universality class depends on:

1) the spatial dimensionality of the system (d)

2) the dimension of the local variables in the Hamiltonian (n)

3) the symmetries of the coupling between the local variables.

The first rule is obvious and needs no explanation. For magnetic systems the second rule depends on the symmetry group of a spin in the system. Uniaxial symmetry would imply n = 1 (Ising), planar symmetry n = 2 (X - Y) and isotropic symmetry n = 3 (Heisenberg) Universality classes. The final rule would for a magnetic system apply to the exchange or to the coupling to an external magnetic field if one is present in the Hamiltonian.

In order that the functions $f^{\pm}(x)$ and $D^{\pm}(x)$ were Universal it was necessary to introduce three length scales ℓ_h, ℓ_ε and ℓ_q. From the dependence of the critical amplitudes $\chi_o^{\pm}$, $A_o^{\pm}$ and $\xi_o^{\pm}$ on these lengths imposed by the requirement that $f^{\pm}(x)$ and $D^{\pm}(x)$ are Universal it is necessary that the ratios χ_o^{+}/χ_o^{-}, A_o^{+}/A_o^{-} and ξ_o^{+}/ξ_o^{-} are also Universal. The Universality of these ratios and the functions $f^{\pm}(x)$ and $D^{\pm}(x)$ therefore depends on the existence of the three independent length scales or scale factors as they are alternatively known. This formulation of the Universality hypothesis could therefore be dubbed 'Three Scale Factor Universality'.

The hypothesis of Two Scale Factor Universality, as originally given by Stauffer et al (1972), proposes that the products $F_s^{\pm}(\varepsilon, 0)(\xi^{\pm})^d$ should be Universal quantities. The temperature independence of these products within the scaling region had been noted earlier by Kadanoff (1966) as a heuristic argument for the hyperscaling relation of $d\nu = 2 - \alpha$. A Universal value for these products however goes further than this and implies that there is a Universal relation between the length scales ℓ_q and ℓ_h given by:

$$\ell_q^d/\ell_h = \text{a Universal constant} \qquad (2.1.9)$$

This relation reduces the number of independent length scales from three to two, hence the name Two Scale Factor Universality. Since the critical amplitudes are related to the length scales a consequence of this relation is that certain combinations of critical amplitudes which mix the critical amplitudes of the thermodynamic quantities with the critical amplitudes of the correlation length should be Universal. If the dependences of the critical amplitudes M_o, $\chi_o^{\pm}$ and $A_o^{\pm}$ on the length scales ℓ_h, ℓ_ε and ℓ_q are found from differentiating equation (2.1.2) then two such combinations would be:

$$\frac{A_o^+}{\alpha} \cdot (\xi_o^+)^d = \text{a Universal constant} \qquad (2.1.10a)$$

and

$$\frac{M_o^2 \ (\xi_o^+)^d}{\chi_o^+} = \text{a Universal constant} \qquad (2.1.10b)$$

Equation (2.1.10a) was used by Stauffer et al (1972) to test the hypothesis with experimental data taken from the literature. A discussion of the results of this test will be given in section (6) where they will be compared with the result of the measurements reported in this chapter.

The hypothesis of Two Scale Factor Universality was considered within the renormalisation group framework by Hohenberg et al (1976) and by Bervillier (1976). It was shown by these authors that to order $(4 - d)^2$ for the Ising model and to order $1/n^2$ for X - Y and Heisenberg models that the combinations of critical amplitudes such as equations (2.1.10a - b) were universal. Another verification of the hypothesis was given by Bruce (1981) who showed that the combination of critical amplitudes in equation (2.1.10b) was equal to an integral which had a universal value. This result was derived by Bruce from a theoretical study of the temperature dependence

of the neutron (or X-ray) scattering cross section close to a second order phase transition. In this study it was shown by Bruce that the combination of critical amplitudes (2.1.10b) could be obtained from the data taken in a single neutron scattering experiment.

Following the suggestion of Bruce (1981) these measurements on Rb_2CoF_4 were performed in order to test the hypothesis of Two Scale Factor Universality. The quantity measured was not quite that given in equation (2.1.13b) but rather was given by:

$$R_s = \frac{\chi_o^+ (\kappa_o^+)^d}{M_o^2} \qquad (2.1.11)$$

where κ_o^+ is the critical amplitude for the inverse correlation length in reciprocal lattice units and is related to ξ_o^+ by $\kappa_o^+ = 1/2\pi\xi_o^+$. Rb_2CoF_4 has critical exponents corresponding to the d = 2 Ising Universality class and the value of R_s obtained for Rb_2CoF_4 has been compared to the value of R_s calculated from the exact solution of the ferromagnetic Ising model of 0.051 (Bruce (1981)).

The rest of this chapter is set out as follows. In section (2) the relation between R_s and the quantities measured in a neutron scattering experiment is derived. The magnetic properties of Rb_2CoF_4 are discussed in section (3) along with a description of the instrumental conditions and the temperature control. In section (2) it will be shown that the instrumental resolution function plays an important part in the theory and therefore in section (4) the formalism used for the resolution function is discussed. The results of the experiment are given in section (5) and finally section (6) contains a discussion of these results.

2.2 Connection with Neutron Scattering

In this section it will be shown how the combination of critical amplitudes R_s (equation (2.1.14)) occurs as a proportionality constant when the ratio of the intensities at an antiferromagnetic Bragg peak position above and below the Néel temperature is taken. The measurement of these intensities and the wavevector dependent susceptibility gives sufficient information to determine R_s. In order to derive the formula for R_s the dynamic structure factor $S(\underline{Q}, \omega)$, introduced in Chapter One, is written for a uniaxial magnet as:

$$S(\underline{Q}, \omega) = \mathrm{Sin}^2 \alpha (g^z \mu_B)^2 S''(\underline{Q}, \omega) + (1 + \mathrm{Cos}^2\alpha) (g^{\perp} \mu_B)^2 S^{\perp}(\underline{Q},\omega) \quad (2.2.1)$$

where α is the angle between the wavevector $\underline{Q}$ and the magnetic ordering direction z, $S''(\underline{Q}, \omega)$ is the scattering from the z components of the spins and $S^{\perp}(\underline{Q},\omega)$ is the scattering from the x-y components. The $S^{\perp}(\underline{Q}, \omega)$ gives the contribution from the spin waves and is neglected since Rb_2CoF_4 is an Ising antiferromagnet and the spin waves will not play a part in either the theory or the experimental measurements. The structure factor $S''(\underline{Q},\omega)$ is given by the equation:

$$S''(\underline{Q},\omega) = \frac{1}{2\pi} \int dt\, e^{-i\omega t} \sum_{ij} e^{i\underline{Q}.\underline{r}_{ij}} \langle S_i^z(o) S_j^z(t) \rangle \quad (2.2.2)$$

where the angular brackets < > denote a thermal average. Since the hypothesis of Two Scale Factor Universality is formulated for static critical phenomena $S''(\underline{Q}, \omega)$ must be integrated over all frequencies to obtain the static structure factor $S''(\underline{Q})$ which will be given by

$$S''(\underline{Q}) = \int_{-\infty}^{\infty} d\omega\, S''(\underline{Q}, \omega) = \sum_{ij} e^{i\underline{Q}.\underline{r}_{ij}} \langle S_i^z S_j^z \rangle \quad (2.2.3)$$

Because Rb_2CoF_4 is a two sublattice antiferromagnet with a ground state pseudo-spin $S = \frac{1}{2}$ level, S_i^z can be replaced by:

$$S_i^z = S\, e^{i\,\underline{\tau}.\underline{R}_i}\, \sigma_i \quad (2.2.4)$$

where the set of vectors $\underline{\tau}$ are the antiferromagnetic reciprocal lattice vectors, σ is an Ising variable which can take on the values ± 1 and $S = \frac{1}{2}$. Then on substituting equation (2.2.4) into equation (2.2.3) and using equation (2.1.2) and the translational invariance of $\langle \sigma_i \rangle$ the static structure factor $S''(\underline{Q})$ becomes:

$$S''(\underline{Q}) = N^2 S^2 \langle\sigma\rangle^2 \Delta(\underline{Q}) + S^2 \Delta(\underline{Q} + \underline{q}) G(\underline{q}) \qquad (2.2.5)$$

where the delta function $\Delta(\underline{q})$ constrains $\underline{Q}$ to be an antiferromagnetic lattice vector. The first term in equation (2.2.5) is the antiferromagnetic Bragg peak and the second term is the Fourier transform of the correlation function.

The intensity measured with the spectrometer set for elastic scattering is given in terms of the dynamic structure factor by the equation

$$I(\underline{Q}) = I_o |f(\underline{Q})|^2 \iint d\underline{g}\, d\omega \; R(\underline{Q},\underline{g},\omega)\, S(\underline{Q},\omega) \qquad (2.2.6)$$

where I_o is an overall scale factor, $f(\underline{Q})$ is the form factor of the magnetic ion and $R(\underline{Q},\underline{g},\omega)$ is the resolution function. The resolution function is defined to be the probability of observing a neutron scattered with wavevector $\underline{Q} + \underline{g}$ and frequency ω given that the spectrometer was set to observe a wavevector transfer $\underline{Q}$ and zero frequency transfer. It is assumed for the present and will be shown in section (4) that the integration over frequency in equation (2.2.6) is a good approximation of equation (2.2.3). The resolution function is then just a function of $\underline{Q}$ and $\underline{g}$ and is defined so that $R(\underline{Q}, 0) = 1$. Then by using equations (2.2.1) and (2.2.5) the intensity $I(\underline{Q})$ can be written as

$$I(\underline{Q},\varepsilon) = I_o |f(\underline{Q})|^2 \sin^2\alpha \int d\underline{g} \left[M^2(\varepsilon)\, \Delta(\underline{Q}+\underline{g}) + k_B T\, \chi(\underline{q} + \underline{g},\varepsilon) \Delta(\underline{Q} + \underline{q}) \right] \times R(\underline{Q},\underline{g}) \qquad (2.2.7)$$

where $M(\varepsilon) = Ng^z \mu_B S\langle\sigma\rangle$ is the sublattice magnetisation and the temperature dependence has been specifically included by writing $I(\underline{Q},\varepsilon)$. The form factor $f(\underline{Q})$ and $\sin^2\alpha$ factors are outside the integration since they only vary slowly with $\underline{Q}$ and are essentially constant over the resolution function.

For values of ε sufficiently close to zero that the scaling forms for $M(\varepsilon)$ and $k_\beta T\,\chi(\underline{q}, \varepsilon)$ hold the intensity $I(\tau,\varepsilon)$, where τ is an antiferromagnetic reciprocal lattice vector, may be written as

$$\frac{I(\underline{\tau},\varepsilon)}{P(\underline{\tau})} = M_o^2(-\varepsilon)^{2\beta} H(-\varepsilon) + \chi_o^{\pm} (\pm\varepsilon)^{-\gamma} V_R C^{\pm}(\kappa) \qquad (2.2.8)$$

where $P(\underline{\tau}) = I_o |f(\underline{\tau})|^2 \sin^2\alpha$, $H(x)$ is the Heaviside (theta) function and $C^{\pm}(\kappa)$ is the convolution of $R(\underline{\tau}, \underline{g})$ with the function $D(^q/_\kappa)$. The function $D^{\pm}(x)$ was introduced in section (1) in equation (2.1.8) where its argument was $q\xi$. The change in argument now reflects the specific change to reciprocal lattice units for q and the inverse correlation length κ. Explicitly then $C^{\pm}(\kappa)$ is given by the integral:

$$C^{\pm}(\kappa) = \frac{1}{V_R} \int d\underline{g}\, R(\underline{\tau}, \underline{g})\, D^{\pm}(^g/_\kappa) \qquad (2.2.9)$$

If values of $\varepsilon > 0$ are denoted by ε^+ then from equation (2.2.8) $I(\underline{\tau}, \varepsilon^+)$ is given by:

$$\frac{I(\underline{\tau}, \varepsilon^+)}{P(\underline{\tau})} = \chi_o^+ (\varepsilon)^{-\gamma} V_R.\ C^+(\kappa) \qquad (2.2.10)$$

For values of $\varepsilon < 0$, denoted by ε^-, $I(\underline{\tau}, \varepsilon^-)$ contains a contribution from both the sublattice magnetisation and the susceptibility. However, since the intensity of the susceptibility decreases as ε becomes more negative and the intensity of the sublattice magnetisation increases the intensity $I(\underline{\tau}, \varepsilon^-)$ will for values of ε sufficiently less than zero be given by:

$$\frac{I(\underline{\tau}, \varepsilon^-)}{P(\underline{\tau})} = M_o^2 (-\varepsilon)^{2\beta} \qquad (2.2.11)$$

Therefore if the ratio of equation (2.2.10) to (2.2.11) is taken for values of ε^+ and ε^- with the same magnitude then the result is:

$$\frac{I(\underline{\tau}, \varepsilon^+)}{I(\underline{\tau}, \varepsilon^-)} = \frac{\chi_o^+}{M_o^2} |\varepsilon|^{-(\gamma+2\beta)} V_R \, C^+(\kappa) \qquad (2.2.12)$$

Hence using the result $|\varepsilon|^{-(\gamma+2\beta)} = (\kappa/\kappa_o^+)^{-d}$, which follows from the scaling form $\kappa = \kappa_o^+ \varepsilon^\nu$, and the scaling relations (Stanley (1971) p. 185) equation (2.2.12) may be written as

$$\frac{I(\underline{\tau}, \varepsilon^+}{I(\underline{\tau}, \varepsilon^-} = R_s \cdot V_R \cdot \frac{C^+(\kappa)}{\kappa^d} \qquad (2.2.13)$$

where R_s is given by equation (2.1.11).

Therefore R_s can be determined given three quantities as a function of reduced temperature, the intensities $I(\underline{\tau}, \varepsilon^+)$ and $I(\underline{\tau}, \varepsilon^-)$ and the inverse correlation length above the Néel temperature. In order to obtain κ it is necessary to measure $I(\underline{Q}, \varepsilon^+)$ as a function of $\underline{Q}$ about the antiferromagnetic reciprocal lattice vector. The intensity $I(\underline{Q}, \varepsilon^+)$ is given by the equation

$$I(\underline{Q}, \varepsilon^+) = P(\underline{Q}) \, \chi_o^+ \, \varepsilon^{-\gamma} \int d\underline{q} \, R(\underline{Q}, \underline{q}) \, D^+ \left({}^{\underline{q}+\underline{q}}/_{\kappa} \right) \Delta(\underline{Q}+\underline{q}) \qquad (2.2.14)$$

A value of κ can be found from equation (2.2.14) using the techniques explained in appendix A if an explicit functional form for $D^+(x)$ is known. There is no exact form for $D^+(x)$ and as a result there are a number of approximants. The two best known approximants are, the Ornstein-Zernike form (Stanley (1971) p. 100), which is

$$D^+(x) = \frac{1}{1 + x^2} \qquad (2.2.15a)$$

and the Fisher approximant (Fisher (1964)), which is

$$D^+(x) = \frac{1}{\left(1 + {}^{x^2}/_{1-\eta/2}\right)^{1-\eta/2}} \qquad (2.2.15b)$$

In the work reported in this chapter The Ornstein-Zernike approximant has been used. This choice of approximant was based on the results of the work of Tracy and McCoy (1975), who studied the applicability of various approximants to $D^+(x)$ for the d = 2 Ising model. Since the d = 2 Ising model has been solved exactly (Onsager (1944))Tracy and McCoy were able to calculate the "exact" $D^+(x)$ by numerical integration. The results of Tracy and McCoy showed that while the Ornstein-Zernike approximant was accurate to within 5% for $x < 11$ the Fisher approximant was only accurate to within 5% for $x < 0.7$ or $x > 163$. Since Rb_2CoF_4 is expected to have a phase transition in the d = 2 Ising universality class and the data was mostly taken for values of $x < 11$ the Ornstein-Zernike approximant is expected to work very well in this case.

2.3 Experimental Method

The purpose of this section is to explain the various aspects associated with the experimental measurements. To this end it is divided into three subsections. The first subsection describes the crystallographic and magnetic properties of Rb_2CoF_4. In the second subsection a description and justification of the way in which scans were performed to take account of the special features of the magnetic ordering in Rb_2CoF_4 will be given. The third subsection contains a description of the spectrometer used and the apparatus for the temperature control.

The experimental measurements were performed at the Institut Laue-Langevin and were carried out with the collaboration of Dr. D. McK Paul.

2.3 i) Properties of Rb_2CoF_4

The crystallographic and magnetic structure of Rb_2CoF_4 is of the K_2NiF_4 type (Birgeneau et al (1970)) and is shown in figure (2.3.1). The Co^{2+} ions in this structure are situated on the sites of a body centred tetragonal lattice and are surrounded by an octahedron of fluorine ions. Application of crystal field theory shows that the lowest level for the Co^{2+} ions is a pseudo spin $s = \frac{1}{2}$ doublet (Breed et al (1969)). The anisotropy of the exchange interaction within this doublet has been estimated by Breed et al (1969) from susceptibility measurements. These authors estimated a ratio of transverse to Ising exchange of 0.23. A more recent value for this ratio of 0.55 can be obtained from the spin wave measurements of Ikeda and Hutchings (1978). This large anisotropy in Rb_2CoF_4 means that the phase transition is expected to be dominated by Ising critical behaviour throughout the scaling region.

The crystal structure of Rb_2CoF_4 is such that the super-exchange path between nearest neighbour Co^{2+} ions in the a - b plane leads to a strong antiferromagnetic exchange. The exchange between Co^{2+} ions in different planes is, however, much weaker. In the isomorphous system K_2CoF_4, Ikeda and Hirakawa (1974) have estimated the interplane exchange to be 10^{-3} times smaller than the intraplane exchange. Since Rb_2CoF_4 and K_2CoF_4 have very similar lattice parameters and Néel temperatures and there is no indication otherwise from spin wave measurements (Ikeda and Hutchings (1978)) the interplane exchange in Rb_2CoF_4 is also assumed to be at least 10^{-3} times smaller than the intraplane exchange.

The weakness of the out of plane exchange means that above the

Figure (2.3.1)

This figure shows the chemical (nuclear) unit cell of Rb_2CoF_4. At 102 K the cell has lattice parameters a = b = 4.128 A and c = 13.622 A. The orientation of the spins on the Co^{2+} ions is shown. The energy of the body centre spin is the same whether it be up or down

FIGURE (2.3.1)

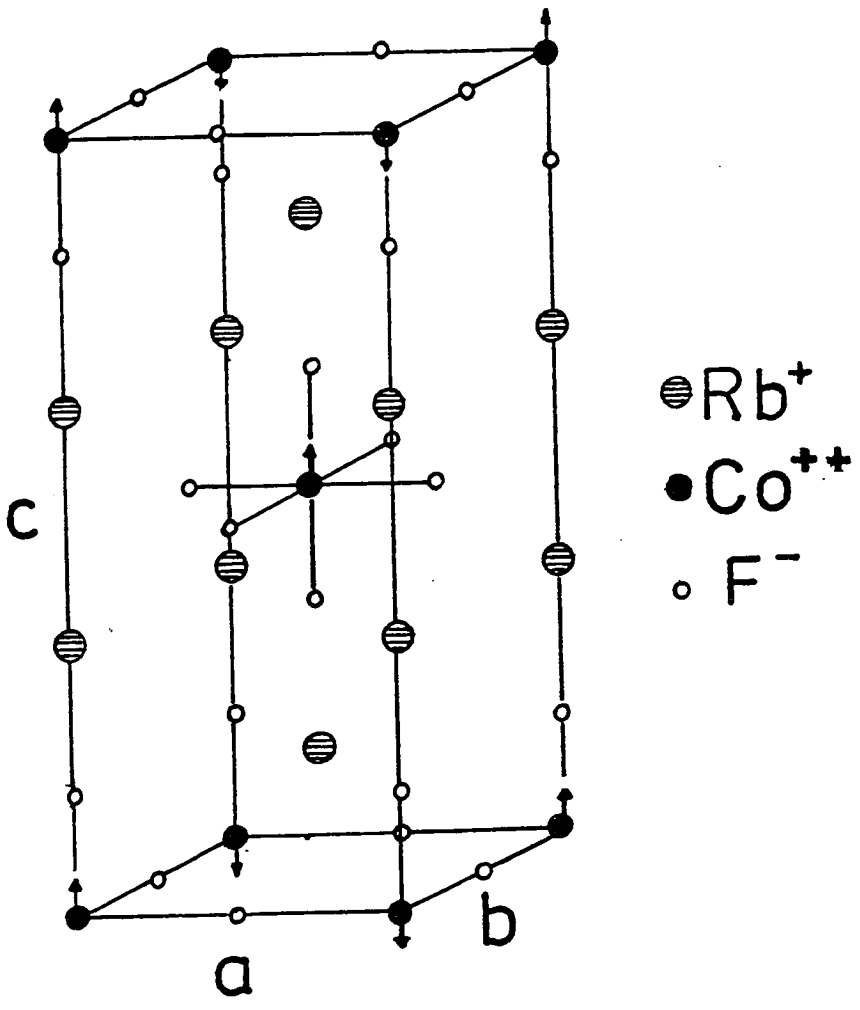

Néel temperature the interplane correlations are insignificant and the critical scattering is given by the intraplane correlations. Therefore above the Néel temperature the properties of Rb_2CoF_4 are those of a two dimensional Ising system. This two dimensional property of the phase transition is typical of the K_2NiF_4 type magnetic materials and is seen in the neutron scattering cross section as rods (or ridges as they are sometimes referred to) of scattering parallel to the c axis in reciprocal lattice. (Birgeneau et al. (1970)). In the experiment reported here the sample of Rb_2CoF_4 was mounted with a $(1, \bar{1}, 0)$ axis vertical and the reciprocal lattice diagram for this scattering plane is shown in figure (2.3.2) with the positions of the rods of scattering marked by the hashed lines. In figure (2.3.3) some scans along the $(\frac{1}{2}, \frac{1}{2}, \ell)$ rod are shown for various temperatures above the Néel temperature. The variation of the rod height with ℓ is through the form factor and $\sin^2\alpha$ terms in equation (2.2.7). The thickness of the rod depends on the correlations between spins in the a - b planes and therefore a scan perpendicular to the rod, along the line C - D in figure (2.3.2), measures the wavevector dependent susceptibility for the two dimensional magnetisation.

Previous work on Rb_2CoF_4 has confirmed the qualitative aspects of this model but has had a wider variation on the quantitative aspects. The bulk susceptibility measurements of Breed et al. (1969) were consistent with Rb_2CoF_4 being in the d = 2 Ising universality class. However, the neutron scattering results of Samuelsen (1974), although they showed the existence of the rod of scattering, gave values for the critical exponents γ and ν of 1.34 ± 0.22 and 0.89 ± 0.10 which were not consistent with the values of 1.75 and 1.00 for the d = 2 Ising model. The data analysis in

Figure 2.3.2

This figure shows the reciprocal lattice space diagram for the scattering plane of the measurements. Nuclear Bragg peaks are indicated by triangles. The rods of scattering above the Néel temperature are indicated by the hashed lines, while the positions of the magnetic peaks below are indicated by the circles and squares for the magnetic domains.

FIGURE(2.3.2)

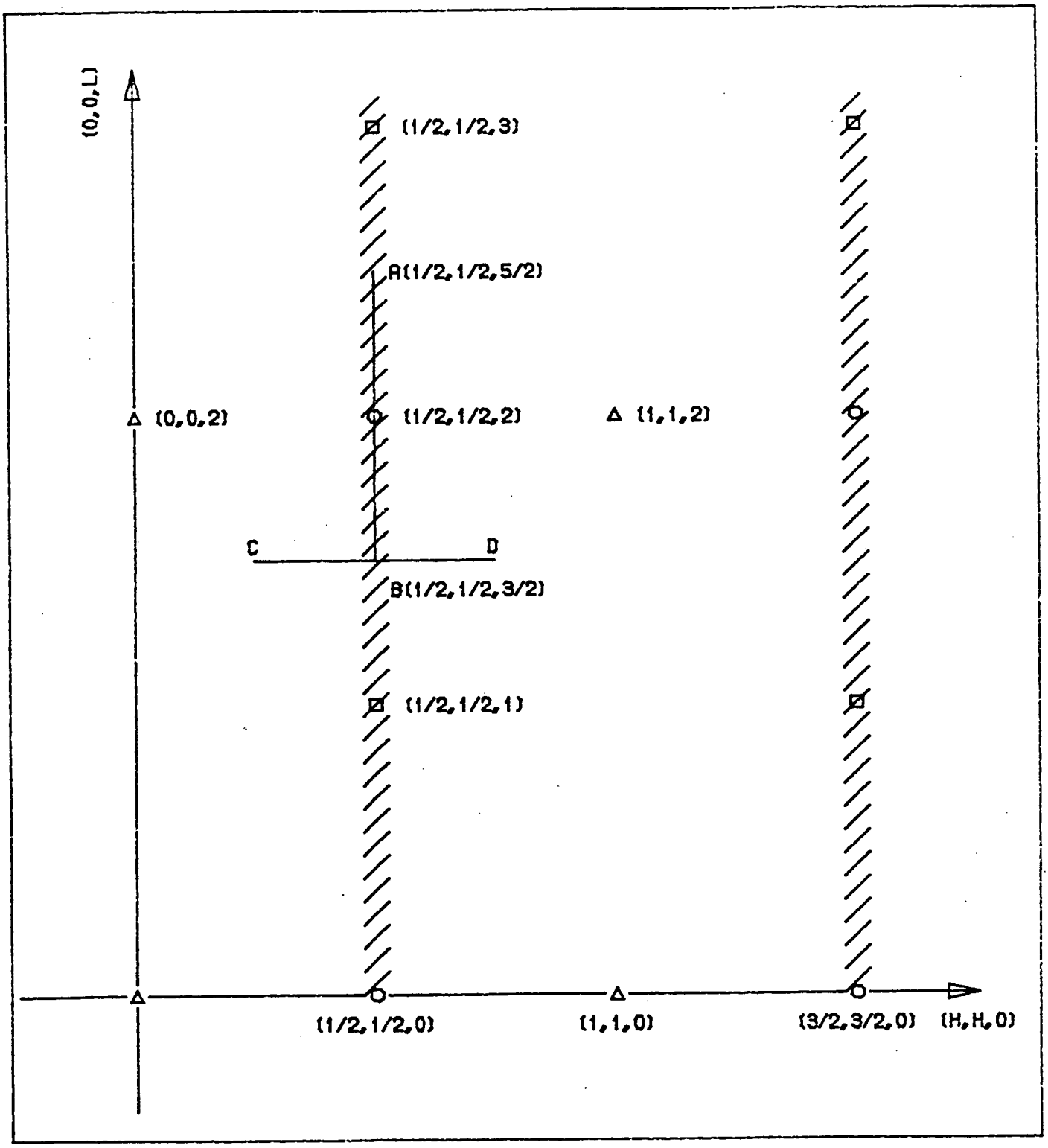
(0,0,L)
(1/2,1/2,3)
R(1/2,1/2,5/2)
(0,0,2)
(1/2,1/2,2)
(1,1,2)
C
D
B(1/2,1/2,3/2)
(1/2,1/2,1)
(1/2,1/2,0)
(1,1,0)
(3/2,3/2,0)
(H,H,0)

Figure (2.3.3)

The variation of the intensity along the rod of scattering above the Néel temperature is shown for three different temperatures in this figure. The solid lines are guides to the eye.

FIGURE(2.3.3)

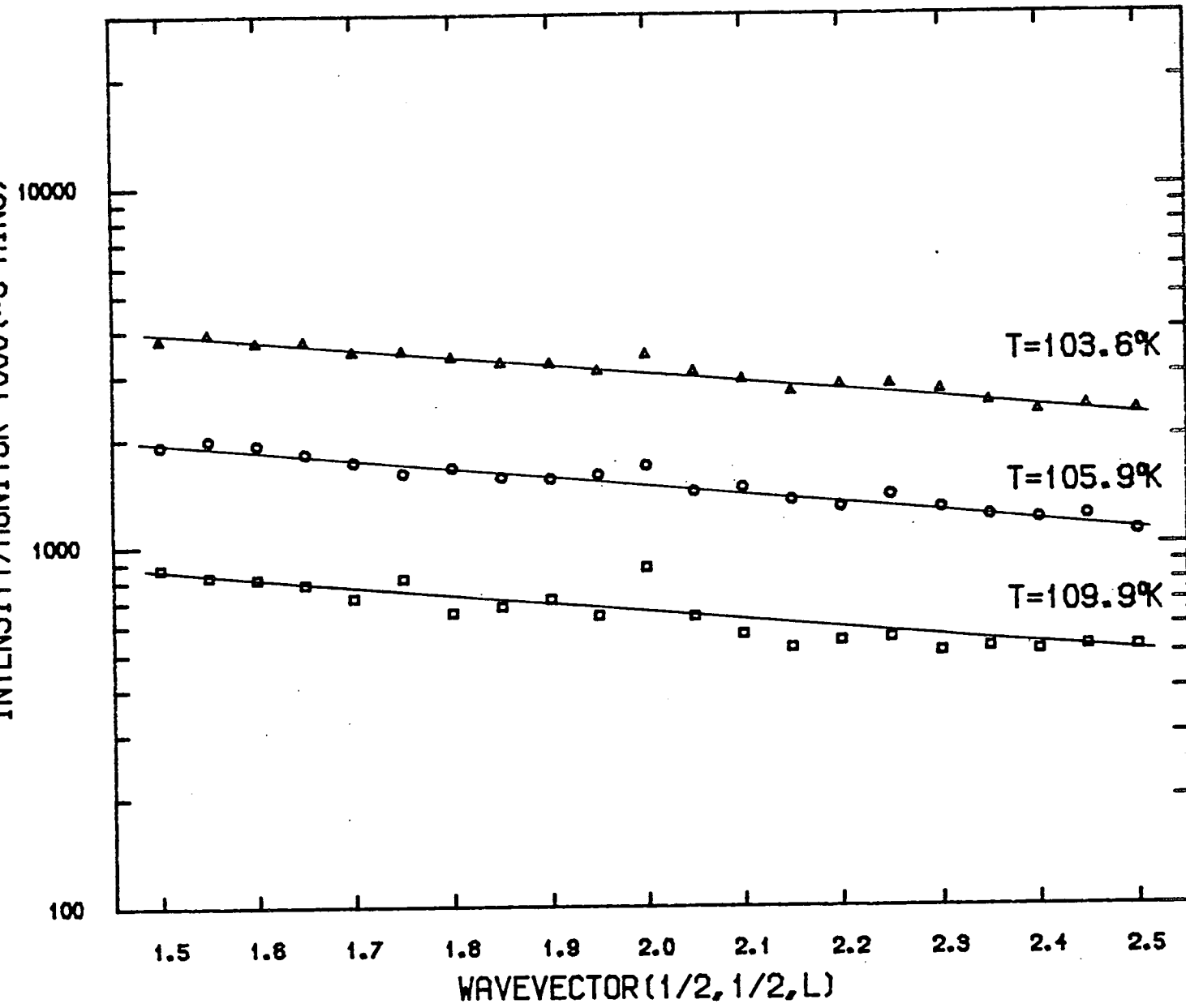
10000
1000
100
T=103.6K
T=105.9K
T=109.9K
1.5
1.6
1.7
1.8
1.9
2.0
2.1
2.2
2.3
2.4
2.5
WAVEVECTOR(1/2,1/2,L)

Samuelsen's paper was done using the Ornstein-Zernike approximant for the wavevector dependent susceptibility. Further neutron scattering measurements on Rb_2CoF_4 (Ikeda et al. (1979)) and on the isomorphous K_2CoF_4 (Ikeda and Hirakawa (1974)) did give values for γ and ν, in better agreement with the theoretical results. Unfortunately in both these papers the data analysis for the wavevector dependent susceptibility was performed using the Fisher approximant which, for the range of wavevectors $0 < q/\kappa < 10$ used in these papers, was shown by Tracy and McCoy (1975) to be a very poor approximant. Therefore as well as determining a value for the combination of critical amplitudes R_s from these measurements on Rb_2CoF_4 the critical exponents γ and β have been determined and the temperature dependence of the inverse correlation length checked. The values obtained for the exponents and the results for the temperature dependence of the inverse correlation length are presented in section (5). These results are consistent with those for the d = 2 Ising model.

The magnetic order in Rb_2CoF_4 below the Néel temperature is, however, much more complicated than that above. When the two dimensional long range order has occured within the a - b planes there will be an "effective exchange" between the next nearest neighbour (n.n.n.) planes. This "effective exchange" is the product of the weak n.n.n. ferromagnetic interplanar exchange and the number of spins in the a - b planes. The "effective exchange" between n.n. planes cancels by symmetry with the body centre spin having the same energy whether it is up or down. Therefore, when a sample of Rb_2CoF_4 is cooled through its Néel temperature the n.n.n. planes attempt to order; however, since the interaction is weak and there are two energetically equal domains a large number of stacking faults occur.

The result is that the Bragg scattering below the Néel temperature is neither a rod of scattering nor a resolution limited peak but is rather the modulus square of the Fourier transform of the stacking distribution of the planes. This distribution of Bragg scattering is peaked at the points in reciprocal space which correspond to the structure factors for a sample with all the body centre spins in an up or down domain. In figure (2.3.2) these points are marked with (O)'s and (□)'s to differentiate between the two domains. Figure (2.3.4) shows some examples of scans between points A and B in figure (2.3.2) below the Néel temperature which show the distribution of the Bragg scattering. This effect has been seen in a number of the K_2NiF_4 type magnetic systems (Birgeneau et al. (1970), Samuelsen (1974), Birgeneau et al. (1980)). In Rb_2CoF_4 it is known (Samuelsen (1974)) that the width and shape of these peaks depends on the rate at which the sample was cooled through its Néel temperature and are therefore not in general reproducible.

2.3 ii) Correcting for the stacking fault effect

In order to apply equation (2.2.13) it is not simply enough to measure the intensity at a point along the rod, instead a modification must be made to account for the effect of the stacking faults below the Néel. In practice this modification is very simple, instead of measuring the intensity at a point a scan is performed to measure the integrated intensity between points A and B in figure (2.3.2). Each of the data points in the scan is corrected for the form factor and $Sin^2\alpha$ prefactors before the scan is integrated. This was done for both the Bragg scattering below the Néel temperature and for the critical scattering above the Néel temperature.

Figure (2.3.4)

The variation of the magnetic scattering between the points A and B in figure (2.3.2) is shown at three temperatures below the Néel temperature.

FIGURE(2.3.4)

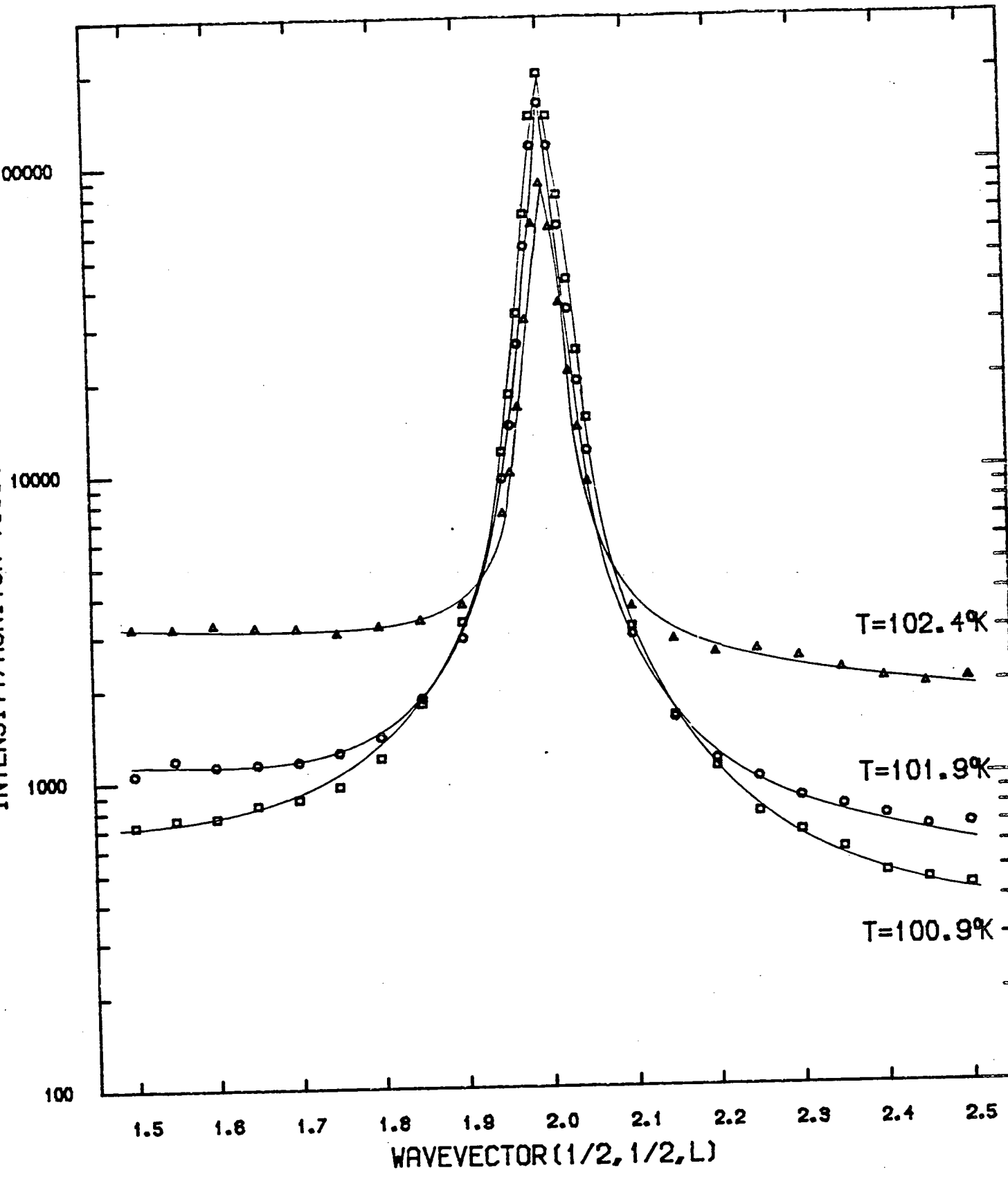
00000
10000
1000
100
T=102.4K
T=101.9K
T=100.9K
1.5
1.6
1.7
1.8
1.9
2.0
2.1
2.2
2.3
2.4
2.5
WAVEVECTOR(1/2,1/2,L)

In order to justify this modification two things are shown, firstly the structure factor below the Néel temperature with stacking faults present is calculated and, secondly, it is shown that variations in the resolution function along the length of the scan do not alter this result significantly.

In order to include stacking faults in $S''(\underline{Q})$ below the Néel temperature equation (2.2.4) is rewritten in the form

$$\langle S_i^z \rangle = S \, \Omega_u \, e^{i \underline{\tau} \cdot \underline{r}_k} \, \langle \sigma_k^u \rangle \qquad (2.3.1)$$

where the site i is at the position $\underline{r}_k$ within the u^{th} a - b plane. The vector $\underline{\tau}$ represents the antiferromagnetic reciprocal lattice vector within the a* - b* plane. Stacking faults are included through the variable Ω_u which is ± 1 depending on whether the u^{th} plane is up or down. Since the interplane exchange is so weak it is quite reasonable to assume that $\langle \sigma_k^u \rangle$ does not depend on the stacking distribution and is therefore translationally invariant. Then if the contribution from the susceptibility is neglected below the Néel temperature $S''(\underline{Q})$ is just given by:

$$S''(\underline{Q}) = N^2 S^2 \, \langle \sigma \rangle^2 \, \Delta_\perp(\underline{Q}_\perp) \, |F(Q_c)|^2 \qquad (2.3.2)$$

where $\underline{Q} = \underline{Q}_\perp + \underline{Q}_c$ with $\underline{Q}_\perp$ in the a* - b* plane and $\underline{Q}_c$ along the c* direction. The factor $\Delta_\perp(\underline{Q}_\perp)$ constrains $\underline{Q}_\perp$ to be an antiferromagnetic reciprocal lattice vector within the a* - b* plane. The $F(Q_c)$ in equation (2.3.2) is the Fourier transform of the stacking distribution and is given by

$$F(Q_c) = \frac{1}{N_c} \sum_u e^{i \underline{Q}_c \underline{u}} \, \Omega_u \qquad (2.3.3)$$

where N_c is the number of a - b planes. Therefore if $R(\underline{Q}\,\underline{g})$ is constant along the scan from points A to B then the integrated intensity $I'(\underline{Q}_\perp) = \int dQ_c \, I(\underline{Q})/P(\underline{Q})$ is given by:

$$I'(\underline{Q}_\perp) = N_c^2 M^2(\varepsilon) \Delta_\perp(\underline{Q}_\perp) \int dQ_c \int dg_c R(g_c) |F(\underline{Q}_c + \underline{g}_c)|^2 \qquad (2.3.4)$$

where $M(\varepsilon)$ is the two dimensional sublattice magnetisation and $R(g_c)$ is the intersection of the resolution function along the rod. Since the resolution function is independent of Q_c the double integral is just the product of the integral of $R(g_c)$ over dg_c and the integral of $|F(Q_c)|^2$ over dQ_c. This last integral can be done by Parsevals theorem whereby:

$$\int dQ_c |F(Q_c)|^2 = \frac{1}{N_c^2} \sum_u |\Omega_u|^2 = \frac{1}{N_c} \qquad (2.3.5)$$

If the intersection of the resolution function with the rod is a Gaussian with standard deviation W_c then the integral of $R(g_c)$ is $\sqrt{2\pi}\, W_c$. Hence equation (2.3.4) is given by

$$I'(\underline{Q}_\perp, \bar{\varepsilon}) = (N_c \sqrt{2\pi}\, W_c) M^2(\varepsilon) \Delta_\perp(\underline{Q}_\perp) \qquad (2.3.6)$$

The integration over Q_c should be done from zone boundary to zone boundary, i.e. from points $(\frac{1}{2}, \frac{1}{2}, \frac{3}{2})$ to $(\frac{1}{2}, \frac{1}{2}, \frac{7}{2})$, but since in a macroscopic sample an equal population of up and down domains is expected it is only necessary in practice to integrate from point A $(\frac{1}{2}, \frac{1}{2}, \frac{3}{2})$ to point B $(\frac{1}{2}, \frac{1}{2}, \frac{5}{2})$.

In order to calculate the integrated intensity above the Néel temperature it is necessary to know slightly more about the resolution function than has been so far assumed. The formalism used for the resolution function will be described in section (4), but for the present it will suffice to note that the resolution function is a four dimensional Gaussian in wavevector and frequency transfer. The component of the Gaussian which is described by the component of the wavevector transfer that is vertically out of the scattering plane decouples from the rest of the function and remains constant throughout reciprocal space. Further, for the conditions under

which the experiment reported in this chapter was performed, the frequency component of the resolution function adequately integrates the frequency dependence of the structure factor and may be neglected. The component of the resolution function within the scattering plane is a Gaussian in the co-ordinates g_c along the rod and g_p perpendicular to the rod and within the scattering plane. In figure (2.3.5) the scattering triangle and full width at half maximum contour of the in-plane component of the resolution function are shown superimposed on the reciprocal space, (the diagram is not to scale). Above the Néel temperature the intensity along the rod is independent of Q_c once the correction for the form factor and $\sin^2\alpha$ has been performed. Hence it is possible to integrate out the g_c component of the resolution function. The result is that the in-plane component of the resolution function is given by:

$$R^{eff}(g_p) = \sqrt{2\pi}\, W_c \exp\left(\frac{-g_p^2}{2W_p^2}\right) \qquad (2.3.7)$$

where W_c is the standard deviation of the Gaussian describing the intersection of the resolution function with the rod, and W_p is an effective standard deviation for the g_p component. If the in-plane component of the resolution function has standard deviations a and b along the semi-major and semi-minor axes and the semi major axis is at an angle Θ to the rod then W_c and W_p are given by:

$$W_c = a\,b \Big/ \sqrt{b^2\cos^2\Theta + a^2\sin^2\Theta} \qquad (2.3.8a)$$

$$W_p = \sqrt{b^2\cos^2\Theta + a^2\sin^2\Theta} \qquad (2.3.8b)$$

Hence if the Gaussian in g_p in equation (2.3.7) is written as $R_p(g_p)$ and the vertical component of the resolution function is given by $R_v(g_v)$ then above the Néel temperature the integrated intensity $I'(\underline{Q}_\perp \varepsilon)$ is given by

Figure (2.3.5)

In this figure the orientation of the scattering triangle and the resolution ellipse to the rod of scattering is shown at the point $(\frac{1}{2}, \frac{1}{2}, \frac{3}{2})$. The incident and final wavevectors used in the measurements were $k_i = k_f = 2.662\ A^{-1}$. The diagram is not to scale.

FIGURE(2.3.5)

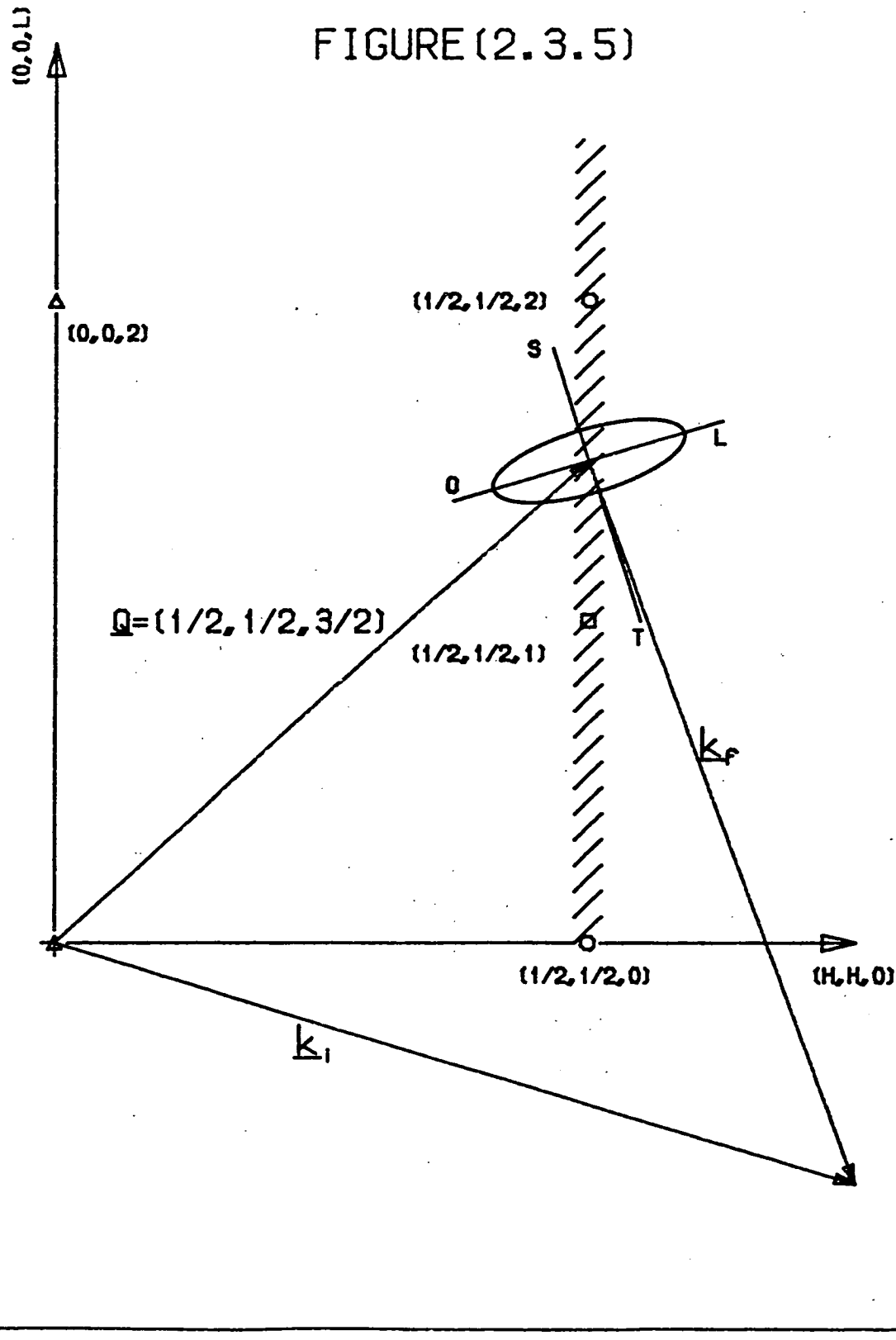

$$I'(\underline{Q}_{\perp}, \varepsilon^{+}) = (N_c \sqrt{2\pi} W_c)\ \chi_o^{+}\ \varepsilon^{-\gamma}\ V_R\ C^{+}(\kappa) \qquad (2.3.9)$$

where $V_R = 2\pi$ Wp Wv and Wv is the standard deviation of the vertical component and the function $C^{+}(\kappa)$ is now given by

$$C^{+}(\kappa) = \frac{1}{V_R} \iint dg_p\ dg_v\ R_p(g_p)\ R_v(g_v)\ D^{+}\left(\frac{\sqrt{g_p^2 + g_v^2}}{\kappa}\right) \qquad (2.3.10)$$

Therefore the ratio of the integrated intensities given by equations (2.3.6) and (2.3.9) is just given by

$$\frac{I'(\underline{Q}_{\perp}, \varepsilon^{+})}{I'(\underline{Q}_{\perp}, \varepsilon^{-})} = R_s\ V_R\ \frac{C+(\kappa)}{\kappa^d} \qquad (2.3.11)$$

where now V_R is the volume of the resolution function within the a* - b* plane and $C^{+}(\kappa)$ is an integral that is performed within the a* - b* plane.

The result in equation (2.3.11) was derived by assuming that the resolution function remains constant along the length of the scan from points A to B. In practice however, the values of Θ, a and b in equation (2.3.8) will all change along the the length of the scan as will the peak height of the resolution function R_o. If the values of W_p and W_c at the point $(\frac{1}{2}, \frac{1}{2}, 2)$ are denoted as W_p^{+} and W_c^{+} and the peak height R_o at $(\frac{1}{2}, \frac{1}{2}, 2)$ is defined to be one then in figures (2.3.6 a - d) the variation of Θ , R_o, (W_c/W_c^{+}) and (W_p/W_p^{+}) with the wavevector $(\frac{1}{2}, \frac{1}{2}, \ell)$ is shown. The values of W_c^{+} and W_p^{+} are 0.00261a* and 0.00575a* respectively. The data shown in figures (2.3.6 a - d) were calculated using the formalism described in section (4) and the parameters listed in table (2.4.1) for the set of collimations labelled (A). For the range of ℓ values $1.5 < \ell < 2.5$ shown in figures (2.3.6 a - d) all of the parameters Θ, R_o, W_c and W_p vary linearly with ℓ. If the empirical formulae $R_o(\ell) = (1 + \delta R\ \ell')$, $W_c = W_c^{+}\ (1 + \delta W_c\ \ell')$ and $W_p = W_p^{+}(1 + \delta Wp\ \ell')$ where $\ell' = \ell - 2$

Figure (2.3.6a)

This figure shows the variation of the angle of orientation (θ) of the major axis of the resolution ellipse along the length of a scan from points A to B in figure (2.3.2).

Figure (2.3.6b)

The variation of the peak height of the resolution function (R_o) along the length of a scan from points A to B is shown. At the point $(\frac{1}{2}, \frac{1}{2}, 2)$, R_o is defined to be 1.

Figure (2.3.6c)

The variation of the standard deviation of the component of the resolution function parallel to the c-axis along the length of a scan between points A and B is shown. The values of W_c are normalised by the value at the point $(\frac{1}{2}, \frac{1}{2}, 2)$.

Figure (2.3.6d)

The variation of the standard deviation of the component of the resolution function in the (1,1,0) direction along the length of a scan between points A and B is shown. The values of W_p are normalised by the value at the point $(\frac{1}{2}, \frac{1}{2}, 2)$.

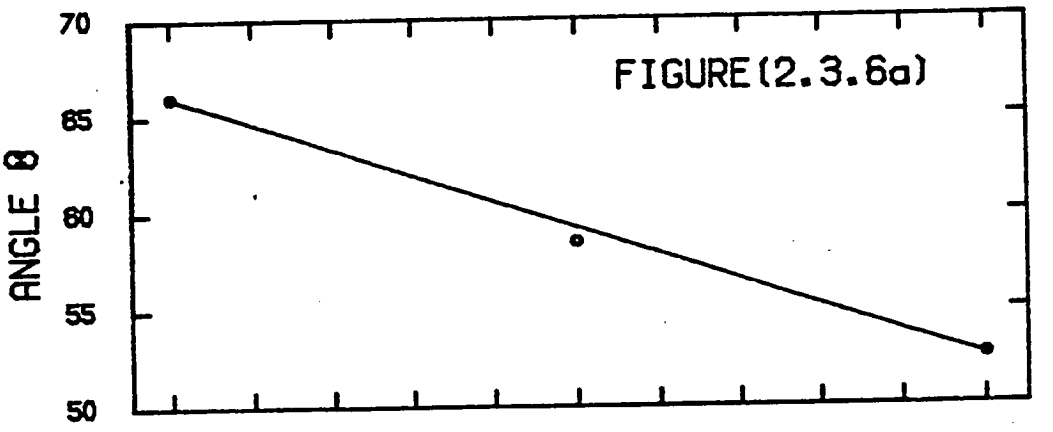

FIGURE(2.3.6a)

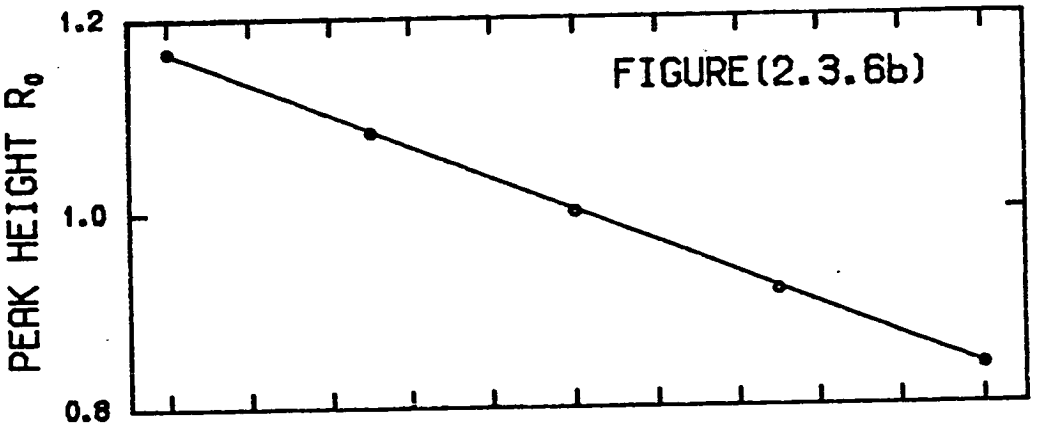

FIGURE(2.3.6b)

WAVEVECTOR (1/2,1/2,L)

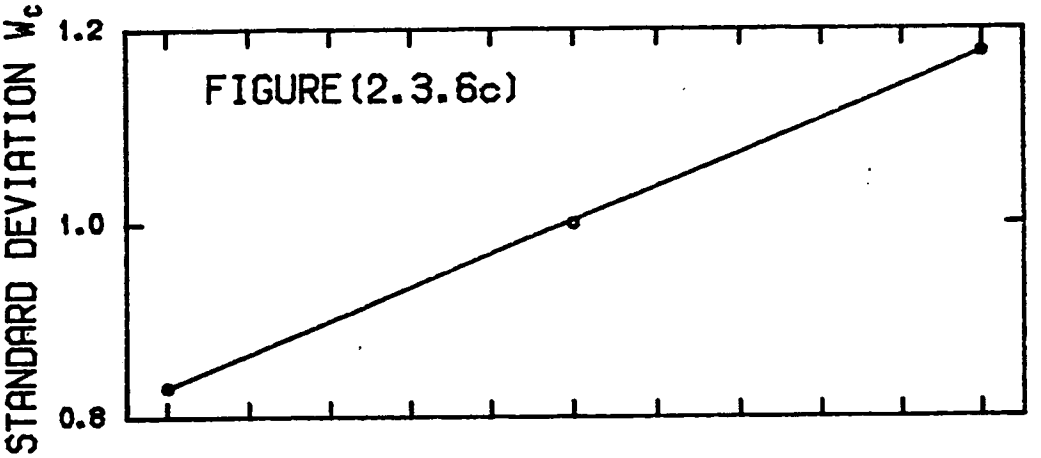
STANDARD DEVIATION W_c
1.2
1.0
0.8
FIGURE(2.3.6c)

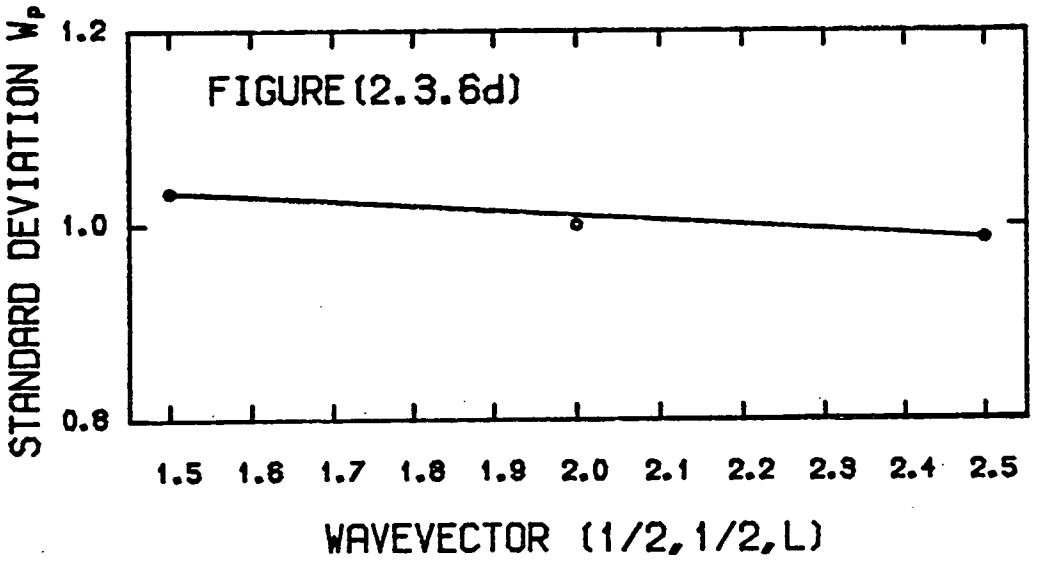
STANDARD DEVIATION W_p
1.2
1.0
0.8
FIGURE(2.3.6d)
1.5 1.6 1.7 1.8 1.9 2.0 2.1 2.2 2.3 2.4 2.5
WAVEVECTOR (1/2,1/2,L)

are used then δR, δWc and δWp are respectively 0.33, 0.35 and 0.05.

It is possible using the empirical formulae for R_o, W_c and W_p to estimate the "worst case" limit for the percentage error introduced into the integrated intensity by these variations. The "worst case" limit below the Néel temperature would be the case of a rod of delta function thickness in the a* - b* plane and constant intensity in the c* direction. The limit gives the greatest weight to the points at which the variation in the resolution function is greatest. If E is the percentage efficiency of integrating the intensity in the scan then below the Neel temperature E is given by:

$$E = \int_{-0.5}^{0.5} d\ell'(1 - \delta R\ell')(1 + \delta W_c \ell') = (1 - 0.083\ \delta R\delta W_c) \qquad (2.3.12)$$

Substituting the values of δR and δW_c found earlier into equation (2.3.12) gives a value of E = 99%. Above the Néel temperature the "worst case" limit is one of a constant intensity throughout reciprocal space. In this case E is given by:

$$E = \int_{-0.5}^{0.5} d\ell'(1 - \delta R\ell')(1 + \delta W_c \ell')(1 + \delta W_p \ell') =$$

$$1 - 0.083(\delta R\delta W_c + \delta W_p \delta W_c - \delta R\, \delta W_p) \qquad (2.3.13)$$

Again if the values of δR, δW_c and δW_p found earlier are substituted into equation (2.3.13) the efficiency is E = 99%.

Therefore in conclusion of this subsection it should be noted that (i) the difficulties introduced by stacking faults can be overcome by using integrated intensities and that (ii) that variations in the resolution function along the length of the scan to obtain the integrated intensity are not expected to be of any significance to the value obtained.

2.3 iii) Experimental apparatus

The measurements were performed using the IN2 spectrometer at the Institut Laue Langevin in Grenoble. In figure (2.3.7) a schematic diagram of IN2 is shown. This spectrometer differs from the standard triple axis by having a double monochromator with a 60' collimator between the two monochromators and no in-pile collimation before the first monochromator. The two monochromating crystals both rotate and translate in such a way that the scattered beam from the second monochromator to the sample table is fixed in direction. Therefore the sample table has rotational motion only, although both the analyser table and detector are free to move on air pads.

The two monochromators which were used in these measurements were both pyrolytic graphite crystals utilising the (0,0,2) reflection. A fixed incident neutron wavevector of 2.662 A^{-1} was used throughout the measurements and this facilitated the use of a pyrolitic graphite filter (Shapiro and Chesser (1972)) between the second monochromator and sample to suppress neutrons scattered from higher order planes in the monochromators. The analyser used was also a pyrolitic graphite crystal utilising the (0,0,2) reflection.

Since equation (2.3.11) contains the resolution volume as a parameter the measurements were performed for two different resolution volumes in order to act as a check on the results. The resolution volume could be varied by changing the horizontal collimations in the monochromator to sample, sample to analyser and analyser to detector positions. The two sets of collimations that were used were, with respect to the above, 40'-40' -60' and 20' -10' -40'.

The sample of Rb_2CoF_4 was mounted in an aluminium can with a

Figure (2.3.7)

This figure shows the arrangement of the components of the triple axis spectrometer IN2 at the Institut Laue Langevin. (Taken from 'Neutron Beam Facilities Available for Users', I.L.L., January 1981 edition).

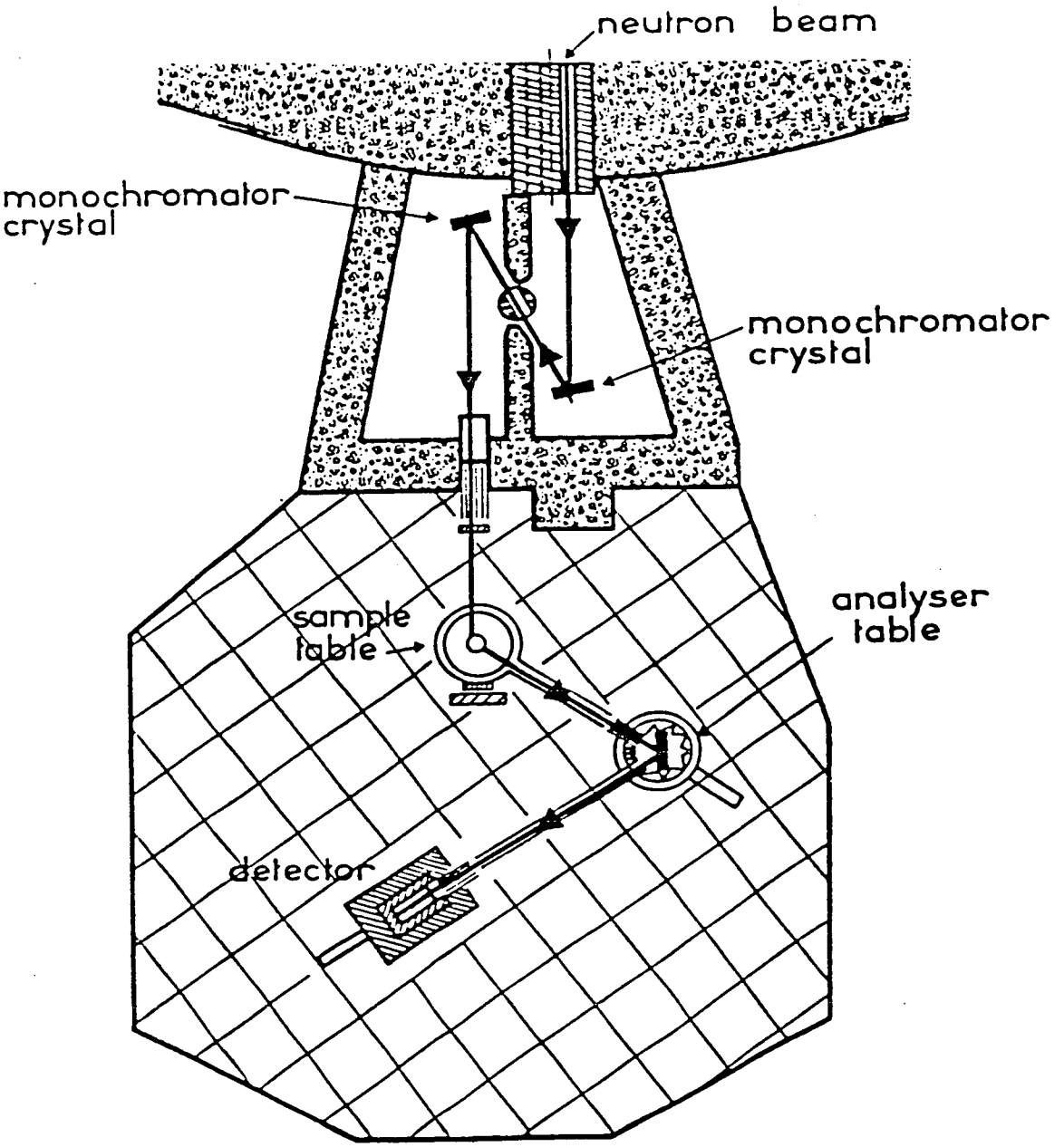

SCHEMATIC DRAWING
OF THE SPECTROMETER IN2

FIGURE (2.3.7)

helium gas atmosphere and attached to the copper block of a standard CT-14 cryostat. Since the Néel temperature of Rb_2CoF_4 is $\sim$ 102 K, (Breed et al. (1969) liquid nitrogen was used as the cryogen in both the inner and outer bins of the cryostat. The temperature of the sample was measured using a platinum resistance thermometer attached to the copper block of the cryostat. The thermometer was connected to an IT-LS1 temperature controller which was used to regulate the power supplied to the heater attached to the copper block. A temperature stability of ± 0.02 K over a period of $\sim$ 3 hours was attainable with the IT-LS1 controller. In order to ensure that the sample had reached thermal equilibrium with the copper block after the temperature was changed between scans no new scan was started until the intensities measured at the points $(\frac{1}{2}, \frac{1}{2}, \frac{3}{2})$, $(\frac{1}{2}, \frac{1}{2}, 2)$ and $(\frac{1}{2}, \frac{1}{2}, \frac{5}{2})$ had been stable for a number of minutes.

2.4 The Resolution Function Formalism

The resolution function for a triple axis spectrometer can be defined as the probability of observing a neutron scattered with a wavevector transfer $\underline{Q} + \underline{g}$ and frequency transfer $\Omega + \omega$ given that the spectrometer was set for a wavevector transfer $\underline{Q}$ and a frequency transfer Ω. The formalism used to describe the resolution function for the measurements reported in this chapter is that given in the paper of Cooper and Nathans (1967). Although in the paper of Cooper and Nathans only spectrometers with a single monochromator were considered it has been shown by Pynn and Passell (1974) that spectrometers with a double monochromator may also be included in this formalism. This is simply done by envisaging the double monochromator as an effective single monochromator in the formalism. When later the parameters for the resolution function are tabulated

those for the monochromator system will refer to an effective single monochromator.

If the wavevector and frequency transfers $\underline{Q}$ and Ω of the neutron are given in terms of the incident and final wavevectors of the scattering process $\underline{k}_i$ and $\underline{k}_f$ by:

$$\underline{Q} = \underline{k}_i - \underline{k}_f \tag{2.4.1a}$$

$$\Omega = \frac{\hbar}{2M_N}(k_i^2 - k_f^2) \tag{2.4.1b}$$

then the resolution function can be thought of as the sum over all paths through the spectrometer with wavevectors $\underline{k}_i + \Delta\underline{k}_i$ and $\underline{k}_f + \Delta\underline{k}_f$ which result in wavevector and frequency transfers $\underline{Q} + \underline{q}$ and $\Omega + \omega$. Therefore for each of the components of the spectrometer, collimators, monochromator, analyser and sample, a transmission function can be defined. This transmission function gives the probability that a neutron incident with a given wavevector relative to the spectrometer co-ordinates is scattered (or transmitted) into a given final wavevector relative to the spectrometer co-ordinates by that component of the spectrometer. The resolution function is thus obtained by convolving all of these transmission functions together and integrating over all paths through the spectrometer subject to the constraints of the conservation of frequency and wavevector transfer.

In the formalism devised by Cooper and Nathans (1967) the transmission functions are assumed to be Gaussian with an appropriately chosen standard deviation. Further, the constraints imposed by Bragg's law on the scattering processes of the monochromator and the analyser were treated by assuming that the angular deviations of the incident and final wavevectors from their set values were small and that small angle approximations

could be used. Then with these two assumptions Cooper and Nathans were able to perform the convolution integral of the transmission functions analytically. The resulting resolution function was a four dimensional Gaussian in wavevector and frequency transfer centred on the wavevector and frequency $\underline{Q}$ and Ω. This Gaussian was written by Cooper and Nathans in the matrix formalism:

$$R(\underline{Q}, g, \Omega, \omega) = R_o(\underline{Q}, \Omega) \exp\left[-\frac{1}{2} \tilde{x}^T \tilde{M} \tilde{x}\right] \qquad (2.4.2)$$

where the (4 x 1) column vector $\tilde{x}$ holds the components of $\underline{g}$ and ω, and $\tilde{M}$ is a (4 x 4) matrix containing the co-efficients generated in the convolution. In the paper of Cooper and Nathans (1967), $\underline{g}$ was given in terms of components parallel to $\underline{Q}$, perpendicular to $\underline{Q}$ but within the scattering plane and vertically out of the scattering plane. It is however easy to convert to the co-ordinates g_c, g_p and g_v used in section (3) by an orthogonal transformation. In their original paper Cooper and Nathans (1967) did not include sample mosaic spread when calculating the elements of $\tilde{M}$. The method for including sample mosaic was given by Werner and Pynn (1971). The prefactor R_o which arises from performing the integrals over the transmission functions was given explicitly in the paper of Chesser and Axe (1973). Therefore given the standard deviations of the transmission functions along with the magnitudes of the incident and final wavevectors and the lattice constants for the monochromator and analyser, the resolution function can be calculated for any $\underline{Q}$ and Ω using equation (2.4.2).

In experiments where a Bragg peak occurs in the low temperature phase, it is usually not necessary to employ this formalism. Since $S(\underline{Q}, \omega)$ for a Bragg peak is $\delta(\underline{Q} - \underline{\tau})\ \delta(\omega)$ scanning through the Bragg peak should project out the resolution function for that

wavevector. Therefore if the deviation of $\underline{Q}$ from $\underline{\tau}$ is not too great in the scans performed, this measured resolution function may be considered as constant throughout the scans performed. Unfortunately in Rb_2CoF_4 there is not a magnetic Bragg peak in the low temperature phase and it is necessary to calculate the resolution function using the Cooper-Nathans expression. The difficulty with doing this lies in determining the standard deviations of the transmission functions. The situation can be simplified somewhat by noting that the vertical component of the resolution function decouples from the other components in equation (2.4.2) (Cooper and Nathans (1967)). For the case of zero sample mosaic the standard deviation of the vertical component W_V is independent of $\underline{Q}$ and in the case of a finite but small sample mosaic it only depends weakly on $\underline{Q}$. The vertical component of the resolution function was therefore determined by lining up the spectrometer on the (1, 1, 0) nuclear Bragg peak and tilting the sample so that the Bragg peak scanned through the scattering plane. From a plot of intensity against the angle of tilt a value of $W_V = 0.0219\ A^{-1}$ was obtained. This value was assumed to remain constant throughout reciprocal space.

This therefore left seven standard deviations to be determined for the in-plane components of the transmission functions for the monochromator, analyser, sample and the four collimators. This was done by performing longitudinal, transverse and frequency scans through the (0,0,4), (0,0,6), (1,1,0), (2,2,0), (1,1,2), (1,1,4) and (2,2,2) nuclear Bragg reflections. These scans were fitted to the expression for the resolution function using a non-linear fitting program RESCAL, written by Dr. D. Mck. Paul, which is available at the I.L.L. The best fit values for the standard deviations using the notation of Cooper and Nathans (1967) are

given in table(2.4.1) for both sets of collimations. It should be noted that the parameters α_o and α_4 in table(2.4.1) were held fixed in the fitting procedure. This was done because it was found that a number of different combinations of the standard deviations could be found which described the scans if α_o and α_3 were allowed to vary. The difference in the calculated resolution function at $(\frac{1}{2}, \frac{1}{2}, \frac{3}{2})$ for these different combinations was small and holding α_o and α_3 fixed should not therefore have greatly affected the values of the resolution functions calculated.

In sections (2) and (3) the resolution function was treated as a function of wavevector only and it was assumed that the frequency integration of the dynamic structure factor was adequately performed by the frequency resolution of the spectrometer. The values for the resolution function $R(\underline{Q}, g)$ referred to in section (3) were values for $R(\underline{Q}, \underline{g}, 0, 0)$ calculated from equation (2.4.2). Below the Néel temperature this is clearly the resolution function for the Bragg scattering since the Bragg scattering is a delta function in frequency. Above the Néel temperature however, it must be justified that $S''(\underline{Q})\ R(\underline{Q},g,0,0)$ is a good approximation to the frequency integral of $S''(\underline{Q},\omega)\ R(\underline{Q},g,0.\omega)$. The frequency dependence of the critical scattering above the Neel temperature in Rb_2CoF_4 has been studied by Hutchings et al. (1982) who found that $S''(\underline{Q},\omega)$ was well described by the form:

$$S''(\underline{\tau}+\underline{q},\omega) = k_B T\ \chi^{+}(\underline{q},\varepsilon) \left[\frac{\hbar\omega/k_B T}{1-\exp(\frac{-\hbar\omega}{k_B T})}\right] (\frac{1}{\pi}) (\frac{\Gamma\ (\underline{q},\varepsilon)}{\Gamma(q,\varepsilon)^2 + \omega^2}) \qquad (2.4.3)$$

where $\underline{\tau}$ was the point $(\frac{1}{2},\frac{1}{2},0.3)$ on the rod and Γ is a characteristic frequency. The dependence of Γ on q and ε was found to be:

Table (2.4.1)

Cooper-Nathans Parameters

		Set A	Set B
Before Monochromator	$(2\alpha_o)$	60.0'	60.0'
Monochromator - Sample	$(2\alpha_1)$	12.2'	5.0'
Sample - Analyser	$(2\alpha_2)$	29.9'	31.87'
Analyser - Detector	$(2\alpha_3)$	60.0'	40.0'
Monochromator mosaic	$(2\eta_M)$	20.2'	19.5'
Analyser mosaic	$(2\eta_A)$	42.9'	42.9'
Sample mosaic	$(2\eta_S)$	13.07'	8.73'

Other Parameters

$$k_i = k_f = 2.662A^{-1}$$

$$d_M = d_A = 3.353A$$

Lattice Parameters

$$a = 4.128\ A$$

$$c = 13.622A$$

$$\Gamma(q,0) = 2\pi(3.6 \pm 1.2)q^{1.67\pm0.08} \text{ rads. THz} \qquad (2.4.4a)$$

and $$\Gamma(0,\varepsilon) = 2\pi(0.325 \pm 0.013)\varepsilon^{1.69\pm0.02} \text{ rads. THz} \qquad (2.4.4b)$$

In section (3) it was noted that since above the Néel temperature $S''(\underline{Q})$ did not depend upon g_c the resolution function could be integrated over g_c to give an effective resolution function which was given in equation (2.3.7). If the frequency integral of $S''(\underline{Q},\omega)$ and $R(\underline{Q}, g_,), \omega)$ is integrated over g_c then it is possible to write

$$\int dg_c \int d\omega S''(\underline{Q},\omega)\, R(\underline{Q},g,0,\omega) = \sqrt{2\pi}\, W_c\, R_p(g_p) R_v(g_v) S''(\underline{Q}) E(\Gamma,g_p) \qquad (2.4.5)$$

where W_c, $R_p(g_p)$ and $R_v(g_v)$ are the same as in section (3) and it has been assumed that the factor in [ ] in equation (2.4.3) is essentially unity over the range of ω covered by the resolution function. The factor $E(\Gamma,g_p)$ is given by the integral:

$$E(\Gamma,g_p) = \int_{\infty}^{\infty} \frac{d\omega}{\pi} \frac{\Gamma}{\Gamma^2+\omega^2} \exp\left[-\frac{1}{2}(\psi^2\omega^2 + 2\phi g_p \omega)\right] \qquad (2.4.6)$$

where it was assumed that Γ is essentially constant over the volume of the resolution function and the factors ψ^2 and ϕ will be defined shortly. Apart from the factor $E(\Gamma,g_p)$ the right hand side of equation (2.4.5) is the same as the integral of the product $R(\underline{Q},\underline{g},0,0)\ S''(\underline{Q})$ over g_c. After performing the integral over g_c $R(\underline{Q},g,0,\omega)$ is the product of the vertical component and a Gaussian in the (g_p,ω) co-ordinates. If the parameters given in table (2.1) for the collimation set A are used in equation (2.4.2) then the full width at half maximum contour of the Gaussian in the (g_p,ω) plane for $\underline{Q} = (\frac{1}{2}, \frac{1}{2}, 2)$ is shown in figure (2.4.1). If the factor $R_p(g_p)$ is extracted from this Gaussian then the remainder is the exponential term in the integrand of equation (2.4.6) where the factors ψ^2 and ϕ are, with respect to figure (2.4.1), given by:

Figure (2.4.1)

This figure defines the notation used in equations (2.4.7a) and (2.4.7b). For the resolution function calculated for the set of collimations A, the parameters shown in this figure took the values θ = 78.11 , a = 0.1032 and b = 0.0089, where the units are in mixed THz and A^{-1}.

FIGURE(2.4.1)

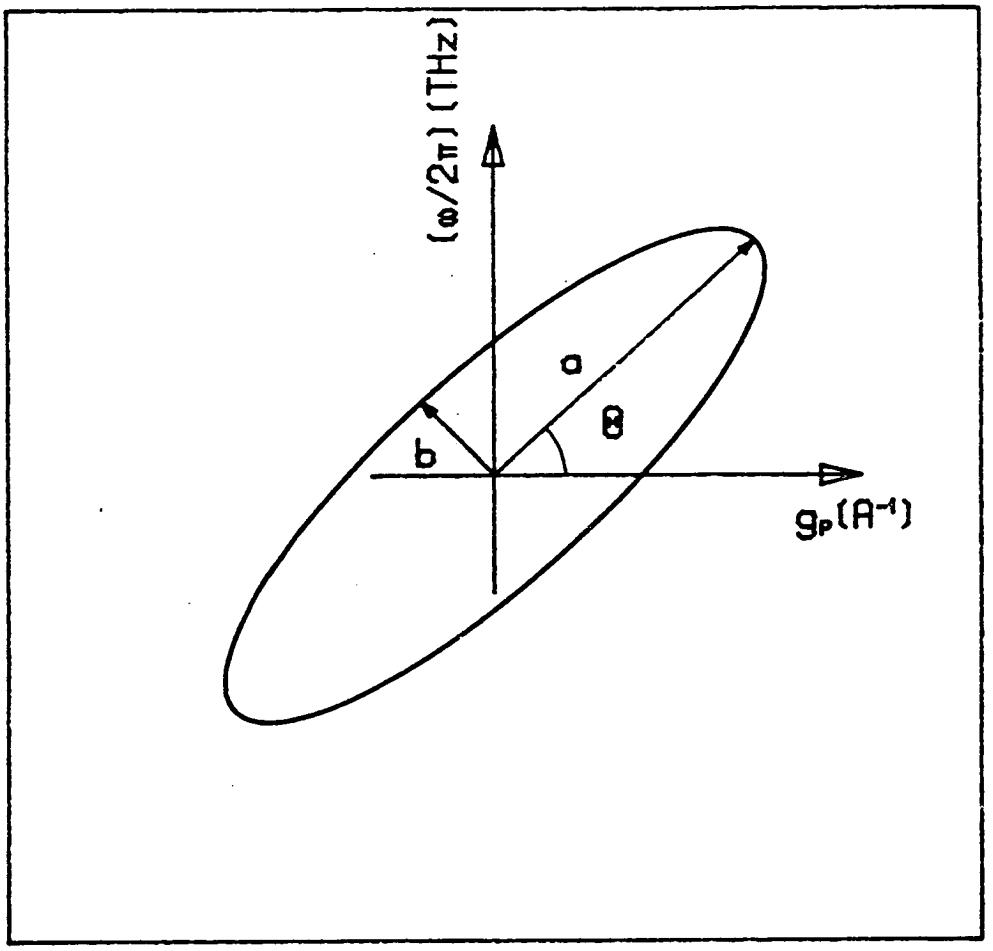

$$\psi^2 = \frac{\mathrm{Sin}^2\Theta}{a^2} + \frac{\mathrm{Cos}^2\Theta}{b^2} \qquad (2.4.7a)$$

and $$\phi = \frac{1}{2}\,\mathrm{Sin}\Theta\ \ \mathrm{Cos}\Theta\ \left(\frac{1}{a^2} - \frac{1}{b^2}\right) \qquad (2.4.7b)$$

The effect of the finite frequency resolution is therefore contained in the efficiency factor $E(\Gamma, g_p)$.

The integral on the right hand side of equation (2.4.6) may be rewritten as

$$E(\Gamma,g_p) = \exp\left|\frac{1}{2}\left(\frac{\phi g_p}{\psi}\right)^2\right| \left(\frac{\psi\Gamma}{\pi}\right)\int_{-\infty}^{\infty} \frac{e^{-t^2}}{\left(t - \frac{\phi g_p}{\psi^2}\right)^2 + (\psi\Gamma)^2}\,dt \qquad (2.4.8)$$

The reason for doing this is that the integral in equation (2.4.8) is given on page 302 of Abramowitz and Stegun (1964) in terms of the complex function W(z). As a result $E(\Gamma,g_p)$ is given by

$$E(\Gamma,g_p) = \exp\left[\frac{1}{2}\left(\frac{\phi g_p}{\psi}\right)^2\right]\ \ \mathrm{Re}\ \left\{W\left[\left(\frac{\phi g_p}{\psi} + i\psi\Gamma\ \right)/\sqrt{2}\right]\right\} \qquad (2.4.9)$$

From the properties of W(z) given in Abramowitz and Stegun it is easy to show that for elastic scattering or complete frequency integration (i.e. the limits $\Theta \to 90$ and $a \to \infty$, in that order) that $E(\Gamma,g_p) = 1$. In general, however, $E(\Gamma,g_p)$ must be evaluated numerically. Calculations of $E(\Gamma,g_p)$ at $\underline{Q} = (\frac{1}{2}, \frac{1}{2}, 2)$ show that for fixed Γ its value varies by less than 1% for $0 < g_p < 3\omega_p$. Thus the width of the resolution function in the g_p direction is unaffected by the frequency integration. In order to assess how efficiently the frequency integration is performed $E(\Gamma,0)$ was evaluated for values of Γ from 0.000 to 0.092 which from equation (2.4.4b) corresponds to reduced temperatures ε from 0.00 to 0.16. These values of $E(\Gamma,0)$ are shown in figure (2.4.2) as a function of the reduced temperature. For the range of reduced temperature $\varepsilon < 0.05$, where the quantitative results given in section (5) were determined the efficiency

Figure (2.4.2)

This figure shows the variation of the efficiency factor $E(\Gamma,0)$ for the frequency integration of the spectrometer with the reduced temperature. In the range of reduced temperatures below 0.05 the efficiency factor is better than 96%.

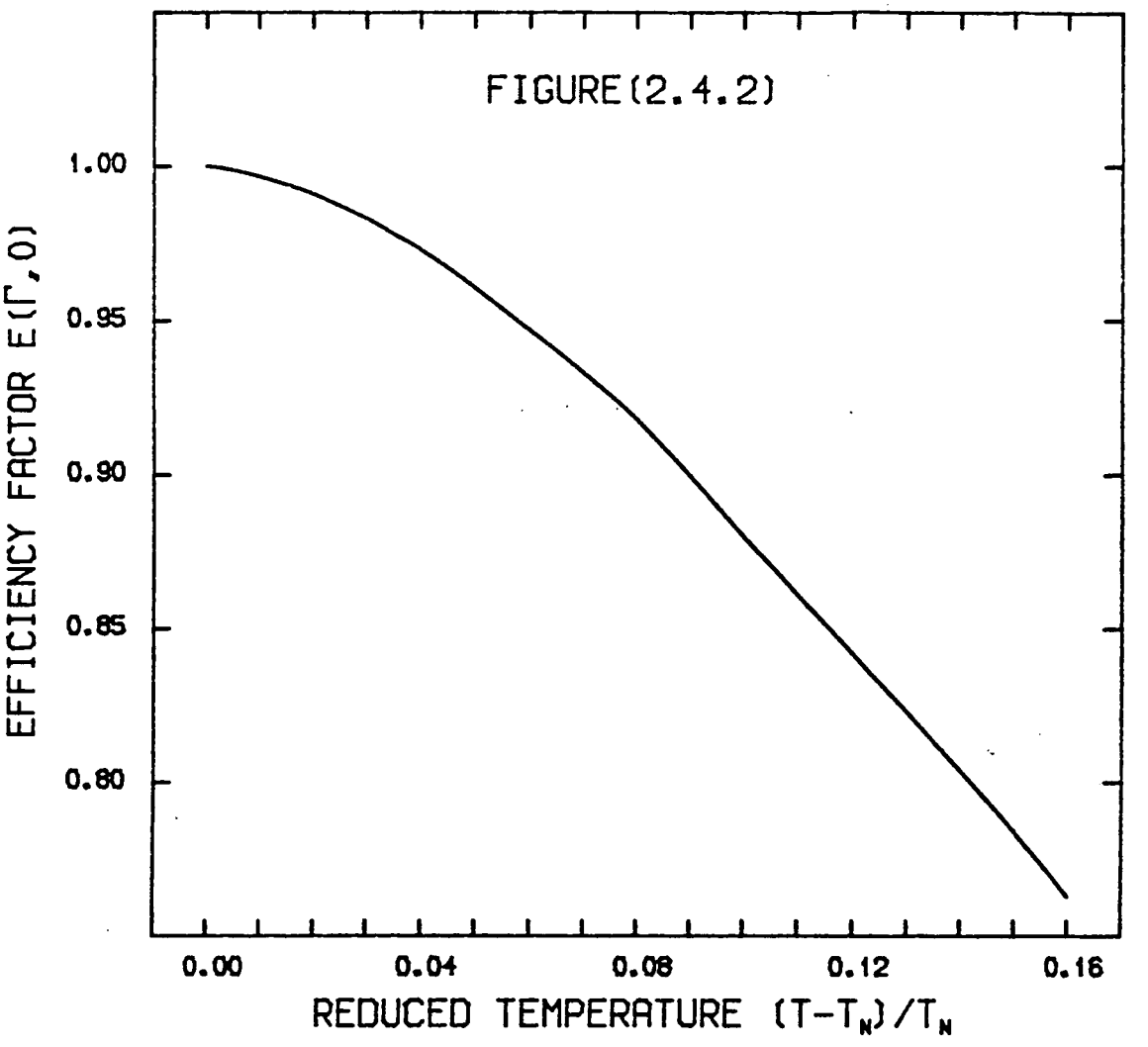
FIGURE(2.4.2)
1.00
0.95
0.90
0.85
0.80
EFFICIENCY FACTOR E(Γ,0)
0.00
0.04
0.08
0.12
0.16
REDUCED TEMPERATURE (T-T$_N$)/T$_N$

of the frequency integration is very good.

2.5 Experimental Results

In subsection (2.3.i) two types of scan were described, one measured the integrated intensity between points A and B shown in figure (2.3.2) and the other measured the wavevector dependent susceptibility by scanning between the points C and D shown in figure (2.3.2). The results derived from these scans as a function of temperature are presented in this section. First the methods by which the Néel temperature was found will be given. Then using this value for the Néel temperature the results for the exponent β will be given. Following this the results for the inverse correlation length found from fitting to the scans along the line C to D in figure (2.4.2) will be presented. After this the values obtained for R_s from the data are given. Drawing on the conclusions from the determination of R_s an analysis of the temperature dependence of the inverse correlation length will be given. Finally, using the conclusions drawn from the previous determination of R_s and the temperature dependence of the inverse correlation length the values for the exponent γ extracted from the data will be presented.

In figure (2.5.1a) the temperature variation of the integrated intensity between the points A and B in figure (2.3.2) is shown for the data taken with the set of collimations (A). As mentioned in subsection (2.3.ii), before integrating, each of the data points in the scans was corrected for the form factor of the Co^{2+} ion and the $Sin^2 \alpha$ term in equation (2.2.7). The values for the form factor were found by linearly interpolating between the values of the average form factor, as a function of wavevector, tabulated by

Figure (2.5.1a)

In this figure the integrated intensity between points A and B in figure (2.3.2) for the data taken with the set of collimations A is shown as a function of temperature. The solid line is a guide to the eye.

Figure (2.5.1b)

The temperature derivative of the curve in figure (2.5.1a) is shown as a function of temperature. The solid line is a guide to the eye.

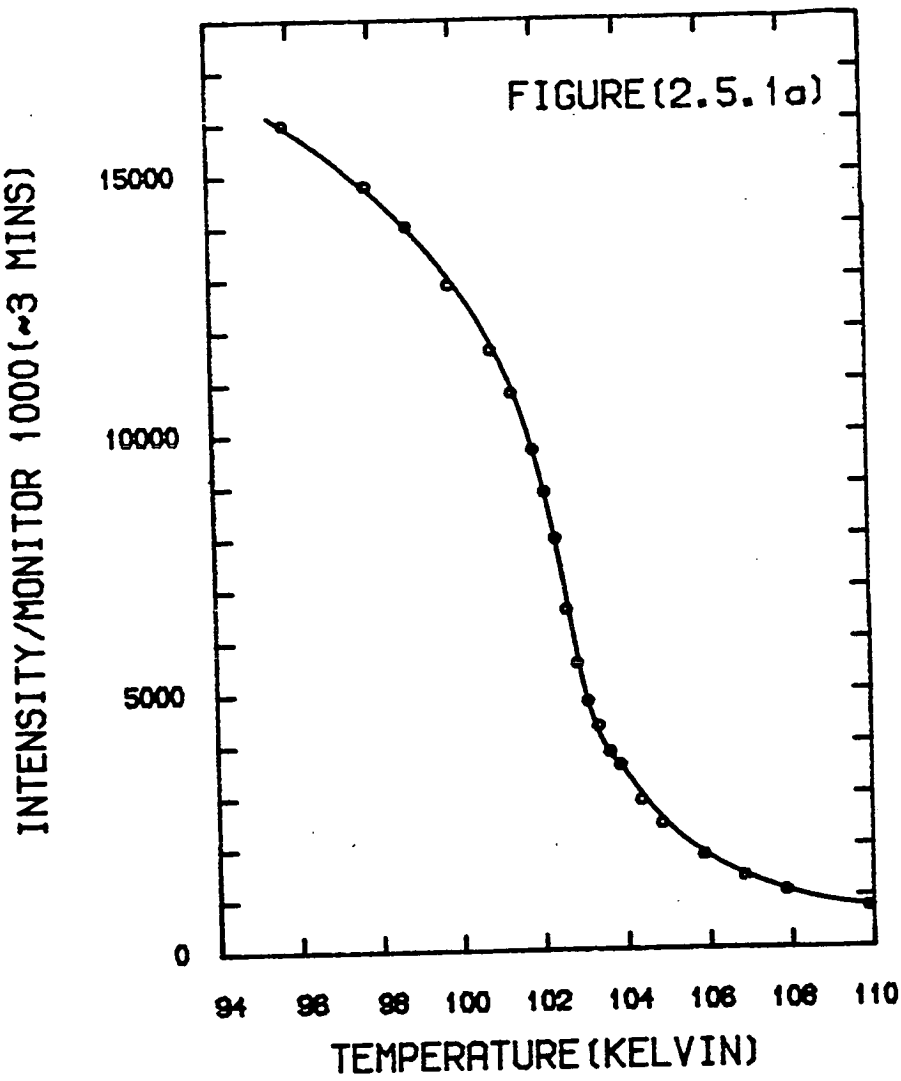
FIGURE(2.5.1a)
INTENSITY/MONITOR 1000(~3 MINS)
15000
10000
5000
0
94
96
98
100
102
104
106
108
110
TEMPERATURE(KELVIN)

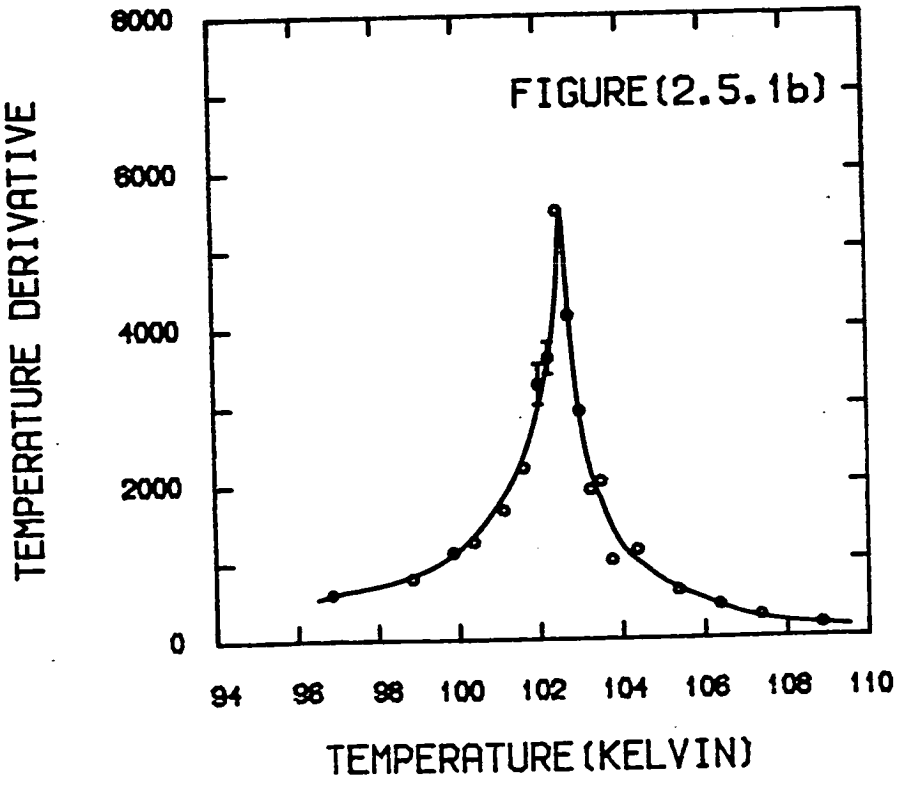
FIGURE(2.5.1b)
TEMPERATURE DERIVATIVE
8000
6000
4000
2000
0
94
96
98
100
102
104
106
108
110
TEMPERATURE(KELVIN)

Watson and Freeman (1961). It is known that the temperature derivative of the measured intensity at a Bragg peak position should have a peak at the transition temperature (Majkrzak et al. (1980), Bruce (1981)). Since the integrated intensity between points A and B represents the equivalent of the intensity at the Bragg peak position its temperature derivative is shown in figure (2.5.1b) for the data taken with the set of collimations (A). The derivatives were calculated from the integrated intensities by using the forward and backward difference approximation. The peak in figure (2.5.1b) occurs at a temperature of 102.6 ± 0.1 K. An alternative method to find the Néel temperature is to measure the peak position of the critical scattering. In figure (2.5.2) the temperature dependence of the measured intensity at the point $(\frac{1}{2}, \frac{1}{2}, \frac{3}{2})$ is shown. Since below the Neel temperature the stacking of the a - b planes causes the Bragg scattering to be peaked at the points $(\frac{1}{2}, \frac{1}{2}, 1)$, $(\frac{1}{2}, \frac{1}{2}, 2)$ etc. it is expected that the intensity at $(\frac{1}{2}, \frac{1}{2}, \frac{3}{2})$ will be dominated by the two dimensional critical scattering. In figure (2.5.2) the peak in the scattering occurs at a temperature of 102.6 K. The residual scattering at this position for temperatures below 102 K is Bragg scattering from the wings of the peaks at $(\frac{1}{2}, \frac{1}{2}, 1)$ and $(\frac{1}{2}, \frac{1}{2}, 2)$. The same value is found for the temperature at which the derivative of the integrated intensity and the critical scattering peak using the data taken with the set of collimations B. It is therefore concluded that the Néel temperature is 102.6 ± 0.1 K. This value is in good agreement with those found previously of 101 K (Breed et al. (1969)), 103.03 ± 0.01 K (Samuelsen (1974)) and 102.06 ± 0.12 K (Ikeda et al (1979)).

In section (2) it was pointed out that the temperature dependence of the integrated intensity would only be dominated by the $(-\varepsilon)^{2\beta}$

Figure (2.5.2)

The variation of the intensity at the point $(\frac{1}{2}, \frac{1}{2}, \frac{3}{2})$ measured as a function of temperature is shown in this figure. The peak in the intensity occurs at the Néel temperature.

FIGURE(2.5.2)

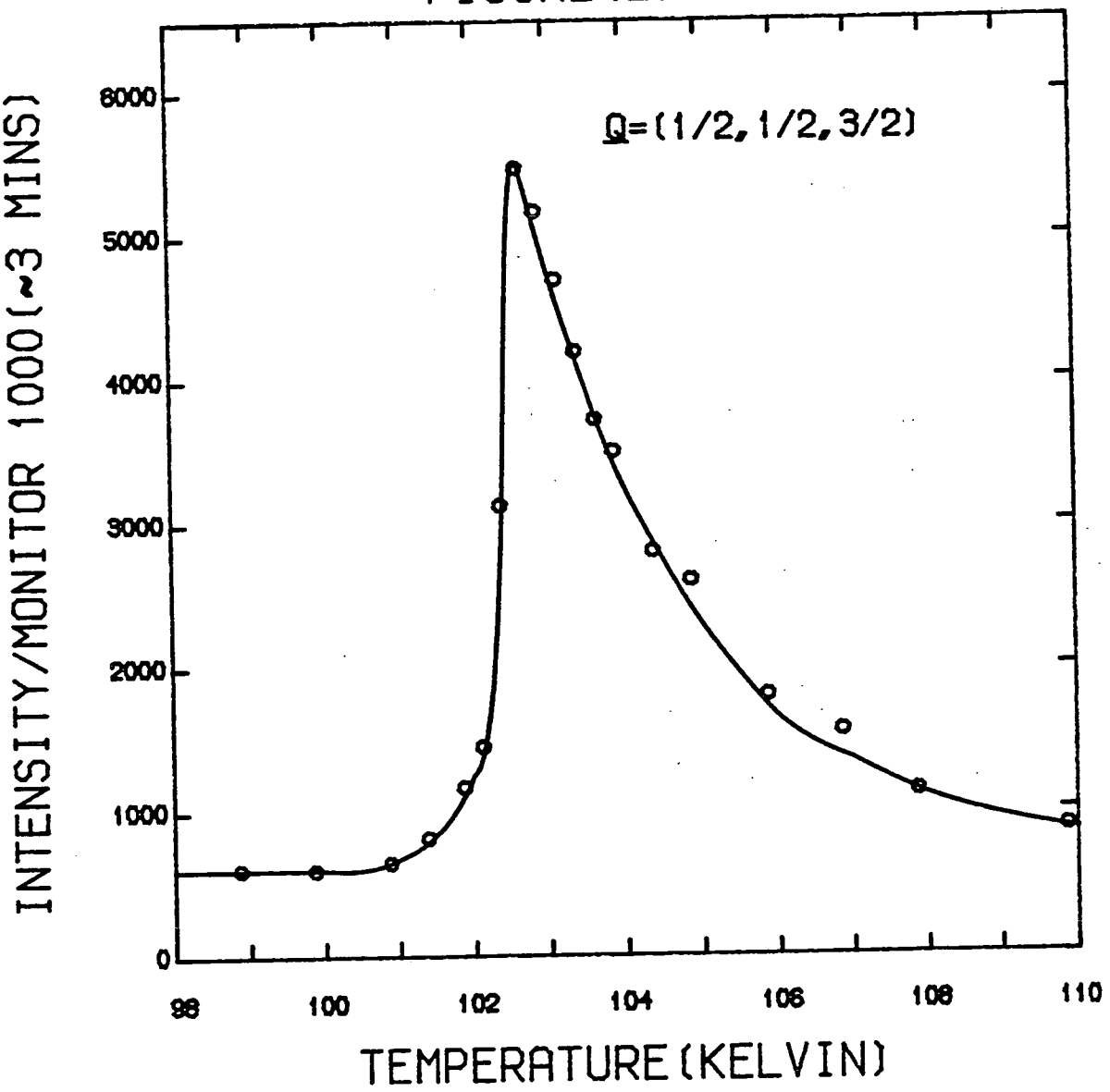
Q=(1/2,1/2,3/2)
INTENSITY/MONITOR 1000(~3 MINS)
TEMPERATURE(KELVIN)
0
1000
2000
3000
4000
5000
6000
98
100
102
104
106
108
110

term if the Bragg scattering was much greater than the intensity of the critical scattering integrated over the resolution function. From figure (2.5.2) it can be seen that the critical scattering has almost totally disappeared for temperatures below 102.1 K (ε= 0.005) and that the above condition should certainly be satisfied in this region. Therefore in figure (2.5.3) a Log-Log plot of the integrated intensity for reduced temperatures ε <0.005 against reduced temperature is shown for both sets of collimations. The solid lines in figure (2.5.3) are the best straight line fits and have χ^2 parameters 0.51 and 0.59 for the data taken with the set of collimations (A) and (B) respectively. Then, if the integrated intensity is written as $I'(\varepsilon) = I_o^-(-\varepsilon)^{2\beta}$ these fits lead to the parameters I_o^- = 29487 ± 171, β = 0.113 ± 0.002 and I_o^- = 11132 ± 78, β = 0.114 ± 0.002 for the data taken with the sets of collimations A and B respectively. The parameter I_o^- is the product of the overall scale factor I_o introduced in section (2), a factor of $\sqrt{2\pi}\ W_c$ and the square of the critical amplitude M_o. The values of β are highly correlated with the value of the Néel temperature. If the Néel temperature is varied in the range 102.5 to 102.7 K then best fit values of β which were obtained are in the range 0.109 to 0.117. Therefore an average value of β = 0.114 ± 0.004 is found where the error includes the effect of the error in the Néel temperature. This value for β is in good agreement with values found previously for Rb_2CoF_4 of 0.119 ± 0.008 (Samuelsen (1974)) and 0.115 ± 0.016 (Ikeda et al (1979)) but is about 9% lower than the value for the d = 2 Ising model of 0.125 (Onsager (1944)).

In figure (2.5.4) some of the scans performed along the line C→D shown in figure (2.3.2) using the set of collimations A are shown for various temperatures. The solid lines in figure (2.5.4)

Figure (2.5.3)

A Log-Log plot of the integrated intensity between points A and B in figure (2.3.2) below the Néel temperature against the reduced temperature is shown for the data taken with both sets of collimations. The solid lines are the best straight line fits as explained in the text.

FIGURE(2.5.3)

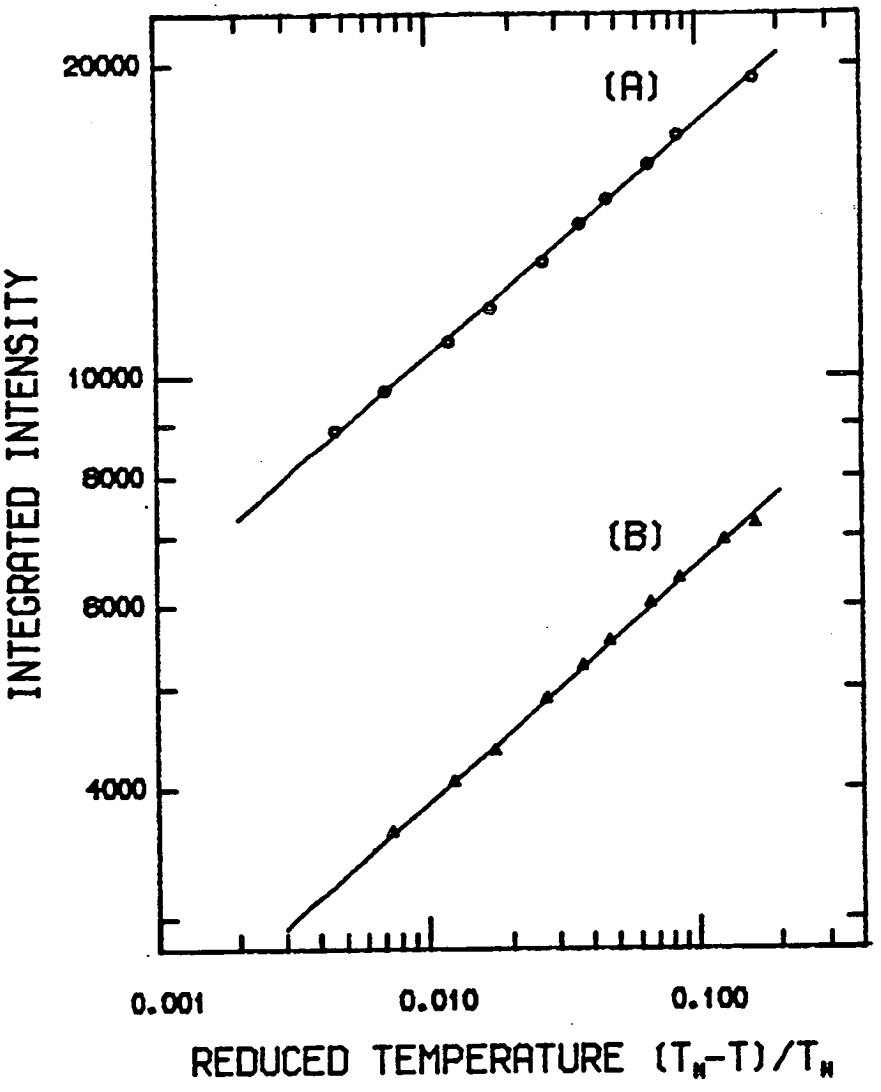
20000
10000
8000
6000
4000
(A)
(B)
INTEGRATED INTENSITY
0.001
0.010
0.100
REDUCED TEMPERATURE $(T_N-T)/T_N$

Figure (2.5.4)

This figure shows four scans along the line C - D in figure (2.3.2) at temperatures above the Néel temperature. These scans have been offset by 0, 100, 200 and 300 counts for clarity. The solid lines are the best fits to the Ornstein-Zernike form for the correlation function convolved with the resolution function as explained in the text.

FIGURE(2.5.4)

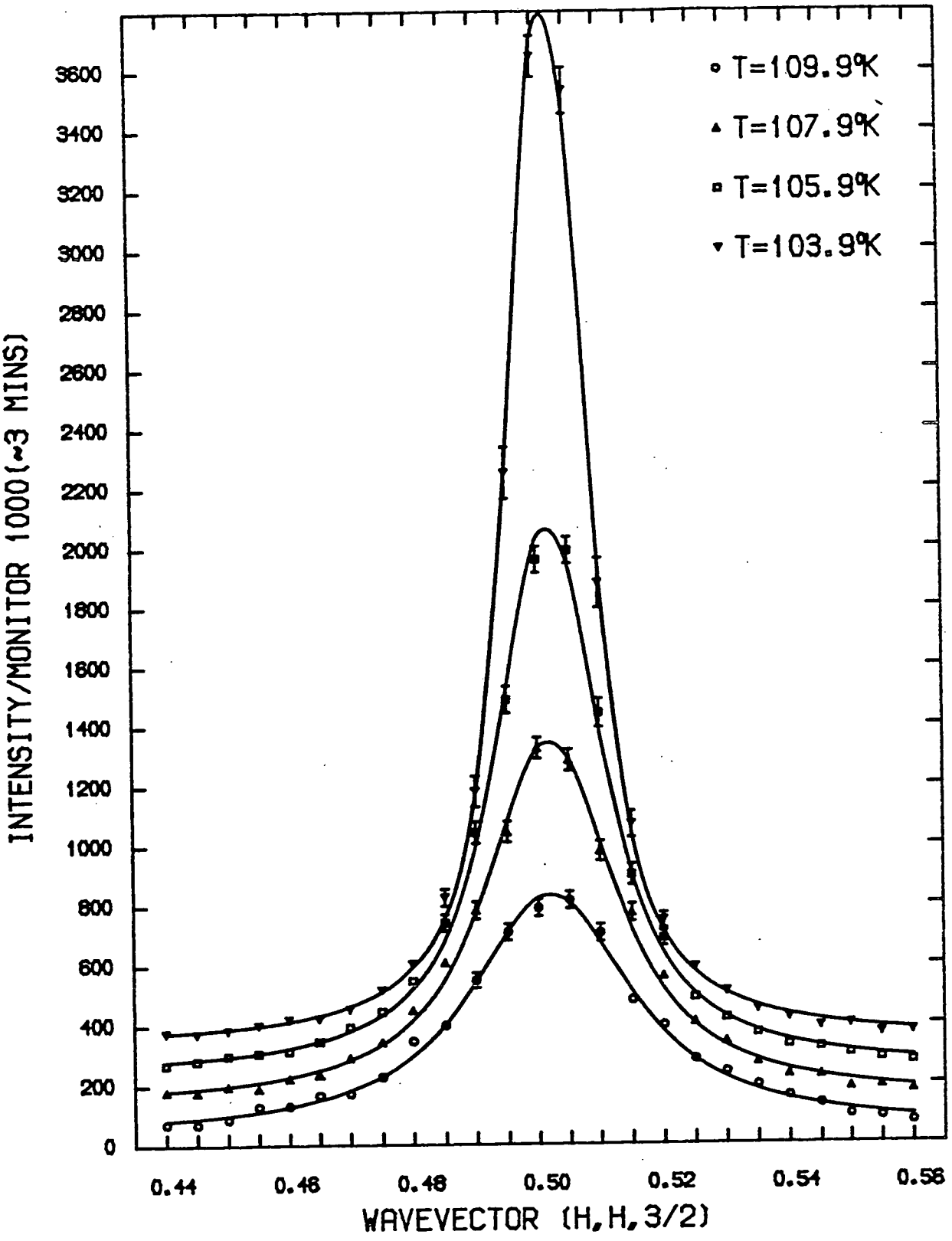
T=109.9K
T=107.9K
T=105.9K
T=103.9K
INTENSITY/MONITOR 1000(~3 MINS)
3600
3400
3200
3000
2800
2600
2400
2200
2000
1800
1600
1400
1200
1000
800
600
400
200
0
0.44
0.46
0.48
0.50
0.52
0.54
0.56
WAVEVECTOR (H,H,3/2)

were given by fitting the data to equation (2.2.14) with the Ornstein-Zernike form (equation (2.2.15a) for $D^+(q/\kappa)$, using a non-linear least squares fitting program RB2FIT. In these fits the variable parameters were the inverse correlation length and a scale factor which accounted for the prefactors to the integral in equation (2.2.14). As pointed out in section (3) above the Néel temperature the resolution function can be reduced to an effective in-plane component perpendicular to the rod and a vertical component. Consequently, the convolution in equation (2.2.14) was only done over the vertical and effective in-plane components of the resolution function. The performance of the convolution in the computer program was greatly expedited by being able to perform the convolution over the vertical component analytically. This is explained explicitly in subsection (v) of appendix A. The convolution over the in-plane component was done numerically out to plus or minus three standard deviations using a mesh of 101 points. The variation of the standard deviation of the effective in-plane component W_p along the length of the scan from C to D was taken into account at each data point in the scan.

The Ornstein-Zernike form for $D^+(q/\kappa)$ provided very good fits to the data, the χ^2 values lying in the range 0.5 to 2.0, for both sets of collimations. In figure (2.5.5) the values of the inverse correlation lengths obtained from these fits are plotted, in reciprocal lattice units $(2\pi/a)$, against temperature. The solid and dashed lines in figure (2.5.5) will be explained later in this section, when the temperature dependence of the inverse correlation length is described.

Therefore given values for the inverse correlation length κ at the same temperatures as the integrated intensities measured above the Néel temperature, it is possible to calculate the factors $C^+(\kappa)$

Figure (2.5.5)

This figure shows the inverse correlation lengths determined from the data taken with both sets of collimations. The values for collimation set B have been offset by 0.005 a* for clarity. The solid lines are the best straight line fits to the data for temperatures below 107 K, while the dotted lines are the best fits to equation (2.5.2).

FIGURE(2.5.5)

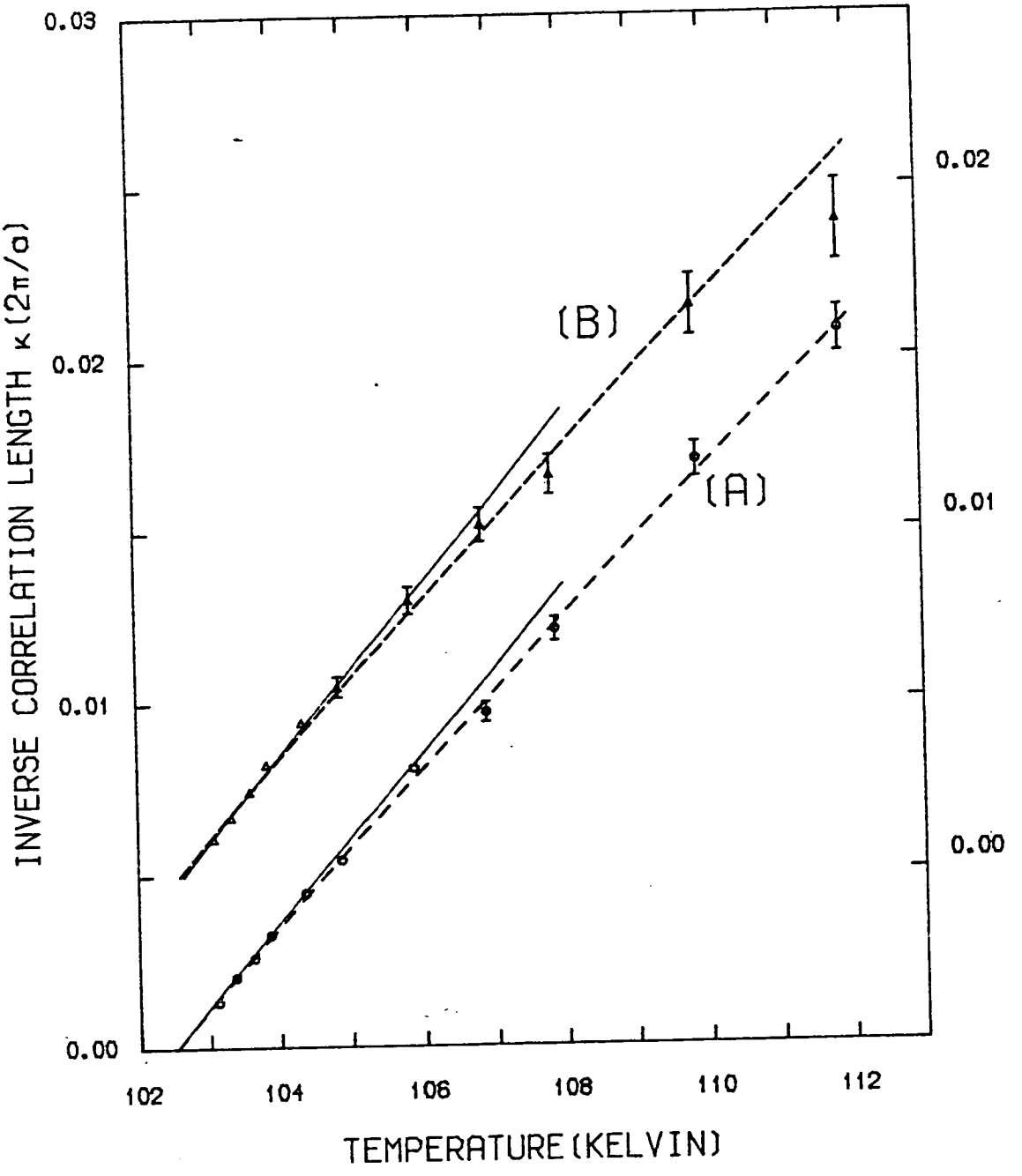
0.03
0.02
0.01
0.00
0.02
0.01
0.00
INVERSE CORRELATION LENGTH κ(2π/a)
(B)
(A)
102
104
106
108
110
112
TEMPERATURE(KELVIN)

in equation (2.3.10). The prescription for calculating R_s from equation (2.3.11) requires the comparison of integrated intensities at equivalent reduced temperatures above and below the Néel temperature. Since the integrated intensities measured below the Néel temperature do not match exactly in reduced temperature with those measured above, it is necessary to interpolate between the integrated intensities measured below the Néel temperature. This was done simply by using the formulae $I = I_o^-(-\varepsilon)^{2\beta}$ and the values of I_o^- and β reported earlier. Equation (2.3.11) holds only within the scaling region and therefore in order to find the limit of the scaling region and hence R_s a quantity $r(\varepsilon)$ is defined by the equation

$$r(\varepsilon) = \frac{1}{V_R} \frac{\kappa^2}{C^+(\kappa)} \left(\frac{I'(\underline{\tau},\varepsilon^+)}{I'(\underline{\tau},\varepsilon^-)}\right) \qquad (2.5.1)$$

From equation (2.3.11) within the scaling region $r(\varepsilon) = R_s$. Outside the scaling region $r(\varepsilon)$ is expected to fall monotonically with increasing ε. The volume of the resolution function V_R is given by $2\pi W_p W_v$ evaluated at the point $(\frac{1}{2},\frac{1}{2},2)$ as explained in subsection (2.3.ii). For both sets of collimations $W_v = 0.0144a^*$, while for set A $W_p = 0.00575a^*$, and for set B $W_p = 0.00518a^*$. The variation of $r(\varepsilon)$,, calculated from the experimental data, with ε is shown in figures (2.5.6 a - b) for the data taken with the sets of collimations A and B respectively. An examination of figures (2.5.6a) and (2.5.6b) shows that for $\varepsilon < 0.043$ $r(\varepsilon)$ is within experimental error constant while for $\varepsilon > 0.043$ $r(\varepsilon)$ falls with increasing ε for both sets of data. The solid lines in figures (2.5.6 a - b) for $\varepsilon > 0.043$ are merely guides to the eye while for $\varepsilon < 0.043$ they represent the mean values of $r(\varepsilon)$ in that range. These mean values are 0.044 ± 0.004 and 0.042 ± 0.004 for the data taken with the sets of collimations

Figure (2.5.6a)

This figure shows the variation of $r(\varepsilon)$ (defined in equation (2.5.1)) with reduced temperature for the data taken with the set of collimations A. For reduced temperatures below 0.043 the solid line represents the mean value of the data points. At reduced temperatures above 0.043 the solid line is a guide to the eye.

Figure (2.5.6b)

This figure shows the same plot as in figure (2.5.6a) but for the data taken with the set of collimations B.

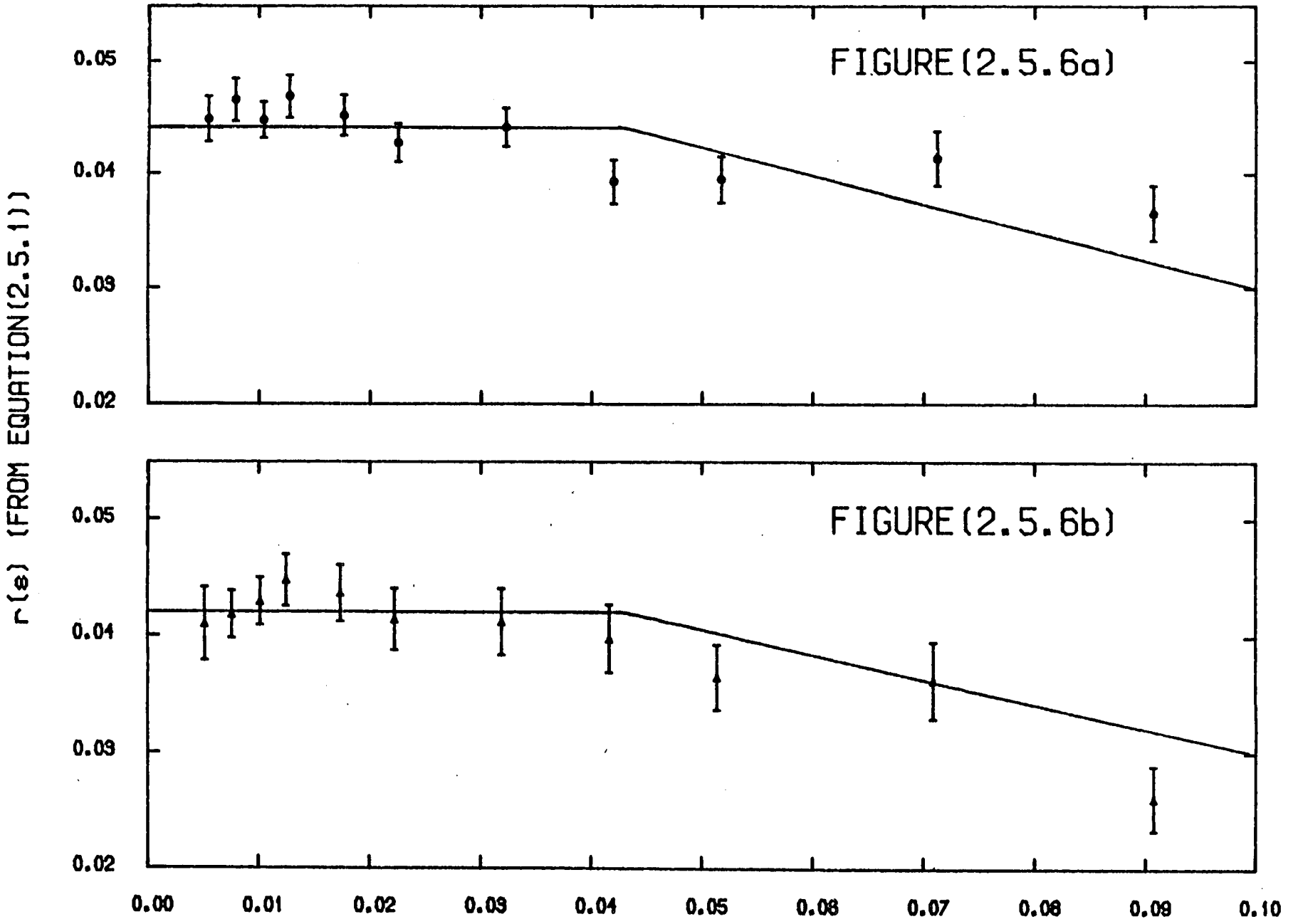
FIGURE(2.5.6a)
FIGURE(2.5.6b)
r(a) (FROM EQUATION(2.5.1))
0.05
0.04
0.03
0.02
0.00
0.01
0.02
0.03
0.04
0.05
0.06
0.07
0.08
0.09
0.10
REDUCED TEMPERATURE (T-T_N)/T_N

A and B respectively. The χ^2 values for these means are 1.60 and 0.40 respectively. These mean values therefore represent the experimentally determined values of R_s. They are in very good agreement with each other but are some 18% lower than the value for the d=2 Ising model of 0.051 (Bruce (1981, 1982)). In section (6) some possible reasons for this discrepancy will be discussed.

The change in behaviour of $r(\varepsilon)$ at $|\varepsilon| = 0.043$ indicates that the limit of one of the scaling regions, above or below the Néel temperature, has been exceeded. An examination of figure (2.5.3) shows that it cannot have been the scaling region below the Néel temperature which was exceeded since the straight line fits would be essentially the same whether the data for $\varepsilon < 0.043$ is included or excluded. It is therefore concluded that the change in $r(\varepsilon)$ occurs because the scaling region above the Néel temperature has been exceeded. That is to say the scaling forms for the susceptibility (equation 2.1.1b) and the correlation length (2.1.7)) are only expected to hold for $\varepsilon < 0.043$.

From the exact solution of the d = 2 Ising model (Onsager (1944)), the inverse correlation length is predicted to depend linearly on ε within the scaling region. Therefore in figure (2.5.5) the solid lines represent a straight line fit of the inverse correlation length to the form $\kappa = mT - c$ for temperatures $T < 107$ K (i.e. $\varepsilon = 0.043$). If the results of these fits are recast in the form $\kappa = \kappa_o(T - T_N)/T_N$ then $\kappa_o = 0.240 \pm 0.006$ with $T_N = 102.52 \pm 0.03$ and $\kappa_o = 0.259$ 0.009 with $T_N = 102.65 \pm 0.03$ for the data collected with the sets of collimations A and B respectively. The χ^2 values for these two fits are 1.09 and 0.54 respectively. It would appear that the values for κ_o and T_N obtained with the different sets of collimations

are in disagreement. This discrepancy will be discussed in section (6) where it will be argued that it arises because of systematic errors. Since the d = 2 Ising model has been solved exactly, there exists a functional form for the inverse correlation length that is valid for all temperatures above the Néel temperature (Onsager (1944)). This functional form is

$$\kappa = \frac{X_o}{2\pi} \left(\text{Log}_e \left[\text{Coth}\left(\frac{Y_o}{T}\right)\right] - \frac{2Y_o}{T}\right) \qquad (2.5.2)$$

where for the d = 2 Ising model on a square lattice $X_o = 1$ and $Y_o = {}^{4I}/_{k_B}$. The dashed lines in figure (2.5.5) represents fits of the measured inverse correlation lengths χ to the form in equation (2.5.2) with X_o and Y_o as variable parameters. The best fits were obtained with $X_o = 0.864 \pm 0.013$ and $Y_o = 45.18 \pm 0.02$ for the inverse correlation length obtained from the data taken with the set of collimations A and $X_o = 0.873 \pm 0.021$ and $Y_o = 45.21 \pm 0.04$ for that taken with the set of collimations B. The χ^2 values for these fits were 0.92 and 1.19 respectively.

In the scaling region above the Néel temperature the integrated intensity $I'(\underline{\tau},\varepsilon^+)$ divided by the product $Y_R\, C^+(\kappa)$ has, from equation (2.3.9) the scaling form $I_o^+\ \varepsilon^{-\gamma}$. The parameter I_o^+ is the product of the overall scale factor, a factor of $\sqrt{2\pi}\ W_c$ and the critical amplitude χ_o^+. A Log-Log plot of these "corrected" integrated intensities against the reduced temperature, in the range $0 < \varepsilon < 0.043$, is shown in figure (2.5.7). The solid lines in figure (2.5.7) are the best straight line fits and have χ^2 values of 0.70 and 0.47 for the data taken with the sets of collimations A and B respectively. The parameters obtained from these best fits were $I_o^+ = 19872 \pm 1922$ with $\gamma = 1.79 \pm 0.06$ and $I_o^+ = 6912 \pm 923$ with $\gamma = 1.77 \pm 0.05$

Figure (2.5.7)

A Log-Log plot of the integrated intensity above the Néel temperature divided by the product $V_R . C^+(\kappa)$ (c.f. equation (2.3.10)) against reduced temperature is shown. The solid lines are the best straight line fits.

FIGURE(2.5.7)

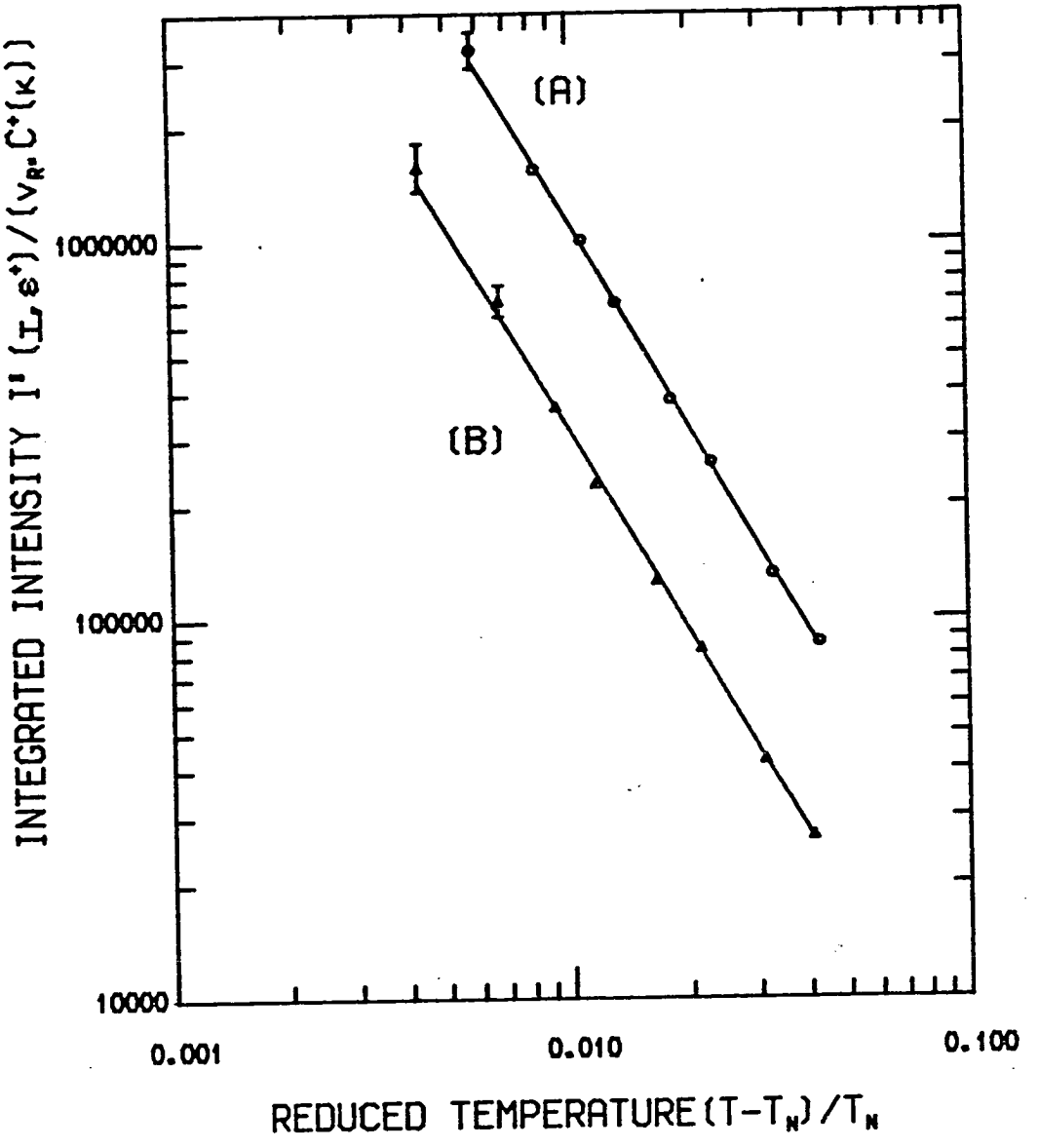
INTEGRATED INTENSITY I' (I, ε')/(v_R, C'(κ))
1000000
100000
10000
(A)
(B)
0.001
0.010
0.100
REDUCED TEMPERATURE (T-T_N)/T_N

respectively. These values for γ are in good agreement with each other and in reasonable agreement with the value of $\gamma = 1.75$ from the exact solution of the d = 2 Ising model (Onsager (1944)). Previous experimental measurements on Rb_2CoF_4 have yielded values for γ of 1.34 ± 0.22 (Samuelsen (1974)) and 1.67 ± 0.09 (Ikeda et al (1979)).

2.6 Discussion

There are a number of aspects of the results presented in section (5) which will be discussed in this section. Firstly, since it is more of a technical point rather than an interpretive one, the discrepancy between the two sets of data for the values of κ_o^+ and T_N determined from the straight line fits of inverse correlation length against temperature will be discussed. After this, a comparison of the various critical exponents and amplitudes for Rb_2CoF_4 and the d = 2 Ising model will be made. Finally, a discussion of how the measured values of R_s may be interpreted with respect to the hypothesis of Two Scale Factor Universality will be given.

In general, in section (5) there was a high degree of consistency between the values of the critical exponents and amplitudes determined using the two different sets of collimations. The exception to this was the values determined for the amplitude κ_o^+ and the Néel temperature T_N from the straight line fits of the inverse correlation length against temperature. The values obtained from these fits were $\kappa_o^+ = 0.240 \pm 0.006$ and $T_N = 102.52 \pm 0.03$ K and $\kappa_o^+ = 0.259 \pm 0.009$ and $T_N = 102.65 \pm 0.03$ K for the data taken with the sets of collimations A and B respectively. The inverse correlation lengths were also fitted to the functional form given in equation (2.5.2) which is the form given by the exact solution of the d = 2 Ising model

but with two variable parameters X_o and Y_o. The Y_o parameter is related to the Néel temperature through the equation $T_N = 2Y_o/\mathrm{Log}_e(1+\sqrt{2})$. If equation (2.5.2) is expanded in powers of ε about $\varepsilon = 0$ then the scaling form for κ can be extracted as:

$$\kappa = \frac{X_o}{2\pi}(1.765\varepsilon)(1 - 1.129\,\varepsilon + 0(\varepsilon^2)) \qquad (2.6.1)$$

Equation (2.6.1) therefore relates X_o to κ_o^+ through the equation $\kappa_o^+ = 1.765\ X_o/2\pi$. Further, equation (2.6.1) can be used to estimate the size of the scaling region. The value of ε for a 5% deviation from the scaling form is 0.045 which is in good agreement with the scaling region found experimentally. If the best fit values of X_o and Y_o given in section (5) are used to calculate κ_o^+ and T_N then the results are $\kappa_o^+ = 0.243 \pm 0.004$ and $T_N = 102.52 \pm 0.05$ K, and $\kappa_o^+ = 0.245 \pm 0.006$ and $T_N = 102.59 \pm 0.09$ K for the data taken with the sets of collimations A and B respectively. These values for κ_o^+ and T_N are in good agreement with each other and with the values determined from the straight line fit for the data taken with the set of collimations A. An explanation for the difference in the values determined for collimation set B can be found if there is assumed to be an error in the value of W_p for this set of collimations. This error in W_p would cause the inverse correlation lengths determined in the fitting analysis to have a systematic error in their value. However, this error will be much more important the smaller the inverse correlation length becomes and would therefore have a greater effect on the straight line fit within the scaling region than on the fit to equation (2.5.2) which is over the whole of the temperature range of the measurements. An estimate of the systematic error in the standard deviation W_p can be obtained from the magnitude of the inverse correlation length calculated from

$\kappa = 0.259(T - 102.65)/102.65$ with $T = 102.52$. This value is 0.00033a* which is 6% of W_p for collimation set B. Considering the way in which the resolution function was determined, an error of 6% in the width of the resolution function does not seem unreasonable.

Apart from the discrepancy discussed above, the temperature dependence of the inverse correlation length in Rb_2CoF_4 is in good agreement with that for the d = 2 Ising model. The critical amplitude of the inverse correlation length in Rb_2CoF_4 of 0.240 ± 0.006 is 15% smaller than the value of 0.281 for the d = 2 Ising model (taken from the tabulation of critical amplitudes by Tarko and Fisher (1975)). Since critical amplitudes are by themselves non-universal there is of course no reason to expect these values to agree. The critical exponents γ measured for Rb_2CoF_4 of 1.79 ± 0.06 and 1.77 ± 0.05 are in good agreement with the value of $\gamma = 1.75$ for the d = 2 Ising model. The other critical exponent measured, β had an average value of 0.114 ± 0.004 for Rb_2CoF_4 which is 9% smaller than the value of $\beta = 0.125$ for the d = 2 Ising model. In obtaining the measured value of β for Rb_2CoF_4, it was assumed that the critical region for the sublattice magnetisation extended as far as $\varepsilon = -0.1$. This can be justified by expanding the functional form for the magnetisation taken from the exact solution of the d = 2 Ising model (Onsager (1944)) in powers of ε about $\varepsilon = 0$. The scaling form can therefore be extracted as:

$$M(-\varepsilon) = \left[1 - \mathrm{Sinh}^{-4}\left(\frac{8T}{k_B T}\right)\right]^{\frac{1}{8}} = 1.223(-\varepsilon)^{\frac{1}{8}}\,(1 - 0.226(-\varepsilon) + O(\varepsilon^2)) \qquad (2.6.2)$$

If $\varepsilon = 0.1$ is substituted into equation (2.6.2), then the deviation from the scaling form would only be 3%. It is therefore unlikely that the difference in β for Rb_2CoF_4 and the d = 2 Ising model is due

to the data not being analysed within the scaling region. It is also thought unlikely that this difference could be due to extinction in the $(\frac{1}{2}, \frac{1}{2}, 2)$ peak because of the presence of the stacking faults. The reason for this low value of β is therefore not known. Previous values of β measured for Rb_2CoF_4 are 0.119 ± 0.008 (Samuelsen (1974)) and 0.115 ± 0.016 (Ikeda et al (1979)). There is therefore a consistent trend for the experimental value of β for Rb_2CoF_4 to be lower than 0.125. This is somewhat strange since in the isomorphous compound K_2CoF_4, β has been measured to be 0.123 ± 0.008 (Ikeda and Hirakawa (1974)) in very good agreement with the value for the d = 2 Ising model. Finally, a comparison of the combination of critical amplitudes χ_o^+/M_o^2 can be made between Rb_2CoF_4 and the d = 2 Ising model. The values of χ_o^+/M_o^2 can be obtained from the ratios of I_o^+ to I_o^-, where I_o^+ and I_o^- were defined when fitting to obtain the exponents γ and β. For the data taken with the sets of collimations A and B respectively the values of I_o^+/I_o^- are 0.674 ± 0.065 and 0.621 ± 0.083. The value for the d = 2 Ising model is $\chi_o^+/M_o^2 = 0.644$, which was obtained from the tabulation of critical amplitudes given by Tarko and Fisher (1975). Since the value of χ_o^+/M_o^2 is not a universal quantity, the agreement between the values for Rb_2CoF_4 and the d = 2 Ising model is therefore surprising.

The values obtained for the combination of critical amplitudes R_s of 0.044 ± 0.004 and 0.042 ± 0.004 for the data taken with the sets of collimations A and B respectively, are in very good agreement with each other. Their average of 0.043 ± 0.003 is, however, some 16% lower than the value of 0.051 calculated from the exact solution of the d = 2 Ising model (Bruce (1981)). If the error bars on the experimental value is taken at face value, then the theoretical value is three standard deviations from the experimental value.

It should be noted that the error bars indicate the effect of random errors only, calculated using standard statistical methods and do not include the possibility of systematic errors in the measurements. A systematic error in the values of κ_o^+ because of an error in the value used for the width of the resolution function has already been discussed. The effect of an error of the size estimated for this error in the resolution function is, however, not enough to bring the experimental and theoretical values into accord.

It is worth noting that the experimental value of R_s seems to be smaller than the theoretical value because the experimental value of κ_o^+ is lower than the theoretical value of κ_o^+ for the d = 2 Ising model. Even though the value of κ_o^+ is not expected to be universal, recent measurements on the isomorphous system K_2CoF_4 by Cowley et al (1983a) have found a value of $\kappa_o^+ = 0.279 \pm 0.005$ for this system, which is very close to the theoretical value of $\kappa_o^+ = 0.281$ for the d = 2 Ising model. Therefore, for K_2CoF_4 the critical exponents (Ikeda and Hirakawa (1974)) and the critical amplitude κ_o^+ are in good agreement with the theoretical values for the d = 2 Ising model, while for Rb_2CoF_4 the values of the exponent β and the critical amplitude κ_o^+ are consistently lower than the theoretical values. A possible explanation for this difference between these two isomorphous systems is the suggestion of Samuelsen (1974) that there might be some small amount of magneto-elastic coupling involved in the phase transition in Rb_2CoF_4. The effect of magneto-elastic coupling on the transition in Rb_2CoF_4 would be to make it first order, although the first order nature of the transition might only be observable very close to the Néel temperature. This would lead to a value for β which would be less than 0.125 but its effect on

the value of κ_o^+ is not known.

Before drawing a final conclusion on the agreement between the theoretical values for R_s and hence on the hypothesis of Two Scale Factor Universality, it is worth briefly reviewing the comparison between theory and experiment made by Stauffer et al (1972). This comparison was based on equation (2.1.10a) with experimental data taken from specific heat, light and neutron scattering results and theoretical values from high temperature series. In table (2.6.1) the values for the amplitude combination and the exponents α and ν tabulated by Stauffer et al are given for $d = 3$ Ising systems. Apart from CO_2, the agreement for both the amplitude combination and the critical exponents is erratic.

Therefore, in conclusion, notwithstanding the discrepancies discussed above, the value of $R_s = 0.043 \pm 0.003$ determined for Rb_2CoF_4 is, to the author's knowledge, the best experimental evidence available for believing in the hypothesis of Two Scale Factor Universality.

Table (2.6.1)

d = 3 Ising System	$100T_s^{(1)}$	α	ν
High Temp Series (S.C.)	1.65 ± 0.01	0.125	0.638
High Temp Series (F.C.C.)	1.65 ± 0.01	0.125	0.638
High Temp Series (B.C.C.)	1.66 ± 0.01	0.125	0.638
β - brass	1.9 ± 0.3	0.159	0.65
Xe	2.0 ± 0.5	0.080	0.58
CO_2	1.4 ± 0.2	0.125	0.63
FeF_2	4.8 ± 0.9	0.160	0.67
$C_6H_{12} - CH_4O$	7.1 ± 0.3	0.125	0.625

$^{(1)}T_s$ is the combination of critical amplitudes given in equation (2.1.10a) divided by the Boltzmann constant k_B.

CHAPTER THREE

Random Fields and Three Dimensional Dilute Antiferromagnets in a Magnetic Field

3.1 Introduction

In the previous chapter the static critical properties of the phase transition in an antiferromagnet which essentially possessed translational invariance, were described. The general features of the phase transitions in simple pure (i.e. translationally invariant) systems is now well understood both theoretically and experimentally. Therefore, in recent years a great deal of effort, both theoretical and experimental, has been expended in studying the phase transitions of systems which do not possess translational invariance (i.e. disordered systems).

There are two simple ways in which disorder could be introduced into a magnetic system, either by making the lattice amorphous or by substitutional replacement of atoms in the crystal. In this chapter and the following two it is the effects of site (i.e. substitutional replacement of the magnetic ions) disorder which will be considered. The use of the term site disorder should be taken to imply that there is a well defined lattice, the sites of which are randomly occupied by one of the two species of ion. There are two cases of site disorder which are easily distinguished, the first is where the magnetic ions are replaced by non-magnetic ions and is known as dilution, while the second is where the two species are both magnetic ions and is therefore termed a mixed magnetic system. This latter case can produce a drastic effect on the phase transition if the exchange interactions are competing, either in sign (ferromagnetic/antiferromagnetic) which can lead

to a spin-glass state (see for example Maletta (1982)) or in anisotropy which can lead to a state of mixed ordering (see for example Aharony (1982)). The situation of random competing anisotropies will be considered in Chapter Five, but in this chapter it is the properties of dilution that are of interest.

The effect of dilution on a three dimensional Ising system leads to the phase diagram shown in figure (3.1.1). For zero dilutant the phase transition is characterised by the critical exponents of the pure system. If a small amount of dilutant is included in the system then Harris (1974) has shown theoretically that a sharp phase transition with different exponents should be expected if the critical exponent for the specific heat of the pure system α is positive. For the d = 3 Ising model α is positive and this new behaviour has been observed experimentally in $Co_xZn_{1-x}F_2$ (Cowley and Carneiro (1980)) and $Fe_xZn_{1-x}F_2$ (Birgeneau et al (1983a)). In the d = 2 Ising model $\alpha = 0$ and it is therefore not clear if there exists a sharp phase transition. However, the results of Ikeda (1981) for the d = 2 dilute Ising antiferromagnet $Rb_2Co_xMg_{1-x}F_4$ certainly suggests that there does exist a sharp phase transition.

The dependence of the transition temperature for a d = 3 dilute Ising system is linear over a large range of concentrations as shown schematically in figure (3.1.1). However, when the concentration of magnetic ions has fallen to a point close to the concentration x_p this linearity breaks down and the transition temperature falls rapidly to zero at x_p. Along the T = 0 line of the phase diagram all the spins will be 'frozen' in their ground state and the properties of the system may be mapped onto the percolation problem (see for example Cowley(1980)). The problem of whether there exists long range magnetic order along the line

Figure (3.1.1)

This figure shows a schematic representation of the phase diagram of a dilute three dimensional Ising magnet. The dotted line is the molecular field phase boundary while the solid line is the real phase boundary.

FIGURE(3.1.1)

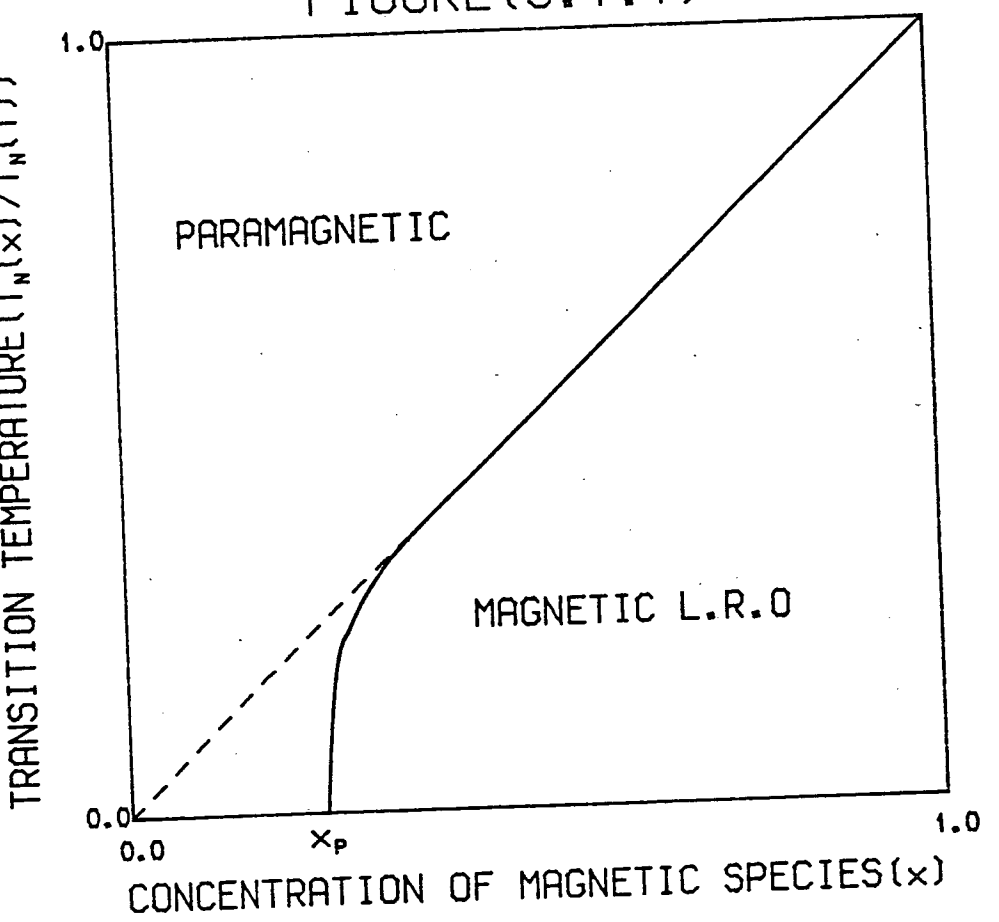
1.0
PARAMAGNETIC
MAGNETIC L.R.O
0.0
0.0
x_p
1.0
TRANSITION TEMPERATURE($T_N(x)/T_N(1)$)
CONCENTRATION OF MAGNETIC SPECIES(x)

T = 0 depends on whether there exists an infinitely connected cluster of spins. The concentration at which such an infinite cluster appears, x_p, is known as the percolation threshold. Therefore the point ($T = 0$, $x = x_p$) in figure (3.1.1) is a multicritical point, and the behaviour close to this point is different both from the behaviour of the pure and dilute systems. Recent reviews of the behaviour close to the percolation multicritical point have been given by Cowley et al (1980a) on the experimental work, and Aharony (1983) on the theoretical work, and there now appears to be reasonable agreement between theory and experiment for Ising systems.

The experimental work referred to above was performed on simple two sublattice Ising antiferromagnets and it is known that in zero external magnetic field these systems should be in the same Universality classes as the equivalent Ising ferromagnets (see for example Fisher and Burford (1967)). However, the application of an external magnetic field to a disordered Ising antiferromagnet has a drastic effect on the phase transition and ordering and it has been suggested (Fishman and Aharony (1979), Cardy (1983)) that the disordered Ising antiferromagnet in non-zero field is in the same Universality class as the random field Ising model (RFIM). The RFIM as proposed by Imry and Ma (1975) is a model of an Ising ferromagnet in a magnetic field that takes a random value at each site of the lattice.

In this chapter an experimental investigation of the effect that a uniform external magnetic field has on the phase transition and ordering of the dilute antiferromagnets $Co_xZn_{1-x}F_2$ and $Mn_xZn_{1-x}F_2$ will be described. These systems are examples of d = 3 dilute Ising and dilute near Heisenberg systems respectively.

The results of these measurements are interpreted in terms of the theoretical predictions for the R.F.I.M. The rest of this chapter is set out as follows. In section (2) a brief review will be given of the theoretical work on the random field models. This will be followed by a description in section (3) of the different mechanisms through which it has been suggested that random fields are induced in a dilute antiferromagnet by the external field. Section (4) contains a description of the experimental method for the measurements on $Co_xZn_{1-x}F_2$ and section (5) contains the results of these measurements. A discussion of how these results relate to the theoretical predictions for the R.F.I.M. will be given in section (6). Section (6) will also contain a comparison with the results of other experiments on dilute Ising antiferromagnets in a magnetic field. Since the experimental conditions for the measurements on the sample of $Mn_xZn_{1-x}F_2$ were different to those for the $Co_xZn_{1-x}F_2$ samples, these will briefly be described in section (7). The results of the measurements on the sample of $Mn_xZn_{1-x}F_2$ will be given in section (8) and a discussion of them in section (9). An overall discussion of the results for both systems will be given in section (10).

3.2 Random Fields - Theoretical Background

The idea of a ferromagnet in a random field was first introduced by Imry and Ma (1975) and was modelled by a Hamiltonian given by:

$$\mathcal{H} = - \sum_{<ij>} J_{ij} \, \underline{S}_i \cdot \underline{S}_j - g\mu_B \sum_i \underline{H}_i \cdot \underline{S}_i \quad . \qquad (3.2.1)$$

where the magnetic field $\underline{H}_i$ varied randomly in direction and magnitude from site to site in the lattice. These random fields were drawn from a distribution function with a mean $< H_i^{\alpha} > = 0$

and a variance $< H_i^{\alpha} H_j^{\beta} > = \delta_{ij}\delta_{\alpha\beta}\Delta^2$ where $\alpha\ \beta = x,y,z$. Imry and Ma produced a simple domain wall argument to show that for $\Delta \neq 0$ the lower critical dimension d_{ℓ} for Ising systems was shifted from 1 to 2 and for Heisenberg systems was shifted from 2 to 4. The lower critical dimension is the dimension below which a system cannot support long range order at any temperature. This simple argument gives a great deal of insight into how a random field can effect the magnetic order and will be briefly restated here.

Since the variance of the random fields is non-zero, within a local domain of volume L^d it is possible for the net magnetic field to have a non-zero value. This fluctuation in the net field would typically be of the order of $L^{d/2}$ and would be random in orientation. Therefore the spins within this domain could gain a magnetostatic energy of the order of $g\mu_B S\Delta L^{d/2}$ by re-orienting themselves along the direction of this net field. This gain in magnetostatic energy would be at the expense of the energy needed to create a domain wall with the rest of the system. Imry and Ma considered the situation for creating smooth (i.e. flat) domain walls. For an Ising system where the spins may only point up or down, the energy cost to create a domain wall is just ρL^{d-1}, where L^{d-1} is the surface area of the domain and ρ is the surface energy per unit area. In a Heisenberg system however, the spins can be rotated continuously and the Bloch domain wall (see for example Kittel (1976) p. 489) will be spread over a length of the order of L. Hence the energy cost to form a domain wall in a Heisenberg system will be ρL^{d-2}. A comparison between the magnetostatic and domain wall energy terms shows that domains will form if a length scale L can be found which satisfies the inequality:

$$L^{(2-d)/2} > O(\rho/\Delta) \quad \text{(Ising systems)} \tag{3.2.2.a}$$

$$\text{or } L^{(4-d)/2} > O(\rho/\Delta) \quad \text{(Heisenberg systems)} \tag{3.2.2b}$$

Therefore for Δ infinitesimally small, but not equal to zero, it is possible to satisfy the inequality for the Ising system for dimensions $d < 2$ and for the Heisenberg system for $d < 4$. The inference from this is that d_ℓ has been shifted from 1 to 2 for the Ising case and from 2 to 4 for the Heisenberg case by the presence of the random fields. It was also shown by Imry and Ma that if the random field were included in the Ginzburg criterion (Amit (1974)) then the upper critical dimension d_c for both Ising and Heisenberg systems was shifted from 4 to 6.

Following the work of Imry and Ma a number of authors (Grinstein (1976), Aharony et al (1976) and Young (1977)) examined the properties of the random field model in dimensions $4 < d < 6$ using perturbation theory techniques. It was shown by these authors that there was an equivalence between the most divergent perturbation theory diagrams in the presence of a random field and those of the relevant pure system in $d - 2$ dimensions. This implied that the critical exponents for a system in the presence of random fields in dimensions $4 < d < 6$ would be given by the critical exponents of the pure system in dimensions $2 < d < 4$. This dimensionality shift was consistent with the shifts in d_c for both Heisenberg and Ising systems and with the shift in d_ℓ for the Heisenberg system given by the Imry and Ma argument. Its range of validity however, excludes determining d_ℓ for the R.F.I.M. The consistency of these results for Heisenberg systems has meant that subsequent to this work, nearly all the theoretical effort has been directed towards determining d_ℓ for the R.F.I.M.

A different derivation of this d goes to d - 2 dimensionality shift was given by Parisi and Sourlas (1979). These authors constructed a differential equation from the most divergent diagrams in the perturbation theory for Ising systems and then studied this equation using supersymmetry methods. They argued from this analysis that the dimensionality shift d goes to d - 2 for the R.F.I.M. should apply for all dimensions d. Since for the pure Ising model d_ℓ is 1, this implies that for the R.F.I.M. d_ℓ is 3 and not 2 as given by the Imry and Ma argument. However, in the Imry and Ma argument, only smooth domain walls were considered. The effect of having rough domain walls in the R.F.I.M. was first considered by Pytte et al (1981). In order to do this, Pytte et al constructed a Hamiltonian for the domain wall interface by extending the capillary wave method of Wallace and Zia (1979) to include random fields by using the replica trick. Then from a renormalisation group analysis of this Hamiltonian Pytte et al concluded that the roughening transition that occurs for d < 3 in the pure Ising model would be shifted to d < 5 for the R.F.I.M. As a result of this, Pytte et al showed that the roughening of the domain walls would shift d_ℓ from 2 to 3. This result was also obtained by Binder et al (1981) using an argument similar to that of Imry and Ma but explicitly including the shift in dimensionality for the roughening transition. From this analysis Binder et al argued that the root mean square deviation (width) of the rough domain wall from the smooth domain wall varied as $L^{(5-d)/2}$ for a domain of volume L^d. Therefore in d = 3 the width of the domain wall is of the same order as the linear dimension of the domain and long range order is destroyed.

An alternative derivation of the above result was given by

Kogon and Wallace (1981) who studied the Hamiltonian for the domain wall interface using the supersymmetry methods of Parisi and Sourlas. Apart from showing that the effect of domain wall roughening could raise d_ℓ from 2 to 3, Kogon and Wallace also obtained a functional form for the correlation function of the R.F.I.M. in d = 3. This correlation function G(q) is the sum of a Lorentzian and a Lorentzian squared and is given by

$$G(q) = \frac{A}{q^2 + \kappa^2} + \frac{B}{(q^2 + \kappa^2)^2} \qquad (3.2.3)$$

where κ is the inverse correlation length and A and B are amplitudes. A heuristic argument for the existence of the Lorentzian squared term comes from noting that for the pure d = 1 Ising model, the real space correlation function is a negative exponential $e^{-\kappa r}$ which if naively Fourier transformed in d = 3, because of the dimensionality shift, leads to the Lorentzian squared. A more precise analysis, given by Kogon and Wallace, shows that there exists a Lorentzian as well as the Lorentzian squared in G(q).

The argument that the roughening of the domain wall shifts d_ℓ from 2 to 3 has, however, recently been challenged by Grinstein and Ma (1982). These authors use a different form for the Hamiltonian describing the domain wall interface in the presence of a random field, arguing that the form used by Pytte et al did not include all the relevant terms. From renormalisation group methods Grinstein and Ma calculate that the root mean square width of the domain wall varies as $L^{(5-d)/3}$. In this case therefore, the roughening transition occurs for d < 5 as was found by Pytte et al, but in d = 3 the width only varies as $L^{\frac{2}{3}}$ and not as L. Therefore for large values of L, i.e. for small values of Δ, the domain walls are effectively smooth and from the Imry and Ma argument, long range order can be

sustained in d = 3. In d = 2 the width of the domain wall, given by the Grinstein and Ma calculation, varies as L and it will not be possible to sustain long range order. Therefore on the basis of the Grinstein and Ma arguments d_ℓ is 2, as originally predicted by Imry and Ma. The variation of the domain wall width with linear domain size L has recently been studied by Mackenzie (1983) in d = 2 and 3 using Monte-Carlo techniques. The results of this study agree well with the form $L^{(5-d)/3}$ predicted by Grinstein and Ma.

The different theoretical approaches do however all agree on one point and that is the dependence of the inverse correlation length on the variance of the random field in $d = d_\ell$. In this case the inverse correlation length is given, for small Δ and at zero temperature by (Pytte et al (1981), Kogon and Wallace (1981), Grinstein and Ma (1982)).

$$\kappa = \kappa_o \exp(-C/\Delta^2) \quad (d = d_\ell) \tag{3.2.4}$$

where κ_o is an amplitude and C is a constant. In dimensionalities less than d_ℓ the inverse correlation length is expected to depend on Δ through a power law behaviour (Grinstein and Ma (1982)) whereby

$$\kappa = \kappa_o \Delta^{\nu_H}, \ \nu_H = \frac{2}{d_\ell - d} \quad (d < d_\ell) \tag{3.2.5}$$

3.3 Experimental Realisation of Random Fields

In the previous section the R.F.I.M. was defined as a ferromagnet in a magnetic field that varied randomly from site to site. This model clearly cannot in this form be realised in an experiment. However, it was pointed out by Fishman and Aharony (1979) that a disordered two sublattice uniaxial antiferromagnet in a uniform

external magnetic field should be equivalent to the R.F.I.M. Fishman and Aharony explicitly demonstrated this for an antiferromagnet with random exchange interactions. This demonstration involved grouping the spins into cells of two spins, one from each sublattice. If the spins within these cells were labelled S_i and S_j then the Hamiltonian could be rewritten in terms of the cell variables $S^+_{ij} = S_i + S_j$ (ferromagnetic) and $S^-_{ij} = S_i - S_j$ (antiferromagnetic). The Hamiltonian therefore contains terms of the form $S^+ S^+$, $S^+ S^-$ and $S^- S^-$. In zero applied magnetic field the S^+ terms have an expectation value zero. However, when an external magnetic field is applied, a ferromagnetic moment will be induced and the S^+ terms will be non-zero, but will vary throughout the sample because of the random exchange interactions. Since there are no critical fluctuations in S^+ the $S^+ S^+$ terms in the Hamiltonian can be neglected. However, the effect of the $S^+ S^-$ terms in the Hamiltonian is to introduce a random field on the antiferromagnetic order parameter S^-. The variance of the random field in this case is therefore proportional to the square of the induced ferromagnetic moment.

Unfortunately there do not exist any uniaxial antiferromagnets with only random exchange interactions. There do, however, exist a number of site random uniaxial antiferromagnets. In this case it is easy to see qualitatively that there will be a random field effect in an external magnetic field, but difficult to quantify this effect. Since the sites of the two sublattice antiferromagnets are occupied randomly by magnetic ions with different magnetic moments the net moment within a local domain can fluctuate. This random moment will couple to the external magnetic field and will lead to a random field effect. In order to put this argument

on a quantitative level, Wong et al (1982) considered the site random uniaxial antiferromagnet in an external field using the same construction as Fishman and Aharony. As a result, Wong et al found two components to the random field acting on the order parameter. The first of these components just arises from the Zeeman interaction and is proportional to the applied magnetic field. The second component which should be much weaker than the first arises from the randomness in the exchange interactions induced by the site randomness and is proportional to the induced ferromagnetic moment. These two components add quadratically to give the variance of the random field. This result was also determined independently by Birgeneau et al (1983b).

An alternative formulation of the problem of a site random Ising antiferromagnet in a uniform magnetic field has been given by Cardy (1983). This has been done by writing the Hamiltonian for the site random antiferromagnet in an external field in its field theoretic form and comparing this with the field theoretic form of the R.F.I.M. As a consequence, Cardy concludes that, up to terms that are irrelevant in the renormalisation group sense, the Hamiltonians for the two problems are equivalent and should be in the same Universality class. Further, Cardy obtained the variance of the random field induced by the external field in the site random antiferromagent as being proportional to the square of the induced ferromagnetic moment. This last result has, however, been questioned (Cowley et al (1983b)).

In applied magnetic fields which are small compared to the exchange field the ferromagnetic moment would, at least approximately, be expected to be linearly proportional to the external field. Therefore all the proposed mechanisms should, in this small field

limit, lead to the variance of the induced random field being proportional to the square of the external field.

3.4 Experimental Method (1) - $Co_xZn_{1-x}F_2$

As discussed in the previous section, a uniform external magnetic field applied to a site disordered antiferromagnet should be equivalent to the random field problem. The site disordered antiferromagnet for which measurements will be described in this and the succeeding two sections is $Co_xZn_{1-x}F_2$. In the main the description of the experimental method and results will apply to measurements on a sample with cobalt concentration x = 35%. The measurements on this sample were performed by the author and Dr S.K. Satija, and the data analysis for these measurements was performed by the author. Where appropriate, reference will also be made to measurements on a sample with 26% cobalt performed by Professor R.A. Cowley. The rest of this section is divided into two subsections, the first briefly describes the properties of CoF_2 and $Co_xZn_{1-x}F_2$ and the second describes the arrangement of the spectrometer and magnet.

3.4 i) Properties of $Co_xZn_{1-x}F_2$

Both CoF_2 and ZnF_2 have the same rutile crystal structure shown in figure (3.4.1) with very similar lattice parameters (Wyckoff (1963) p. 250. It is therefore possible to obtain good single crystals of $Co_xZn_{1-x}F_2$ with a homogeneous distribution of Co^{2+} and Zn^{2+} ions. The samples used for the measurements reported here were grown by Dr. H.J. Guggenheim using the Czochralski method. Estimates of the concentration of cobalt ions for these two samples were obtained from their Néel temperatures. CoF_2 has a Néel temperature of 38.04 K (Cowley and Carneiro (1980)) and ZnF_2 is

Figure (3.4.1)

This figure shows the rutile crystal structure of CoF_2 and indicates the orientation of the magnetic moments of the Co^{2+} ion within the unit cell.

FIGURE(3.4.1)

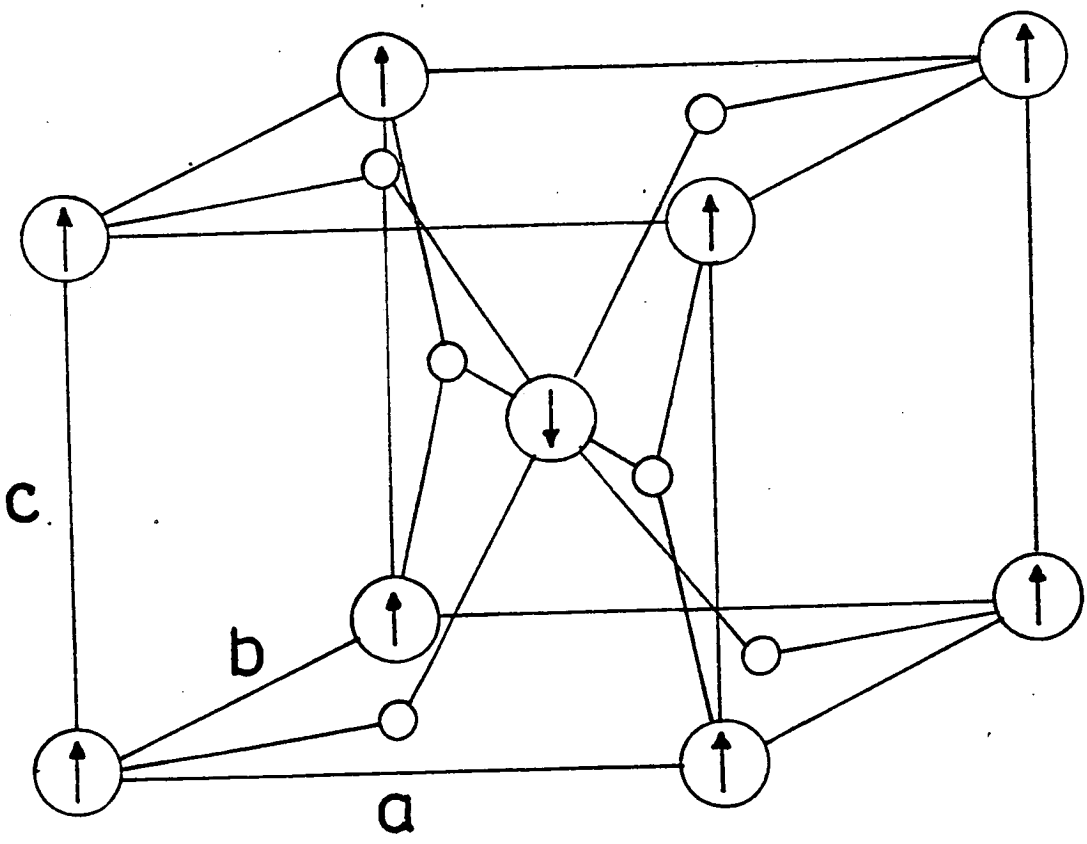

$\bigcirc Co^{++}$ $\circ F^{-}$

non-magnetic and therefore $Co_xZn_{1-x}F_2$ is a dilute antiferromagnet. Therefore assuming that the Néel temperature is proportional to the number of spins in the infinite cluster, then the observed Néel temperatures of 13.25 K and 6.20 K imply concentrations of 35% and 26% cobalt respectively. In order to convert the fraction of spins in the infinite cluster into a concentration, the results of Kirkpatrick (1973) for the number of spins in the infinite cluster as a function of concentration on a b.c.c. lattice were used. It should be noted that the 26% sample is very close to the percolation threshold for a b.c.c. lattice of 24.5%.

The orientation of the Co^{2+} spins in the unit cell of CoF_2 is shown in figure (3.4.1). In this structure the combination of the crystal field and spin-orbit coupling cause the ground state of the Co^{2+} ion to be a pseudo spin $s = \frac{1}{2}$ doublet (Martel et al (1968)). The exchange interaction within this doublet is highly anisotropic with a strong antiferromagnetic exchange between nearest neighbours and a weak ferromagnetic exchange between next nearest neighbours. Values for these exchange interactions have been determined from spin wave measurements (Cowley et al (1973)) which reveal a ratio of transverse to Ising exchange for nearest neighbours of 0.68. The critical exponents β and ν for CoF_2 were measured by Cowley and Carneiro (1980) and were found to be in very good agreement with the best estimates for the d = 3 Ising model. Further, Cowley and Carneiro measured the same critical exponents for a sample of $Co_{0.85}Zn_{0.15}F_2$ and found these to be in good agreement with those for the dilute d = 3 Ising model.

3.4 ii) Experimental apparatus

The measurements reported here were performed using the H-7 triple axis sprectometer at Brookhaven National Laboratory. However, for these measurements the analyser was removed and the spectrometer operated in a two-axis mode. The monochromator used was pyrolytic graphite and an incident neutron wavevector of 2.67 A^{-1} was obtained by reflection from the (0,0,2) planes. This value of the incident wavevector allowed the use of two tunable pyrolytic graphite filters to suppress the contamination of the monochromatic beam by neutrons scattered from higher order planes in the monochromator. One of the filters was positioned before the monochromator and the other between the sample and detector. For the 35% cobalt sample horizontal collimations of 10' were used before the monochromator, in the monochromator to sample position and in the sample to detector position. In the measurements on the 26% sample 20' collimations were used in these positions. A schematic representation of the layout of the components of H-7 spectrometer is shown in figure (3.4.2).

In both cases the samples of $Co_xZn_{1-x}F_2$ were mounted with their (0,0,1) axes vertical in the long tail section of a Cryogenics Associates CT-14 flow cryostat. The cryogen used was liquid helium which meant that under normal conditions, temperatures down to 4.2 K could be attained. In order to obtain temperatures down to 1.85 K the bath of liquid helium was "pumped". The temperature of the sample was measured using a germanium resistance thermometer attached to the copper block of the cryostat.

The tail section of the cryostat was mounted inside the coils of a Cryogenics Associates superconducting magnet, which could produce vertical fields in the range from 0 to 6T. From the

Figure (3.4.2)

A schematic representation of the layout of H - 7 spectrometer used for the measurements on the $Co_xZn_{1-x}F_2$ samples is shown.

FIGURE(3.4.2)

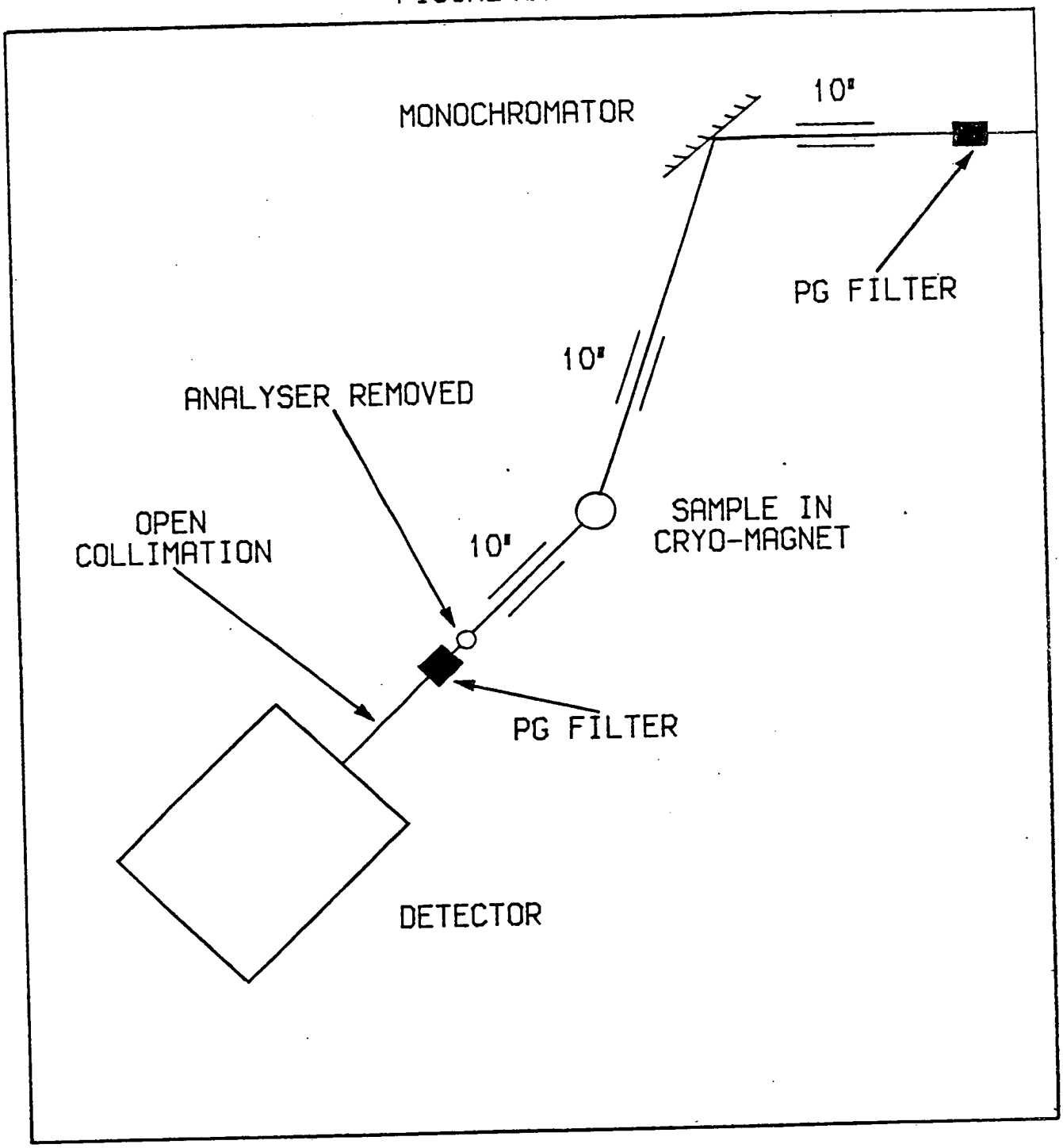
MONOCHROMATOR
10"
PG FILTER
10"
ANALYSER REMOVED
SAMPLE IN
CRYO-MAGNET
OPEN
COLLIMATION
10"
PG FILTER
DETECTOR

arrangement of the coils of the magnet and the long tail section of the cryostat, a uniform magnetic field was produced across the sample. The field strength close to the sample position was measured by a Hall probe and this value taken as the field strength at the sample position.

The reciprocal space diagram for the scattering plane is shown in figure (3.4.3). In this diagram Bragg peaks that are purely magnetic are indicated by circles, those that are purely nuclear are indicated by squares and those that are mixed nuclear and magnetic are indicated by triangles. Measurements of the magnetic structure factor were performed about the $(1,0,0)_M$ Bragg peak position. The relative positions of the incident and final wavevectors and the orientation of the resolution function at the $(1,0,0)_M$ position is also shown. The frequency width of the critical fluctuations in CoF_2 was measured by Cowley et al (1973) and was found to be less than 0.12 THz in the range from 38 K to 70 K. Therefore the frequency integration performed by using the spectrometer in a two axis mode was very accurate and it is quite satisfactory to treat the resolution function for the spectrometer only in terms of its wavevector components.

The component of the resolution function within the scattering plane was measured by performing a mesh of scans through the $(1,0,0)_M$ Bragg peak in zero applied magnetic field. The mesh of scans showed that the full width at half maximum (F.W.H.M.) of the in-plane component of the resolution function was essentially an ellipse with its long axis oriented along the wavevector transfer. The F.W.H.M. of the resolution function for the 35% cobalt sample parallel to the wavevector transfer was 0.0090 A^{-1} and perpendicular to the wavevector transfer was 0.0024 A^{-1}. Consequently

Figure (3.4.3)

A diagram of the scattering plane used for the measurements on the $Co_xZn_{1-x}F_2$ samples is shown. The purely magnetic Bragg reflections are indicated by circles and the purely nuclear Bragg reflections by squares. Bragg reflections which are mixed nuclear and magnetic are indicated by triangles. The relative orientations of the incident and final neutron wavevectors and the resolution ellipse are also shown. The diagram is not to scale.

FIGURE(3.4.3)

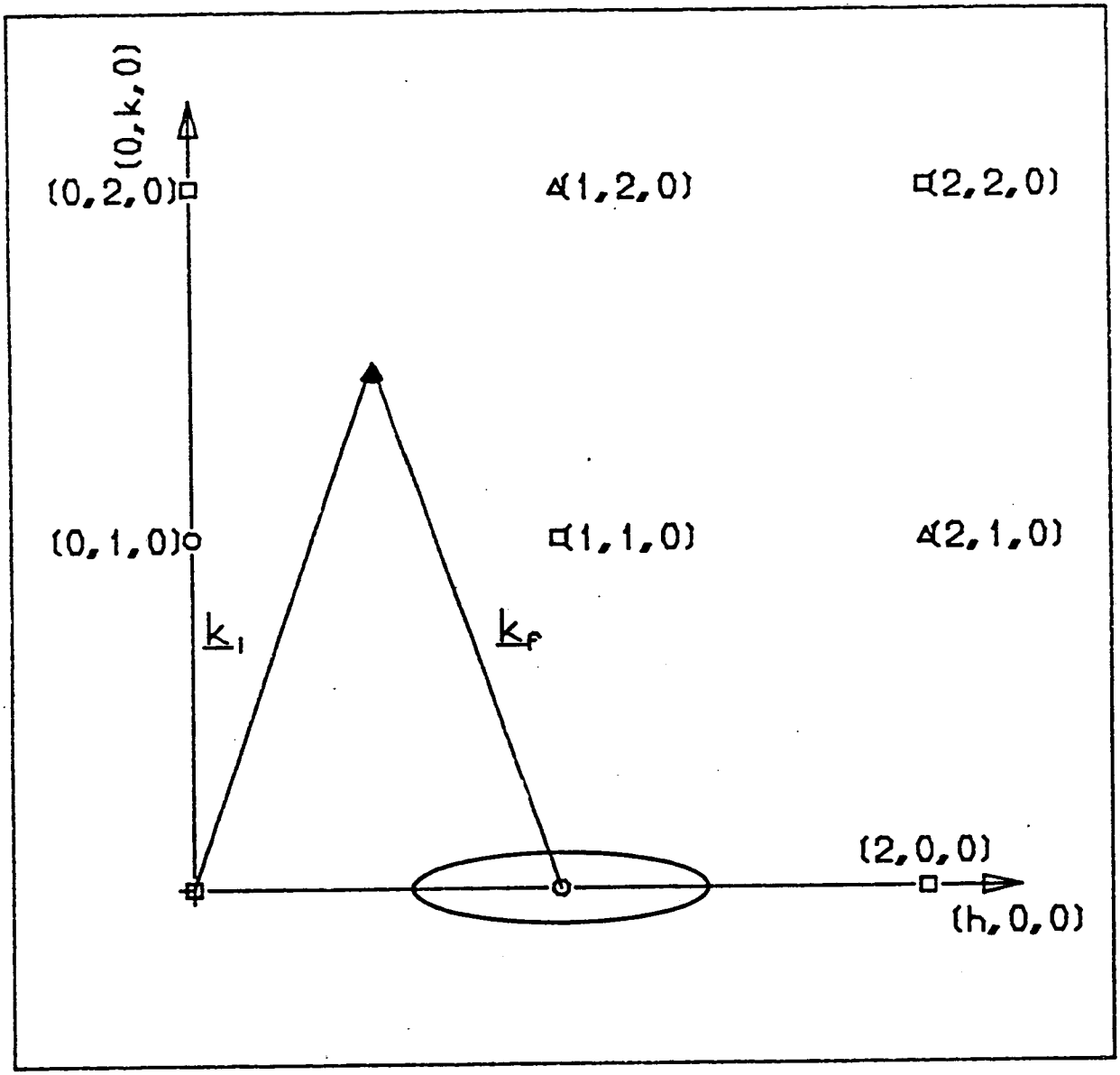

the in-plane component of the resolution function was modelled as the product of two Gaussians in the parallel and perpendicular wavevector components with the F.W.H.M. given above. The vertical component of the resolution function was measured by tilting the sample on the set of calibrated arcs and measuring the intensity at the $(1,0,0)_M$ Bragg peak position as a function of the angle of tilt. From this it was found that the vertical component more closely resembled a triangle rather than a Gaussian, with a F.W.H.M. of $0.085A^{-1}$. As a consequence the vertical component of the resolution function was modelled as a triangle with a F.W.H.M. of $0.085A^{-1}$.

3.5 Experimental Results (1) $Co_xZn_{1-x}F_2$

As described in the previous section, the samples of $Co_xZn_{1-x}F_2$ were mounted on the spectrometer in a cryo-magnet which allowed the static structure factor to be measured at various temperatures and applied magnetic fields. The results will be described in essentially two parts. Firstly, a qualitative description of the behaviour when the magnetic field was applied will be given. This will be followed by a brief description of the data analysis and finally a description of the dependence of the parameters obtained from the data analysis on temperature and magnetic field.

The various combinations of magnetic field and temperature at which measurements were performed were reached by cooling the sample from a temperature above the zero field Néel temperature in the desired magnetic field. This 'field cooled' method was used because it was found that at low temperatures the spins became 'frozen' in a given state. That is to say that whatever the line-shape was at low temperature it could not be changed simply by

changing the magnetic field at low temperature. The inability of the system to respond to changes in the applied field at low temperature held throughout the range of fields from 0 to 5T applied to the 35% sample. In the 26% sample, however, this freezing of the spins at low temperature only occurred for fields of less than 1.2T. For fields greater than 1.2T in this sample the same state could be reached by any combination of changes in temperature and applied field. All the following results described in this section were obtained in a field cooled mode. In spin glasses where a similar freezing effect has been observed this is the accepted method for obtaining an equilibrium state.

Implicit in the previous comments is the fact that the lineshape of the structure factor at the $(1,0,0)_M$ position was different with a field applied to that in zero field, and further that the lineshape was different in different applied fields. In figure (3.5.1) the lineshape at 2 K in fields of 3.5T and 5.0T is shown for the 35% sample. The lineshape in zero field at 2 K is limited by the resolution function, which is shown in figure (3.5.1) for comparison with a peak height equal to that of the $(1,0,0)_M$ Bragg peak at 2 K in zero field. A comparison of the peak intensities in figure (3.5.1) shows that in 3.5T there has been a reduction by a factor of 6, and in 5.0T a reduction by a factor of 100 from the zero field value. Although the intensity scale in figure (3.5.1) is logarithmic it is still clear that the F.W.H.M. in 3.5T and 5.0T fields is considerably greater than that in zero field. Further, the lineshapes in 3.5T and 5.0T field have large wings of scattering which are significantly greater than the zero field background level (horizontal dashed line in figure (3.5.1)). It is therefore clear from figure (3.5.1) that the lineshapes at 2 K in 3.5T and

Figure (3.5.1)

The lineshape at the $(1,0,0)_M$ Bragg position at 2 K in fields of 3.5 T and 5.0T are shown for the $Co_{0.35}Zn_{0.65}F_2$ sample. For clarity the 3.5T lineshape has been offset by an order of magnitude. The dotted lines represent the resolution function and background levels.

Figure (3.5.2)

The lineshape at the $(1,0,0)_M$ Bragg position at 1.85 K in fields of 0.33T, 0.84T, 1.3T and 1.7T are shown for the $Co_{0.26}Zn_{0.74}F_2$ sample.

FIGURE (3.5.1)

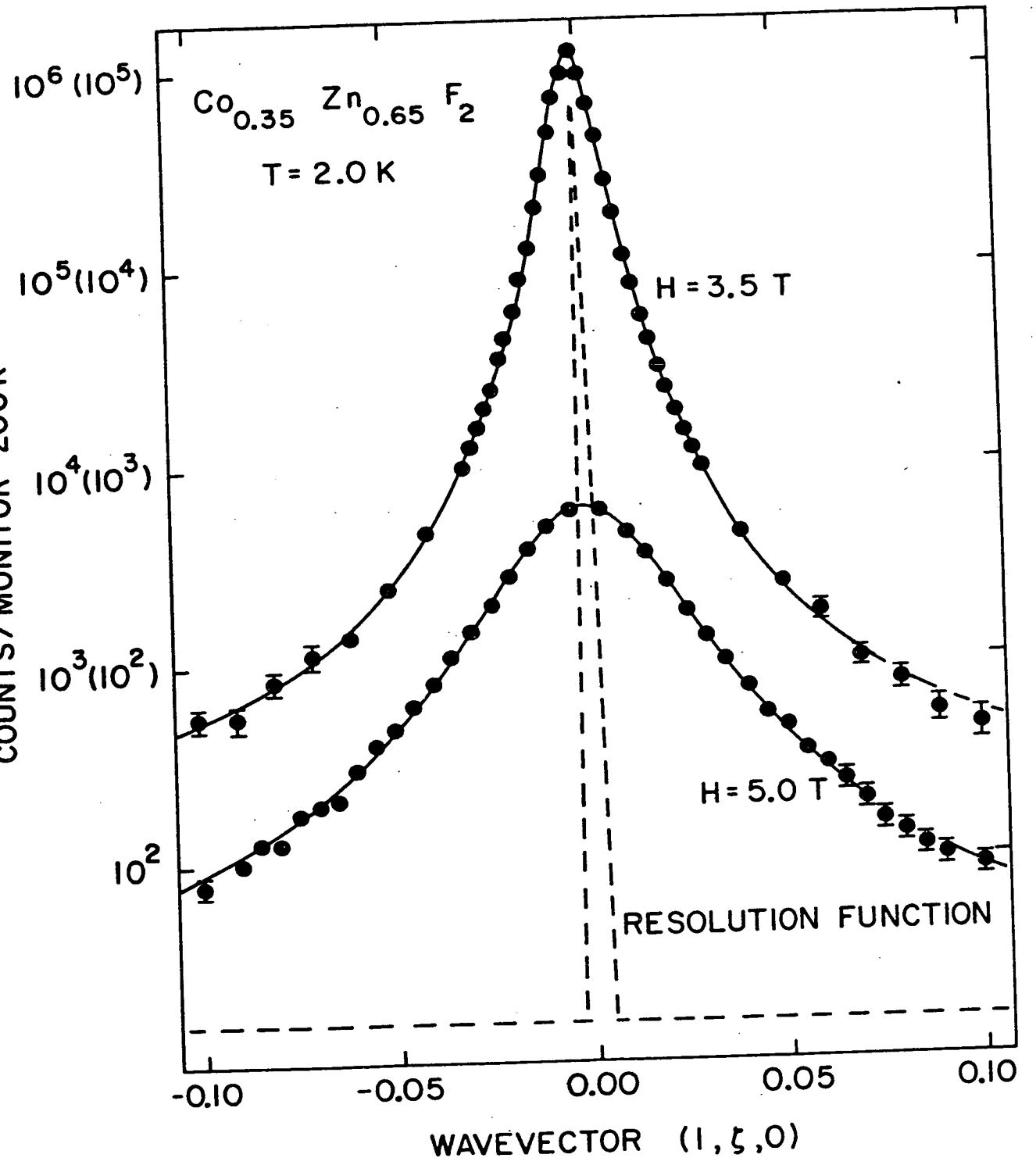
$Co_{0.35}$ $Zn_{0.65}$ F_2
T = 2.0 K
H = 3.5 T
H = 5.0 T
RESOLUTION FUNCTION
10^6 (10^5)
10^5(10^4)
10^4(10^3)
10^3(10^2)
10^2
COUNTS / MONITOR 200K
-0.10
-0.05
0.00
0.05
0.10
WAVEVECTOR (1, ζ, 0)

FIGURE (3.5.2)

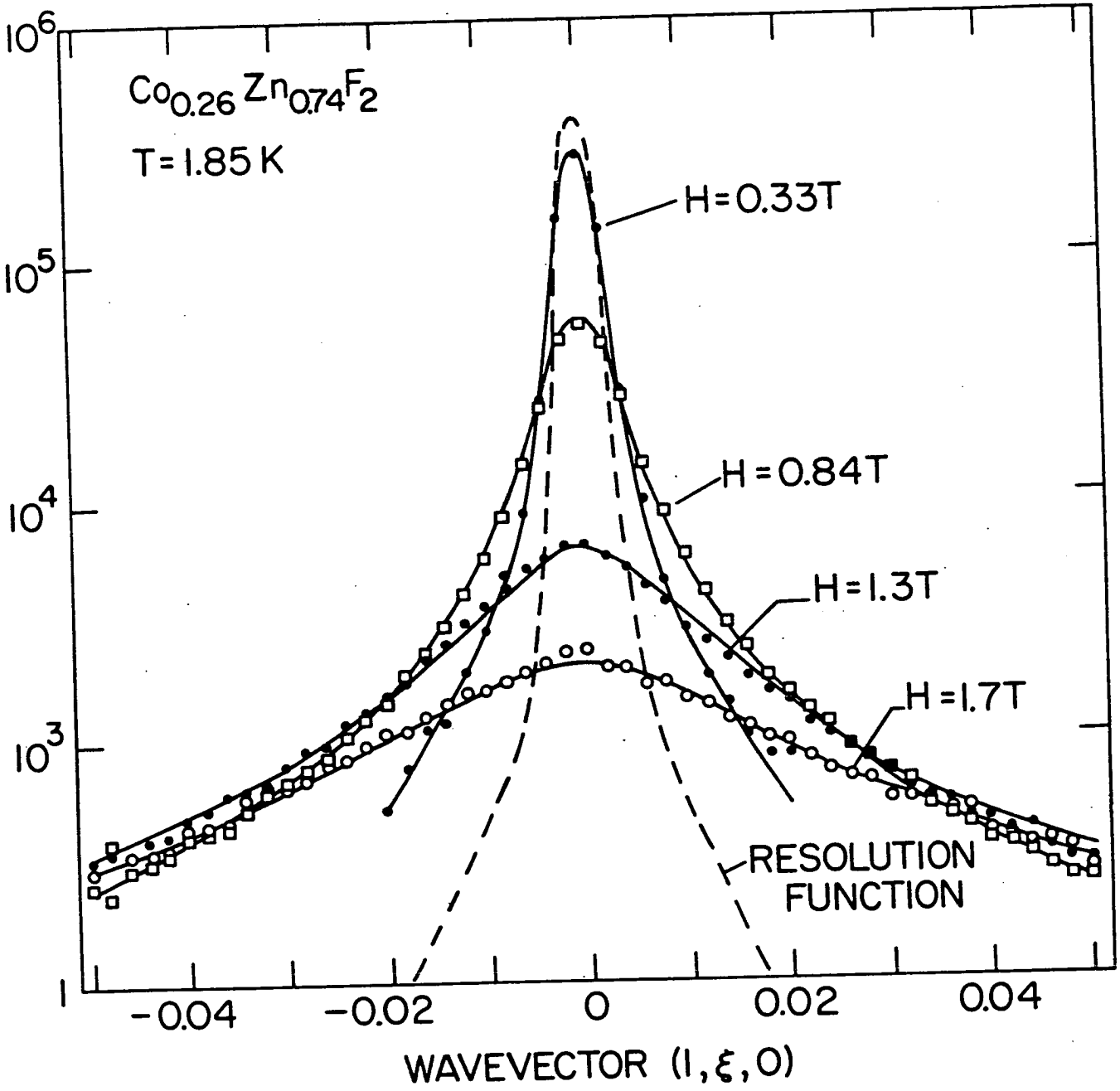
$Co_{0.26}Zn_{0.74}F_2$
T = 1.85 K
H = 0.33T
H = 0.84T
H = 1.3T
H = 1.7T
RESOLUTION FUNCTION
10^6
10^5
10^4
10^3
1
-0.04
-0.02
0
0.02
0.04
WAVEVECTOR (1, ξ, 0)

5.0T field do not represent states of long range antiferromagnetic order. Since the F.W.H.M. decreases with decreasing magnetic field it was not possible for the samllest non-zero field applied to this sample of 0.8T to determine the difference in F.W.H.M. from the zero field value. There are, however, at this field, still significant wings of scattering, indicating that the state of the sample was not one of long range order. Therefore it is concluded that at all of the non-zero magnetic fields applied long range antiferromagnetic order was destroyed in this sample. Similar results were obtained for the 26% sample and a selection of lineshapes at 1.85 K are shown in figure (3.5.2). Since the concentration of this sample is much closer to the percolation threshold, the effect for a given magnetic field is very much larger than in the 35% sample.

The above description of the variation of the peak intensity at 2 K with magnetic field needs to be qualified for the 35% sample. In figures (3.5.3a) and (3.5.3b) the variation of the peak intensity as a function of magnetic field is shown for the 35% sample at temperatures of 2 K and 12 K and the the 26% sample at 1.85 K and 4.5 K respectively. For the 26% sample the intensity falls monotonically with increasing field at both temperatures. This is just what one would naively expect since the induced random field is breaking up the long range order. For the 35% sample, however, the peak intensity at 2 K increases with increasing magnetic field for fields below 1.5T and then falls monotonically for fields above this value. Since at the same time the F.W.H.M. is increasing and wings of scattering are developing the integrated intensity must also increase with increasing magnetic field below 1.5T. In zero magnetic field the $(1,0,0)_M$ Bragg peak is extinction limited and the explanation for this anomalous

Figure (3.5.3a)

The variation of the peak intensity at the $(1,0,0)_M$ position as a function of field at temperatures of 2 K and 12 K for the $Co_{0.35}Zn_{0.65}F_2$ sample is shown. The solid lines are merely guides to the eye.

Figure (3.5.3b)

A similar plot to that in figure (3.5.3a) is shown but for the $Co_{0.26}Zn_{0.74}F_2$ sample at temperatures of 1.85 K and 4.5 K.

FIGURE (3.5.3a)

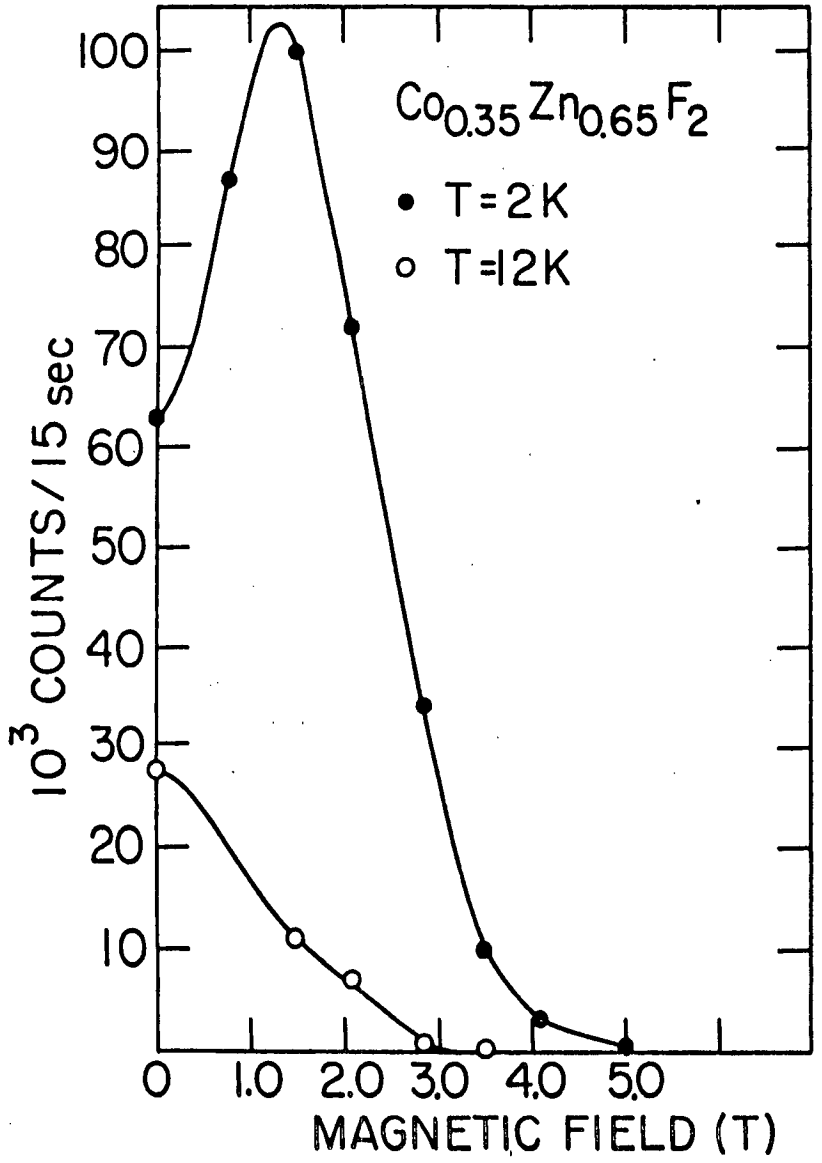

FIGURE (3.5.3b)

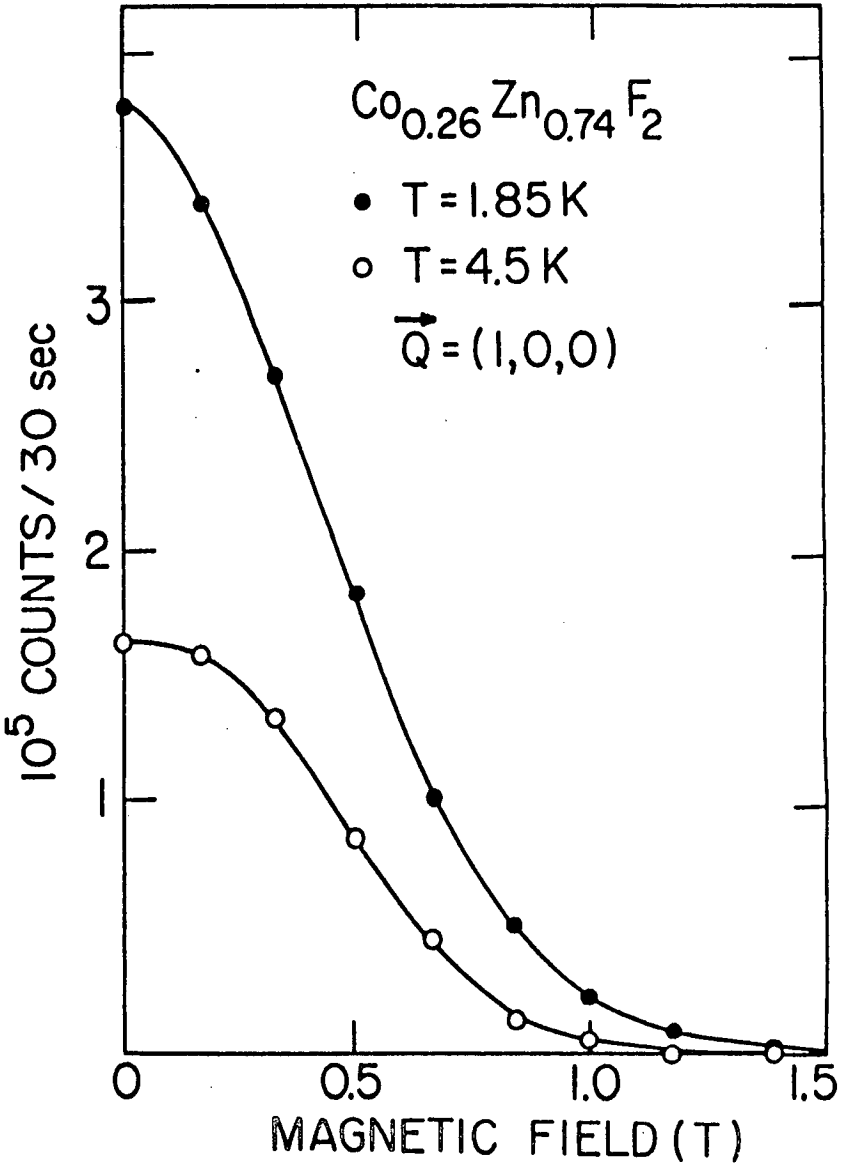

increase in intensity lies in the effect the induced random field has on extinction. Although the sample is termed a single crystal it of course consists of many mosaic blocks whose individual crystallographic axes are closely aligned. Each of these mosaic blocks may be thought of as an ideal crystal and therefore has a small Darwin angle (see for example Bacon 1975) p. 68). The induced random field breaks up the mosaic blocks into domains and hence increases their Darwin angles, allowing them to scatter a greater proportion of the incident neutron beam. As a consequence, the integrated intensity will increase until the extinction present has been relieved. At 12 K where in zero field the extinction would be much smaller, no anomaly is seen in the variation of the peak height with magnetic field in this sample. The same effect has been observed in samples of $Fe_xZn_{1-x}F_2$ in an external magnetic field (Cowley et al (1983c)) and a similar effect has been observed in the ferromagnet Rb_2CrCl_4 in a magnetic field (Fyne and Hutchings (1982)).

Since there is no long range antiferromagnetic order, the magnetic structure factor is simply the Fourier transform of the correlation function. The solid lines in figures (3.5.1) and (3.5.2) represent the best fits obtained using the form for the correlation function proposed by Kogon and Wallace (1981) (c.f. equation (3.2.3)). These fits involved convolving equation (3.2.3) with the instrumental resolution function and then varying the values of the parameters A, B and κ using the methods described in appendix A to obtain the best fit in a least squares sense. The fits were performed using a computer program FITIT6. The speed and accuracy of this program was greatly enhanced by using the

analytical result for the convolution of the structure factor with the vertical component of the resolution function. In subsection (v) of appendix A the analytical result for this integral is described explicitly. Equation (3.2.3) provided very good fits to all of the data taken in non-zero magnetic field with χ^2 values less than 2.5 in all cases for the 35% sample. It should be emphasised that at low temperatures other forms for the structure factor, notably a Gaussian plus Lorentzian, did not provide satisfactory fits. The relative contribution of the two components of the structure factor of course varied with magnetic field and temperature. In figures (3.5.4a) and (3.5.4b) the regions of temperature and field over which the data could be fitted by a Lorentzian alone and where it needed a Lorentzian squared as well are shown. The error bars join the highest temperatures for which a Lorentzian squared was required in the fit and the lowest temperature at which a Lorentzian alone was sufficient for the fit. The dashed lines are guides to the eye through these points. If the state in which the structure factor was only Lorentzian is considered paramagnetic, then for the 26% sample it was possible to obtain paramagnetic states all the way down to 1.85 K with fields greater than 1.2T. In figure (3.5.5) the variation of the lineshape at the $(1,0,0)_M$ position as a function of temperature is shown for the 35% sample in 3.5T field. The solid lines are fits to equation (3.2.3) and the data has been offset for clarity.

In figures (3.5.6a) and (3.5.6b) the values of the inverse correlation lengths deduced from the fitting procedure are shown for the various fields and temperatures at which measurements were performed. The general behaviour of the inverse correlation length as a function of temperature is the same for each of the applied

Figure (3.5.4a)

This figure indicates the regions where for the $Co_{0.35}Zn_{0.65}F_2$ sample the magnetic structure factor could be represented by a Lorentzian alone and where it needed a Lorentzian plus Lorentzian squared.

Figure (3.5.4b)

A similar plot to that in figure (3.5.4a) is shown but for the $Co_{0.26}Zn_{0.74}F_2$ sample.

FIGURE(3.5.4a)

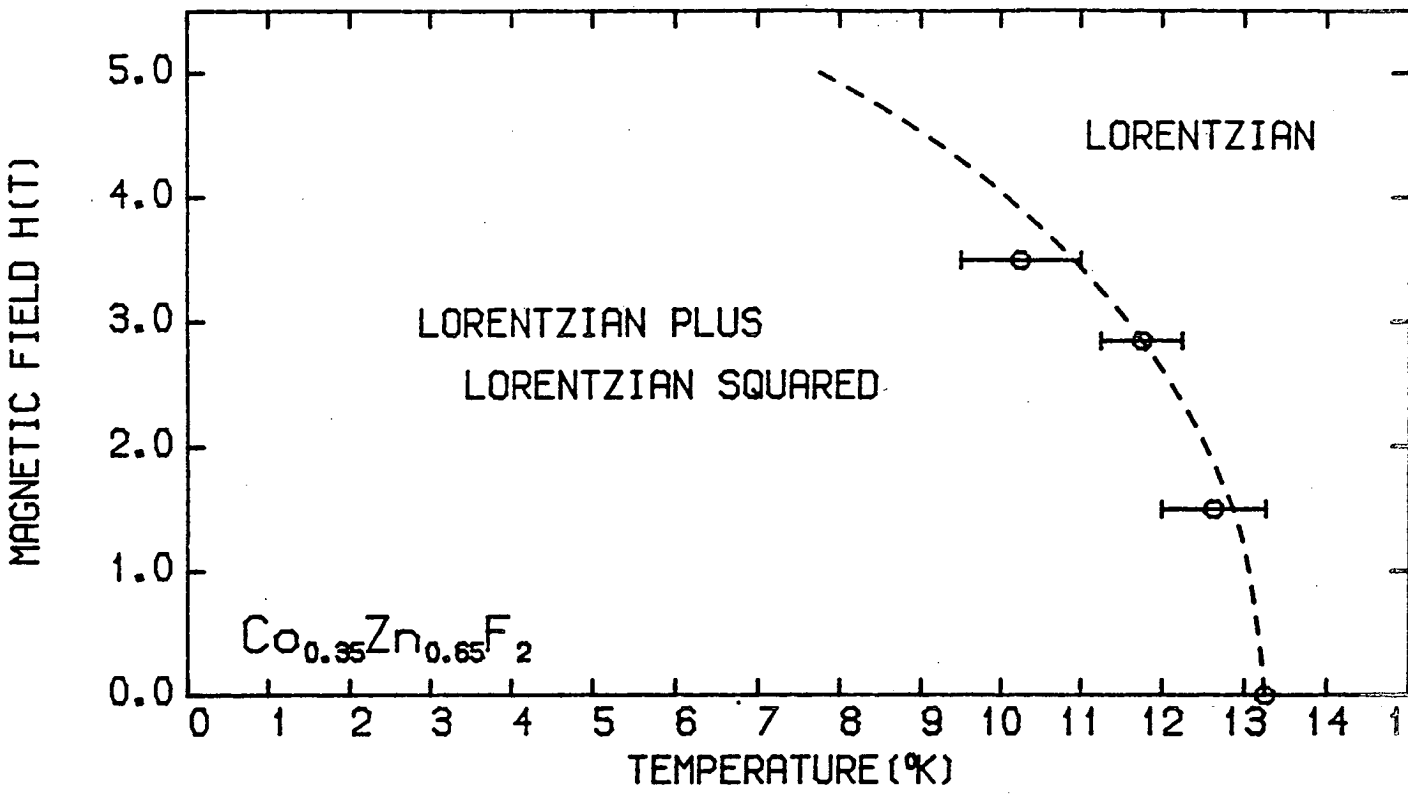

FIGURE(3.5.4b)

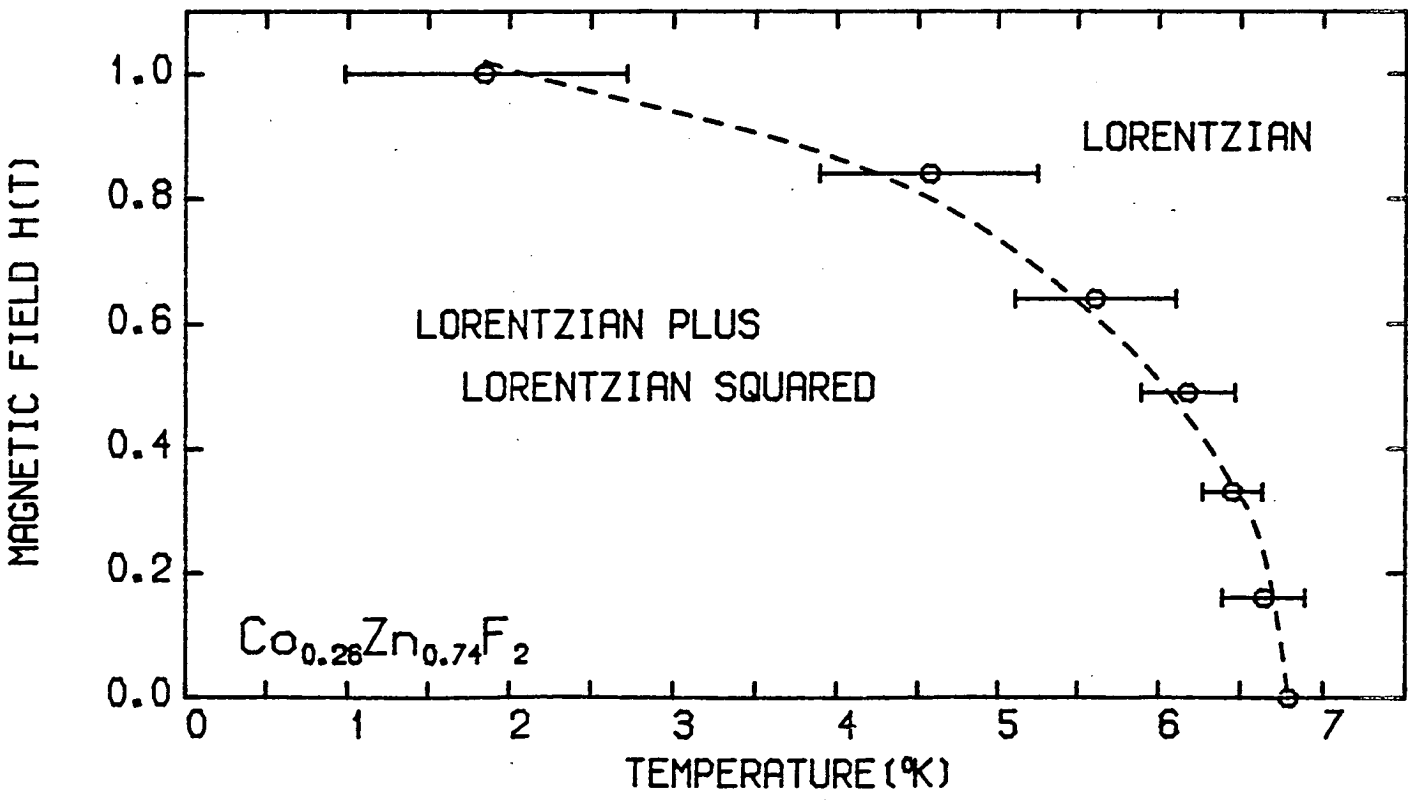

Figure (3.5.5)

In this figure the variation of the lineshape at the $(1,0,0)_M$ Bragg position in a field of 3.5T is shown as a function of temperature. The lineshapes at different temperatures have been offset for clarity. At 4 K and 7 K the solid lines are the best fits to Lorentzian plus Lorentzian squared lineshapes while at 11 K and 12.5 K the solid lines represent fits to a Lorentzian only.

FIGURE (3.5.5)

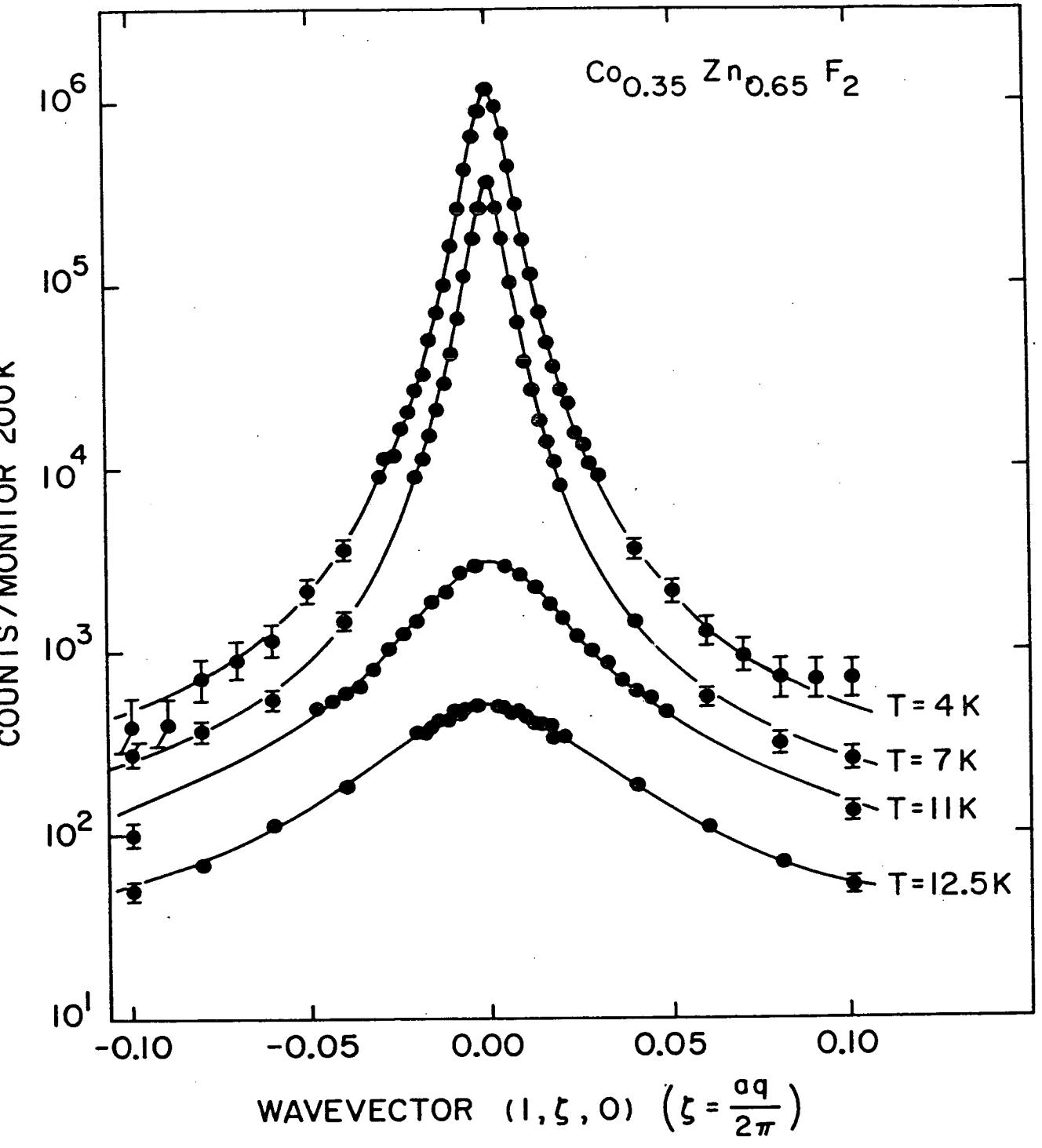
$Co_{0.35}\ Zn_{0.65}\ F_2$
10^6
10^5
10^4
10^3
10^2
10^1
COUNTS / MONITOR 200K
T = 4 K
T = 7 K
T = 11 K
T = 12.5 K
-0.10
-0.05
0.00
0.05
0.10
WAVEVECTOR (1, ζ, 0) $\left(\zeta = \frac{aq}{2\pi}\right)$

Figure (3.5.6a)

This figure shows the dependence of the inverse correlation length as a function of temperature for the various fields applied to the $Co_{0.35}Zn_{0.65}F_2$ sample.

Figure (3.5.6b)

This figure shows the dependence of the inverse correlation length as a function of temperature for the various fields applied to the $Co_{0.26}Zn_{0.74}F_2$ sample.

FIGURE (3.5.6a)

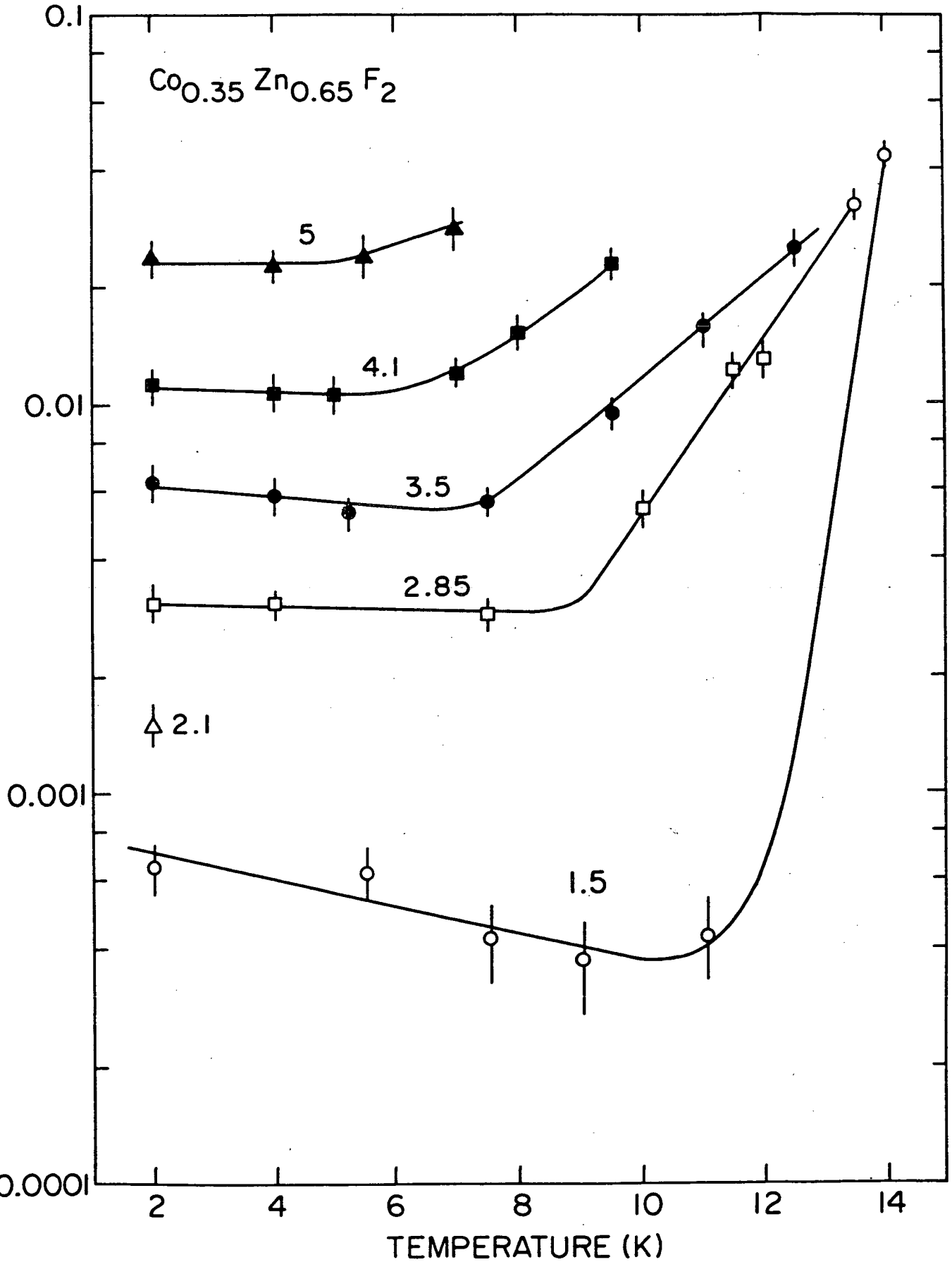
0.1
0.01
0.001
0.0001
$Co_{0.35}Zn_{0.65}F_2$
5
4.1
3.5
2.85
2.1
1.5
2
4
6
8
10
12
14
TEMPERATURE (K)

FIGURE (3.5.6b)

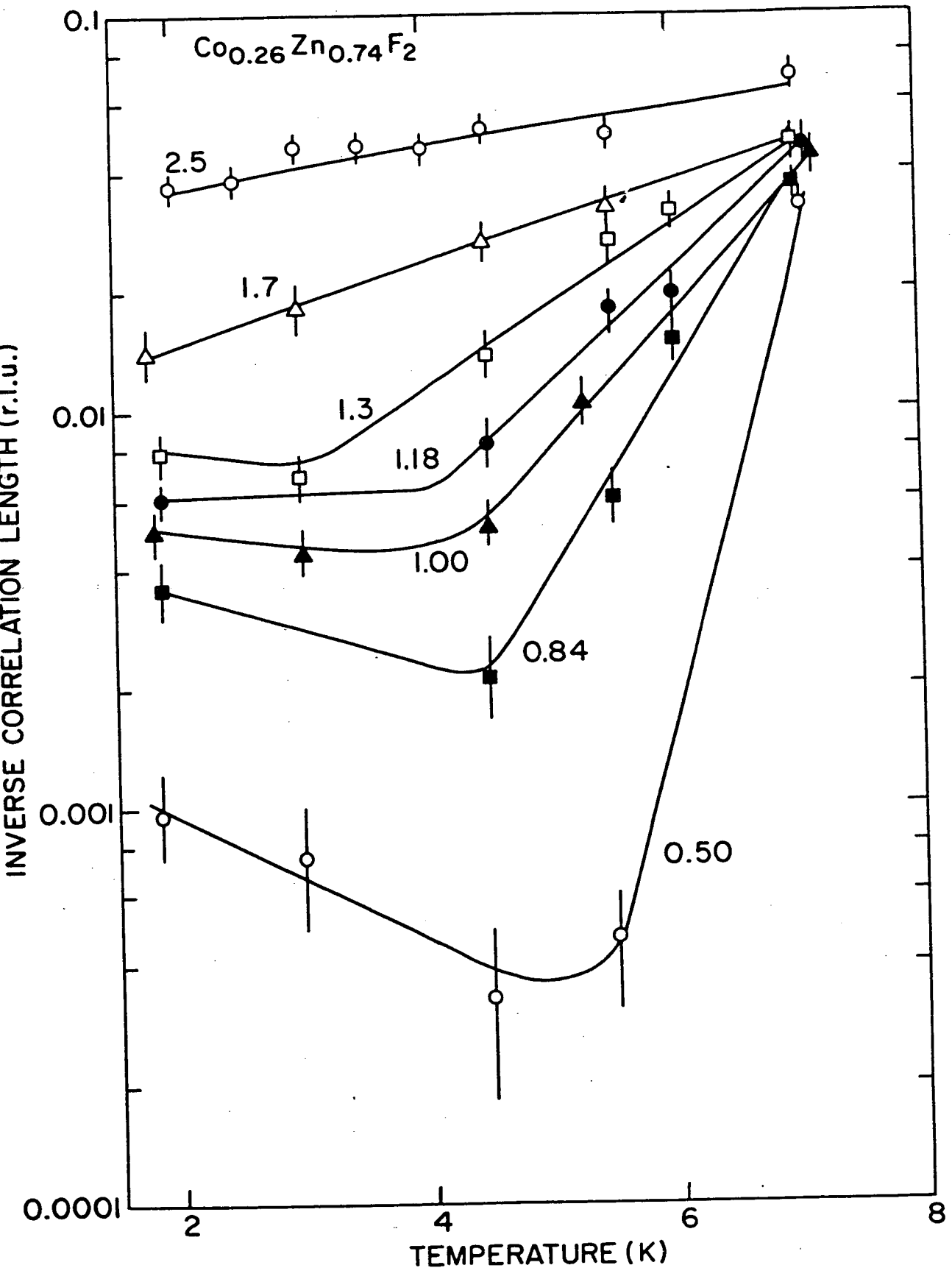
0.1
0.01
0.001
0.0001
$Co_{0.26}Zn_{0.74}F_2$
2.5
1.7
1.3
1.18
1.00
0.84
0.50
INVERSE CORRELATION LENGTH (r.l.u.)
2
4
6
8
TEMPERATURE (K)

fields in the 35% sample. Initially the inverse correlation length falls rapidly as the temperature is reduced from the region where the structure factor is given by a Lorentzian only to the region where a Lorentzian squared appears in the structure factor. Once within this lower temperature region, however, the inverse correlation length is essentially constant as a function of temperature. The low temperature results in a field of 1.5T are of course influenced by the extinction effect discussed earlier and these values are most probably larger than the 'true' values. In the region where the structure factor contains a Lorentzian squared in the 26% sample the results are similar, although the data is much more sparse in this sample. For fields greater than 1.2T where the structure factor is Lorentzian for all temperatures greater than 1.85 K the inverse correlation length essentially just falls with decreasing temperature.

At the end of section (2) the theoretical predictions for the dependence of the inverse correlation length on the variance of the random field were given. It was argued at the end of section (3) that the variance of the induced random field was proportional to the square of the applied field. Therefore if d_ℓ were 3 for the R.F.I.M.,equation (3.2.4) would imply that a graph of the logarithm of the inverse correlation length against the reciprocal of the square of the applied field at a fixed low temperature would be a straight line. In figure (3.5.7) such a plot is shown for the 35% sample using the values of the inverse correlation length at 2 K. The data in figure (3.5.7) clearly does not fall on a straight line. The alternative form for the field dependence of the inverse correlation length given in equation (3.2.5) implies that the data should fall on a straight line in a Log-Log plot of inverse

Figure (3.5.7)

A plot of the logarithm of the inverse correlation length against the square of the reciprocal of the applied field for the $Co_{0.35}Zn_{0.65}F_2$ sample at 2 K is shown.

FIGURE(3.5.7)

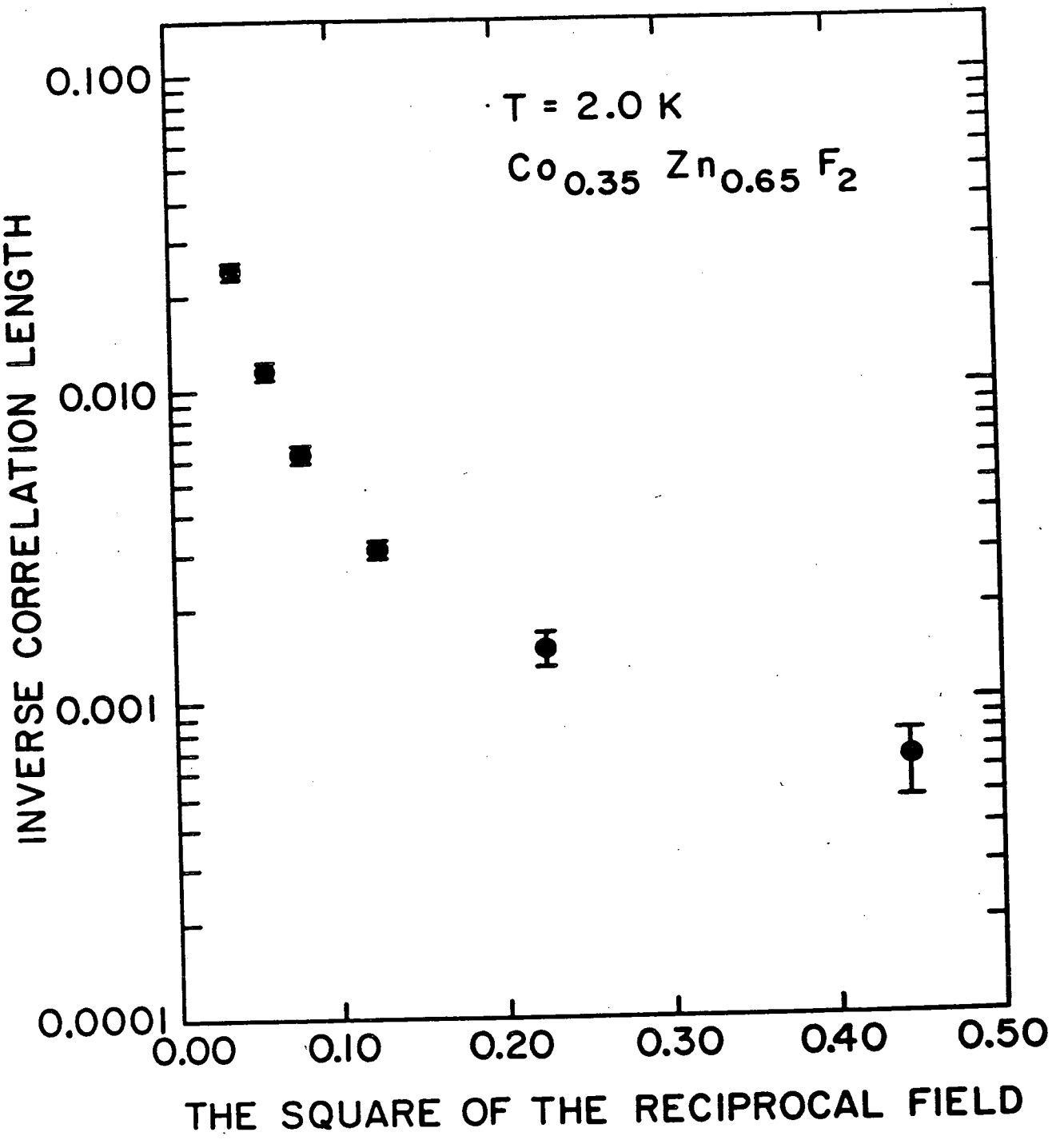
T = 2.0 K
Co0.35 Zn0.65 F2
INVERSE CORRELATION LENGTH
0.100
0.010
0.001
0.0001
0.00
0.10
0.20
0.30
0.40
0.50
THE SQUARE OF THE RECIPROCAL FIELD

correlation length against applied field. Such plots are shown in figures (3.5.8a) and (3.5.8b) for the 35% and 26% samples respectively. The solid lines in these figures are the best straight line fits. For the 35% sample the data point at 1.5T has been omitted from the fit because it is affected by the presence of the extinction. These straight line fits give values for ν_H and κ_o (defined in equation (3.2.5) of $\nu_H = 3.63 \pm 0.12$ with $\kappa_o = 0.000069 \pm 0.000012$ and $\nu_H = 2.17 \pm 0.16$ with $\kappa_o = 0.0047 \pm 0.004$ for the 35% and 26% samples respectively. The χ^2 parameters for these fits are 2.62 and 1.12 respectively.

If equation (3.2.3) is to go over smoothly to a Bragg peak as the inverse correlation length (i.e. the induced random field) goes to zero, then constraints can be placed upon the field dependence of the amplitudes A and B. These are that the integrated intensity in the Lorentzian squared term must go over to the integrated intensity of the Bragg peak and the Lorentzian term must go to zero. The integrated intensity in the Lorentzian squared term in d = 3 is $\pi^2 B/\kappa$,which implies that in the 'small field' limit B/κ is a constant. The Lorentzian term will be zero at zero field if the amplitude A goes to zero as a positive power of the field. In figures (3.5.9a) and (3.5.9b) the variation of the amplitude A and the ratio B/κ with the field at 2 K are shown for the two samples. For the 35% sample the ratio B/κ is constant within experimental error for fields above 2.0T. The fall in (B/κ) for fields below 2.0T in this sample is due to the effect of extinction, as would be expected from the previous discussion of the extinction effect. In figure (3.5.9a) the amplitude A appears to be going to zero at zero field, although the extinction effect will also influence the value of this amplitude at low fields. The behaviour of A and B/κ for the 26% sample, shown in figure (3.5.9b) is,

Figure (3.5.8a)

A Log-Log plot of the inverse correlation length against the applied magnetic field at 2 K for the $Co_{0.35}Zn_{0.65}$ sample is shown. The solid line is the best straight line fit to the data omitting the data point at 1.5T.

Figure (3.5.8b)

This figure shows a Log-Log plot of the inverse correlation length against the applied magnetic field at 1.85 K for the $Co_{0.26}Zn_{0.74}F_2$ sample. The solid line is the best straight line fit.

FIGURE(3.5.8a)

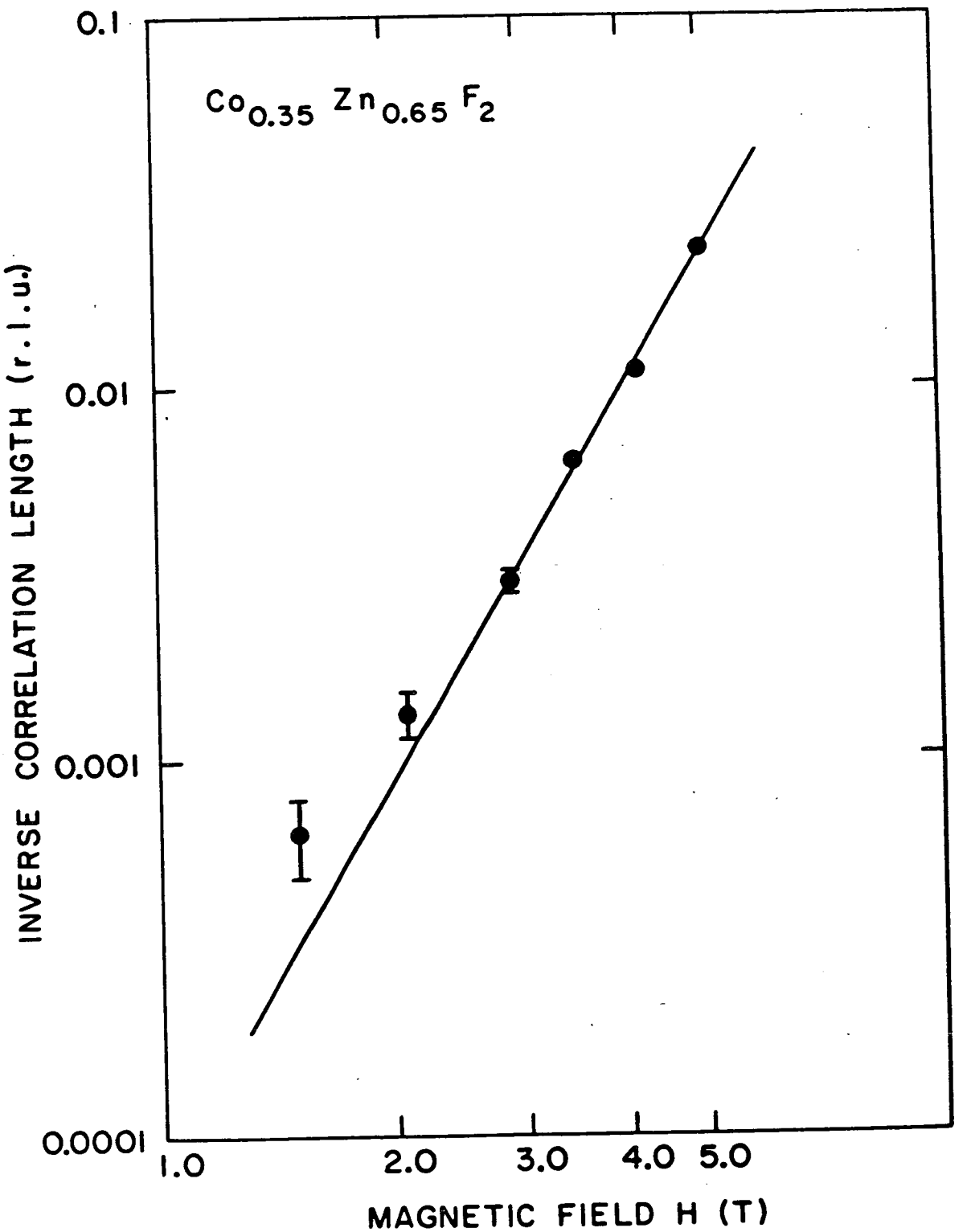
0.1
0.01
0.001
0.0001
$Co_{0.35}\ Zn_{0.65}\ F_2$
INVERSE CORRELATION LENGTH (r.l.u.)
1.0
2.0
3.0
4.0
5.0
MAGNETIC FIELD H (T)

FIGURE (3.5.8b)

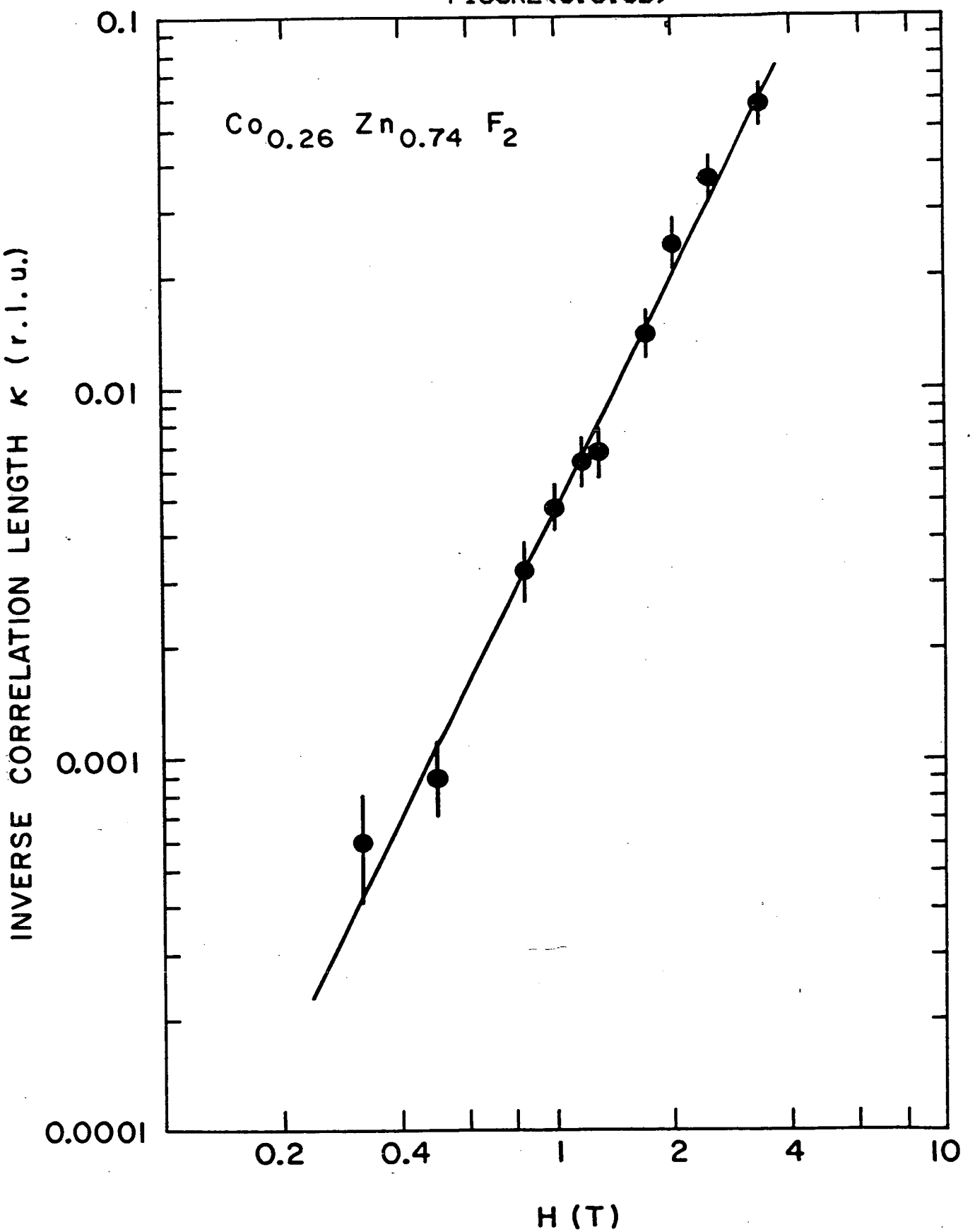
$Co_{0.26}\ Zn_{0.74}\ F_2$
INVERSE CORRELATION LENGTH κ (r.l.u.)
0.1
0.01
0.001
0.0001
0.2
0.4
1
2
4
10
H (T)

Figure (3.5.9a)

The dependence of the amplitude A and the ratio B/κ on the applied magnetic field at a temperature of 2 K for the $Co_{0.35}Zn_{0.65}F_2$ sample is shown.

Figure (3.5.9b)

A similar plot to that in figure (3.5.9a) is shown but for the $Co_{0.26}Zn_{0.74}F_2$ sample at 1.85 K. The ratio B/κ in this figure has been multiplied by a factor of 10 relative to the amplitude A for clarity.

FIGURE (3.5.9a)

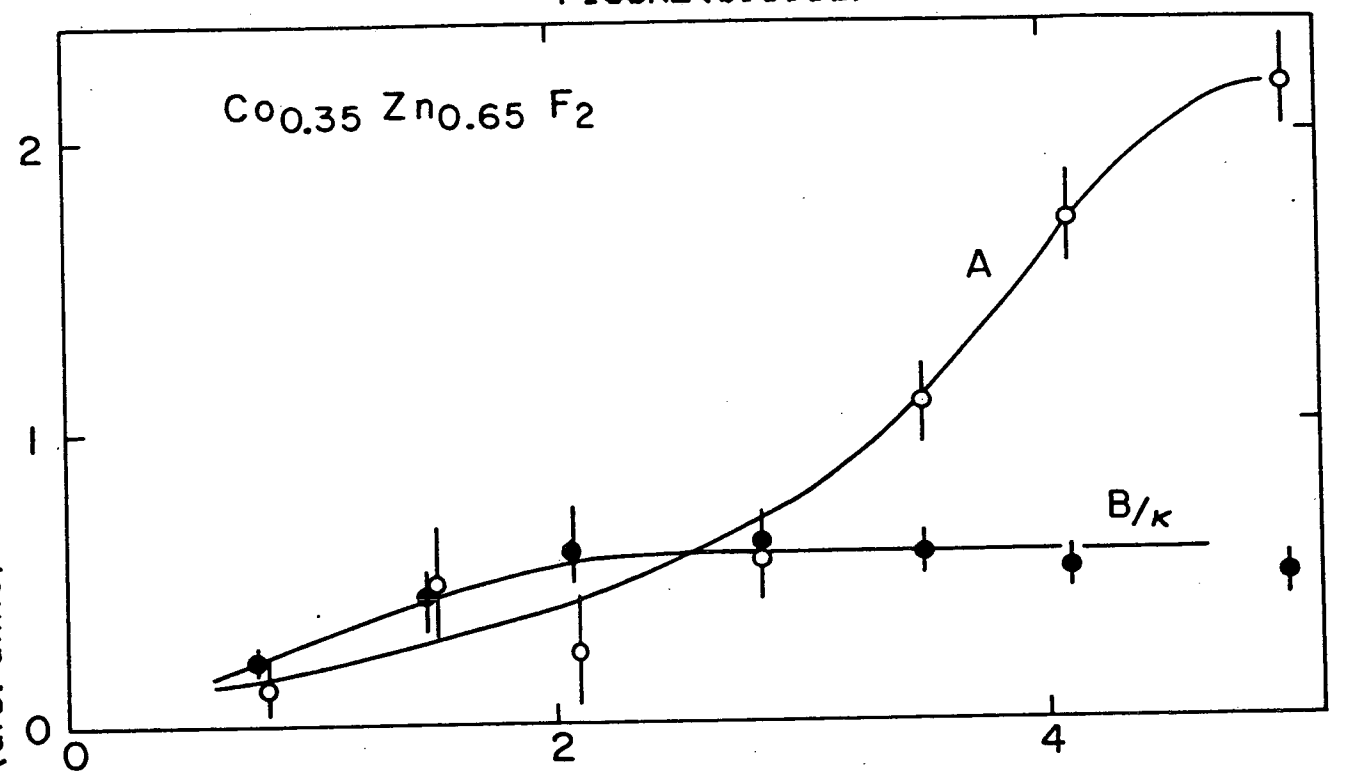

FIGURE (3.5.9b)

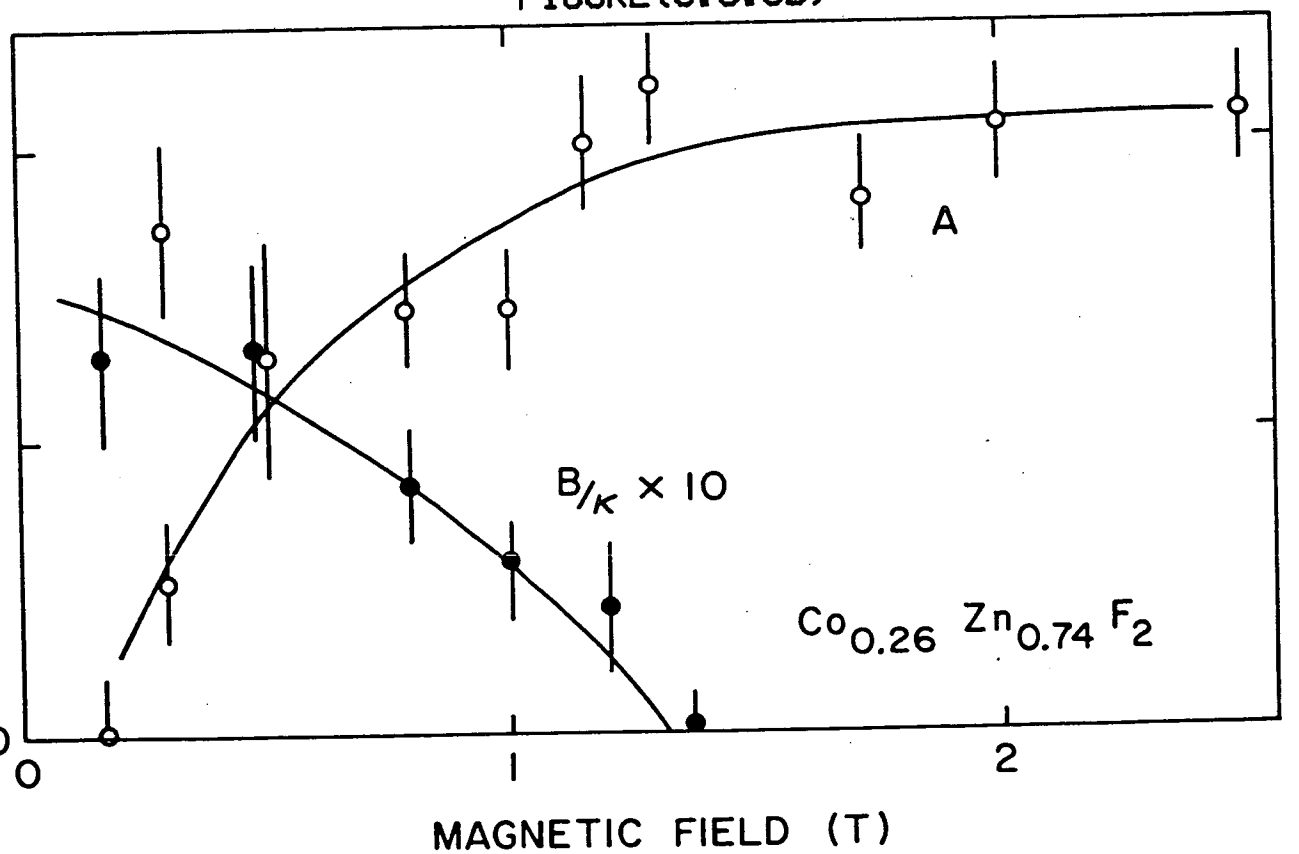

AMPLITUDE (arb. units)

MAGNETIC FIELD (T)

however, quite different. There is no range of applied fields over which the ratio $^{B}/_{K}$ may be considered constant. Instead $^{B}/_{K}$ appears to fall monotonically and goes to zero at 1.2T, since the structure factor is purely Lorentzian at higher fields. The amplitude A, as far as can be determined from the data, is going to zero at zero field. Above 1.2T the amplitude A is, within experimental error, constant with increasing field.

The temperature dependence of the ratio $^{B}/_{K}$ for the 35% sample is shown in figure (3.5.10) for the various applied fields. Allowing for the effects of extinction the values of $^{B}/_{K}$ for temperatures below 10 K appear, to within experimental error, to have collapsed to a single curve. Since the temperature at which the Lorentzian squared term vanishes varies with the applied field, above 10 K the values of the ratio must by necessity deviate from a single curve. The temperature dependence of the amplitude A of the 35% sample is shown in figure (3.5.11) for the various applied fields. There is a peak in the value of A for each of the applied fields, which shifts to lower temperature and becomes more rounded with increasing field. Again the values at 1.5T will be influenced by the effect of extinction.

3.6 Discussion (1) - $Co_xZn_{1-x}F_2$

From the results presented in section (5) it is quite clear that in neither sample of $Co_xZn_{1-x}F_2$ was there a state of long range antiferromagnetic order at any of the fields applied. Further to this the results also implied that there was not a threshold field, less than the fields applied, at which long range order would occur. The results of section (5) are therefore inconsistent with a value of $d_\ell = 2$ since this would have implied long range order at some non-zero

Figure (3.5.10)

This figure shows the ratio $^{B}/_{\kappa}$ plotted for the various fields applied to the $Co_{0.35}Zn_{0.65}F_2$ sample as a function of temperature.

FIGURE(3.5.10)

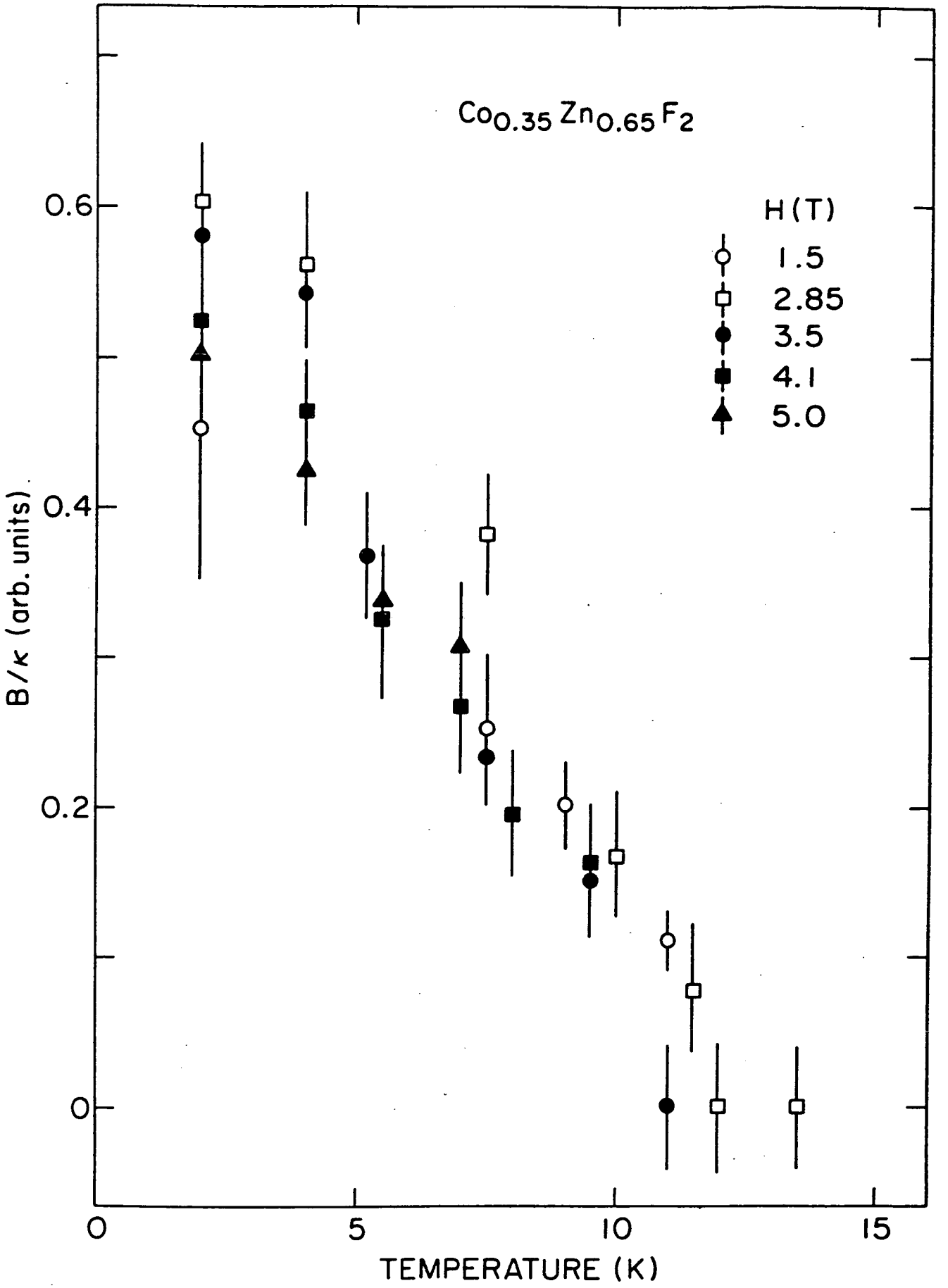
$Co_{0.35}Zn_{0.65}F_2$
H(T)
1.5
2.85
3.5
4.1
5.0
0.6
0.4
0.2
0
B/κ (arb. units)
0
5
10
15
TEMPERATURE (K)

Figure (3.5.11)

This figure shows the temperature dependence of the amplitude A for the various fields applied to the $Co_{0.35}Zn_{0.65}F_2$ sample. The solid lines are merely guides to the eye.

FIGURE(3.5.11)

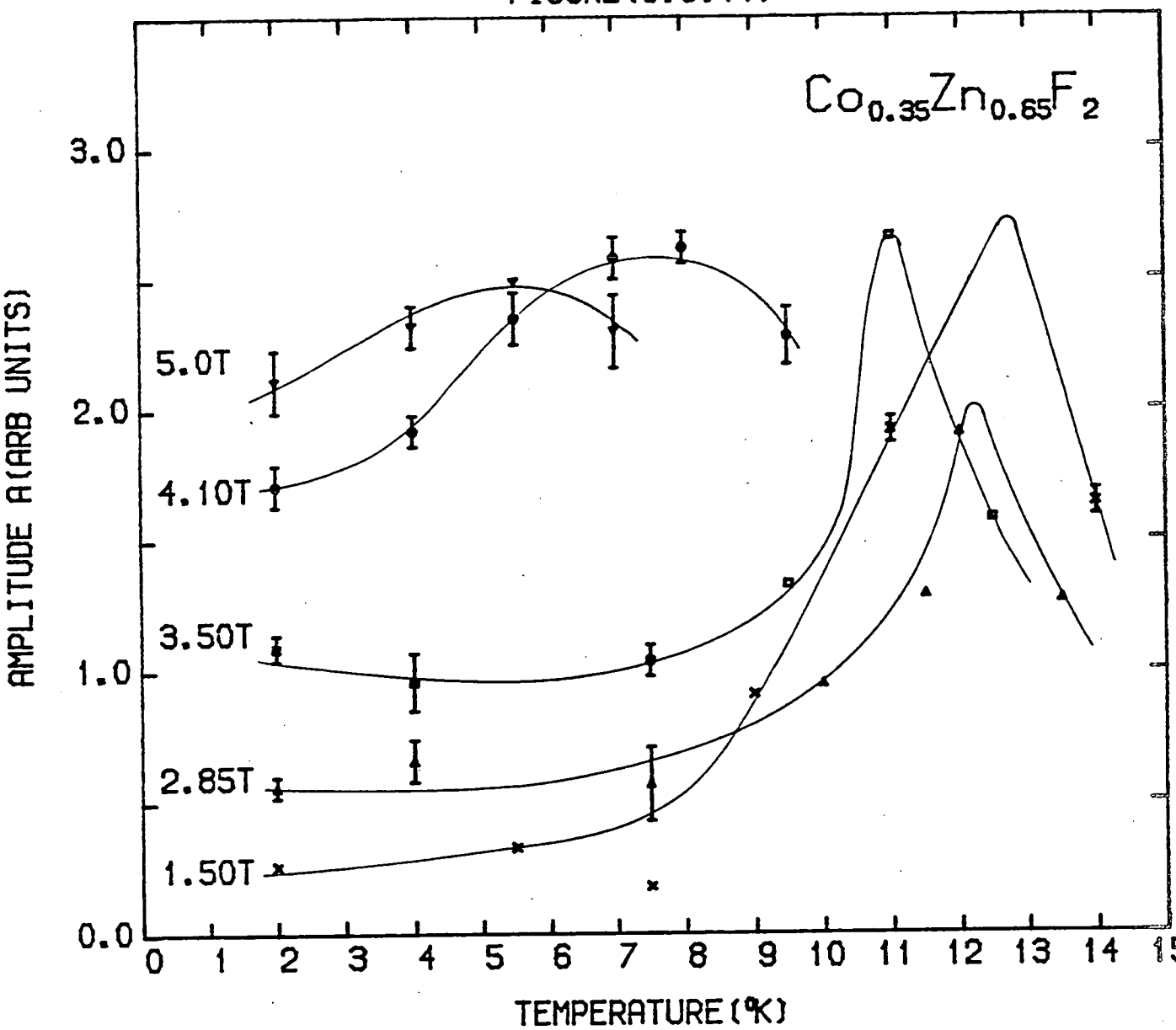
$Co_{0.35}Zn_{0.65}F_2$
AMPLITUDE A(ARB UNITS)
TEMPERATURE(°K)
5.0T
4.10T
3.50T
2.85T
1.50T
0.0
1.0
2.0
3.0
0 1 2 3 4 5 6 7 8 9 10 11 12 13 14 15

field. The very good description of the measured structure factor provided by the correlation function proposed by Kogon and Wallace (1981) lends some support to the supersymmetry arguments of these authors. However, Grinstein and Mukamel (1983) have shown that this form can be obtained from other theories which do not predict $d_\ell = 3$ and have argued that this form may well apply generally to systems with competing interactions. On this last point it is worth commenting that Rhynne (1983) has found that the magnetic structure factor in amorphous $TbFe_2$ which is a random anisotropy system is well described by the Lorentzian plus Lorentzian squared form. The power law dependence of the inverse correlation length on the applied field reported in section (5) is not consistent with $d_\ell = 3$. Therefore, if the results reported in section (5) are taken at face value, they imply a value for d_ℓ which is greater than 3. There are qualifications to this conclusion and these will be discussed later. However, before this a brief review of other measurements on dilute Ising systems in an external magnetic field will be given and compared to the results for $Co_xZn_{1-x}F_2$.

Prior to these measurements on $Co_xZn_{1-x}F_2$ a study of the dilute Ising antiferromagnet $Rb_2Co_{0.7}Mg_{0.3}F_4$ was performed by Yoshizawa et al (1982): (see also Birgeneau et al (1983b)) using neutron scattering techniques. As discussed in chapter two, Rb_2CoF_4 is in the d = 2 Ising Universality class and studies of $Rb_2Co_xMg_{1-x}F_2$ (Ikeda et al (1979), Ikeda (1981)) have shown the properties expected for the dilute d = 2 Ising Universality class. In zero field the sample of $Rb_2Co_{0.7}Mg_{0.3}F_4$ had a Néel temperature of 42.5 K. The effect of the applied magnetic field destroyed the long range antiferromagnetic order in $Rb_2Co_{0.7}Mg_{0.3}F_4$ and lead the magnetic structure factor to have a two dimensional Lorentzian

plus Lorentzian squared form. At low temperatures the spins were frozen as in $Co_xZn_{1-x}F_2$ and measurements were performed in the field cooled mode. The inverse correlation lengths at 10 K derived from the data analysis depended on the applied field through a power law dependence with an exponent $\nu_H = 1.6 \pm 0.1$. In d = 2 the integrated intensity in the Lorentzian squared term is $\pi B/\kappa^2$ and a plot of the values of B/κ^2 obtained from the analysis of the data at 10 K against the applied field was constant to within experimental error. The results found for $Rb_2Co_{0.7}Mg_{0.3}F_4$ in an external magnetic field are therefore inconsistent with $d_\ell = 2$.

Following the measurements on the sample of $Co_xZn_{1-x}F_2$ reported in section (5), Cowley et al (1983c) have studied, using neutron scattering techniques another dilute d = 3 Ising antiferromagnet $Fe_xZn_{1-x}F_2$ in an external magnetic field. The crystallographic and magnetic structure of FeF_2 is the same as that for CoF_2, as shown in figure (3.4.1). The effect of the crystal field and spin-orbit coupling in FeF_2 lead to the ground state of the Fe^{2+} ion being a pseudo-spin S = 2 state. Within this lowest level the spin Hamiltonian is the sum of an isotropic exchange interaction $J_{ij}\,\underline{S}_i.\underline{S}_j$ and a single ion term $D(S_i^z)^2$ (Hutchings et al (1970)). The single ion term leads to a large gap in the spin wave spectrum (Hutchings et al (1970)) and causes FeF_2 to have a phase transition in the d = 3 Ising Universality class with a Néel temperature of 78.4 K (Hutchings et al (1972)). A recent study of a sample of $Fe_{0.5}Zn_{0.5}F_2$ by Birgeneau et al (1983a) has shown that $Fe_xZn_{1-x}F_2$ is a good example of a system in the dilute d = 3 Ising Universality class. The samples of $Fe_xZn_{1-x}F_2$ used by Cowley et al had concentrations x = 0.35 and 0.50, with zero field Néel temperatures of 26.7 and 42.5 K respectively. Qualitatively, the results obtained

by Cowley et al were very similar to those for the $Co_xZn_{1-x}F_2$ samples. Once again the spins were frozen at low temperature and measurements were performed in the field cooled mode. The effect of the applied field destroyed the long range antiferromagnetic order and the magnetic structure factor was given by a Lorentzian plus a Lorentzian squared. In both samples the extinction effect described for the $Co_{0.35}Zn_{0.65}F_2$ sample was observed and in the $Fe_{0.5}Zn_{0.5}F_2$ this made a reliable determination of the parameters A, B and κ very difficult. As a consequence, only the results for the $Fe_{0.35}Zn_{0.65}F_2$ sample will be considered quantitatively. At 8 K the inverse correlation lengths obtained from the data analysis procedure had a power law dependence on the applied field with an exponent $\nu_H = 2.18 \pm 0.05$. The ratio B/κ was, excluding the effects of extinction, constant as a function of field at 8 K and essentially collapsed to a single curve as a function of temperature for the various fields applied. At low fields and temperatures the structure factor could be represented by a Lorentzian squared and therefore the parameter A was identically zero at zero field.

Qualitatively the experimental data on dilute Ising antiferromagnets in an external magnetic field is therefore all very similar. In each case, long range antiferromagnetic order is destroyed by the application of the field and the magnetic structure factor becomes a Lorentzian plus Lorentzian squared. Further to this the field dependence of the inverse correlation length is not consistent with values of $d_\ell = 2$ or 3. The results for $Co_xZn_{1-x}F_2$ and $Fe_xZn_{1-x}F_2$, however, give differing values for the exponent ν_H. There are two aspects to the difference in the values of ν_H, firstly the difference between the values of ν_H for the 26% and 35% samples of $Co_xZn_{1-x}F_2$ and secondly the difference between the values

of ν_H for the 35% samples of $Co_xZn_{1-x}F_2$ and $Fe_xZn_{1-x}F_2$.

The difference between the 26% and 35% samples of $Co_xZn_{1-x}F_2$ is symptomatic of the general differences between the two samples. In the 35% sample the ratio $B/_K$ is constant as a function of applied field at low temperatures, indicating that the random fields induced in this sample are in the small field limit. In the 26% sample the reverse is true, at low temperature th ratio $B/_K$ is nowhere constant as a function of the applied field and goes to zero at a field of 1.2T. This behaviour suggests the existence of a large induced random field in this sample. An examination of figure (3.5.8b) shows that of the 10 data points used to obtain ν_H for this sample, 8 were for fields greater than 1.0T. As a consequence the exponent $\nu_H = 2.17 \pm 0.16$ found for this sample corresponds to the large field limit. The induction of such a large random field in the $Co_{0.26}Zn_{0.74}F_2$ sample can be attributed to the proximity of its concentration to the percolation threshold of 24.5% for b.c.c. type lattices (Kirkpatrick (1973)). Indeed, it has been argued by Fähnle (1983) that the application of an external magnetic field to a dilute antiferromagnet with a concentration at the percolation threshold will destroy long range antiferromagnetic order in all spatial dimensions. This argument is based on the large degree of ramification of the infinite cluster at the percolation threshold. The structure of the infinite cluster for concentrations close to the percolation threshold may be considered as a network of nodes, links and blobs (Coniglio (1983)). On a lattice, nodes are points which are connected to infinity by more than two disjoint paths. The paths between nodes consist of blobs (clusters of spins) connected together by links (one dimensional chains of spins). For concentrations x which are close to the percolation threshold x_p the

mean distance between nodes : L(x) obeys a power law dependence $L(x) \alpha (x - x_p)^{-z}$ where $z > 0$ (de Gennes (1976)). At the percolation threshold the distance between nodes is infinite and therefore if it is possible to break up a path of links and blobs into domains by applying a magnetic field it is possible to destroy long range order. This is always possible for any non-zero field since the "domain wall energy" is just the exchange energy required to break two links, i.e. two bonds. The magnetostatic energy however, arises from the fluctuating moments on the blobs and it is therefore possible since $L(x_p)$ is infinite to find a length of path in which the fluctuation in the magnetostatic energy exceeds the energy needed to break two bonds. This is essentially the argument that would apply to a one dimensional R.F.I.M. and it is the one-dimensional character (ramification) of the infinite cluster that leads to this destruction of long range order.

When the concentration x is greater than x_p the mean distance between nodes is finite and this picture must be modified. The "normal" picture of the effect of an induced random field is that it leads the system to break up into domains whose linear size L is given by the competition between the fluctuation of the magnetostatic energy within the domain and the domain wall energy. Therefore for $x > x_p$ if the applied field leads to a domain size $L >> L(x)$ then behaviour typical of a d-dimensional system is expected while if $L << L(x)$ behaviour typical of that at percolation (i.e. one dimensional) is expected. Since $x = 0.26$ is close to x_p this is a very appealing though not rigorous explanation for the behaviour of the $Co_{0.26}Zn_{0.74}F_2$ sample.

The 35% samples of $Co_xZn_{1-x}F_2$ and $Fe_xZn_{1-x}F_2$ are however sufficiently far from the percolation threshold that the effect

described above should be unimportant. Therefore the difference between the values of the exponent ν_H of 3.6 ± .3 and 2.18 ± 0.05 respectively for these two samples is very surprising. This is especially so since the samples have (i) the same crystallographic and magnetic structure in zero field, (ii) nominally the same concentration of magnetic ions and (iii) have been shown experimentally (Cowley and Carneiro (1980), Birgeneau et al (1983a)) to both be good examples of a dilute d = 3 Ising system in zero field. It would therefore be expected that in non-zero field these two systems would belong to the same Universality class and have the same critical exponent ν_H. Since the difference between $Co_xZn_{1-x}F_2$ and $Fe_xZn_{1-x}F_2$ lies at the level of the details of the spin Hamiltonian this suggests that ν_H depends on the details of the Hamiltonian. If this were so, then it would be very surprising indeed since one of the postulates of Universality is that the critical exponents are independent of the details of the Hamiltonian.

The results reported in section (5) have so far been presented as contradicting the theoretical predictions for the R.F.I.M. There are three qualifications to this interpretation of the experimental results. Two of these qualifications will be discussed here while the third will be discussed in the concluding section of this chapter.

The first qualification is that the experiments have been performed at finite temperature whereas the quantitative theoretical calculations for the R.F.I.M. have been performed for zero temperature. It is however unlikely that the experimental results would be significantly different at temperatures lower than those at which quantitative measurements were performed. The inverse correlation length in non-zero field is constant as a

function of temperature at low temperatures in all of the samples of $Rb_2Co_xMg_{1-x}F_4$, $Co_xZn_{1-x}F_2$ and $Fe_xZn_{1-x}F_2$ discussed and it would be very surprising if these low temperature values could not be extrapolated to zero temperature.

The second qualification concerns the freezing of the spins found at low temperatures in all of the samples discussed so far. In a recent paper Grant and Gunton (1983) have considered theoretically the dynamics of the R.F.I.M. and have shown within a certain approximation that there is no spin freezing in the R.F.I.M. The spin freezing in the experiments must therefore arise from an effect peculiar to the experiments, rather than the R.F.I.M. This effect is almost certainly 'domain wall pinning' due to the dilutant sites. The overall scale of the domain wall energy will be reduced if it passes through dilutant sites. Therefore, if the field is changed at low temperature there is an energy barrier due to this pinning effect which must be overcome in order for the domain wall to move through the system and create a new configuration of the spins. The question is, therefore, whether the state of the system when the spin freezing sets in is typical of the random field state or of some transient behaviour. Aharony et al (1976) have given a heuristic argument to show that in the R.F.I.M. below the zero random field transition temperature it is the fluctuations in the random field that are the dominant source of disorder rather than the thermal fluctuations. It would therefore be expected that the state into which the system freezes is one in which the disorder on large length scales is dominated by the effect of the induced random field rather than some transient behaviour.

3.7 Experimental Method (2) - $Mn_xZn_{1-x}F_2$

In this and the following two sections the effect of applying an external magnetic field to a sample of the dilute near-Heisenberg antiferromagnet $Mn_xZn_{1-x}F_2$ will be described. The experimental measurements on this sample, which had x = 0.65, were performed by Professor R.A. Cowley and the data analysis of the results obtained was performed by the author. The rest of this section is divided into two subsections. In the first subsection the properties of $Mn_xZn_{1-x}F_2$ will be described, along with a brief description of the results of an earlier neutron scattering experiment on a sample of $Mn_{0.78}Zn_{0.22}F_2$ in an external magnetic field performed by Cowley and Buyers (1982). The second subsection will contain a brief description of the spectrometer arrangement which differed from the arrangement for $Co_xZn_{1-x}F_2$.

3.7 i) Properties of $Mn_xZn_{1-x}F_2$

The crystallographic structure of MnF_2 is the same rutile structure as for CoF_2, which was shown in figure (3.4.1). Since the Mn^{2+} ion has a ^6S ground state there is no effect on the magnetic interactions from either the crystal field or spin-orbit coupling and the exchange is therefore of an isotropic Heisenberg character. There is, however, because of the tetragonal crystal structure, a dipolar interaction between the magnetic moments of the Mn^{2+} ions which causes them to align parallel to the c-axis. This dipolar interaction causes the phase transition in MnF_2, which occurs at 67.5 K (Schulhof et at (1971)) to be in the d = 3 Ising Universality class and leads to a gap of 0.066 THz in the spin wave spectrum (Nikotin et al (1969)).

For values of the concentration x away from the percolation threshold the spin wave spectrum (Coombs et al (1976)) and the

phase transition (Meyer and Dietrich (1978)) of $Mn_xZn_{1-x}F_2$ have been measured. The critical properties of $Mn_xZn_{1-x}F_2$ only cross over from Heisenberg to Ising behaviour close to the transition temperature and therefore at low temperatures $Mn_xZn_{1-x}F_2$ is a dilute near-Heisenberg antiferromagnet. The properties of $Mn_xZn_{1-x}F_2$ when x is close to the percolation threshold are however much more complicated (Cowley et al (1980b)). Since x = 0.65 is well away from the percolation threshold this was not a problem in these measurements.

The effect of a uniaxial random field on a near-Heisenberg ferromagnet has been considered theoretically by Aharony (1978). For a random field near Heisenberg model (R.F.N.H.M.) the general form of the phase diagram is expected to be similar to that shown in figure (3.7.1) (Aharony (1978)). If the variance of the random field is small then the behaviour of the R.F.N.H.M. is expected to be the same as for the R.F.I.M. For larger values of the variance of the random field the R.F.N.H.M. unlike the R.F.I.M. undergoes a spin-flop transition. In this phase there will be long range magnetic order since the spins will essentially be perpendicular to the uniaxial random field which cannot therefore effect the magnetic order. Around the bicritical point Aharony (1978) also predicts the possible existence of a mixed phase of both spin-flop and R.F.I.M. order.

In MnF_2 the spin flop field at 4.2 K is 9.2T (Shapira and Foner (1970)) and therefore in $Mn_{0.65}Zn_{0.35}F_2$ it has been possible to observe the effect of the external magnetic field up to and including the spin-flop transition. A preliminary study of the magnetic order in the R.F.I.M. phase of $Mn_xZn_{1-x}F_2$ in an external magnetic field was performed by Cowley and Buyers (1982)

Figure (3.7.1)

This figure shows a schematic phase diagram for a near Heisenberg ferromagnet in a uniaxial random field (After Aharony (1978)).

FIGURE(3.7.1)

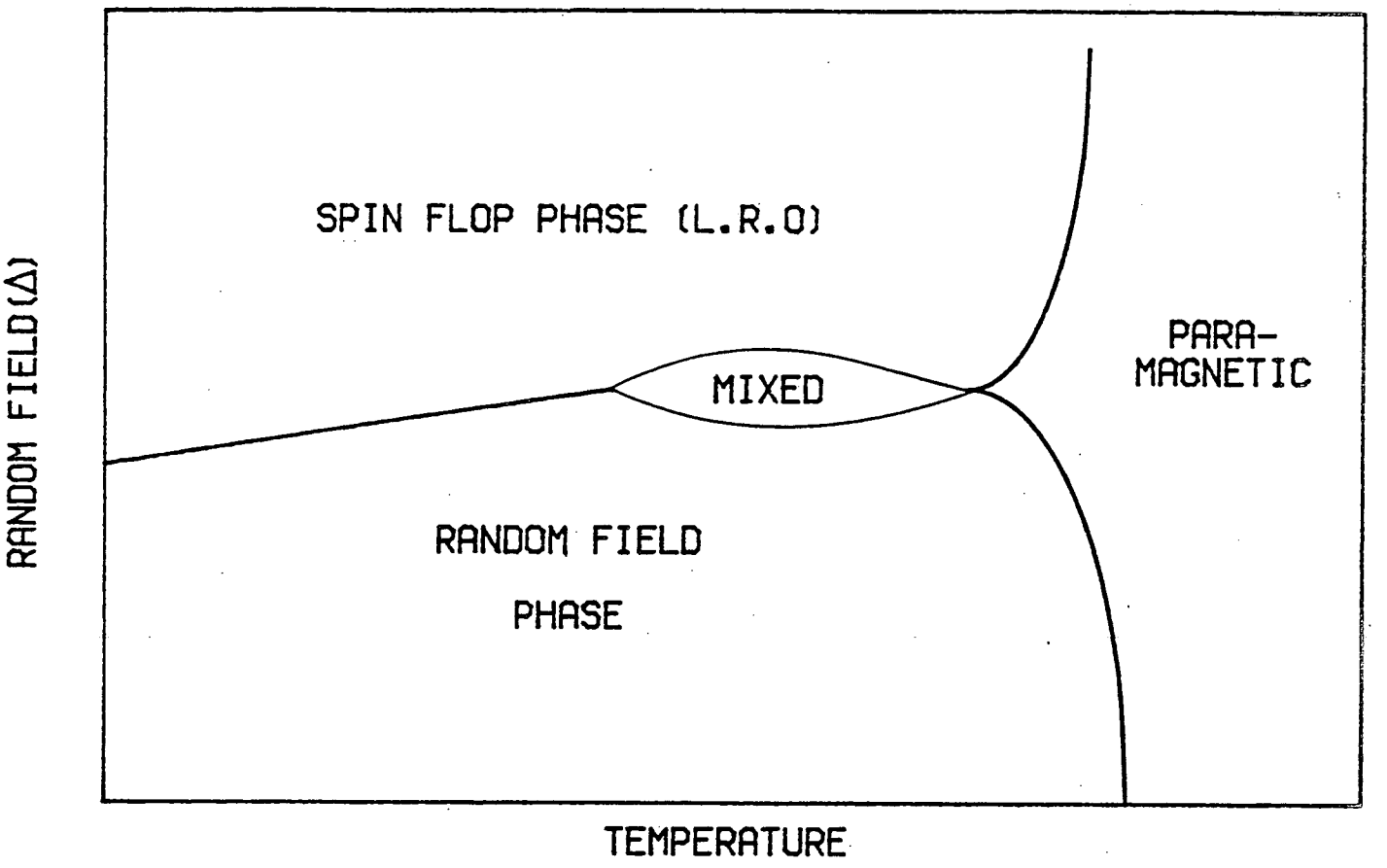
SPIN FLOP PHASE (L.R.O)
MIXED
PARA-
MAGNETIC
RANDOM FIELD
PHASE
RANDOM FIELD(Δ)
TEMPERATURE

for a sample with x = 0.78, using neutron scattering methods. The results of this study showed properties different to those found for $Co_xZn_{1-x}F_2$ and $Fe_xZn_{1-x}F_2$. In zero field the sample of $Mn_{0.78}Zn_{0.22}F_2$ had a Néel temperature of 48.7 K. Above the Néel temperature the structure factor was found to have a Lorentzian lineshape, while below it consisted of a separable Bragg peak and Lorentzian. The inverse correlation length had a minimum at the Néel temperature and the intensity of the critical scattering measured at (1, 0.006, 0) peaked at a temperature very close to the Néel temperature. This is just the sort of behaviour that is expected at a paramagnetic to antiferromagnetic phase transition. The application of the 4.0T field changed this behaviour. Above 48.2 K the structure factor was found to be Lorentzian as before, but in the range from 47 to 48 K the data was only well described by a Lorentzian plus Lorentzian squared structure factor. The inverse correlation lengths derived from fitting these forms to the data fell monotonically with decreasing temperatures down to 47 K. As a consquence below 47 K the lineshape at the $(1,0,0)_M$ position had essentially become a resolution limited peak. There was, however, a significant increase in the intensity measured between the positions (1, ±0.004, 0) and (1,± 0.016, 0) over that in zero field. Further, the peak in the intensity at the position (1, 0.006, 0) was shifted down to 47.7 K and was five times more intense than in zero field. Attempts to fit the lineshape at the $(1,0,0)_M$ position to the Lorentzian plus Lorentzian squared lineshape for temperatures below 47 K only produced fits with χ^2 parameters in the range 6 to 9.

The dependence of the structure factor and inverse correlation length with temperature for $Mn_{0.78}Zn_{0.22}F_2$ in a 4.0T field was

therefore quite different to that in $Co_xZn_{1-x}F_2$ and $Fe_xZn_{1-x}F_2$. Since the lineshape at the $(1,0,0)_M$ position was essentially resolution limited at low temperatures, this would seemingly imply that a state of long range order had been established. However, if there were a state of long range order at low temperature then the transition to this state from the paramagnetic state is quite different to that in zero field and is certainly not sharp. The existence of the wings of scattering in the range (1, ±0.004, 0) to (1, ±0.016, 0) suggests the alternative interpretation that long range order has not been established. Instead, the size of the domains formed is very large, too large to be resolved by the spectrometer, because of the higher value of x in the sample used by Cowley and Buyers.

In order to investigate further the properties of the R.F.N.H.M. the measurements reported in this and the following two sections were performed. The $Mn_{0.65}Zn_{0.35}F_2$ sample used in these measurements has a lower concentration of Mn^{2+} ions than the sample used by Cowley and Buyers. Therefore if the difference between the results of Cowley and Buyers and those found for $Co_xZn_{1-x}F_2$ and $Fe_xZn_{1-x}F_2$ lies in the concentration then this should be observable. This sample of $Mn_{0.65}Zn_{0.35}F_2$ was the same as that used previously by Belanger et al (1982) for birefringence measurements and Yasuoka et al (1982) for NMR measurements.

3.7 ii) Spectrometer arrangement

As for the measurements on the $Co_xZn_{1-x}F_2$ and $Fe_xZn_{1-x}F_2$ samples these measurements on $Mn_{0.65}Zn_{0.35}F_2$ were performed using the H-7 triple axis spectrometer at Brookhaven National Laboratory. Unlike the previous measurements however on this occasion the analyser was left in position. This was done in order to discriminate against

scattering from the spin wave modes since it is the ordering of the spins that is of interest. The use of the analyser does mean that close to and above the zero field Néel temperature it is quite probable that the critical scattering will not be adequately integrated over frequency. Further, even with the analyser present, at these temperatures there will almost certainly be some scattering from the spin wave modes contributing to the observed intensity. However, since these measurements are of a more qualitative nature than those for $Co_xZn_{1-x}F_2$ and $Fe_xZn_{1-x}F_2$ this should not significantly alter the conclusions drawn from the results. The monochromator and analyser used were both pyrolytic graphite utilising the (0,0,2) planes. The incident neutron wavevector was 2.67 A^{-1} and therefore pyrolytic graphite filters were positioned before the monochromator and between the sample and analyser. Horizontal collimations of 10' were used, before the monochromator, between the monochromator and sample, and between the sample and analyser with a 40' collimator between the analyser and detector.

The components of the resolution function in the scattering plane and in the frequency co-ordinates were determined by scanning the $(1,0,0)_M$ Bragg peak in zero field. The F.W.H.M. of the resolution function in these co-ordinates at the $(1,0,0)_M$ position were, in the scattering plane 0.0024 A^{-1} perpendicular to and 0.0094 A^{-1} parallel to the wavevector transfer and in the frequency co-ordinates 0.12 THz. A F.W.H.M. of 0.10 A^{-1} was found for the vertical component of the resolution function by rocking the sample on calibrated arcs as described previously for $Co_xZn_{1-x}F_2$.

The $Mn_{0.65}Zn_{0.35}F_2$ sample was mounted with its (0,0,1) axis vertical in the cryo-magnet as described previously. The arrangement of the magnet, cryostat and temperature sensors were as before

for the $Co_xZn_{1-x}F_2$ measurements. Measurements of the magnetic structure factor were made, as before for the $Co_xZn_{1-x}F_2$ samples, about the $(1,0,0)_M$ position using scans along the (0,1,0) reciprocal lattice direction.

3.8 Experimental Results (2) $Mn_xZn_{1-x}F_2$

In zero applied field the $Mn_{0.65}Zn_{0.35}F_2$ sample was found to have a normal paramagnetic to antiferromagnetic phase transition with a Néel temperature of 39.8 K. Above the Néel temperature the magnetic structure factor was a Lorentzian and below it was a Bragg peak plus Lorentzian. The effect of a 4.0T field on the lineshape at the $(1,0,0)_M$ position at temperatures above and not far below the zero field Néel temperature is shown in figures (3.8.1a) and (3.8.1b). These measurements were performed in a field cooled mode. Since this is the same field as used by Cowley and Buyers (1982) the properties of these lineshapes may be compared directly with those for $Mn_{0.78}Zn_{0.22}F_2$. For the lineshape shown in figure (3.8.1a) at temperatures above 38.5 K the solid lines are the best fits in a least squares sense to a Lorentzian structure factor convolved with the resolution function. The solid lines in figures (3.8.1a) and (3.8.1b) at temperatures of 38.5 K and below are the best fits with a Lorentzian plus Lorentzian squared structure factor. These fits had χ^2 parameters in the range 0.4 to 2.0. As in the measurements of Cowley and Buyers the lineshape develops smoothly from a Lorentzian to a Lorentzian plus Lorentzian squared structure factor, but with a F.W.H.M. that continues to narrow until at 33 K it is essentially equal to the resolution limit. In the measurements on the $Mn_{0.78}Zn_{0.22}F_2$ sample by Cowley and Buyers, this resolution limit for the F.W.H.M. was reached at about two degrees below the zero field Néel temperature

Figure (3.8.1a)

This figure shows the lineshape at the $(1,0,0)_M$ Bragg position of the $Mn_{0.65}Zn_{0.35}F_2$ sample in a field of 4.0T at the temperatures 39 K, 41 K and 43 K. The solid lines are the best fits to a Lorentzian structure factor.

Figure (3.8.1b)

This figure shows the lineshape at the $(1,0,0)_M$ Bragg position of the $Mn_{0.65}Zn_{0.35}F_2$ sample in a field of 4.0T at the temperatures 33 K, 35 K and 37.5 K. The solid lines are the best fits to a Lorentzian plus Lorentzian squared structure factor.

FIGURE(3.8.1a)

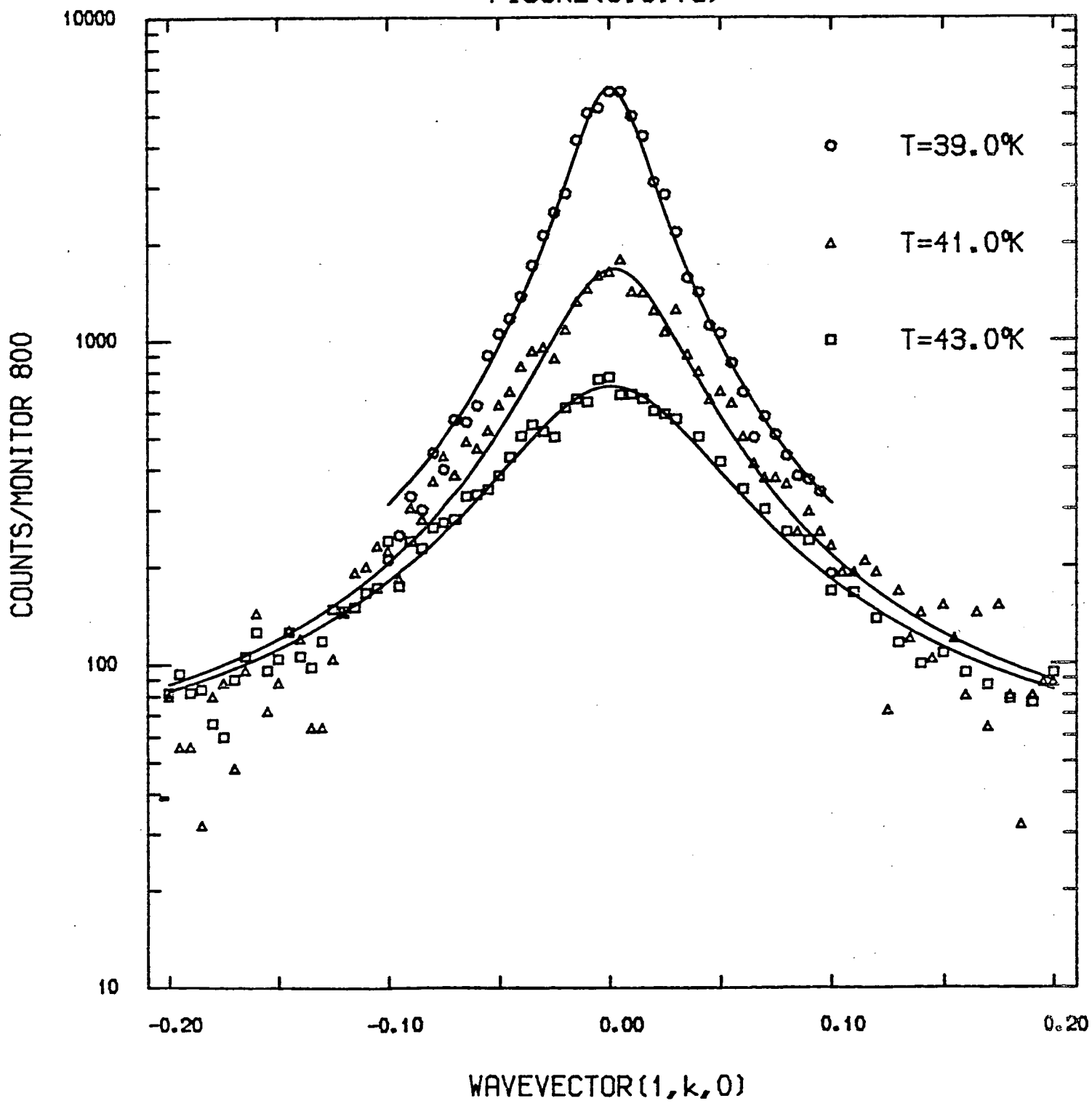
10000
1000
100
10
COUNTS/MONITOR 800
T=39.0°K
T=41.0°K
T=43.0°K
-0.20
-0.10
0.00
0.10
0.20
WAVEVECTOR(1,k,0)

FIGURE(3.8.1b)

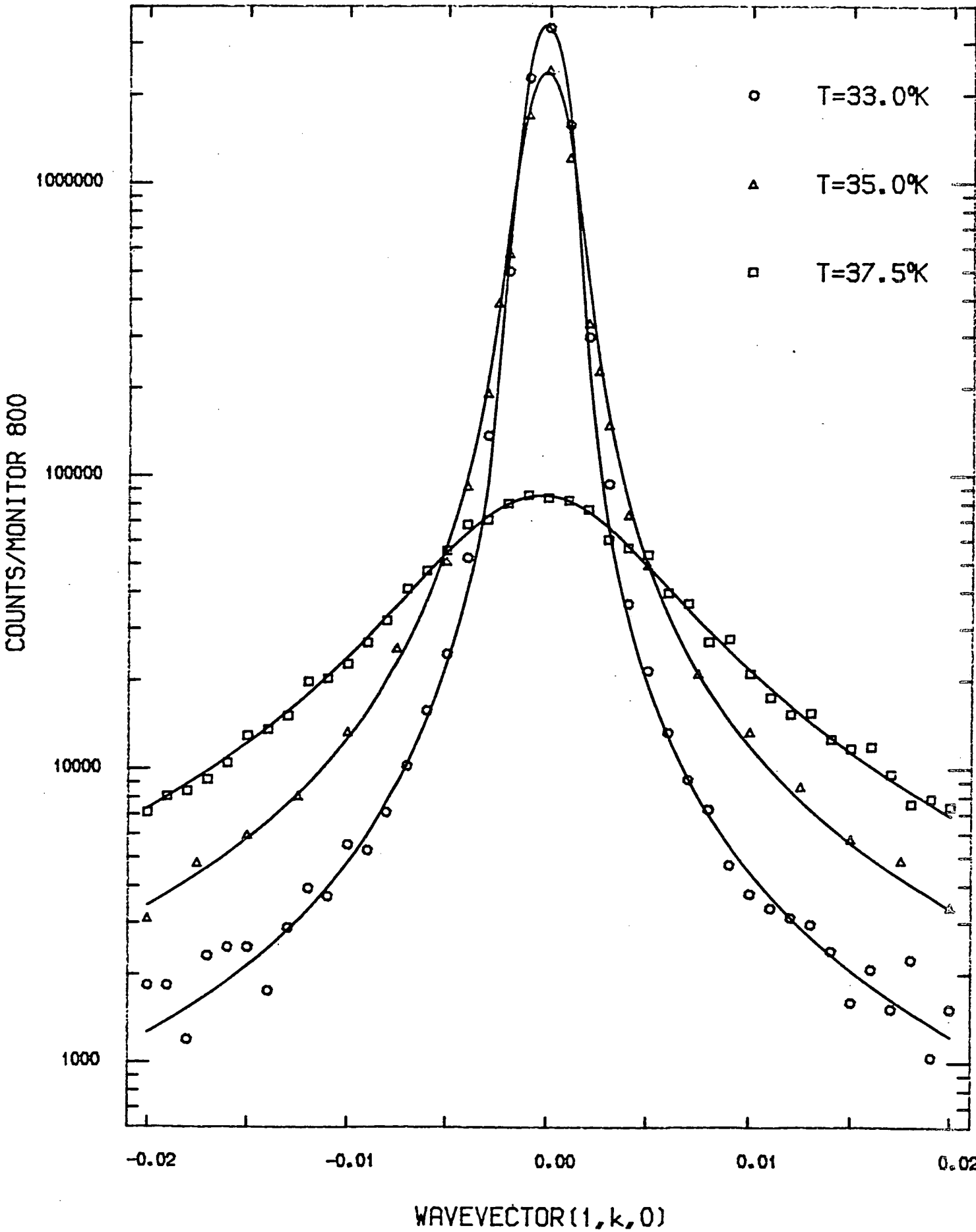
T=33.0K
T=35.0K
T=37.5K
1000000
100000
10000
1000
COUNTS/MONITOR 800
-0.02
-0.01
0.00
0.01
0.02
WAVEVECTOR(1,k,0)

while in this sample of $Mn_{0.65}Zn_{0.35}F_2$ the limit was about six degrees below the Néel temperature. Even allowing for the difference in resolution between these measurements and those of Cowley and Buyers this is a significant difference in temperature range and clearly shows that the range of temperatures at which observable 'random field' behaviour occurs does depend strongly on the concentration. Although the F.W.H.M. of the lineshape at the $(1,0,0)_M$ position is resolution limited at 33 K in 4.0T field there are significant wings of scattering to this lineshape which persist down to 7 K as shown in figure (3.8.2). In figure (3.8.2) the peak height of the resolution function is equivalent to the peak height of the zero field Bragg peak and the solid line represents a fit to a Lorentzian plus Lorentzian squared structure factor. The method for performing this fit and the significance of the parameters obtained from it will be given later.

The results in 4.0T described above were obtained in a field cooled mode. Since the anisotropy in $Mn_xZn_{1-x}F_2$ is much smaller than in $Co_xZn_{1-x}F_2$ and $Fe_xZn_{1-x}F_2$ it might be expected that spin freezing would be less severe because of the low lying spin waves. This was not however found to be the case. In figure (3.8.3) three scans of the $(1,0,0)_M$ lineshape at 7 K in a field of 5T are shown. These scans correspond to three different ways of obtaining that combination of field and temperature, which were: field cooled, cooled in zero field and the field then raised to 5.0T, and, cooled in the spin flop phase in a field of 7.0T and the field then lowered to 5.0T. As can be seen from figure (3.8.3) there is a significant difference between the field cooled results and those obtained by changing the field at low temperature. Again the solid line through the field cooled data is the result of a fit to a

Figure (3.8.2)

The lineshape at the $(1,0,0)_M$ Bragg position is shown for the $Mn_{0.65}Zn_{0.35}F_2$ sample in a field of 4.0T at a temperature of 7.0 K. The solid line is the best fit to a Lorentzian squared structure factor and the dotted line is the resolution function with a peak intensity equal to the zero field peak intensity.

FIGURE(3.8.2)

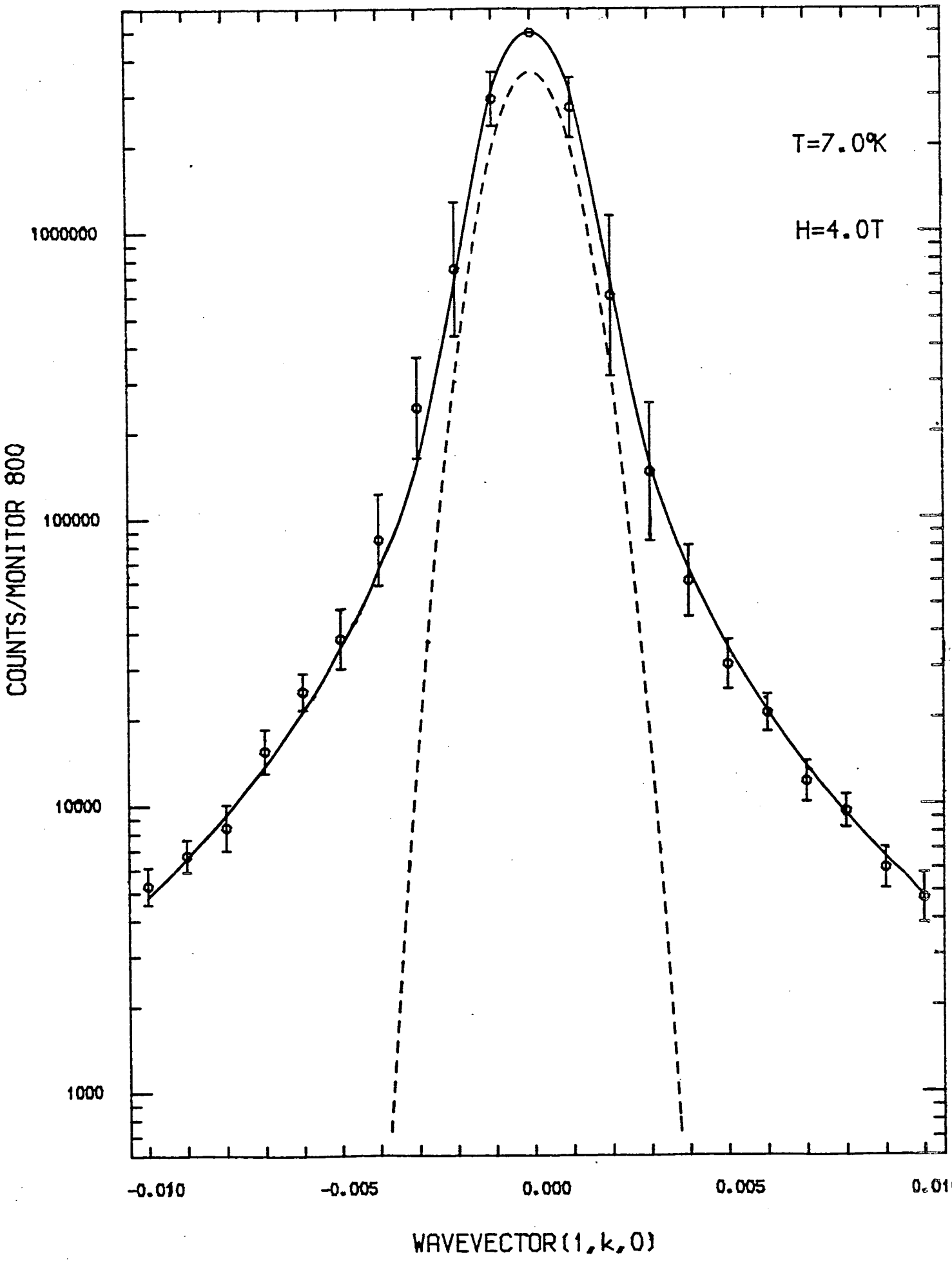
T=7.0K
H=4.0T
1000000
100000
10000
1000
COUNTS/MONITOR 800
-0.010
-0.005
0.000
0.005
WAVEVECTOR(1,k,0)

Figure (3.8.3)

The lineshape at the $(1,0,0)_M$ Bragg position at 7 K in 5.0T field for three different approaches to that combination of field and temperature. The solid line for the field cooled data is the best fit to a Lorentzian plus Lorentzian squared lineshape.

FIGURE(3.8.3)

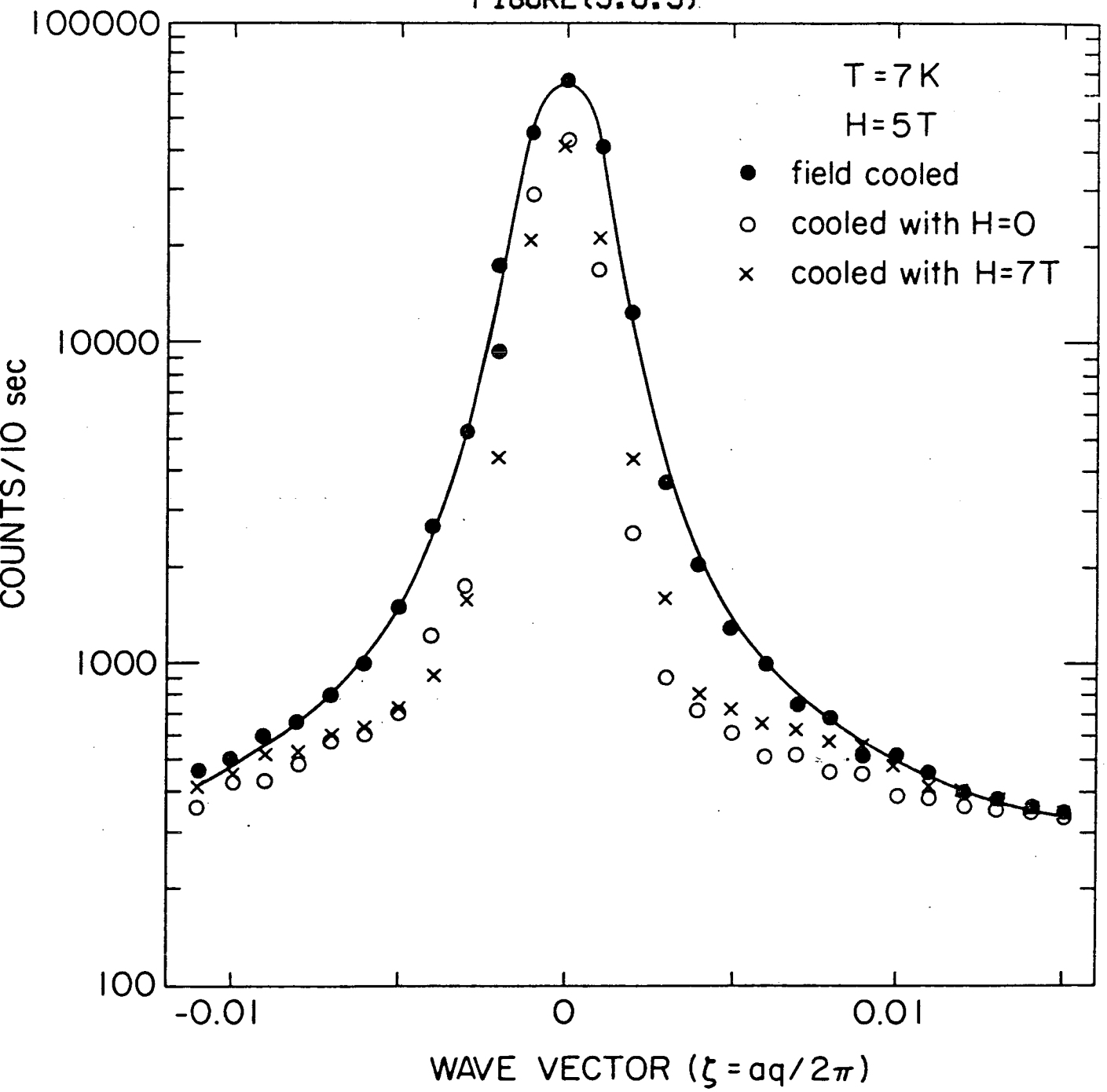
100000
10000
1000
100
COUNTS/10 sec
-0.01
0
0.01
WAVE VECTOR (ζ = aq/2π)
T = 7 K
H = 5 T
field cooled
cooled with H=0
cooled with H=7T

Lorentzian plus Lorentzian squared structure factor. It is apparent that at low temperatures the spins were frozen and could not respond to changes in the magnetic field.

In figures (3.8.2) and (3.8.3) the peak height of the field cooled results is greater than the zero field results and the results obtained by changing the field at low temperature. Since there are wings of scattering in the field cooled results this increase in peak height implies an increase in integrated intensity as well. In figure (3.8.4) the variation of the integrated intensity with field at 7 K is shown both for the data taken in the field cooled mode and that taken after varying the field at 7 K. The increase in the integrated intensity for fields below 5.0T can be explained by the extinction effect discussed for the $Co_{0.35}Zn_{0.65}F_2$ sample. Above 5.0T the rapid decline in the integrated intensity is attributed to the system being in the spin-flop phase. Apart from the decline in the integrated intensity there are two other indicators of a spin flop transition at 5.0 ± 0.2T. Firstly, above 5.0T the $(1,0,0)_M$ lineshape cannot be fitted by a Lorentzian plus Lorentzian squared structure factor but can by a Bragg peak plus Lorentzian structure factor. Secondly, the intensity at the point (1, 0.005, 0) peaks as a function of field at 5.0T, as shown in figure (3.8.5) for both the data taken in the field cooled mode and that taken by varying the field at 7 K. If the random field effect is ignored then Brady-Moreira et al (1977) have calculated that in $Mn_xZn_{1-x}F_2$ the spin-flop critical field should scale with the concentration x. From the spin-flop field of 9.2T in MnF_2 (Shapira and Foner (1970)) this would imply a critical field in $Mn_{0.65}Zn_{0.35}F_2$ of $\sim$ 5.8T at zero temperature. The observed spin flop field is 16% lower than this value and therefore suggests that the spin-flop transition has been lowered by the presence

Figure (3.8.4)

This figure shows the integrated intensity in the lineshape at the $(1,0,0)_M$ position at 7.5 K as a function of field both for data taken in the field cooled mode (solid line) and for the data taken by altering the field at 7.5 K.

Figure (3.8.5)

This figure shows the intensity at the point (1, 0.005, 0) at 7.5 K as a function of field both for the data taken in the field cooled mode (triangles) and the data taken by altering the field at 7.5 K (circles).

FIGURE(3.8.4)

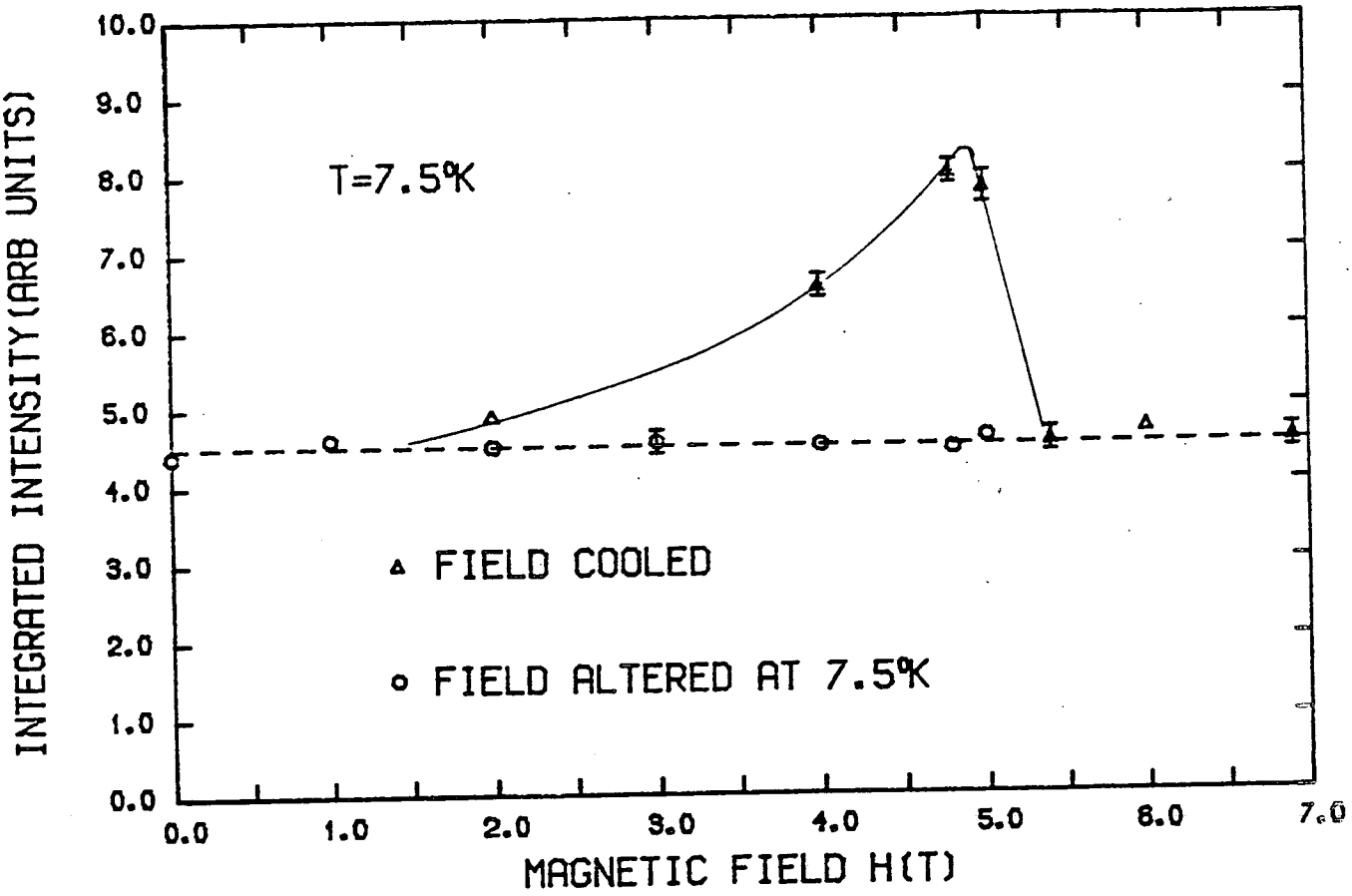

FIGURE(3.8.5)

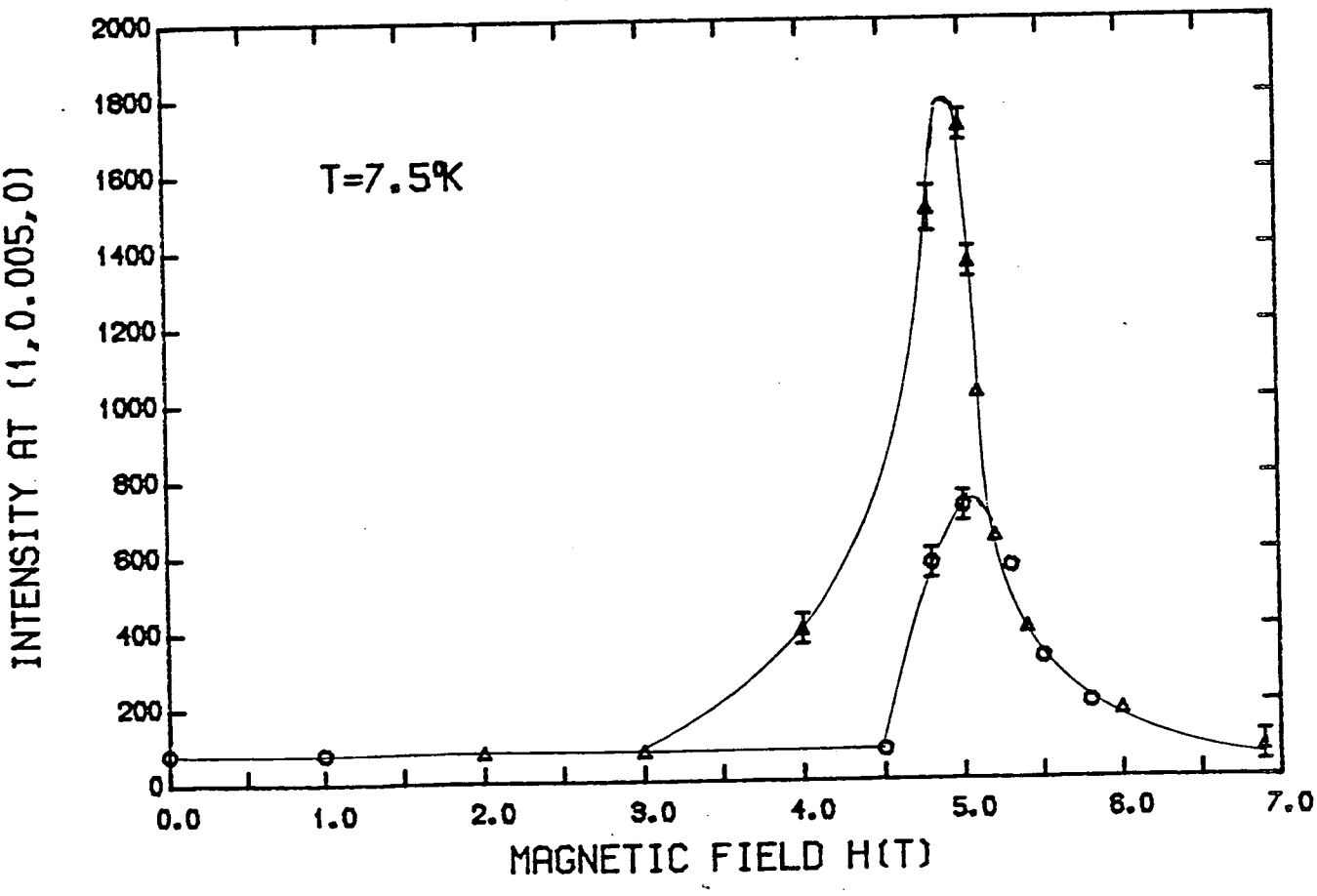

of the induced random field, in a similar way to the prediction by Aharony (1978) that the R.F.N.H.M. would undergo a spin flop transition. A similar lowering of the spin flop field has been observed by Shapira and Oliveira (1983) in a sample of $Mn_{0.875}Zn_{0.125}F_2$ using magnetostriction and ultrasonic attenuation measurements. Shapira and Oliveira have given in their paper a discussion of why the induced random field causes a spin flop transition at a field lower than that expected for an antiferromagnet. The peak in the intensity at the point (1, 0.005, 0) can be used to estimate the spin-flop field at higher temperatures and in figure (3.8.6) these peaks are shown at higher temperatures. The critical field for the spin-flop transition rises with increasing temperature and has a value of about 6.0T in the temperature range from 30 - 36 K.

As mentioned previously the lineshape at the $(1,0,0)_M$ position in a 4.0T field, in the temperature range from 33 to 43 K, could be fitted using a Lorentzian plus Lorentzian squared form for the structure factor. For temperatures above and not far below the zero field Néel temperature this was also true for the fields 2.0T and 5.0T in which the lineshape was measured as a function of temperature. In figure (3.8.7) the inverse correlation lengths deduced from the fits at these three fields are shown as a function of temperature. The solid lines in figure (3.8.7) are merely guides for the eye. The shape of the curves through the data points is qualitatively similar to that in the good Ising systems $Rb_2Co_xMg_{1-x}F_4$, $Co_xZn_{1-x}F_2$, $Fe_xZn_{1-x}F_2$ for temperatures above and just below their zero field Néel temperatures. However, in the Ising systems the inverse correlation length does not continue to fall with decreasing temperature but at a lower temperature becomes a constant as a function of temperature. The difficulty in determining whether this

Figure (3.8.6)

The intensity at the point (1, 0.005, 0) is shown as a function of field at various temperatures. The data was taken in the field cooled mode.

FIGURE(3.8.6)

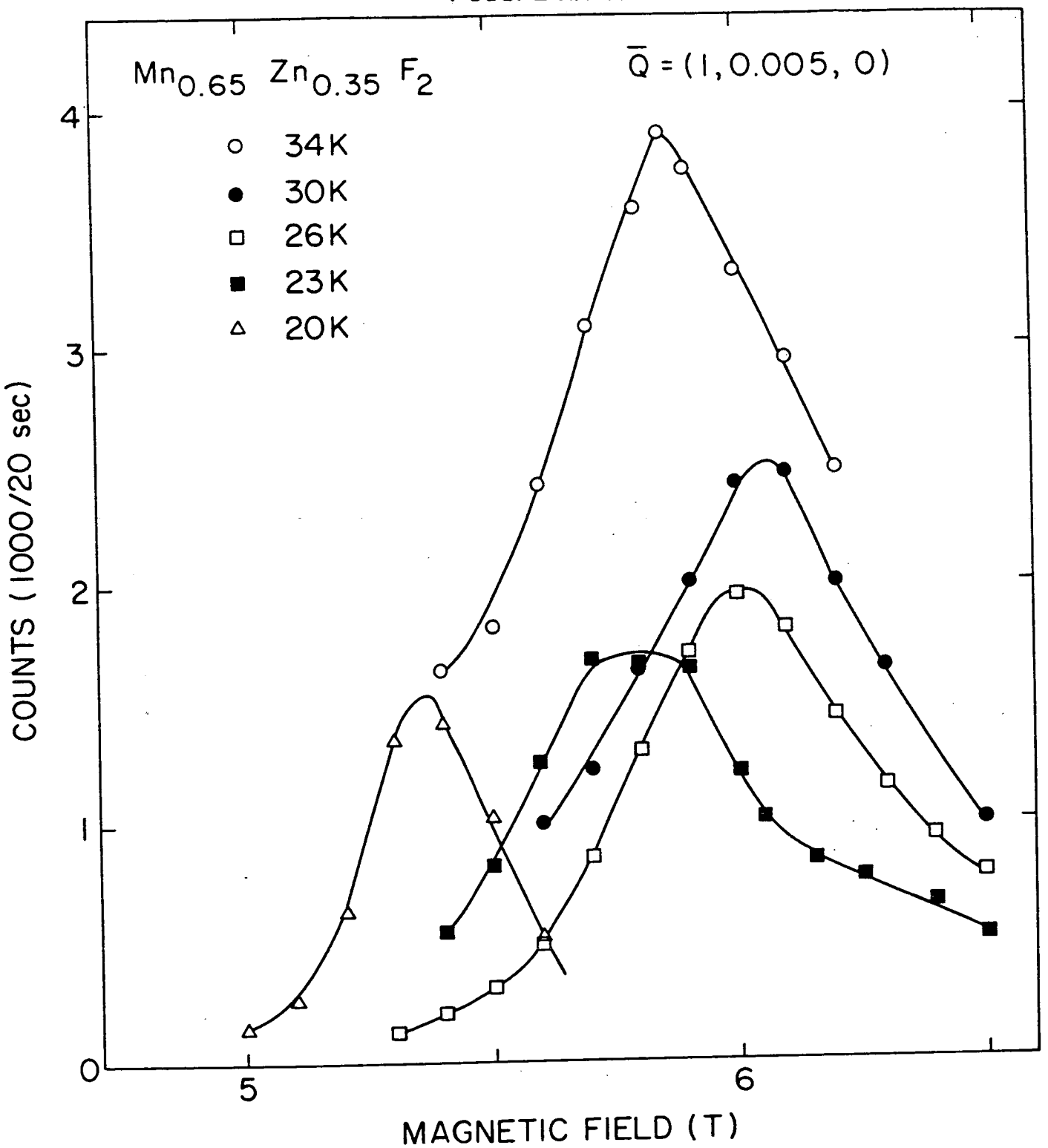
$Mn_{0.65}$ $Zn_{0.35}$ F_2
$\bar{Q}$ = (1, 0.005, 0)
34K
30K
26K
23K
20K
COUNTS (1000/20 sec)
MAGNETIC FIELD (T)
0
1
2
3
4
5
6

Figure (3.8.7)

The temperature dependence of the inverse correlation lengths in fields of 2.0T, 4.0T and 5.0T are shown for the temperature range from 30 to 43 K. The solid lines are merely guides to the eye.

FIGURE(3.8.7)

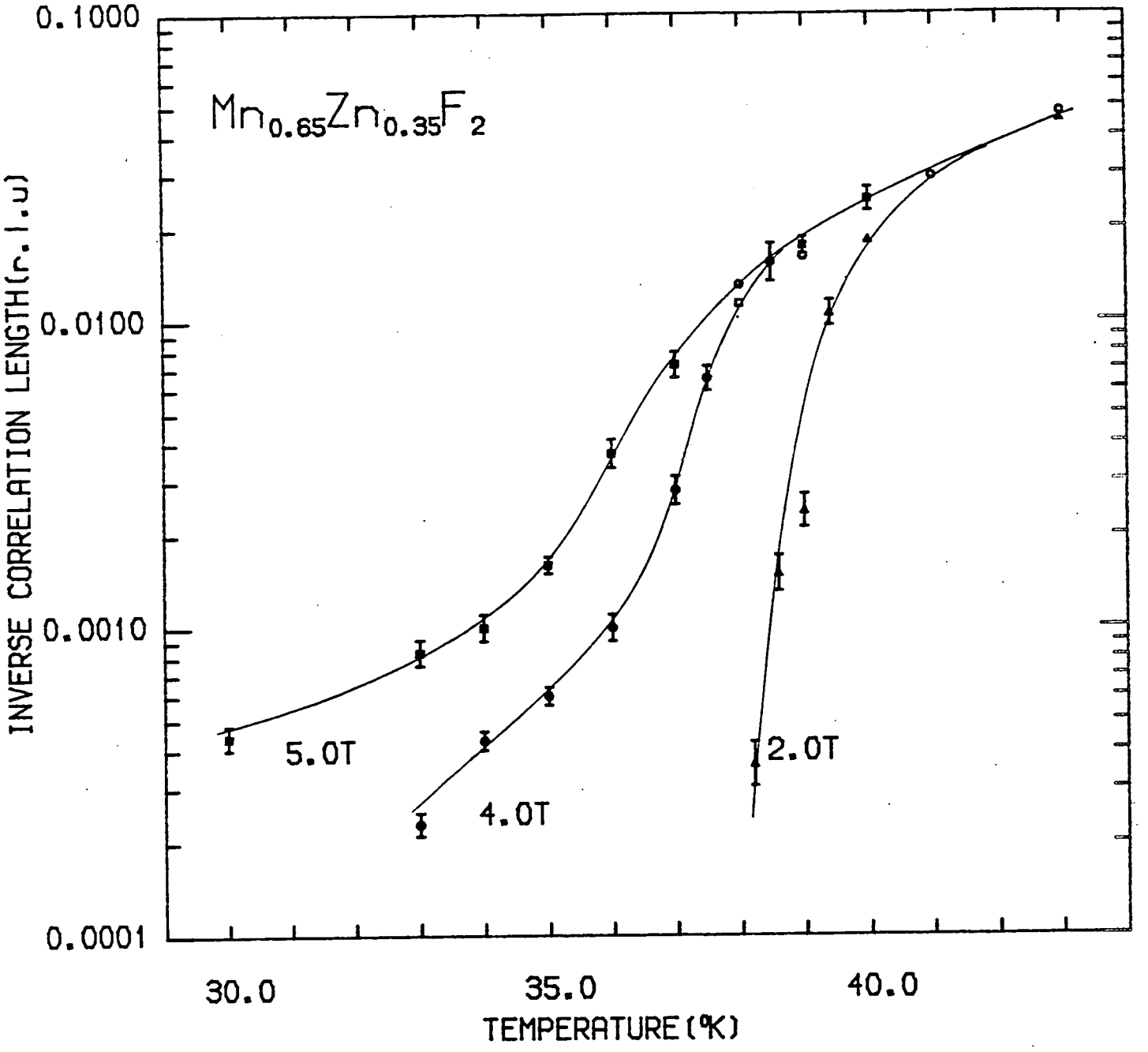
0.1000
0.0100
0.0010
0.0001
INVERSE CORRELATION LENGTH(r.l.u)
$Mn_{0.65}Zn_{0.35}F_2$
5.0T
4.0T
2.0T
30.0
35.0
40.0
TEMPERATURE(°K)

also happens in this sample of $Mn_{0.65}Zn_{0.35}F_2$ lies in the fact that the inverse correlation length is becoming very small at lower temperatures. This leads to two problems, firstly in performing the fits to the experimental scans accurately to obtain the parameters A, B and κ and determine the goodness of fit, and secondly in deciding what significance to attach to these derived parameters.

The first of these problems was overcome by noting that in a certain limit the convolution of the Lorentzian plus Lorentzian squared structure factor with the resolution function could be done analytically for the wavevector components in the (1,0,0) and (0,0,1) directions. In subsection (vi) of appendix A the method for performing this convolution is given explicitly. For the scans in which the inverse correlation length was greater than 0.0015* the FITIT computer program was used to perform the data analysis. This was the program used to analyse the $Co_xZn_{1-x}F_2$ data, with the exception of the 1.5T data below 12 K in the $Co_{0.35}Zn_{0.65}F_2$ sample, and it uses the convolution method given in subsection (v) of appendix. However, to analyse the scans in which the inverse correlation length was less than 0.0015a* a new computer program SHARP was written, which used the convolution method given in subsection (vi) of appendix A. This program was also used to analyse the 1.5T data for temperatures below 12 K in the $Co_{0.35}Zn_{0.65}F_2$ sample.

The second problem concerns how accurately the inverse correlation length obtained from the fitting analysis represents the 'true' inverse correlation length. The origin of this difficulty can be illustrated by rewriting equation (3.2.3) as a power series in (κ/q) whereby

$$S(q) = \frac{A}{q^2} + \frac{B}{q^4} - \left(\frac{A}{q^2} + \frac{2B}{q^4}\right)\left(\frac{\kappa}{q}\right)^2 + O\left(\left(\frac{\kappa}{q}\right)^4\right) \qquad (3.8.1)$$

Hence for wavevectors $q > \kappa$ the difference between the $\kappa = 0$ form for $S(q)$ and that for $\kappa \neq 0$ is only of order $(\kappa/q)^2$. Since in an experimental scan there is a limit to the step size with which one can scan through the (1,0,0) lineshape as κ gets smaller so the number of data points significantly affected by the value of κ gets smaller. As an example the 'worst case' shown in figure (3.8.7) of $\kappa = 0.000225a^*$ for a temperature of 33 K and a field of 4.0T will be considered. The scan through the (1,0,0) position in a field of 4.0T at a temperature of 33 K was shown previously in figure (3.8.1b). If the convolution over the resolution function is performed using the method given in subsection (vi) of appendix A then at (1, 0.004, 0) the difference in the Lorentzian squared term with $\kappa = 0$ and $\kappa \neq 0$ has fallen to 5%. Therefore in the fitting analysis of a scan along (1, ξ,0) only those data points with $|\xi| < 0.004$ will have a significant effect on the value of κ. In the scan at 33 K in 4.0T field there were in total 41 data points over a range $\xi = -0.02$ to 0.02 with 9 data points in the range $|\xi| < 0.004$. The data points outwith the range $|\xi| < 0.004$ because they are insensitive to the value of κ will determine the values of the amplitudes A and B. Therefore in effect what the fitting program will do is to obtain the best fit values for the amplitudes A and B from the wings of the scan and then to adjust κ to obtain the best fit to the lineshape and intensities in the centre of the scan. As a consequence the values of κ obtained by the data analysis can be expected to be within a factor of perhaps 2 or 3 of the 'true' value for κ. There is a qualification of course, because of the possible effects of extinction which will disproportionately affect the centre points of the scan because these are the most intense. An examination

of figure (3.8.8) which shows the temperature dependence of the peak intensity suggests that extinction should not be a severe problem in the temperature range from 30 K upwards.

The lineshape at the (1,0,0) position at temperatures lower than 30 K have been fitted using the SHARP program for the data taken in fields of 4.0 and 5.0T. In figure (3.8.9) the values of the inverse correlation lengths deduced from these fits along with those determined at higher temperatures in these fields are shown. If these values for the inverse correlation length are taken at face value then qualitatively the behaviour is very similar to that for the Ising systems. The fits which gave these values for the inverse correlation lengths had χ^2 parameters in the range 0.3 to 1.5. It should be noted that at low temperature the scans fitted are expected to contain some degree of extinction.

From an examination of figure (3.8.7) it can be seen that it would not have been possible to determine values for κ at lower temperatures from the data taken in 2.0T field. However, even at temperatures as low as 7.0 K in 2.0T field there are significant wings of scattering on the peak at the (1,0,0) position. In order to determine whether these wings of scattering were consistant with a Lorentzian plus Lorentzian squared form,another fitting program ABFIT was written. This program fitted the data points in a scan along (1, ξ, 0) to equation (3.2.3) with κ set equal to zero for values of $|\xi|$ >0.006. As argued above, the dependence of the intensity in κ for $|\xi|$ >0.006 should be insignificant. As a consequence of setting κ to zero the calculated intensity depends linearly on the variable parameters, i.e. the amplitudes A and B, and the linear fitting methods given in subsection (ii) of appendix A were used. The convolution of the $1/q^2$ and $1/q^4$ terms with the resolution function

Figure (3.8.8)

The measured peak intensity at the $(1,0,0)_M$ Bragg position is shown for various magnetic fields as a function of temperature.

FIGURE(3.8.8)

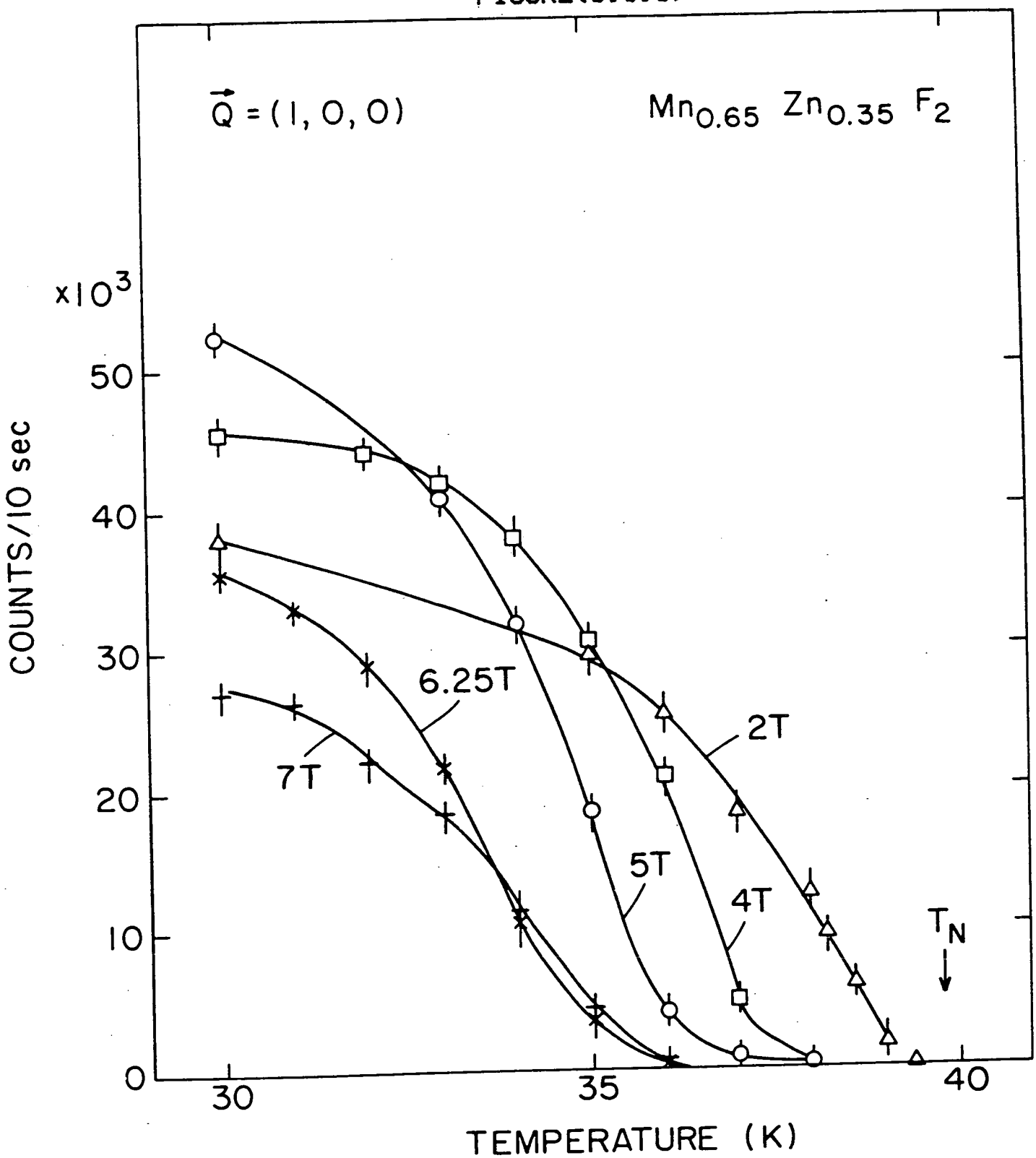
$\vec{Q}$ = (1, 0, 0)
$Mn_{0.65}$ $Zn_{0.35}$ F_2
x10³
COUNTS/10 sec
50
40
30
20
10
0
6.25T
7T
2T
5T
4T
T_N
30
35
40
TEMPERATURE (K)

Figure (3.8.9)

The inverse correlation lengths in fields of 4.0T and 5.0T are shown as a function of temperature in the range from 7 K to 43 K.

FIGURE(3.8.9)

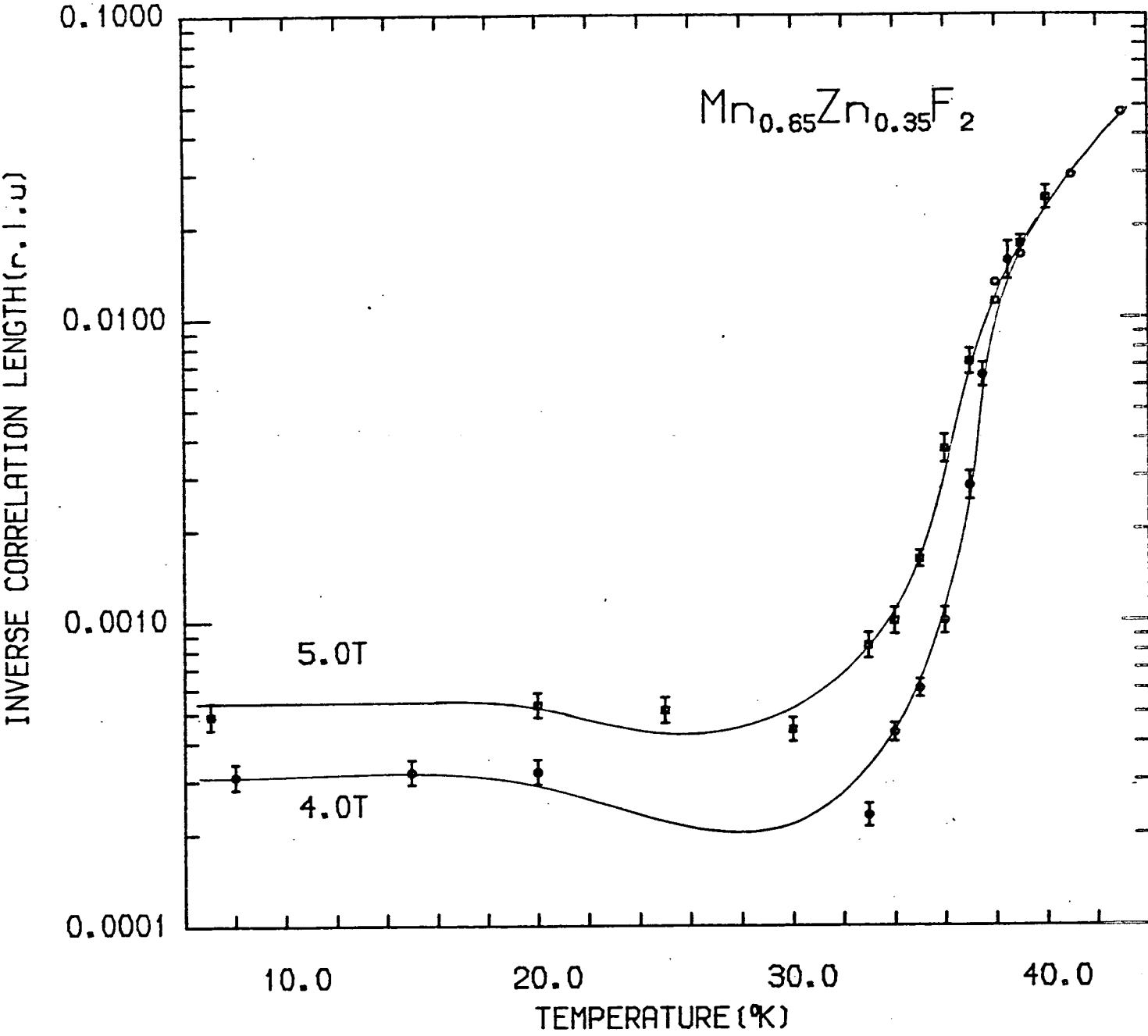
0.1000
0.0100
0.0010
0.0001
INVERSE CORRELATION LENGTH(r.l.u)
$Mn_{0.65}Zn_{0.35}F_2$
5.0T
4.0T
10.0
20.0
30.0
40.0
TEMPERATURE(°K)

was done using the convolution method given in subsection (vi) of appendix A. In figure (3.8.10) the scan at 7.0 K in 2.0T field is shown along with the fit to the wings of the scan given by the program ABFIT which is given by the solid line. The χ^2 parameter for this fit was 1.28. It should be pointed out that the value of A found from this fit was essentially zero. An analysis of the scans in 2.0T field using ABFIT showed that the amplitude A became zero at a temperature of about 32 ± 2 K. This also occurred for the data taken in 4.0T where the amplitude A essentially became zero at a temperature of about 20 K. However, for the data analysed in 5.0T field the amplitude A was significantly non-zero at all temperatures above 7 K.

In the $Co_xZn_{1-x}F_2$ and $Fe_xZn_{1-x}F_2$ samples it was found that the ratio $B/_K$ for various different fields and temperatures essentially collapsed to a single curve as a function of temperature. A plot of the various ratios $B/_K$ determined from the fits to the Lorentzian plus Lorentzian squared structure factor for the $Mn_{0.65}Zn_{0.35}F_2$ sample in the temperature range from 30 to 38.5 K is shown in figure (3.8.11). Although the spread from a single curve is somewhat larger in figure (3.8.11) than for the $Co_{0.35}Zn_{0.65}F_2$ data shown in figure (3.5.10) the data points do seem to indicate the existence of a common curve. The solid line in figure (3.8.11) is merely a guide to the eye. In figure (3.8.12) the variation of the amplitude A with temperature is shown for the applied fields of 2.0T, 4.0T and 5.0T in the temperature range from 30 K to 43 K. The behaviour shown in figure (3.8.12) is very reminiscent of the temperature dependence of the amplitude A in the $Co_{0.35}Zn_{0.65}F_2$ sample.

In figure (3.8.13) the results obtained for this sample of $Mn_{0.65}Zn_{0.35}F_2$ are summarised in a "phase diagram" showing the

(Figure (3.8.10)

The lineshape at the $(1,0,0)_M$ Bragg position is shown at a temperature of 7.0 K in a field of 2.0T. The solid lines are the best fits of the wings to a Lorentzian squared form with $\kappa = 0$, while the dotted lines are the resolution function and background level.

FIGURE(3.8.10)

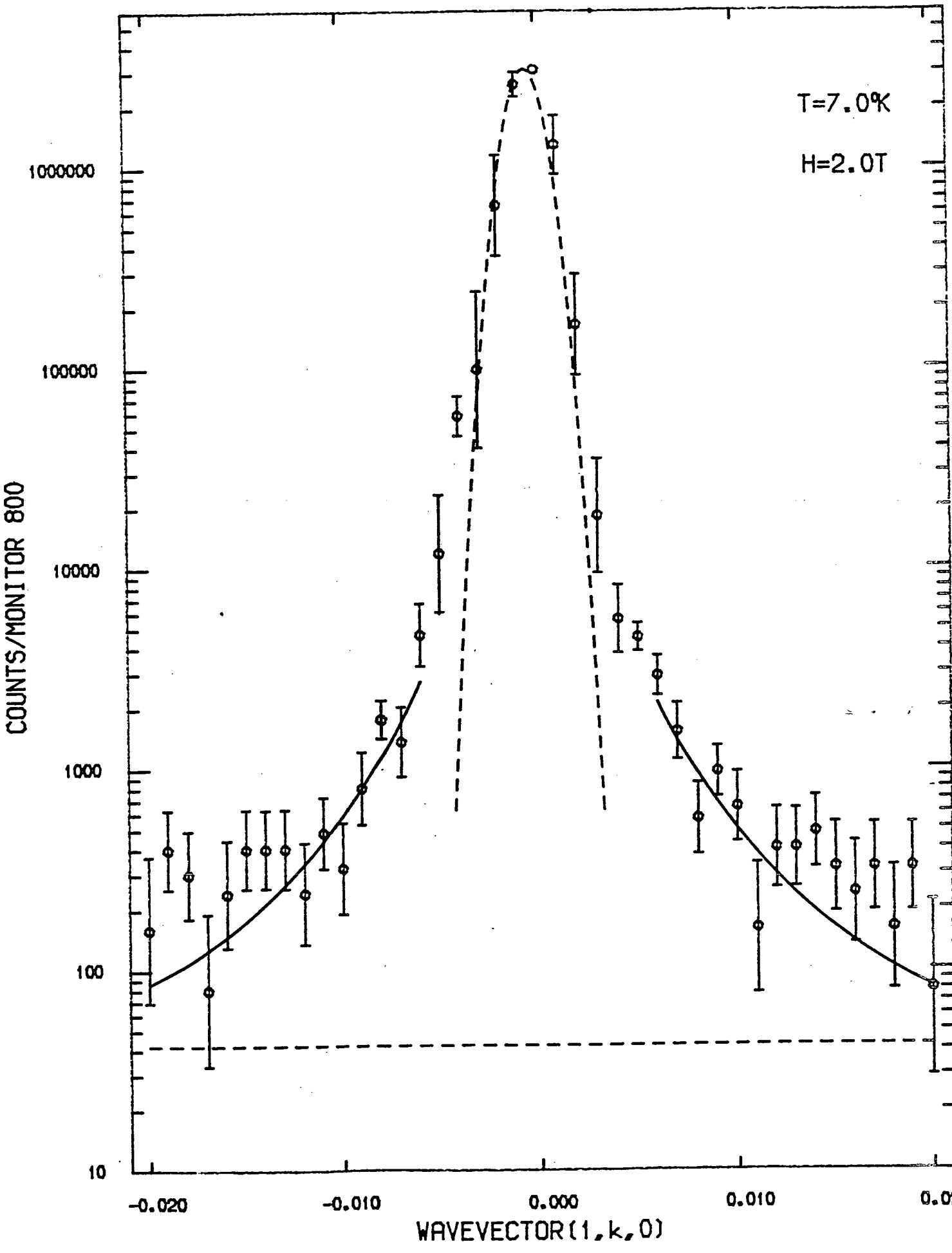
T=7.0K
H=2.0T
1000000
100000
10000
1000
100
10
COUNTS/MONITOR 800
-0.020
-0.010
0.000
0.010
WAVEVECTOR(1,k,0)

Figure (3.8.11)

A plot of the ratio $B/_{\kappa}$ is shown as a function of temperature for the fields 2.0T, 4.0T and 5.0T. The solid line is merely a guide to the eye.

FIGURE(3.8.11)

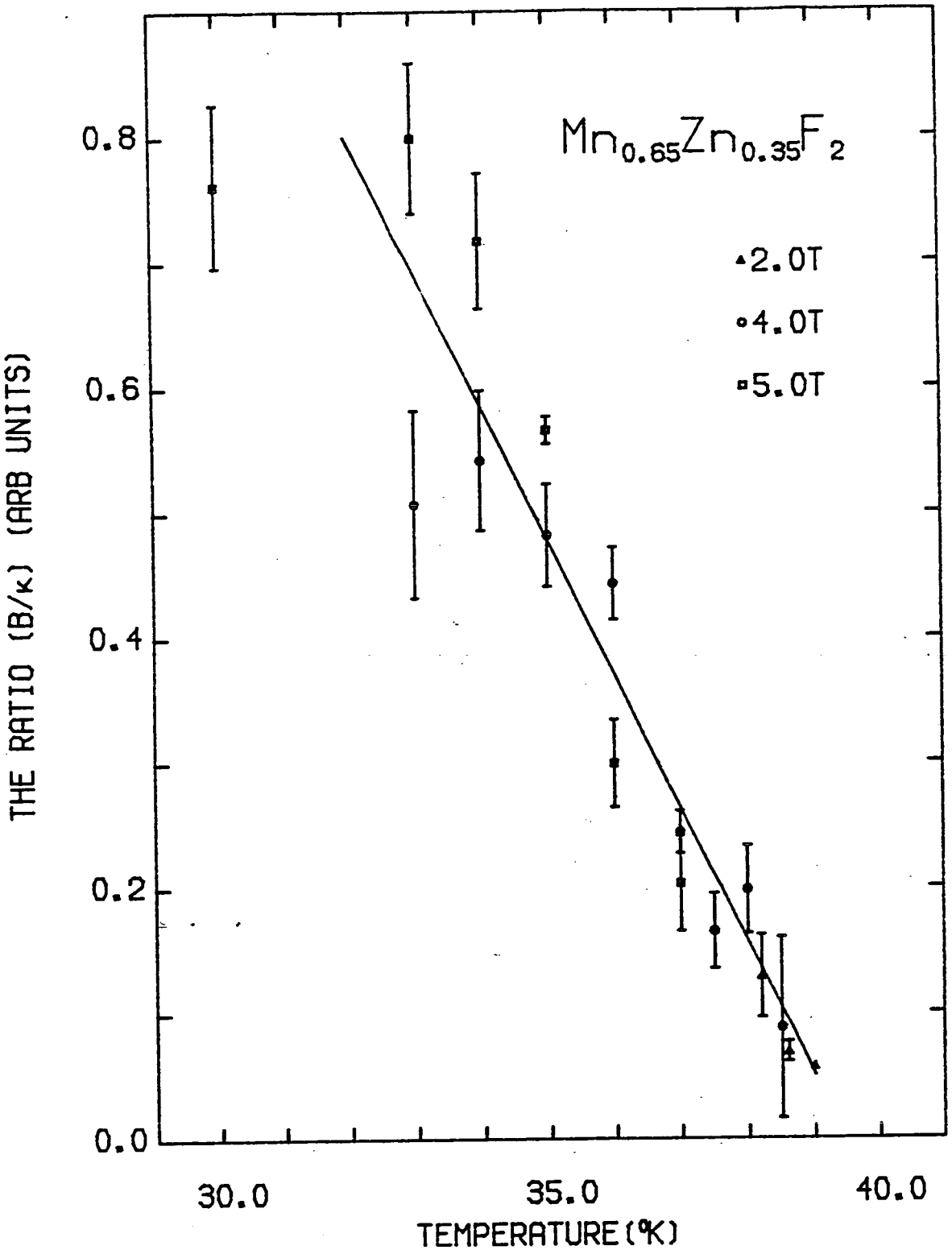
$Mn_{0.65}Zn_{0.35}F_2$
▲2.0T
○4.0T
□5.0T
THE RATIO (B/K) (ARB UNITS)
0.0
0.2
0.4
0.6
0.8
30.0
35.0
40.0
TEMPERATURE(°K)

Figure (3.8.12)

The temperature dependence of the amplitude A is shown for the fields 2.0T, 4.0T and 5.0T. The solid lines are merely guides to the eye.

FIGURE(3.8.12)

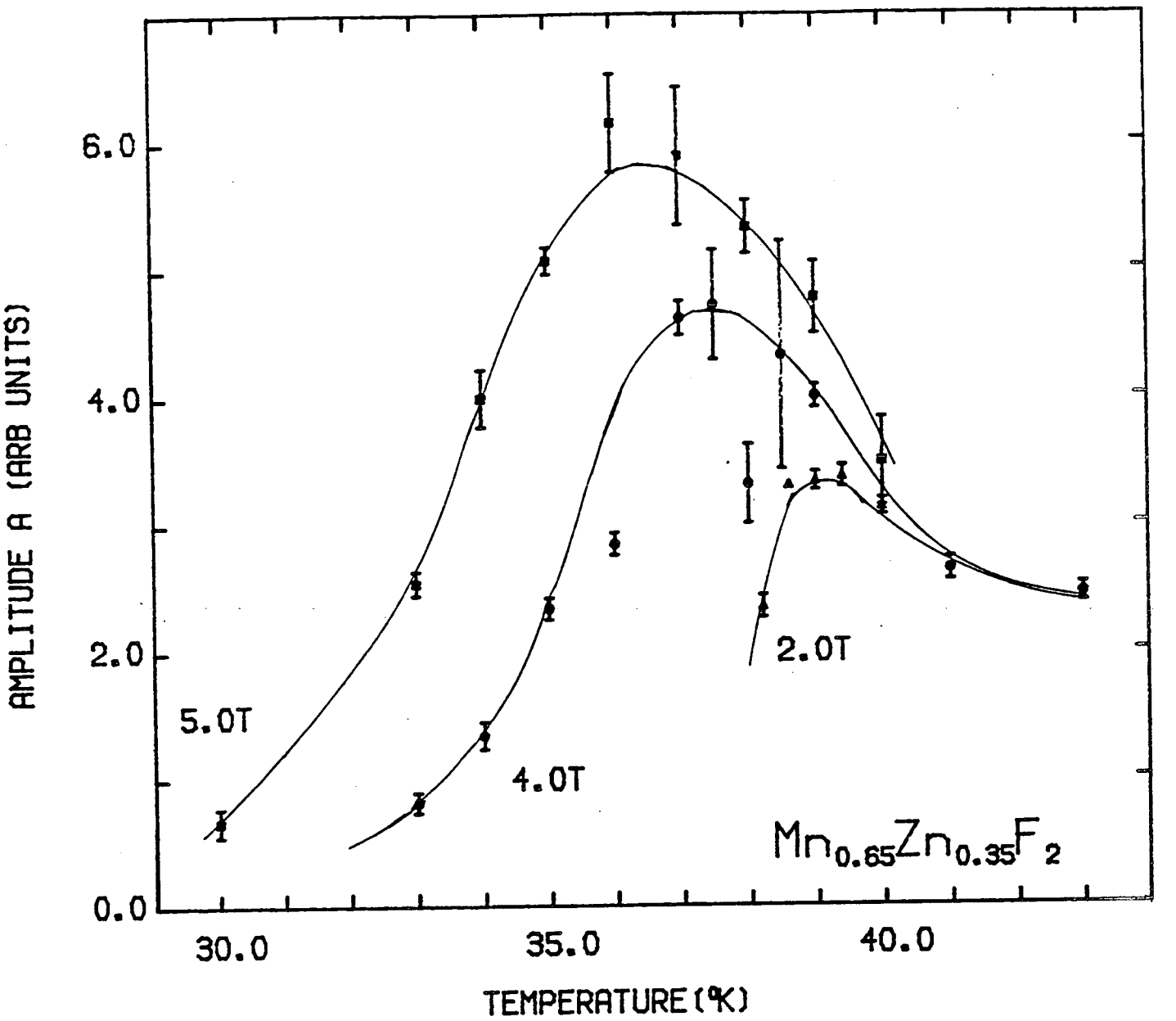
6.0
4.0
2.0
0.0
AMPLITUDE A (ARB UNITS)
30.0
35.0
40.0
TEMPERATURE(°K)
5.0T
4.0T
2.0T
Mn0.65Zn0.35F2

Figure (3.8.13)

A 'phase diagram' for the $Mn_{0.65}Zn_{0.35}F_2$ sample is shown. The different symbols represent the combinations of field and temperature at which, a Lorentzian squared is needed in the structure factor as well as a Lorentzian (Δ), only a Lorentzian squared is needed in the structure factor (□), there is a spin flop transition (O) and there is a transition from the paramagnetic to spin flop states (∇). The solid lines are merely guides to the eye.

FIGURE(3.8.13)

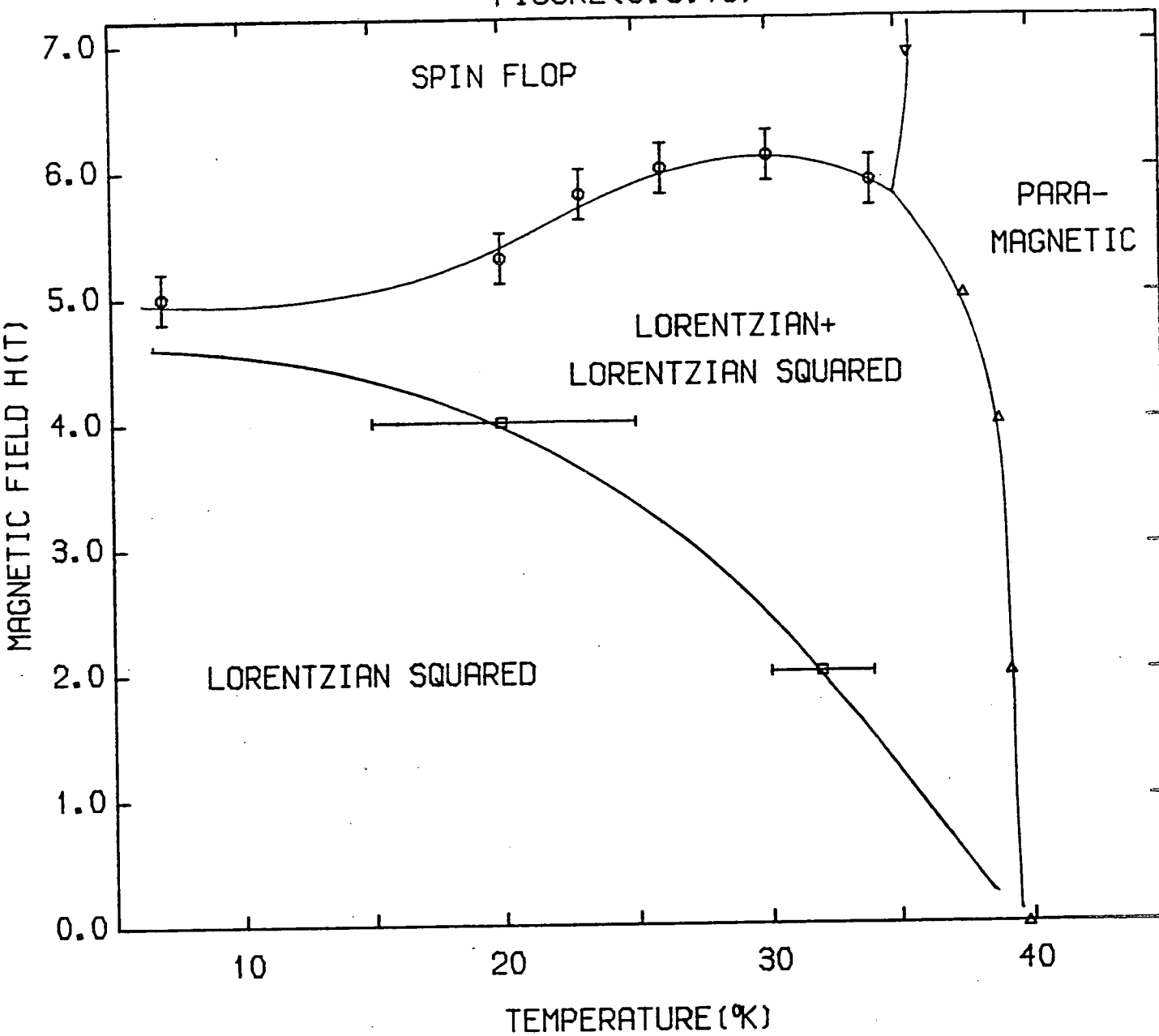
SPIN FLOP
PARA-
MAGNETIC
LORENTZIAN+
LORENTZIAN SQUARED
LORENTZIAN SQUARED
MAGNETIC FIELD H(T)
TEMPERATURE(°K)
7.0
6.0
5.0
4.0
3.0
2.0
1.0
0.0
10
20
30
40

different regions of behaviour. The lines drawn are guides to the eye through those points where a change is known to take place. The error bars were drawn in the same way as for figure (3.5.4). No detailed measurements of the behaviour around, or the position of, the bicritical point were made and the lines drawn in this region are merely extensions of the other lines.

3.9 Discussion (2) - $Mn_xZn_{1-x}F_2$

A comparison of the results reported in section (8) with those obtained by Cowley and Buyers (1982) shows a similar qualitative behaviour at temperatures around the zero field Néel temperature. The effects observed in this sample of $Mn_{0.65}Zn_{0.35}F_2$ are significantly bigger than those observed by Cowley and Buyers in a $Mn_{0.78}Zn_{0.22}F_2$ sample in the same applied field. In the $Mn_{0.65}Zn_{0.35}F_2$ sample there is evidence to suggest that long range order is not established in any of the non-zero fields applied for temperatures above 7 K. This evidence comes from two sources. Firstly, the relief of extinction as a function of applied field observed in the integrated intensity for the (1,0,0) lineshape at 7 K. Secondly, the wings of scattering found at low temperatures in non-zero field are consistent with a Lorentzian plus Lorentzian squared structure factor. However, the correlation length at these low temperatures is very large, of the order of at least 1000 lattice spacings. The qualitative similarity between these results and those of Cowley and Buyers suggests that this was also the case in their measurements on $Mn_{0.78}Zn_{0.22}F_2$. The poor fits to the Lorentzian plus Lorentzian squared structure factor at low temperatures obtained by these authors being attributable to extinction

effects and difficulty in accurately performing the convolution with the resolution function.

The results of section (8) for fields of 5.0T and less are also qualitatively similar to those obtained for the Ising systems $Co_xZn_{1-x}F_2$ and $Fe_xZn_{1-x}F_2$. These similarities are apart from the Lorentzian plus Lorentzian squared structure factor, the temperature dependence of the ratio B/κ and the amplitude A and the effect of the spin freezing. The temperature dependence of the inverse correlation length also has a similar shape to that in the Ising systems. The difference with the Ising systems is one of the magnitude of the inverse correlation length at low temperatures. In the sample of $Fe_{0.5}Zn_{0.5}F_2$ studied by Cowley et al (1983c) the inverse correlation length at 10 K in 5.5 T field was 0.0015a* while for $Mn_{0.65}Zn_{0.35}F_2$ it was 0.0005a* in 5.0T field at 7.5 K. This is a surprising result since the Mn^{2+} ion has a moment that is 25% larger than that of the Fe^{2+} ion and an exchange JS^2 which is 14% lower. It is most unlikely that the magnitude of the inverse correlation length would depend so strongly on the difference in concentration in this region.

As mentioned in section (7.i) this sample of $Mn_{0.65}Zn_{0.35}F_2$ has been used previously by Belanger et al (1982) and Yasuoka et al (1982) for the measurement in an applied field of the birefringence and NMR relaxation time respectively. The results of these authors will be briefly described and their significance discussed. As discussed by Gehring (1977) the birefringence δn of an Ising magnet is related to a two site correlation function by $\delta n \propto \sum_{ij} g_{ij} < S_i^z S_j^z >$ where g_{ij} is a short range coupling term. The birefringence is therefore similar to the internal energy $U = \sum_{ij} J_{ij} < S_i^z S_j^z >$

when J_{ij} is of short range and it is believed that the temperature derivative of the birefringence follows the specific heat capacity. Belanger et al measured the birefringence in the sample of $Mn_{0.65}Zn_{0.35}F_2$ for temperatures around the zero field Néel temperature and in magnetic fields of 2.0T and less. The temperature derivatives of the measured birefringence showed sharp peaks as a function of temperature in these fields. Accordingly these authors interpreted this as a transition from paramagnetic to long range antiferromagnetic order. The position of these peaks shifted to lower temperature with increasing magnetic field. Assuming these peaks indicated the Néel temperature in non-zero field Belanger et al fitted their data to the form

$$T_N(H) = T_N(H = 0) - bH^2 - aH^{2/\phi} \qquad (3.9.1)$$

Equation (3.9.1) was proposed by Fishman and Aharony (1979) for the reduction of the Néel temperature in a dilute antiferromagnet by induced random fields. The exponent ϕ is a crossover exponent which Fishman and Aharony argued should be equal to the susceptibility exponent, which for a d = 3 Ising system is 1.25. From their data analysis Belanger et al found a value for ϕ of 1.4 ± 0.1, in fair agreement with the prediction of Fishman and Aharony.

Yasuoka et al (1982) measured the NMR relaxation time of ^{19}F ions with no magnetic neighbours in this sample for temperatures around the zero field Néel temperature and applied fields of less than 2.3T. The NMR relaxation time is related to the dipolar field at the ^{19}F ion sites due to the surrounding magnetic ions. This dipolar field will be proportional to the average of the sublattice magnetisation over the range of the dipolar interactions. From their NMR relaxation time measurements Yasuoka et al were able to determine

the temperatures at which there was a spontaneous magnetisation as a function of field. Again, this was interpreted as a phase transition from paramagnetic to long range antiferromagnetic order and these authors fitted their data to equation (3.9.1) to obtain an exponent $\phi = 1.38 \pm 0.20$.

However, in an antiferromagnet such as $Mn_xZn_{1-x}F_2$ the dipole sum converges rapidly because of the alternating two sublattice structure and therefore the dipole field experienced by the ^{19}F nucleus is only related to the average sublattice magnetisation within a short range from that site. This was also true for the birefringence measurements which will only measure the spin-spin correlation function between nearest or perhaps also next nearest neighbours. The domains induced in the small fields applied by Belanger et al and Yasuoka et al will be large in size, very much larger than the range of correlations over which these measurements are sensitive. As a consequence these measurements do not indicate a phase transition from paramagnetic to antiferromagnetic long range order but instead measure the properties of the spins within the large domains formed by the induced random field. As a consequence these measurements indicate the temperatures at which there is a change from behaviour dominated by thermal fluctuations to that dominated by random field fluctuations.

3.10 Overall Discussion

A comprehensive comparison of the experimental results for the properties of dilute antiferromagnets in an external magnetic field and the theoretical predictions for the R.F.I.M. and R.F.N.H.M. were given in sections (6) and (9). This section will not repeat the previous two sections but instead will discuss the outstanding

qualification to the experimental results from section (3) and will then conclude with a brief discussion of possible future experiments and theories to elucidate further on the current knowledge.

The final qualification to the experimental results is a somewhat fundamental qualification to the interpretation of the results. This qualification is that of whether the dilute antiferromagnet in an external magnetic field is in the same Universality class as the random field problem. Although the different mechanisms discussed in section (3) all gave rise to induced random fields, the Hamiltonians they lead to are not exactly the same as that for the random field model originally proposed by Imry and Ma (1975) There are two differences between the dilute antiferromagnet in a field and the R.F.I.M. The first is the presence of the randomness in the exchange part of the Hamiltonian due to the dilution and the second is the existence of short range correlations between the induced random fields. This last point by itself should not be important since short range correlations amongst the random fields are known not to change the behaviour of the R.F.I.M. (Aharony et al (1976)). However since the random fields are induced because of the dilution,there is a correlation between the distribution of induced random fields and the distribution of exchange interactions. This correlation may remove the dilute antiferromagnet in a field from the same Universality class as the random field problem (Imry (1983)). The full extent of such a correlation is not known at this time.

Future work, both experimental and theoretical should, therefore, be aimed firstly at resolving this last qualification. It is well recognised that the problem of a dilute antiferromagnet in an external magnetic field is a difficult theoretical problem. However, a useful theoretical study would be to consider the effect of

dilution on the R.F.I.M. itself. Apart from the question of the lower critical dimension for such a system, it would be interesting to know whether the effect of domain wall pinning occurs and if the spins become frozen at low temperatures. Experimentally the objective should be to move in the opposite direction and remove the effect of dilution from the systems studied. This can be done by studying mixed antiferromagnets with differing magnetic moments. Although this would still leave a correlation between the distributions of the induced random fields and the exchange interactions, this effect should be much smaller. Further to this any effect from domain wall pinning should also be much smaller.

As a final conclusion, whether the dilute antiferromagnet in an external magnetic field is in the same Universality class as the random field problem or not, the effect of the magnetic field on the phase transition and ordering is drastic. It destroys long range antiferromagnetic order in both d = 2 and 3 and leads to a completely new state of order.

CHAPTER FOUR

Spin Waves in Diluted and Mixed $FeCl_2$

4.1 Introduction

Whereas the previous two chapters have been on the phase transitions and ordering of magnetic systems, this chapter and the next will be concerned with the low temperature spin-wave excitation spectra of disordered magnets. A spin wave is the linear excitation of a magnet from its groundstate to a state in which the total angular momentum has been reduced by h. In pure ferromagnets with simple interactions the methods for calculating the spectrum of spin wave energies is well known (see for example Ziman (1971) p. 366). The situation for antiferromagnets is more complicated because of problems in determining the quantum mechanical ground state (see for example Keffer (1966) p. 113). However, for antiferromagnets in which the magnetic interactions are of a simple form there is good agreement between experimental measurements of the spin wave spectrum (for references to many of these systems see the review of Cowley (1982)) and calculations using simple spin wave theory (see for example Ziman (1971) p. 372). These methods for calculating the excitation spectrum in pure systems all utilise the translational invariance of the system to diagonalise the Hamiltonian via a Fourier transform of the spatial co-ordinates. In a site disordered magnet, however, the translational invariance is broken and, consequently, the calculation of the spin wave excitations is a much harder problem than for pure systems.

In the last fifteen years a great deal of work has been done in developing techniques to calculate the excitation spectra of

disordered systems. The simplest approximation that can be applied in an effort to calculate the spin wave spectrum of a disordered magnet is the Virtual Crystal Approximation (V.C.A.) (see for example Ziman (1979) p. 325). In this approximation the Hamiltonian is written as the sum of an average Hamiltonian, which is translationally invariant (i.e. a virtual crystal) plus a perturbation term which includes the fluctuations from the average Hamiltonian. The V.C.A. ignores the effect of the perturbation term and calculates the excitation spectra of the average Hamiltonian. Since this is translationally invariant the Hamiltonian can be diagonalised by a Fourier transformation and the spin waves are eigenstates of the wavevector but with energies shifted by the disorder. In practice the V.C.A. is almost never valid and the perturbation term must be included. Therefore, in order to go beyond the V.C.A. by analytical techniques it is necessary to evaluate the perturbation series arising from the perturbation term. The techniques developed so far have only been able to sum certain classes of term in the perturbation series and therefore have had varying degrees of success. The most successful analytical method is the Coherent Potential Approximation (C.P.A.) (a review of the development from the V.C.A. to C.P.A. is included in the article by Elliott (1982)). The C.P.A. has been applied to magnetic systems by a number of authors (Coombs and Cowley (1975), Buyers et al (1972), Tonegawa (1974)) and has been successful for cases of weak disorder. However, for strong disorder the C.P.A. has not provided a good description of the spin wave spectrum. A review of the successes and limitations of the C.P.A. applied to magnetic systems is included in the article by Cowley (1982). Therefore, in recent years computer simulation techniques has been developed to calculate the spin wave

spectrum of highly disordered magnets. There are two basic methods for carrying out these simulations, one due to Kirkpatrick and Harris (1975) and the other due to Alben and Thorpe (1975). In both of these methods a finite, but large, model of a disordered magnet is constructed within the computer and the equations of motion for the Greens functions (see for example Elliott (1982)) describing the motion of the spins on the lattice solved numerically. The spin wave spectrum of this model is then taken to be a good approximation to the spectrum of an infinite system. The two methods differ in the way in which the equations of motion are solved.

In the Kirkpatrick and Harris method the temporal Fourier transform of the differential equations of motion for the real space Greens function is taken, which transforms the equations of motion into a set of linear simultaneous equations. Kirkpatrick and Harris demonstrated that for a fixed frequency ω these simultaneous equations could be solved efficiently using specialised algorithms. It should be noted that for a lattice of N sites there are N^2 simultaneous equations. The solution of these equations are the real space Greens functions at a given frequency. The imaginary part of the spatial Fourier transform of these Greens functions for various wavevectors is equivalent to a section through the dynamic structure factor $S(\underline{Q}\ \omega)$ (Marshall and Lovesey (1971) p. 241) at fixed ω. In other words the results of such calculations simulate a constant E scan in a triple axis neutron scattering experiment.

The method of Alben and Thorpe (1975) however, effectively reverses the order of these operations. There are N^2 linear differential equations for the real space Greens function in the time domain. The number of these equations is reduced to N by performing

a one sided spatial Fourier transform and the resulting differential equations are then solved by a numerical integration scheme. This integration results in the partially Fourier transformed Greens functions as a function of time. If the spatial Fourier transform is then completed the result is the time dependence of the Greens function for a particular wavevector. The temporal Fourier transform of this Greens function for various frequencies, therefore, leads to a section through $S(\underline{q}, \omega)$ for fixed $\underline{q}$ and varying ω. In other words, this method simulates a constant Q scan in a triple axis neutron scattering experiment. This method is usually referred to in the literature as the 'Equation of Motion' (E.O.M.) method.

Since for most disordered magnetic insulators inelastic neutron scattering measurements are performed in the constant Q mode the E.O.M. method has been used by a number of authors for comparisons with neutron scattering experiments. This comparison has so far been for antiferromagnets rather than for ferromagnets. In the paper of Thorpe and Alben (1976) a comparison between the spectra calculated for the mixed two dimensional antiferromagnet $Rb_2Mn_{0.5}Ni_{0.5}F_4$ was made with the measurements of Als-Nielsen et al (1975). This comparison between simulation and experiment was very favourable with the simulations reproducing the frequencies and features of the experimentally measured lineshapes very well. A comparison between E.O.M. method simulations and inelastic neutron scattering measurements was made by Cowley et al (1977) for the dilute two dimensional antiferromagnet $Rb_2Mn_{0.54}Mg_{0.46}F_4$. This is a case of very strong disorder since the concentration of Mn^{2+} ions is less than the percolation threshold for a d = 2 square lattice. The simulation technique however, produced very good agreement with the experimental measurements, very much better than the results of

C.P.A. calculations. In another paper, Cowley et al (1980d) have compared the results of E.O.M. simulations for the two dimensional dilute antiferromagnet $Rb_2Co_{0.58}Mg_{0.42}F_4$ with experimental measurements. Although not as good as the agreement for $Rb_2Mn_{0.54}Mg_{0.46}F_4$ there was still good agreement between simulation and experiment. The E.O.M. method has also been used by Alben et al (1977) for calculations of the spin wave spectra of mixed and diluted three dimensional ferromagnets. Since there are very few three dimensional ferromagnetic insulators these calculations have not, to the author's knowledge, been compared with experimental measurements.

However, the results of the calculations for the two dimensional antiferromagnets have been questioned by Halley and Holcomb (1978). In the calculations quoted above for the two dimensional antiferromagnets the assumed ground state was the Néel state. Halley and Holcomb tested the self consistency of this assumption within the E.O.M. framework for the $Rb_2Mn_xMg_{1-x}F_4$ case. Halley and Holcomb drew two conclusions from this study. The first was that a linearised Greens function technique would not adequately calculate the excitation spectrum of small clusters of spins. This was a point that had been noted previously by Cowley and Buyers (1972). The second point made by Halley and Holcomb was that close to the percolation threshold there is a large effect in dilute antiferromagnets due to zero point motion which is not correctly accounted for in the E.O.M. method.

In this chapter and the next the results of E.O.M. method simulations for the diluted and mixed compounds of $FeCl_2$ are presented. $FeCl_2$ is a layered antiferromagnet but has a low temperature spin wave spectrum which can be treated as that of an anisotropic two-dimensional ferromagnet. The simulations presented have been performed assuming that the low temperature spin wave spectrum of diluted and mixed

$FeCl_2$ is well approximated by the spin wave spectrum of a two-dimensional anisotropic ferromagnet. As a consequence the second point made by Halley and Holcomb is not applicable to these simulations. In the dilute study the first point made by Halley and Holcomb was taken into account by removing all of the small clusters from the simulation.

The calculations presented in this chapter are for dilute $FeCl_2$ e.g. $Fe_xMg_{1-x}Cl_2$ and for $FeCl_2$ mixed with $MnCl_2$. In the next chapter the case of $FeCl_2$ mixed with $CoCl_2$ will be considered. The rest of this chapter is set out as follows. Section (2) contains a description of the magnetic properties of $FeCl_2$. The E.O.M. method for calculating the dynamic structure factor $S^{\perp}(\underline{q}, \omega)$ is described in section (3) and its implementation for $FeCl_2$ in section (4). The results for $Fe_xMg_{1-x}Cl_2$ are presented and discussed in section (5). In section (6) results for $Fe_xMn_{1-x}Cl_2$ are presented and compared with the inelastic neutron scattering measurements of Bertrand et al (1981).

4.2 Properties of $FeCl_2$

The crystallographic structure of $FeCl_2$ is of the rhombohedral $CdCl_2$ type (Wyckoff (1963) p. 272) and the primitive unit cell is shown in figure (4.2.1). However, it is usual to consider $FeCl_2$ in terms of a hexagonal set of crystallographic axes. The structure shown in figure (4.2.1) can be generated by an ABCAB stacking of hexagonal planes of Fe^{2+} ions with Cl^- ions at relative positions $\pm(0,0,u)$ where $u = 0.25$. $FeCl_2$ is an antiferromagnet and has a Néel temperature of 23.6 K (Yelon and Birgeneau (1972)). The magnetic moments of the Fe^{2+} ions order parallel to the c-axis in ferromagnetic sheets alternately stacked along the c-axis (Wilkinson et al

Figure (4.2.1)

This figure shows the crystal structure of $FeCl_2$. The cell indicated is the rhombohedral primitive unit cell.

FIGURE(4.2.1)

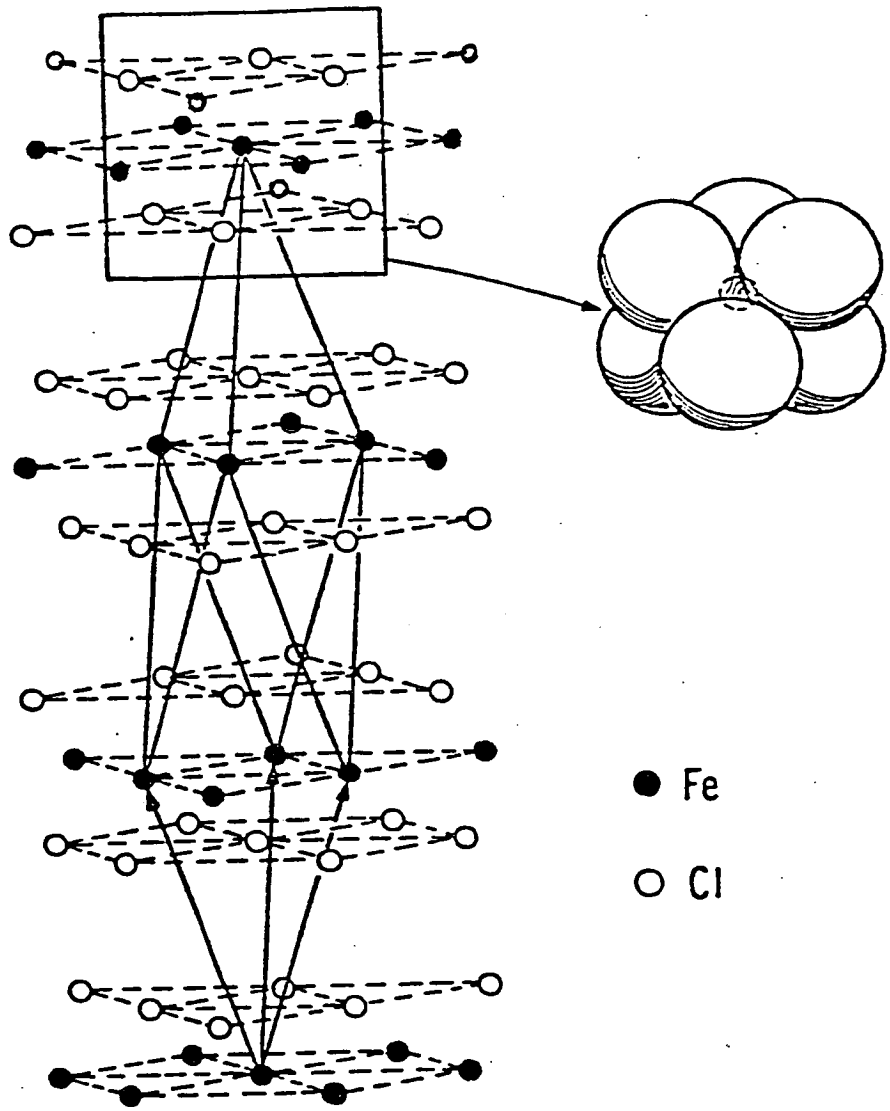

(1959)). As a consequence the magnetic unit cell is double the length of the nuclear unit cell along the c-axis. From now on all reference to unit cell and reciprocal space co-ordinates will be with respect to this magnetic unit cell. The cell has lattice parameters a = 3.583 A and c = 34.89 A at 4 K (Birgeneau et al (1972)). The structure factor rules for the allowed Bragg peaks for this cell are:

$$h - k + \frac{1}{2}\ell = 3n \qquad \text{(nuclear)} \tag{4.2.1a}$$

$$-h + k + \ell = 3n \text{ and } \ell \text{ odd} \qquad \text{(magnetic)} \tag{4.2.1b}$$

where n is an integer and (h,k,ℓ) are the hexagonal reciprocal space co-ordinates. In figure (4.2.2) the reciprocal space diagram of the $k = 0$ plane is shown with a magnetic Brillouin zone indicated.

The Fe^{2+} free ion has a ^5D ground state. In $FeCl_2$ the crystal field surrounding the Fe^{2+} ion can be decomposed into a cubic field plus a trigonal distortion. The strong cubic field splits the ^5D level and makes the ground state a $^5T_{2g}$ orbital triplet. This triplet can be treated as an effective $\ell = 1$ level (Birgeneau et al (1972)) i.e. a ^5P state. Then acting on this state is the trigonal crystal field and the spin orbit coupling which may be written as:

$$\Delta \mathcal{H} = \delta\left[(\ell^z)^2 - \frac{2}{3}\right] - \lambda\, \underline{\ell}.\underline{S} \tag{4.2.2}$$

where δ and λ are the phenomenological parameters for the trigonal crystal field and spin orbit coupling respectively. Values for δ and λ have been determined by Alben (1969) and are:

$$\delta = -88 \text{ cm}^{-1}, \quad \lambda = 67 \text{ cm}^{-1} \tag{4.2.3}$$

The splitting of the ^5P level by these two terms has been evaluated be calculating the matrix elements of equation (4.2.2) within the 15 ^5P states and diagonalising the resulting (15 x 15) matrix. In figure (4.2.3) the resulting energy level picture is shown along with the wavefunctions for the three lowest levels. It is the excitation

Figure (4.2.2)

The reciprocal space diagram a* - c* plane of $FeCl_2$ is shown. Magnetic Bragg peaks are indicated by triangles and nuclear and magnetic Bragg peaks are indicated by circles. A magnetic Brillouin zone is shown about the (1,0,7) Bragg peak.

FIGURE(4.2.2)

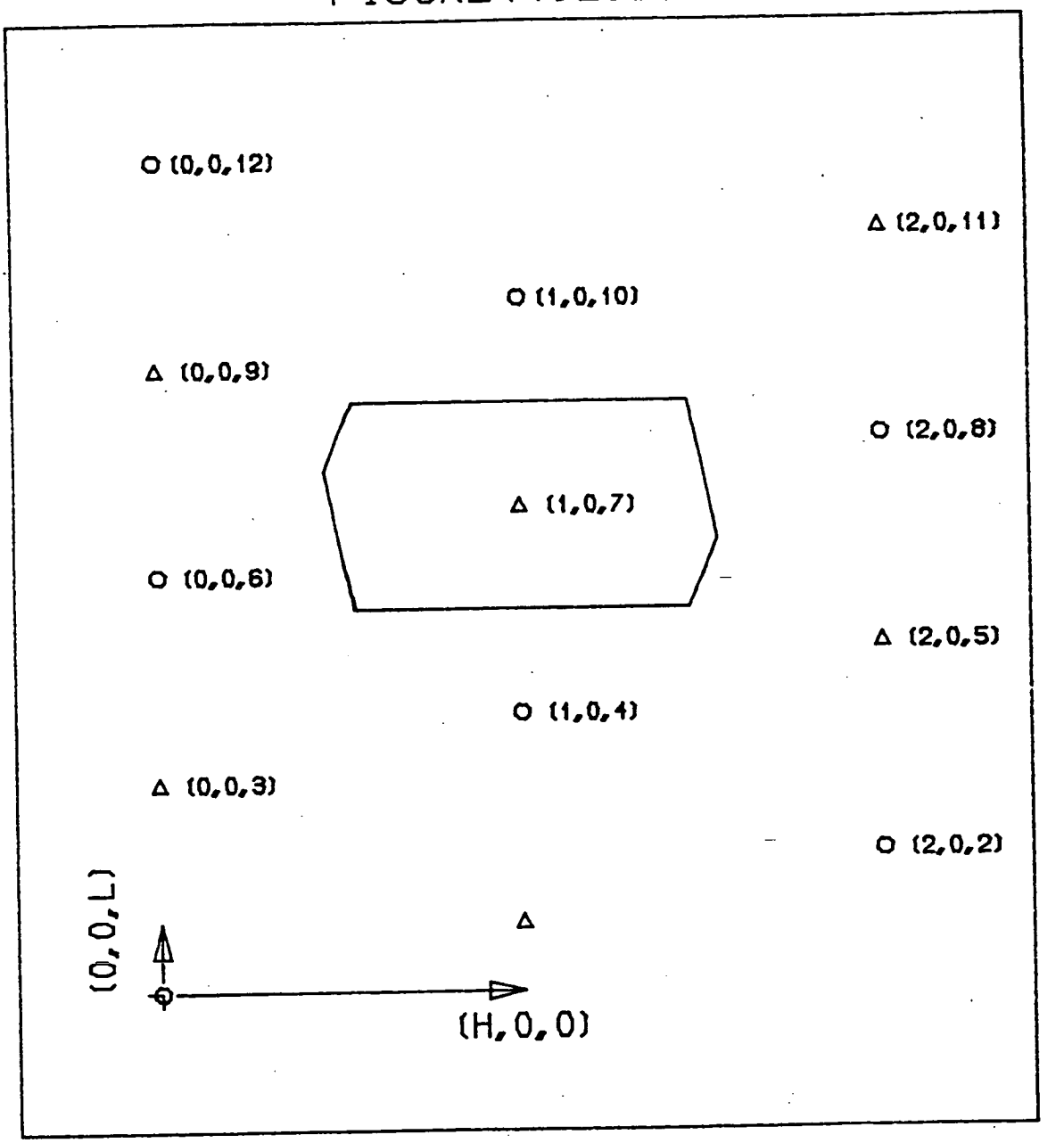
O (0,0,12)
Δ (2,0,11)
O (1,0,10)
Δ (0,0,9)
O (2,0,8)
Δ (1,0,7)
O (0,0,6)
Δ (2,0,5)
O (1,0,4)
Δ (0,0,3)
O (2,0,2)
Δ
(0,0,L)
(H,0,0)

Figure (4.2.3)

The various single ion levels of an Fe^{2+} ion in $FeCl_2$ are shown. The diagram is not to scale and nor is necessarily the level with respect to the ^5P level correct. Also shown are the wave-functions for the three lowest levels.

FIGURE(4.2.3)

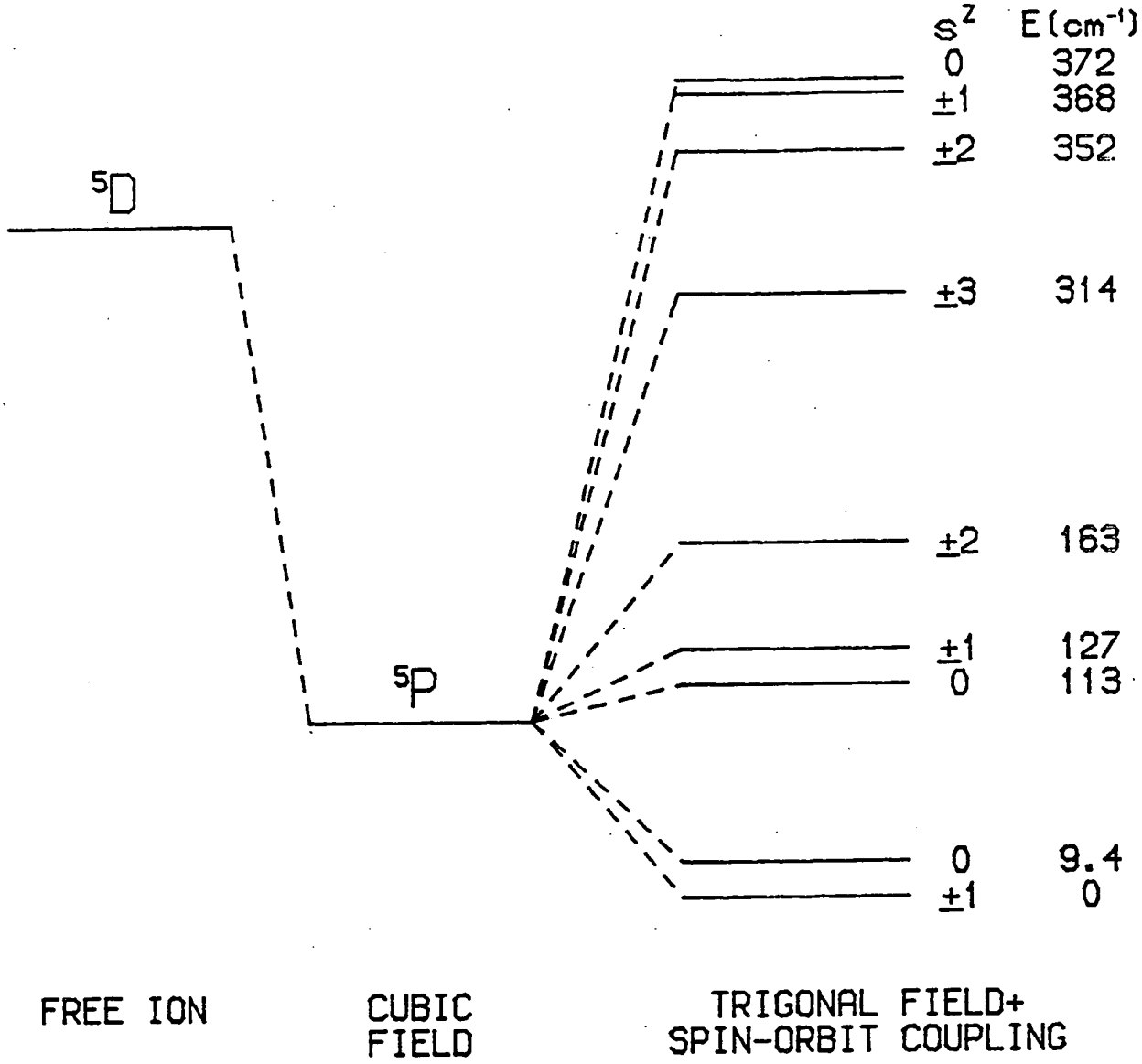

GROUND STATE WAVEFUNCTIONS

$$|+1\rangle = 0.864|1,1\rangle|2,+2\rangle - 0.423|1,0\rangle|2,+1\rangle + 0.272|1,+1\rangle|2,0\rangle$$

$$|0\rangle = 0.597|1,1\rangle|2,-1\rangle - 0.535|1,0\rangle|2,0\rangle + 0.597|1,-1\rangle|2,1\rangle$$

$$|-1\rangle = 0.864|1,1\rangle|2,-2\rangle - 0.423|1,0\rangle|2,-1\rangle + 0.272|1,-1\rangle|2,0\rangle$$

spectrum of $FeCl_2$ within these levels that is of interest in this chapter and the next. These three levels may be approximated as a pseudo spin s = 1 level (Birgeneau et al (1972)). From the wave-functions given in figure (4.2.3) the various proportionality factors (cf equation (1.2.2)) are calculated to be

$$\alpha_s^z = 1.672 \quad , \quad \alpha_s^\perp = 1.403 \tag{4.2.4a}$$

$$\alpha_\ell^z = -0.673 \quad , \quad \alpha_\ell^\perp = -0.398 \tag{4.2.4b}$$

$$g^z = 4.02 \quad , \quad g^\perp = 3.20 \tag{4.2.4c}$$

For this chapter and most of the next chapter it will be assumed that $FeCl_2$ has an isotropic exchange interaction between the real spins of the Fe^{2+} ions. Then from the above description of the lowest three levels the Hamiltonian within these levels, including exchange, may be written as

$$\mathcal{H} = -\Sigma D_i (s_i^z)^2 - \sum_{ij} I_{ij} \hat{s}_i^z \hat{s}_j^z + J_{ij}(\hat{s}_i^x \hat{s}_j^x + \hat{s}_i^y \hat{s}_j^y) \tag{4.2.5}$$

where the pseudo spin operators have been written as small s's. The spin wave spectrum of $FeCl_2$ in the (h,0,0) direction has been measured by Birgeneau et al (1972) and fitted in terms of the Hamiltonian given in equation (4.2.5). In table (4.2.1) the values of the exchange interactions and the single ion anisotropy energy given by $2D(s - \frac{1}{2})$, determined by Birgeneau et al are given. The exchange between nearest neighbour Fe^{2+} spins within the a-b plane is strong and ferromagnetic while that between next nearest neighbour spins, both interplanar and intraplanar, is weak and antiferromagnetic. Birgeneau et al observed no measurable dispersion along the $(0,0,\ell)$ direction and the spin wave spectrum therefore strongly resembled that of an anisotropic two dimensional ferromagnet. Although the

Table (4.2.1)

Exchange Interactions for $FeCl_2$

In-plane (n.n.)	$2I_1 = 0.97$ meV,	$2J_1 = 0.68$ meV
In plane (n.n.n.)	$2I_2 = -0.13$ meV,	$2J_2 = -0.09$ meV
Out of plane (n.n.n.)	$2I_2' = -0.04$ meV,	$2J_2' = -0.03$ meV
Single ion anisotropy	$2D(s - \frac{1}{2}) = 1.043$ MeV	

(After Birgeneau et al (1972))

spin wave spectrum of $FeCl_2$ is insensitive to the interplanar ... the critical properties of $FeCl_2$ are, and the phase transition is in the d = 3 Ising Universality class (Yelon and Birgeneau (1972)).

In the calculations of the spin wave spectra to be presented in this chapter and the next, $FeCl_2$ has been modelled as a two dimensional anisotropic ferromagnet on a hexagonal lattice. Further to this only the nearest neighbour exchange interaction has been included in the model Hamiltonian since this is the dominant interaction. As a consequence of these two approximations the resulting calculations may not precisely represent the spin wave spectra in 'real' diluted and mixed compounds of $FeCl_2$. However, the calculations should be quantitatively close to the 'real' spectra and should certainly contain all the qualitative features to be expected.

4.3 The Equation of Motion Method

In this section the equation of motion formalism as applied to $Fe_xX_{1-x}Cl_2$, where X = Mg or Mn (this chapter) or Co (next chapter), will be set out. The aim of this formalism is to arrive at a series of equations that can be easily converted into a computer program, the output from which should be directly comparable to the results of an inelastic neutron scattering experiment.

In the previous section the form of the exchange Hamiltonian for $FeCl_2$ within the lowest three levels of the single ion spectrum was discussed. The form of the Hamiltonian was

$$\mathcal{H} = -\sum_i D_i (S_i^z)^2 - \sum_{ij} I_{ij} S_i^z S_j^z + J_{ij}(S_i^x S_j^x + S_i^y S_j^y) \qquad (4.3.1)$$

This Hamiltonian will suffice to discuss the $Fe_xMg_{1-x}Cl_2$ and $Fe_xMn_{1-x}Cl_2$ compounds and will also be used for the $Fe_xCo_{1-x}Cl_2$

compound, although its applicability in this case will be discussed further in the next chapter. The disorder caused by the Mg^{2+} and Mn^{2+} ions will enter into equation (4.3.1) through the variation of the exchange interactions and single ion energies throughout the crystal. In order to calculate the spin wave excitation spectrum for equation (4.3.1) the operators S_i^z, S_i^x and S_i^y are replaced by the operators (Ziman (1971) p. 368):

$$S_i^z = S_i - a_i^* a_i \tag{4.3.2a}$$

$$S_i^x = \sqrt{\frac{S_i}{2}} \; (a_i + a_i^*) \tag{4.3.2b}$$

$$S^y = -i \sqrt{\frac{S_i}{2}} (a_i - a_i^*) \tag{4.3.2c}$$

where the operator a_i^* creates a spin deviation on site i and a_i destroys a spin deviation on site i. Equations (4.3.2) already involve an approximation whereby the operator $\sqrt{S_i^z}$ has been replaced by $\sqrt{S_i}$ (Ziman (1971) p. 368). If the equations (4.3.2) are substituted into equation (4.3.1) and the terms higher than quadratic in the operators a_i and a_i^* are neglected then the exchange Hamiltonian becomes:

$$\mathcal{H} - \mathcal{H}_o = \sum_i 2D_i (S_i - \tfrac{1}{2}) a_i^* a_i + 2 \sum_{ij} I_{ij} S_j a_i^* a_i - J_{ij} \frac{\sqrt{S_i S_j}}{2}$$

$$(a_i a_j^* + a_i^* a_j) \tag{4.3.3}$$

where $\mathcal{H}_o$ is the ground state energy and is independent of the operators a_i and a_i^*. The earlier approximation of replacing $\sqrt{S_i^z}$ by $\sqrt{S_i}$ can be shown (Keffer (1966) p. 55) only to effect higher terms than quadratic and therefore equation (4.3.3) is consistent up to quadratic order.

Following Thorpe and Alben (1976) a function $C_{iq}(t)$ is defined

by the equation:

$$C_{i\underline{q}}(t) = \frac{1}{\sqrt{N}} \sum_j g_j^{\perp} \sqrt{S_j}\, e^{-i\underline{q}.\underline{r}_j} < 0 \left| \left[a_i(t),\, a_j^*(0) \right] \right| 0 > \qquad (4.3.4)$$

for times t that are greater than or equal to zero. The $C_{i\underline{q}}(t)$ are related to the dynamic structure factor $S^{\perp}(q, \omega)$ (equation (1.3.10)) through the relation:

$$S^{\perp}(q, \omega) = \frac{1}{2\pi\sqrt{N}} \mathrm{Re} \int_0^{\infty} dt\, e^{i\omega t} \sum_i g_i^{\perp} \sqrt{S_i}\, e^{i\underline{q}.\underline{r}_i} C_{i\underline{q}}(t) \qquad (4.3.5)$$

Therefore if it is possible to obtain the $C_{i\underline{q}}(t)$ as a function of t then it is possible to calculate $S^{\perp}(q, \omega)$ from the integral in equation (4.3.5).

The equation of motion for $C_{i\underline{q}}(t)$ is:

$$i\hbar \frac{\partial C_{i\underline{q}}}{\partial t}(t) = \frac{1}{\sqrt{N}} \sum_j g_j^{\perp} \sqrt{S_j}\, e^{-i\underline{q}.\underline{r}_j} < 0 \left| \left[\left[a_i(t), \mathcal{H} \right], a_j^*(0) \right] \right| 0 > \qquad (4.3.6)$$

The commutator of $a_i(t)$ with $\mathcal{H}$ can be evaluated by noting that the time dependence of $a_i(t)$ commutes with $\mathcal{H}$ so that one only needs to calculate the commutator of a_i with $\mathcal{H}$. Using equation (4.3.3) for equation (4.3.6) can be evaluated as:

$$i\hbar \frac{\partial C_{i\underline{q}}(t)}{\partial t} = \Omega_i\, C_{i\underline{q}}(t) - \sum_j J_{ij} 2\sqrt{S_i\, S_j}\, C_{j\underline{q}}(t) \qquad (4.3.7)$$

where $\Omega_i = 2D_i \left(S_i - \frac{1}{2}\right) + 2 \sum_j I_{ij}\, S_j$ is the Ising energy for the i^{th} spin. Equation (4.3.7) is one of N coupled linear differential equations, one for each of the $C_{i\underline{q}}(t)$. These equations along with the initial conditions given by the $C_{i\underline{q}}(t = 0)$ in principle contain all the information required to describe the spin wave spectrum. The 'Equation of Motion' method (Alben and Thorpe (1975) seeks to solve the equations (4.3.7) by numerical integration. The simplest and most easily applied scheme for doing this is to use the method of forward and backward difference, in which the derivative in equation (4.3.7) is approximated by:

$$\frac{\partial C_{i\underline{q}}(t)}{\partial t} = \frac{C_{i\underline{q}}(t + \delta t) - C_{i\underline{q}}(t - \delta t)}{2\delta t} + O((\delta t)^2) \qquad (4.3.8)$$

where the timestep δt is small. Therefore neglecting terms that are cubic in δt the coupled first order differential equations in equation (4.3.7) can be replaced by a set of N coupled second order difference equations given by:

$$C_{i\underline{q}}(t + \delta t) = C_{i\underline{q}}(t - \delta t) - \frac{2i\delta t}{\hbar}\left[\Omega_i C_{i\underline{q}}(t) - 2\sum_j J_{ij}\sqrt{S_i S_j}\, C_{j\underline{q}}(t)\right] \qquad (4.3.9)$$

Therefore given the sets of initial conditions $C_{i\underline{q}}(t = 0)$ and $C_{i\underline{q}}(t = \delta t)$ equations (4.3.9) may be iterated to obtain the $C_{i\underline{q}}(t)$ at later times. The first of these initial conditions is easily evaluated from equation (4.3.4) and is given by:

$$C_{i\underline{q}}(t = 0) = \frac{1}{\sqrt{N}} g_i^{\perp} \sqrt{S_i}\, e^{-i\underline{q}.\underline{r}_i} \qquad (4.3.10)$$

The second initial condition, however, can only be obtained approximately by expanding $C_{i\underline{q}}(t)$ in a Taylor expansion about t = 0, so that

$$C_{i\underline{q}}(t = \delta t) = C_{i\underline{q}}(t = 0) + \delta t \left.\frac{\partial C_{i\underline{q}}(t)}{\partial t}\right|_{t=0} + \frac{1}{2}(\delta t)^2 \left.\frac{\partial^2 C_{i\underline{q}}(t)}{\partial t^2}\right|_{t=0} + O((\delta t)^3) \qquad (4.3.11)$$

The second derivatives in equation (4.3.11) can be calculated by differentiating equation: (4.3.6).

Two questions arise from replacing equation (4.3.7) by equation (4.3.9). The first is, what is the size of the timestep δt and the second is, how good an approximation is the $C_{i\underline{q}}(t)$ calculated from equation (4.3.9) after a given number of timesteps. The answer to

the first question is that δt must be smaller than the minimum periodic time for the oscillation of the spins. If E_{max} is the upper bound on the spectrum of the disordered system then δt will be given by:

$$\delta t = \frac{1}{n}\left(\frac{h}{E_{max}}\right) \tag{4.3.12}$$

where n is a number whose value will be subject to criteria to be discussed later. The value for E_{max} can be found from a knowledge of the various exchange interactions (Ziman (1979) p. 345). An answer to the second question can be estimated in the limit of translational invariance, where both equations (4.3.7) and (4.3.9) may be solved analytically. These solutions are:

$$C_{i\underline{q}}(t = (p+1)\delta t) = \frac{1}{\sqrt{N}} \sum_{\underline{q}} g_i^{\perp} \sqrt{S_i}\, e^{i\underline{q}\cdot\underline{r}_i} e^{-i\delta t\Omega(\underline{q})} e^{ip\delta t\Omega(\underline{q})} \tag{4.3.13a}$$

$$C_{i\underline{q}}(t = (p+1)\delta t) = \frac{1}{\sqrt{N}} \sum_{\underline{q}} g_i^{\perp} \sqrt{S_i}\, e^{i\underline{q}\cdot\underline{r}_i}\left(1 - i\delta t\Omega(\underline{q}) - \frac{(\delta t\Omega(\underline{q}))^2}{2}\right) e^{-ip\,\mathrm{Sin}^{-1}(\delta t\Omega(\underline{q}))} \tag{4.3.13b}$$

for equations (4.3.7) and (4.3.9) respectively where $\Omega(\underline{q})$ is the dispersion relation of the pure system. The magnitude of the difference between these solutions is of the order of $(\delta t\Omega(q))^3$. If the difference in the phase of the two solutions is denoted by ϕ then after p timesteps ϕ is given, in the limit of the worst possible case where $\Omega(\underline{q}) = E_{max}/h$, by:

$$\phi = p\left[\mathrm{Sin}^{-1}\left(\frac{2\pi}{n}\right) - \frac{2\pi}{n}\right] \tag{4.3.14}$$

Equation (4.3.14) can be inverted to obtain an estimate of the number

of timesteps for which equation (4.3.9) will not vary by more than say 10% from the phase of the exact solution.

Therefore, given a set of values of $C_{i\underline{q}}(t)$ at discrete times $S^{\perp}(\underline{q}, \omega)$ can be calculated by numerical integration. However, the integral in equation (4.3.5) has an upper limit of ∞ whereas the $C_{i\underline{q}}(t)$ can only be calculated up to some finite time T. Therefore instead of using equation (4.3.5) to calculate $S^{\perp}(\underline{q}, \omega)$ an approximation to the integral is made so that $S^{\perp}(\underline{q}, \omega)$ is given approximately by:

$$S^{\perp}(\underline{q}, \omega) = \frac{1}{2\pi} \text{ Re } \int_0^T dt\, e^{-i\omega t}\, e^{-\lambda t^2}\, C_{\underline{q}}(t) \tag{4.3.15}$$

where $C_{\underline{q}}(t)$ is given by:

$$C_{\underline{q}}(t) = \frac{1}{\sqrt{N}} \sum_i g_i^{\perp} \sqrt{S_i}\, e^{i\underline{q}.\underline{r}_i}\, C_{i\underline{q}}(t) \tag{4.3.16}$$

If the limits $T \to \infty$ and $\lambda \to 0^+$ were taken for equation (4.3.15) then equation (4.3.5) would be recovered. The effect of the finite limit to the integral and the damping factor $e^{-\lambda t^2}$ can be demonstrated by evaluating equation (4.3.15) in the limit of translational invariance. In this limit the factor $C_{\underline{q}}(t)$ will be given by:

$$C_{\underline{q}}(t) = (g^{\perp})^2 S\, e^{i\Omega(\underline{q})t} \tag{4.3.17}$$

Then substituting equation (4.3.17) into equation (4.3.15) leads to the result:

$$S^{\perp}(\underline{q},\omega) = \frac{1}{2\pi} (g^{\perp})^2 S \left\{A(T) \sqrt{\frac{\pi}{\lambda}}\, e^{\frac{-(\omega-\Omega(\underline{q}))^2}{4\lambda}} + \frac{e^{-\lambda T^2}}{\sqrt{\lambda}}\, f\left(\frac{\omega-\Omega(\underline{q})}{2\sqrt{\lambda}}\right)\right\} \tag{4.3.18}$$

$$\text{where } A(T) = 1 - \text{erfc}\left(\frac{T}{\sqrt{\lambda}}\right) \tag{4.3.19}$$

and

$$f(x) = e^{-x^2} \int_0^x e^{y^2} \sin(2.\sqrt{\lambda}\, Ty)\, dy \qquad (4.3.20)$$

There are two parts to equation (4.3.18). The first is a Gaussian centred on the spin wave energy $\Omega(\underline{q})$ and the second is an oscillatory noise term. The magnitude of the noise term can be estimated by noting that

$$|f(x)| < e^{-x^2} \int_0^{\ddot{x}} e^{y^2}\, dy < 0.55 \qquad (4.3.21)$$

where the integral in between the inequalities is Dawsons integral (Abramowitz and Stegun (1964) p. 298). Hence by a suitable choice of λ and T the ratio of the amplitude of the noise term to the Gaussian can be reduced to a small value. The result is that $S^{\perp}(\underline{q},\omega)$ calculated from equation (4.3.15) instead of being a delta function centred on $\Omega(\underline{q})$ is a Gaussian lineshape centred on $\Omega(\underline{q})$. In general, therefore, $S^{\perp}(\underline{q},\omega)$ calculated from equation (4.3.15) is the convolution of the temporal Fourier transform of $C_{\underline{q}}(t)$ with a Gaussian frequency resolution function. Since the spectrometer in a triple axis neutron scattering experiment has a Gaussian resolution function in frequency, a direct comparison between the calculated $S^{\perp}(\underline{q}, \omega)$ and the measured intensity of neutrons can be made by adjusting λ to reproduce the experimental resolution function.

Therefore having chosen a value for λ the parameter T is chosen to reduce the level of the noise term. However, T will be equal to $p_{max}\delta t$ where p_{max} is the total number of timesteps. Substituting p_{max} into equation (4.3.14) and fixing a value for ϕ then leads to the value of n needed to obtain the required degree of accuracy. In practice the amount of computer time required to

perform the calculations also has some effect on the values chosen for these parameters.

There is a final manipulation to be made to equation (4.3.15) to put it in a more tractable form for computational purposes. This is to write it in the form:

$$S^{\perp}(\underline{q},\omega) = -\frac{1}{\pi}\int_{o}^{T} dt\ e^{-\lambda t^2}\ \mathrm{Sin}(\omega t)\ \mathrm{Im}\ C_{\underline{q}}(t) \qquad (4.3.22)$$

In going from equations (4.3.15) to (4.3.22) use has been made of the relation:

$$\mathrm{Cos}(\omega t)\ \mathrm{Re}\ C_{\underline{q}}(t) = -\mathrm{Sin}\ (\omega t)\ \mathrm{Im}\ C_{\underline{q}}(t) \qquad (4.3.23)$$

which is a result of $C_{\underline{q}}(\omega)$ satisfying the Kramers-Kronig relations (Marshall and Lovesey (1971) p. 576).

4.4 Method of Implementation

In this section a brief description will be given of how the formalism set out in the previous section was implemented in the various computer programs written. As discussed in section (2), the model employed for $FeCl_2$ is that of a two dimensional anisotropic ferromagnet on a hexagonal lattice. The hexagonal lattice was modelled by decomposing it into two interpenetrating rectangular sublattices as shown in figure (4.4.1). A site on a given sublattice therefore has two horizontal nearest neighbours on its own sublattice and four nearest neighbours on the other sublattice. In the calculations each of the sublattices was an $(\frac{L}{2} \times L)$ array giving a total number of sites $N = L^2$. The value of N used varied for the different calculations but has always been in the range from

Figure (4.4.1)

This figure indicates how a hexagonal lattice was constructed from two interpenetrating rectangular sublattices. The two sublattices are indicated by the triangles and circles.

FIGURE(4.4.1)

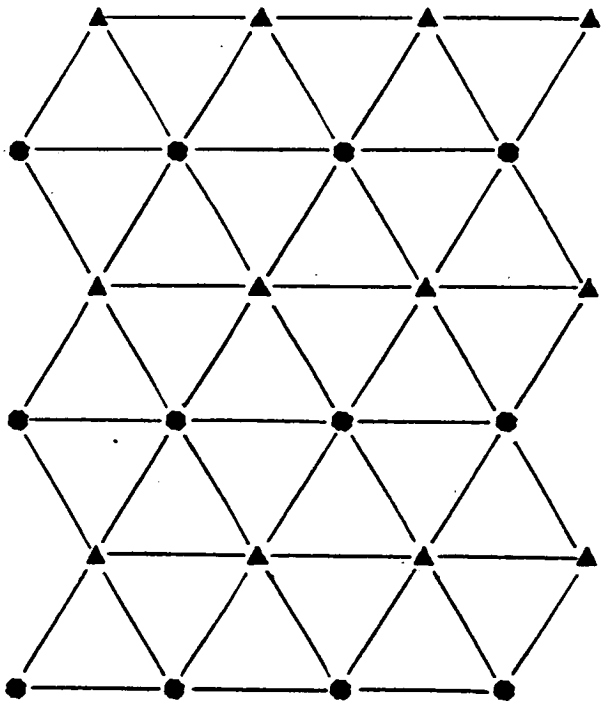

3600 to 6400 sites.

The occupation of the sites on the lattice by "Fe^{2+} ions" was determined using a random number generator GO5CAF contained in the NAG library (NAGFLIB (1977)). This routine generates a random number in the range 0 to 1 from a rectangular distribution. The occupation of each site was tested by generating a random number and then comparing this number to the preset concentration of Fe^{2+} ions. If the number was smaller than the concentration the site was occupied by an Fe^{2+} ion. For the lattice sizes used the concentration of sites occupied in this way was always very close to the preset concentration. Further, the 'randomness' of the occupation was tested by determining the distribution of the number of nearest neighbour sites to an occupied site that were occupied, from the generated lattice. For an infinite lattice of randomly occupied sites this should be a binomial distribution given by:

$$p(n) = \binom{6}{n} x^n (1 - x)^{6-n} \qquad (4.4.1)$$

where n is the number of sites occupied, p(n) is the probability of occupation and x is the concentration of Fe^{2+} ions. The distributions obtained from the generated lattices were in agreement with this distribution for the values of N quoted above and concentrations $x > 0.55$ to better than 5%.

As mentioned previously, linearised equations of motion do not accurately calculate the excitation spectra of small clusters of spins. Therefore, in the calculations for $Fe_xMg_{1-x}Cl_2$ and $Fe_xMn_{1-x}Cl_2$ isolated clusters of spins were eliminated and only the excitation spectra of spins in the "infinite cluster" were calculated. The method for eliminating clusters or rather for identifying the infinite cluster was a very simple algorithm, and

uses the fact that only the infinite cluster can touch all four sides of the lattice. If an occupied site on one side of the lattice is initially labelled and an iterative scheme of labelling sites if their nearest neighbours are labelled is employed then only when the initial site is in the infinite cluster can sites on the other three sides of the lattice become labelled. Therefore sequentially the occupied sites on one side of the lattice were tested to see if they belonged to the infinite cluster. Once a site in the infinite cluster was found,the labelling scheme was carried out exhaustively until all the sites in the infinite cluster were labelled. Hence, it was possible to separate the infinite cluster from the clusters.

The model for $FeCl_2$ used in the calculations only assumed that the nearest neighbour exchange interaction was of any significance. Therefore, in equation (4.3.9) the summation over the index j was for nearest neighbours only. In order to identify the sites in the lattice each one was given a numerical label from 1 to N. However, rather than labelling the sites sequentially the labels were first attached to the Fe^{2+} sites so that the Fe^{2+} sites always had labels less than IFE = Nx + 1. For the $Fe_xCo_{1-x}Cl_2$ calculations the remaining sites were then labelled from IFE up to N. In labelling the sites in this way the type of each site can be identified from the value of its label. After this labelling a 'dictionary' was created of the labels of the nearest neighbours to a site. This dictionary was a two dimensional array with the labels of the nearest neighbours in the (I,J) element where I is the label of the site and J runs from 1 to 6 for the nearest neighbours. The summation over j in equation (4.3.9) was

therefore, done by using the dictionary to 'look up' the labels of the nearest neighbours. The lattice was constructed with periodic boundary conditions so that sites at one side of the lattice had nearest neighbours on the opposite side of the lattice.

The real and imaginary parts of the function $C_{i\underline{q}}(t)$ were contained in two two-dimensional arrays. These arrays had elements (I,J) in which the index I was the label of a site and the index J represented the timestep. Since at any one point in the iteration procedure only the values of $C_{i\underline{q}}(t)$ at $t - \delta t$, t and $t + \delta t$ are required, the index J only ran from one to three. In order to keep track of the position of a value for a particular timestep the index J was calculated using periodic boundary conditions. Explicitly, if the number of the timestep was M then the positions of the three values of $C_{i\underline{q}}(t)$ would have been in the elements with index J given by:

$$\begin{aligned} C_{i\underline{q}}(t - \delta t) \text{ in } J &= 1 + \text{MOD}(M - 1, 3) \\ C_{i\underline{q}}(t) \text{ in } J &= 1 + \text{MOD}(M, 3) \\ C_{i\underline{q}}(t + \delta t) \text{ in } J &= 1 + \text{MOD}(M + 1, 3) \end{aligned} \qquad (4.4.2)$$

At each timestep a new value is calculated for $C_{i\underline{q}}(t + \delta t)$ and stored in the 1 + MOD (M + 1,3) element which overwrites the value for $C_{i\underline{q}}(t - \delta t)$ from the previous timestep.

The arrays holding the real and imaginary parts of $C_{i\underline{q}}(t)$ were initialised for the first two timesteps using equations (4.3.10) and (4.3.11) respectively. Successive values for the $C_{i\underline{q}}(t)$ were therefore calculated at each timestep using equation (4.3.9) and the dictionary of nearest neighbours and stored in the elements given by equation (4.4.2). At each timestep $C_{\underline{q}}(t)$ was

calculated from equation (4.3.16). Since the wavevector $\underline{q}$ is equal to (h,0,0) all of the elements in a given horizontal row of the lattice (cf figure (4.4.1)) had the same complex exponential prefactor. Therefore it was only necessary to calculate L cosines and sines corresponding to the real and imaginary parts of the exponential prefactors for the rows. These values were calculated prior to the iteration scheme and were stored in an array, to be called when needed. The summation in equation (4.3.16) was therefore done by summing the real and imaginary parts of $C_{i\underline{q}}(t)$ along a row in the lattice, then multiplying this sum by the exponential prefactor and then summing with successive rows.

The integral for $S^{\perp}(\underline{q},\omega)$ given in equation (4.3.22) was evaluated using the trapezoidal rule for numerical integration (Stephenson (1973) p. 245). Therefore $S^{\perp}(\underline{q},\omega)$ was stored in an array whose elements corresponded to discrete values of ω. At each timestep the values of $\mathrm{Sin}(\omega t)e^{-\lambda t^2}\ \mathrm{Im}C_{\underline{q}}(t)$ were evaluated for the various values of ω and then added to the respective elements of the array holding $S^{\perp}(\underline{q},\omega)$.

4.5 Results of Simulations for $Fe_xMg_{1-x}Cl_2$

In this section the results of the simulations of $S^{\perp}(\underline{q},\omega)$ for diluted $FeCl_2$ are presented. The values used for the exchange interaction and single ion anisotropy in this simulation were those of Birgeneau et al (1972) given in table (4.2.1). A value of λ = 0.075 (rads. THz)^2 was used in the Gaussian damping factor in equation (4.3.15) which gave an energy resolution corresponding to a full width at half maximum of 0.6 meV. Since the possible frequencies in the model of $FeCl_2$ are less than 8 meV this was chosen

as the value of E_{max}. The parameter n(cf equation (4.3.12) was chosen to be 30 and the iteration procedure was carried out for 300 time-steps. This meant that the noise term $S^{\perp}(q, \omega)$ was less than 1%. Numerical values of $S^{\perp}(\underline{q}, \omega)$ were calculated for five wavevectors in the (h,0,0) direction with values of h= 0.000, 0.125, 0.250, 0.375 and 0.500, and for energies in the range 0.1 to 8.0 meV at intervals of 0.1 meV.

The effect of site disorder on $S^{\perp}(\underline{q}, \omega)$ is greatest at the zone boundary wavevector $\underline{q}_{zB}$ = (0.5, 0, 0). Consequently in figures (4.5.1a - e) the calculated $S^{\perp}(\underline{q}_{zB}, \omega)$ are shown for various concentrations. Figure (4.5.1a) shows the zone boundary spin wave calculated by the E.O.M. method for x = 1.0, which is, as expected, a "resolution limited" Gaussian lineshape with a full width at half maximum of 0.6 meV. The "intensity" scale in figures (4.5.1a - e) is in arbitrary units. However, the relative scale of these figures is such that they all have the same integrated intensity as in figure (4.5.1a). In figure (4.5.1b) $S^{\perp}(\underline{q}_{zB}, \omega)$ for x = 0.80 is shown. The most striking effect shown in this figure is the large decrease in the peak intensity, by a factor of $\sim$ 3 from the peak intensity in the x = 1.0 simulation. The peak intensity has also been shifted down in energy from the x = 1.0 simulation by about 0.5 meV. Also, the peak is much broader than the x = 1.0 result by a factor of $\sim$ 3 at the full width at half maximum. Further to this, the lineshape has a tail extending down through the band of spin wave energies which appears to contain some structure. In figure (4.5.1c) $S^{\perp}(\underline{q}_{zB}, \omega)$ for x = 0.70 is shown, and shows the further development of the features noted for figure (4.5.1b). The peak intensity has fallen further, both in intensity and energy, and there is an increased intensity for energies

Figures (4.5.1a - e)

These figures show the zone boundary lineshape computed for $S^{\perp}(\underline{q}, \omega)$ computed for various concentrations from x = 1.0 to 0.55.

FIGURE(4.5.1a)

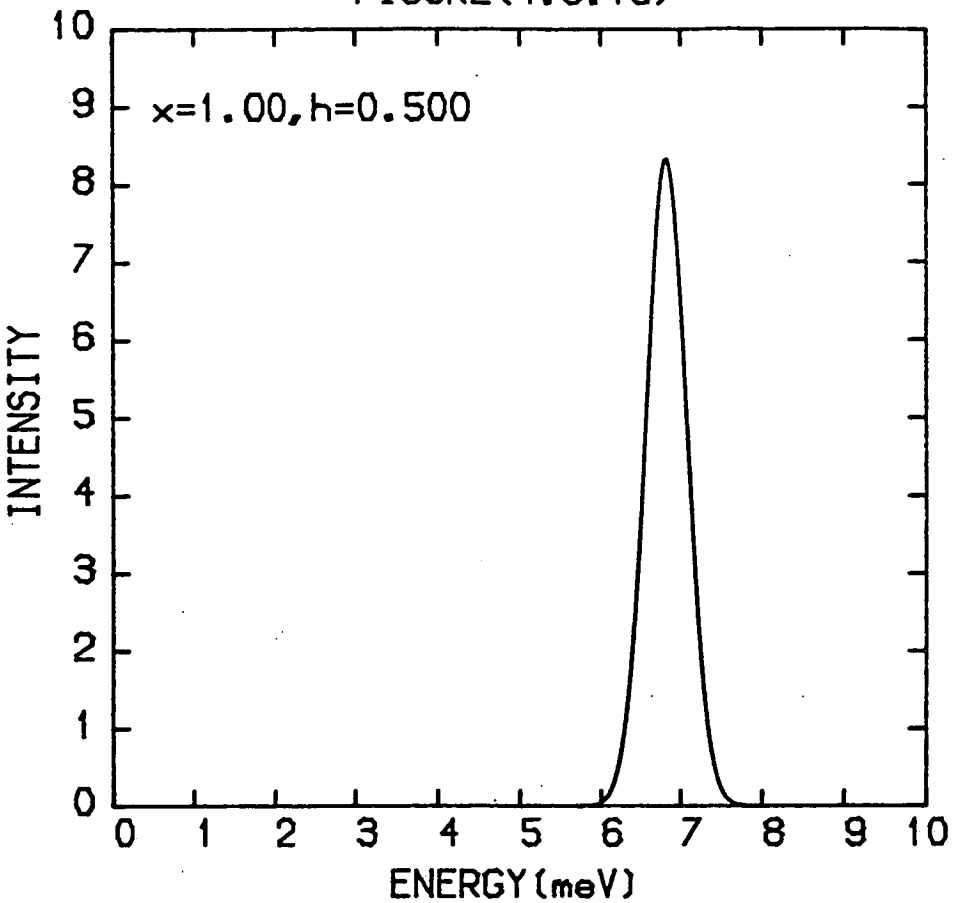

FIGURE(4.5.1b)

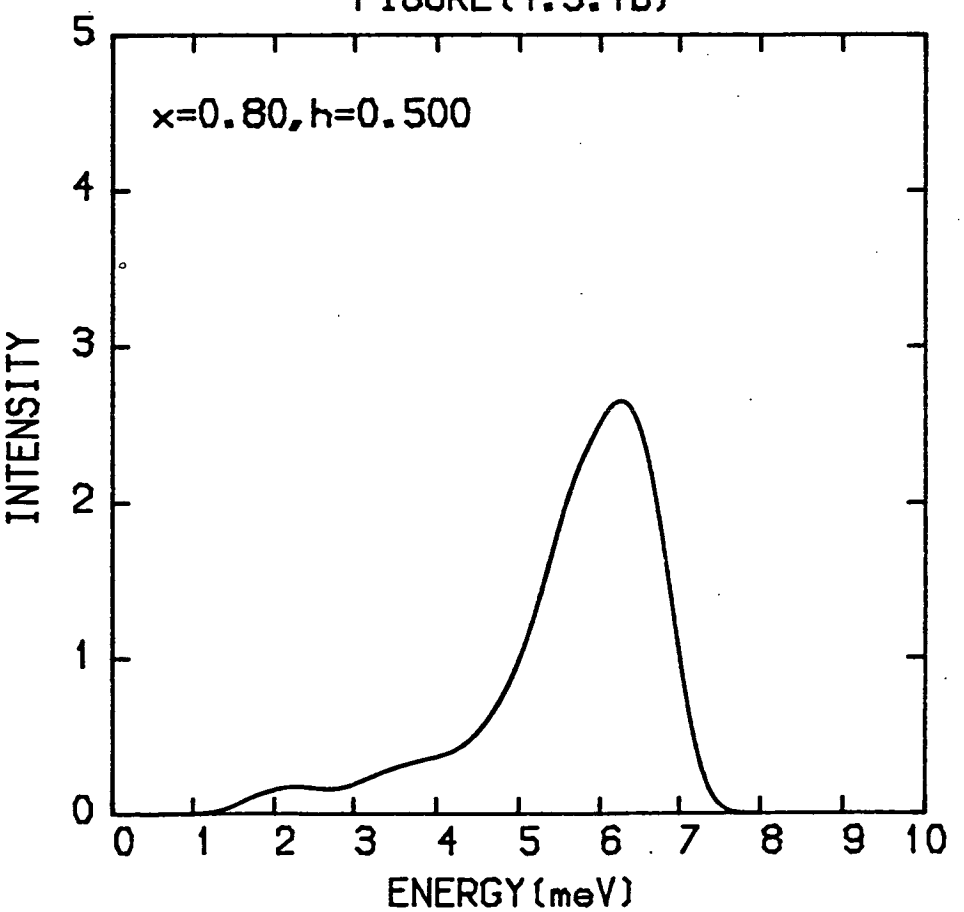

FIGURE(4.5.1c)

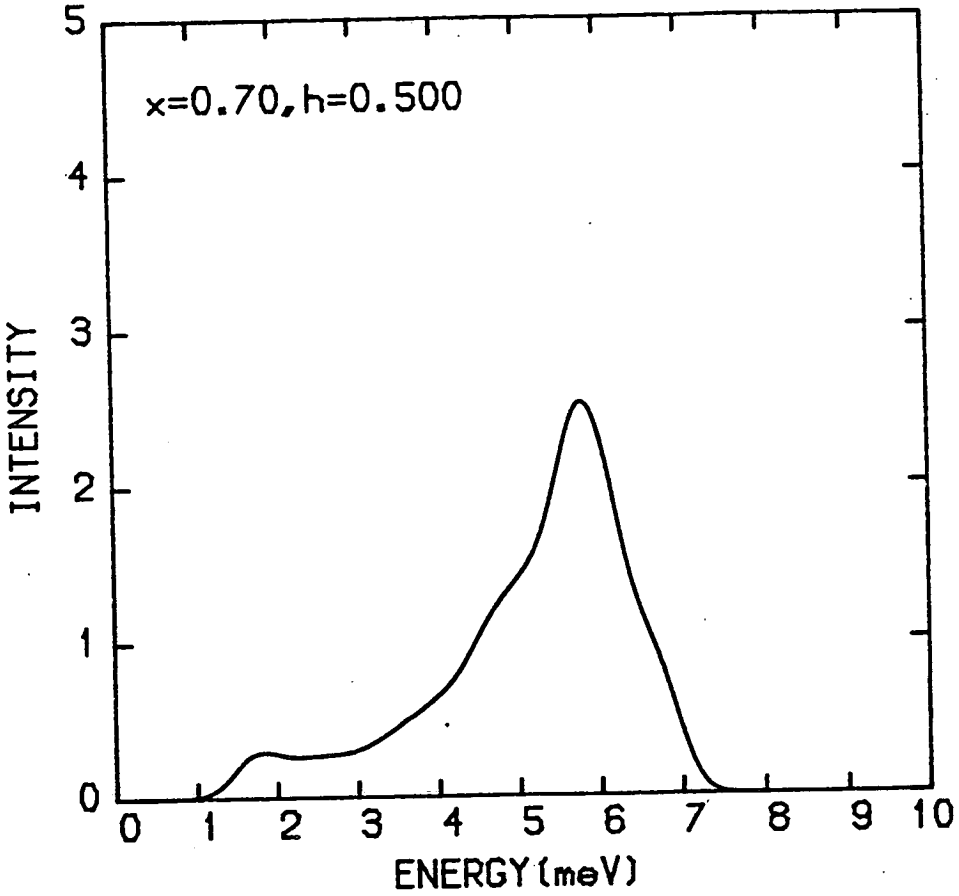

FIGURE(4.5.1d)

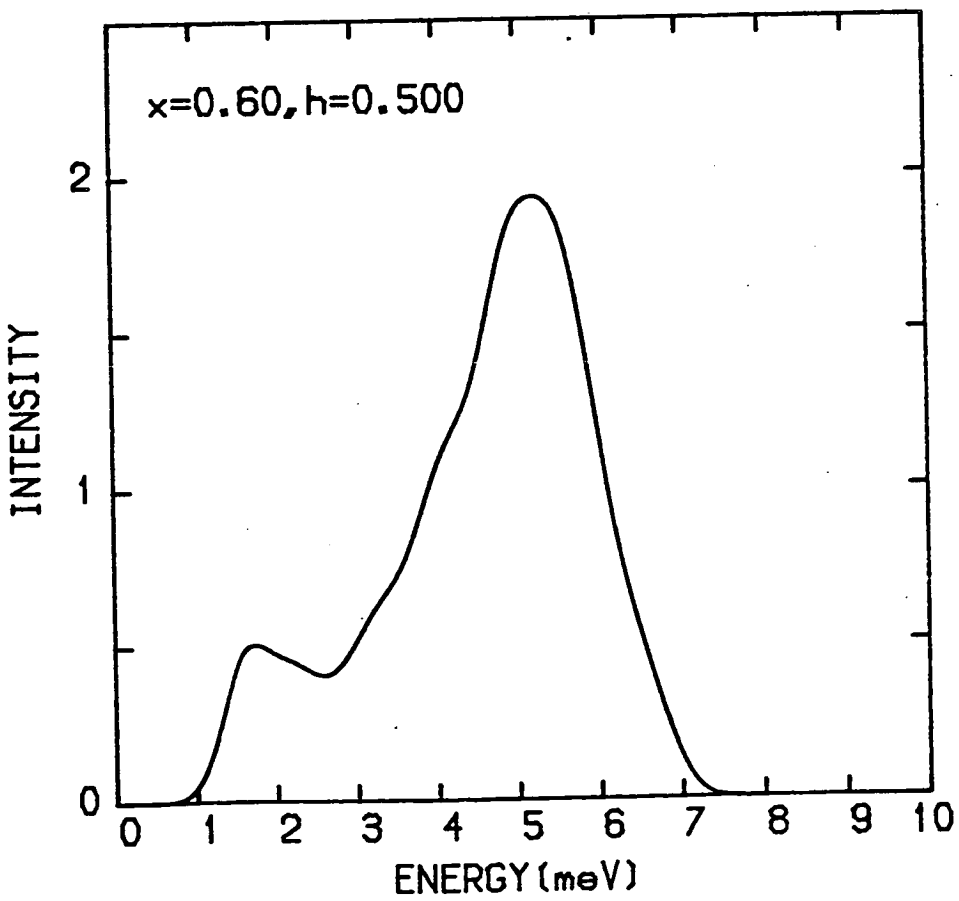

FIGURE(4.5.1e)

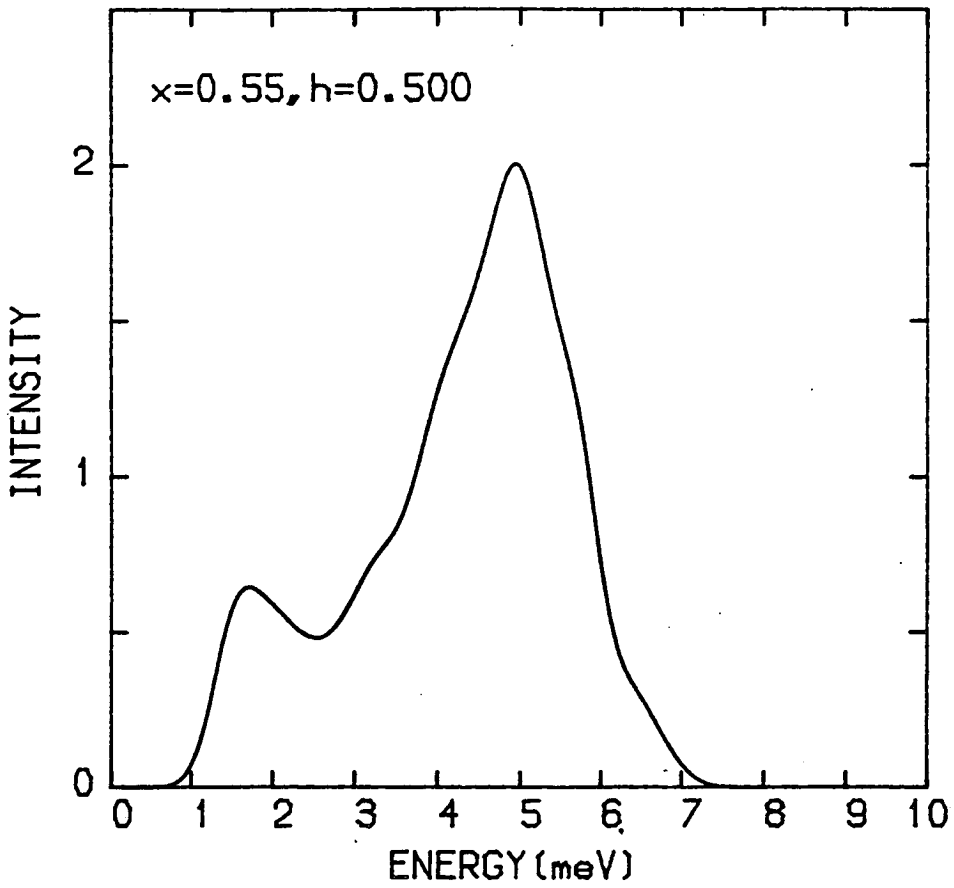

at the lower edge of the spin wave band. Further to this, the peak has broadened and is now clearly showing the existence of structure in its lineshape. Figure (4.5.1d) shows $S^{\perp}(q_{ZB}, \omega)$ for x = 0.60. The shift in intensity to lower energies has continued and has led to the interesting feature of a second peak at an energy just less than 2.0 MeV. This energy is lower than the bottom of the spin wave band for x = 1.0. Finally, in figure (4.5.1e) $S^{\perp}(\underline{q}_{ZB}, \omega)$ for x = 0.55 is shown. In this figure the peak at low energy is now more clearly resolved and the peak at higher energy shows the existence of some structure. The peak intensity has now fallen to 5.0 meV which is 1.74 meV lower than the x = 1.0 energy. The percolation threshold for a two dimensional triangular lattice is x = 0.5 and therefore simulations were not performed for lower concentrations.

In figures (4.5.2a - d) the lineshapes for $S^{\perp}(\underline{q}, \omega)$ for the concentration x = 0.55 are shown at other points across the Brillouin zone in the (h,0,0) direction. The lineshape of $S^{\perp}(\underline{q},\omega)$ at the zone centre, shown in figure (4.5.2a), has essentially remained a resolution limited Gaussian. A small tail which extends into the higher energies in the band has arisen and consequently the peak intensity is slightly lower than in figure (4.5.1a). The energy of the peak has fallen from the x = 1.0 zone centre energy of 2.04 meV to 1.55 meV. In figure (4.5.2b) the lineshape of $S^{\perp}(\underline{q}, \omega)$ at h = 0.125 is shown. The effect on $S^{\perp}(\underline{q}, \omega)$ of moving away from the zone centre is to reduce the peak intensity and to increase the intensity in the tail to higher energies. The lineshape of $S^{\perp}(\underline{q}, \omega)$ half way across the zone, at h = 0.250 is shown in figure (4.5.2c). The peak intensity has fallen further and the

Figures (4.5.2a - d)

These figures indicate the lineshape of $S^{\perp}(q, \omega)$ for a concentration x = 0.55 at wavevectors $\underline{q}$ = (h,0,0) where h = 0.000, 0.125, 0.250 and 0.375.

FIGURE(4.5.2a)

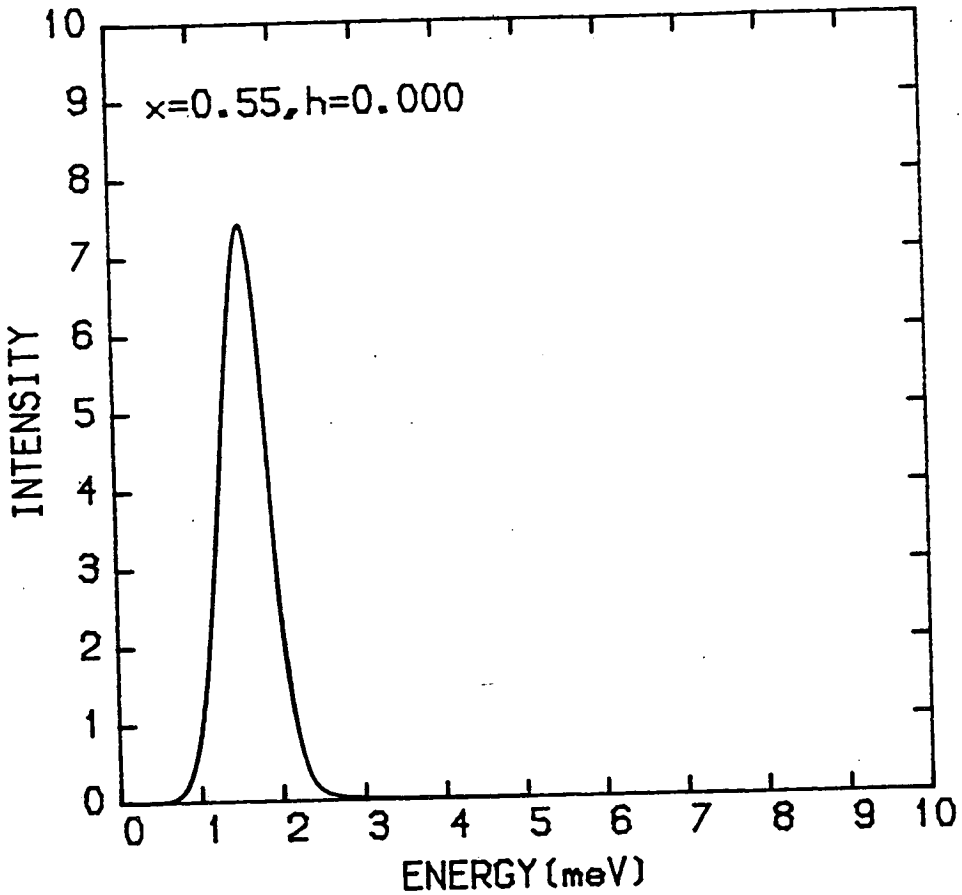

FIGURE(4.5.2b)

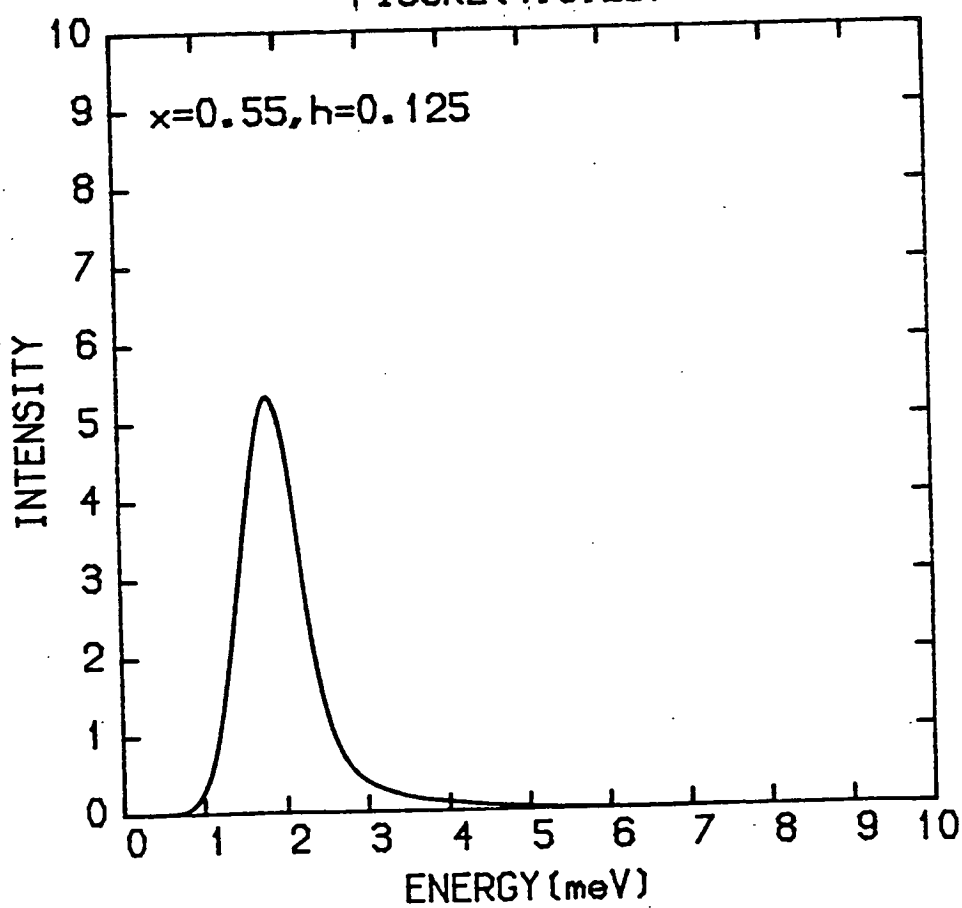

FIGURE(4.5.2c)

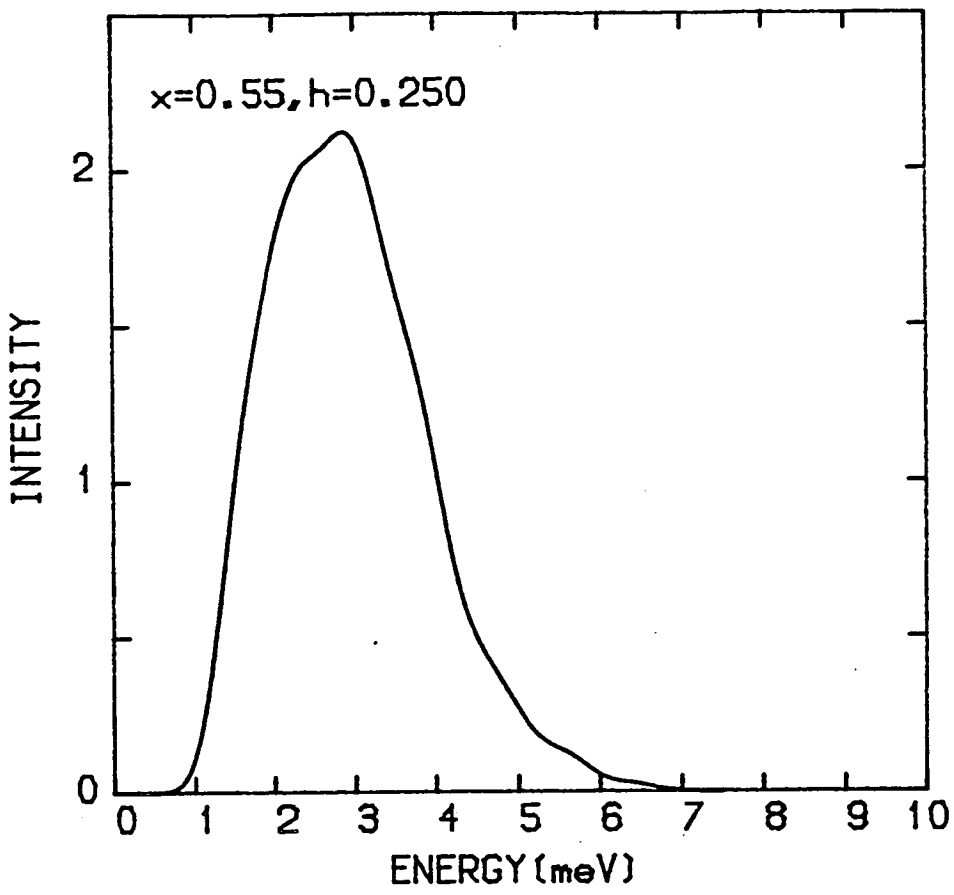

FIGURE(4.5.2d)

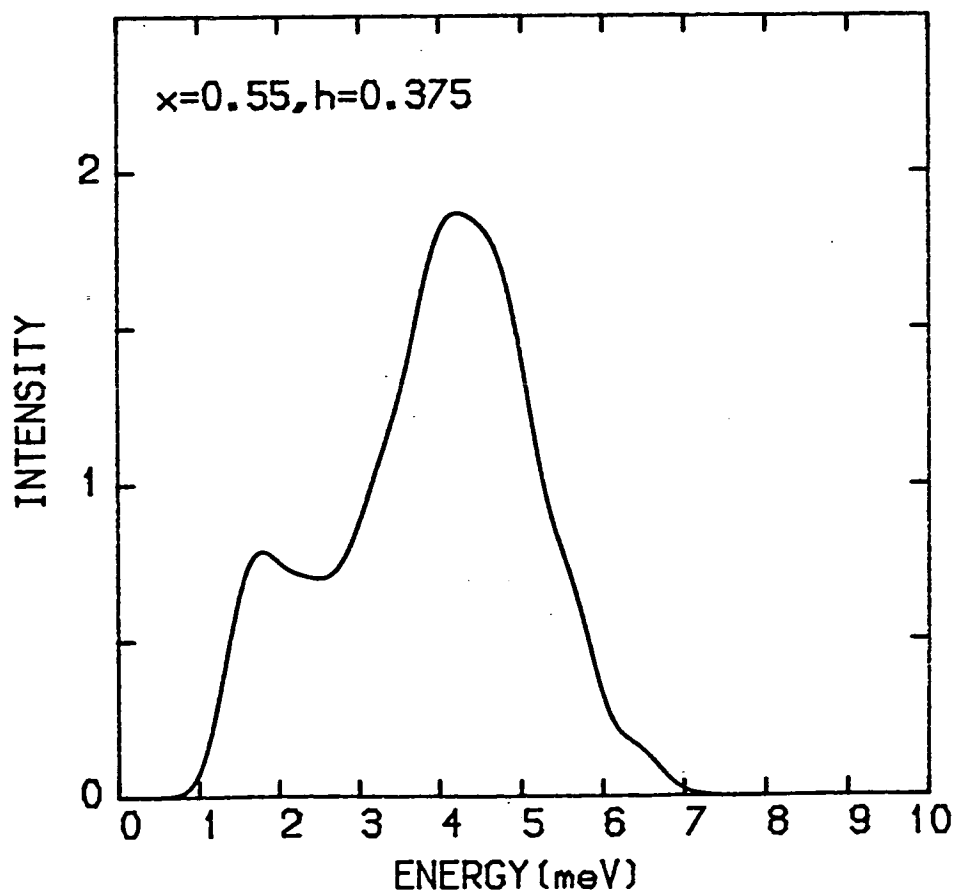

lineshape shows signs of structure, with a width that is much greater than the resolution limit of 0.6 meV. In figure (4.5.2d) the lineshape of $S^{\perp}(\underline{q},\omega)$ at h = 0.375 is shown. The lineshape now clearly shows the double peak structure of the zone boundary lineshape.

In figure (4.5.3) the variation with concentration of the energies of the peak intensities at the zone centre and zone boundary are shown. The zone centre energy (lower points in figure (4.5.3)) falls linearly with concentration. The solid line through these points is the V.C.A. result for the zone centre energy which is:

$$E(\underline{q} = 0,x) = 2D(S - \tfrac{1}{2}) + 2(I - J)\left[6(1 - x)\right] \qquad (4.5.1)$$

Since the $\underline{q}$ = 0 mode corresponds to a uniform excitation of all the spins it is not surprising that the excitation energy is fairly well described by the V.C.A. The energy of the peak intensity at the zone boundary (upper points in figure (4.5.3)) however does not follow the V.C.A. as a function of concentration. The V.C.A. result for the energy of the zone boundary spin wave is shown in figure (4.5.3) by the dotted line while the solid line is a guide to the eye.

Unfortunately there is no experimental data available on the spin wave spectrum of diluted $FeCl_2$. As a consequence of this no further analysis of the calculations has been performed and no new calculations carried out.

Figure (4.5.3)

This figure shows the variation with concentration of the peak intensities in $S^{\perp}(\underline{q}, \omega)$ at the zone centre (lower points) and zone boundary (upper points). The solid line through the lower points and the dotted line are the V.C.A. predictions for the concentration dependence of these energies. The solid line through the upper points is a guide to the eye.

FIGURE(4.5.3)

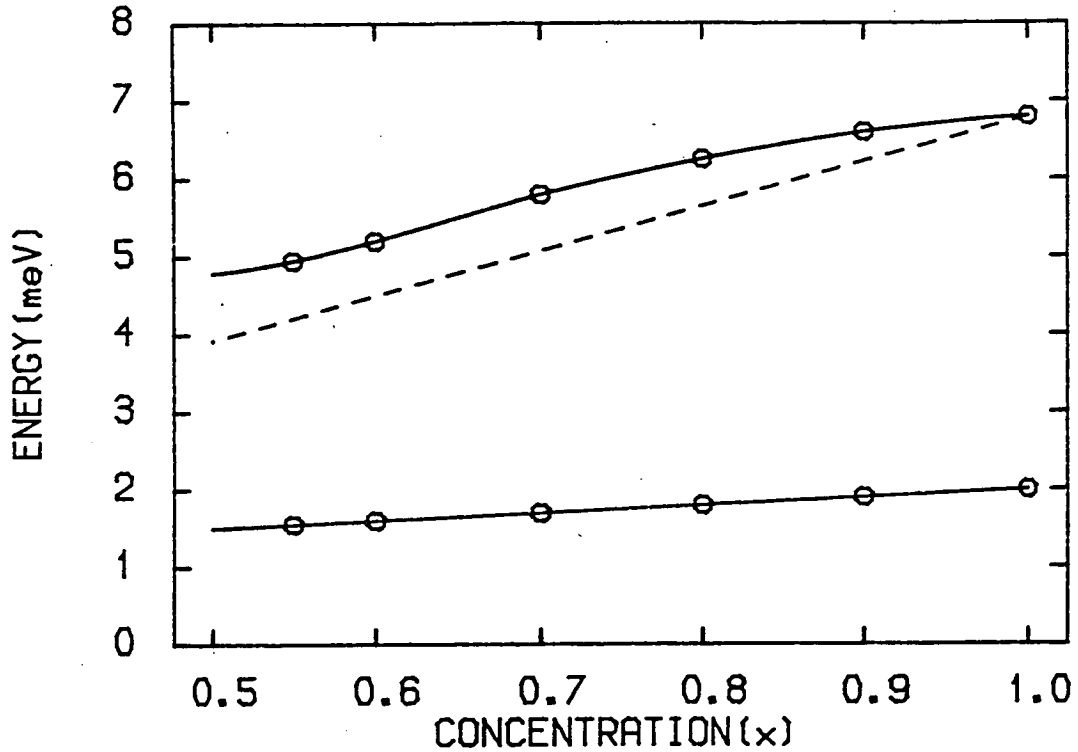

4.6 Results for $Fe_xMn_{1-x}Cl_2$

Although experimental measurements of $S^+(\underline{q}, \omega)$ are not available for dilute $FeCl_2$, there are some experimental measurements in the literature for $Fe_xMn_{1-x}Cl_2$. These measurements were performed by Bertrand et al (1981) using inelastic neutron scattering techniques on samples of $Fe_{0.91}Mn_{0.09}Cl_2$ and $Fe_{0.75}Mn_{0.25}Cl_2$. Since the Mn^{2+} ion has a magnetic moment $Fe_xMn_{1-x}Cl_2$ is a mixed compound rather than dilute. However, $MnCl_2$ only has a Néel temperature of $\sim$ 2 K (Bertrand et al (1981)) and therefore the exchange between Mn^{2+} - Mn^{2+} ions can be estimated from the Néel temperatures to only be $\sim$ 0.013 times that of the Fe^{2+} - Fe^{2+} exchange in $FeCl_2$. The exchange interaction between the Fe^{2+} and Mn^{2+} ions in $Fe_xMn_{1-x}Cl_2$ has been determined by Tuchendler et al (1980) from AFMR measurements to be:

$$I_{Fe,Mn} = 0.019 \text{ meV}, \quad J_{Fe,Mn} = 0.017 \text{ meV} \tag{4.6.1}$$

The excitation spectrum of $Fe_xMn_{1-x}Cl_2$ is therefore expected to be dominated by the Fe^{2+} ions. A complication that arises on the introduction of the Mn^{2+} ions into the lattice is that the strength of single ion crystal field term D_i for the Fe^{2+} ions changes. This presumably arises due to the change in the lattice parameter from $FeCl_2$ to $Fe_xMn_{1-x}Cl_2$. The evidence for such a change is that the energy of the zone centre spin wave falls more rapidly with decreasing concentration of Fe^{2+} ions than the (1 - x) dependence expected. In the simulation to be discussed below the single ion energy for the Fe^{2+} ion has been determined by fitting the experimentally observed energy for the zone centre spin wave to the formula:

$$E(\underline{q} = 0) = 2\tilde{D}(S - \tfrac{1}{2}) + 6x(I_{FF} - J_{FF})S_F + 6(1 - x)(I_{FM} - J_{FM}\sqrt{\frac{S_M}{S_F}})S_F \qquad (4.6.2)$$

where labels F and M refer to Fe^{2+} and Mn^{2+} ions respectively, and the exchange energies I and J are the values for pure $FeCl_2$ and those given in equation (4.6.1). For x = 0.75 $\tilde{D}$ was found to be 0.20 meV, a considerable change from the 1.043 meV for $FeCl_2$. This change in the crystal field will also affect the value of $g^{\perp}$ for the Fe^{2+} ions. However, since the effect of the change in crystal field has not been included in the proportionality factors between real and pseudo spins, it was also neglected for $g^{\perp}$ and the value for pure $FeCl_2$ used. Since the Mn^{2+} ion is a ^5S state the value of $g^{\perp}$ is 2.

A calculation of $S^{\perp}(q, \omega)$ for $Fe_{0.75}Mn_{0.25}Cl_2$ was performed using the methods described previously and the parameters described above. The exchange interaction between the Mn^{2+} - Mn^{2+} ions was set equal to zero in the calculation since it is so much smaller than the other interactions. A model of $Fe_xMn_{1-x}Cl_2$ was constructed in the computer by generating a lattice as for the dilute $FeCl_2$ case and labelling those dilutant sites which were nearest neighbours of occupied sites. The infinite cluster was then found as before and isolated Fe^{2+} and Mn^{2+} ion sites discarded. In figures (4.6.1a - e) $S^{\perp}(q, \omega)$ is shown for wavevectors across the Brillouin zone in the (h,0,0) direction. A comparison with the results calculated for dilute $FeCl_2$ for concentrations x = 0.70 and 0.80 shows that there is a marked increase in intensities at the lower edge of the spin wave band in $Fe_xMn_{1-x}Cl_2$. The peak at very low energy is a localised mode on the Mn^{2+} ions.

Figures (4.6.1a - e)

These figures show the computed lineshape of $S^{+}(\underline{q}, \omega)$ for $Fe_xMn_{1-x}C\ell_2$ with x = 0.75 at wave-vectors $\underline{q}$ = (h,0,0) where h = 0.000, 0.125, 0.250, 0.375 and 0.500.

Figure (4.6.2)

This figure shows the dispersion relations for the peak intensities in figures (4.6.1a - e) (circles and triangles) and the measured peak intensities of Bertrand et al (1981) (squares). The solid lines are guides to the eye.

FIGURE(4.6.1a)

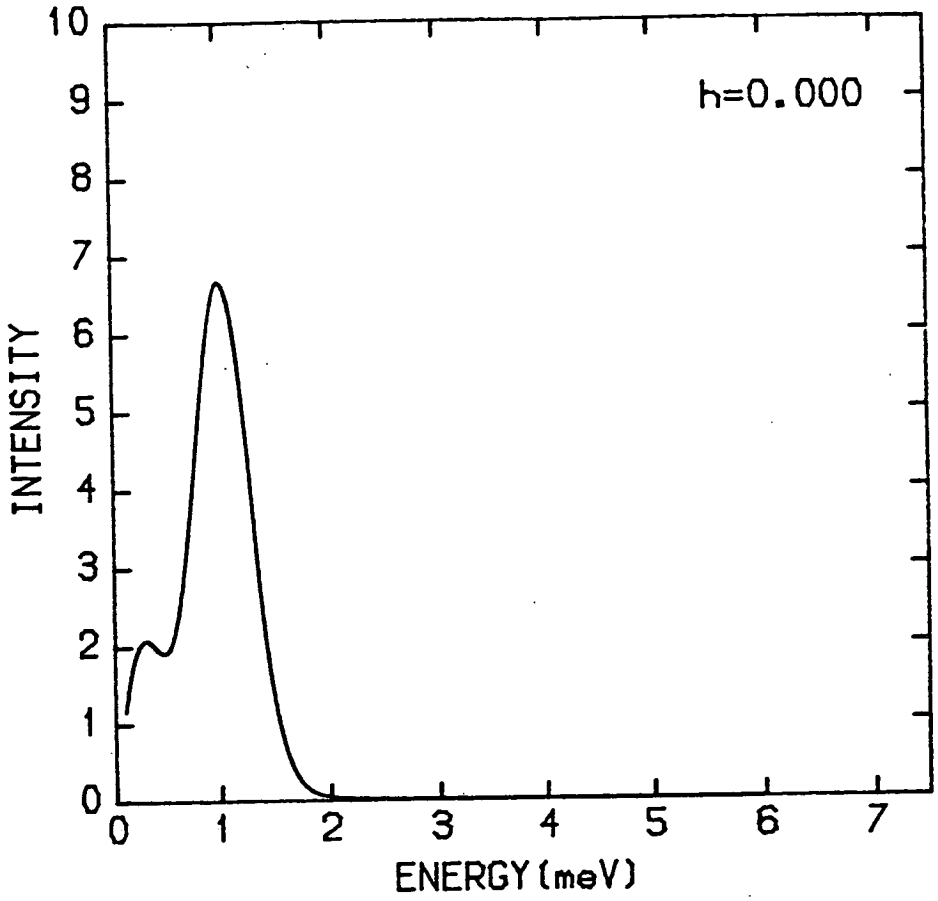

FIGURE(4.6.1b)

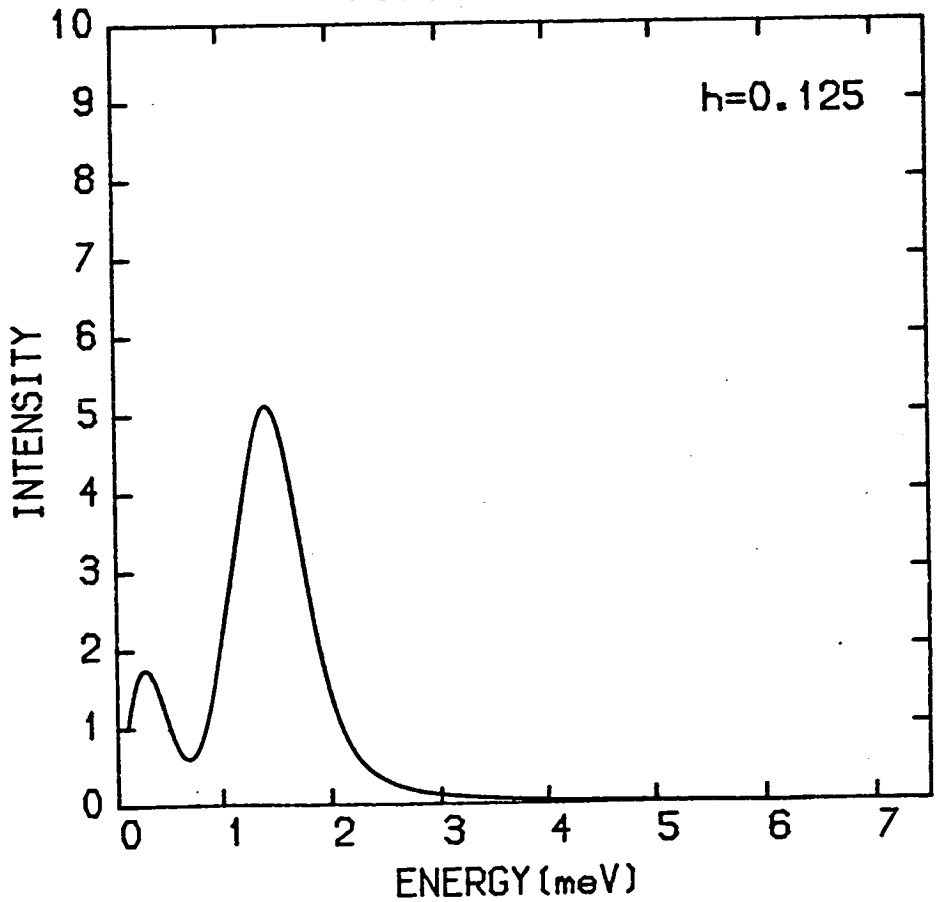

FIGURE(4.6.1c)

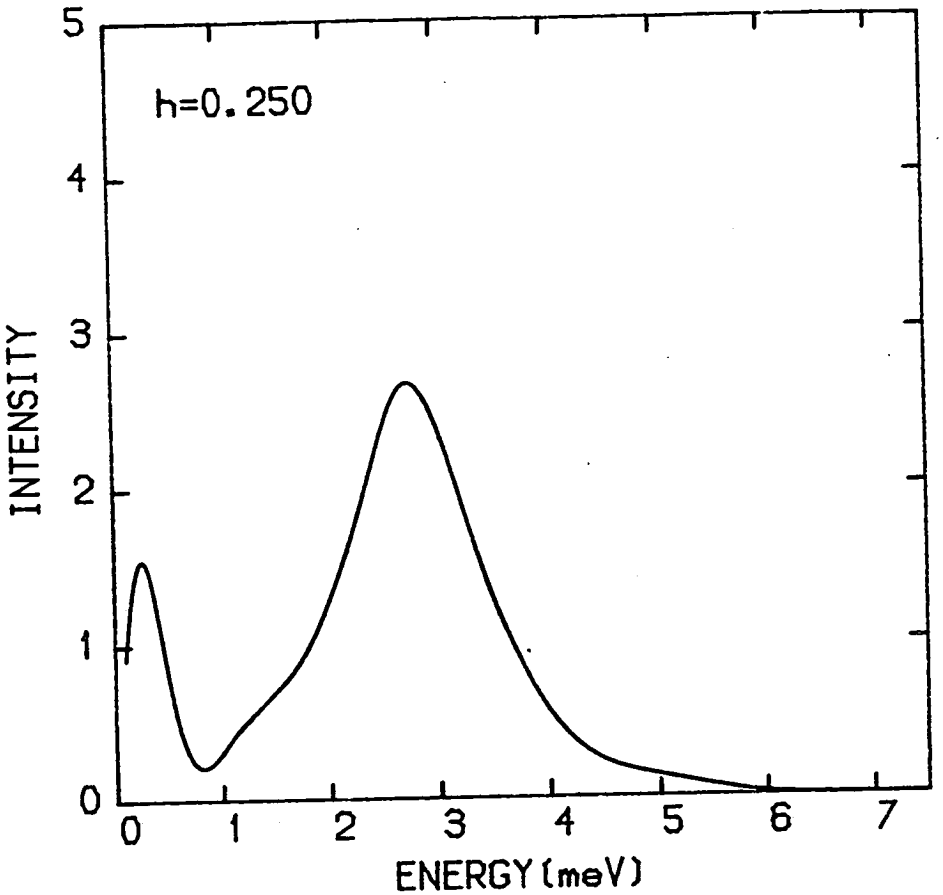

FIGURE(4.6.1d)

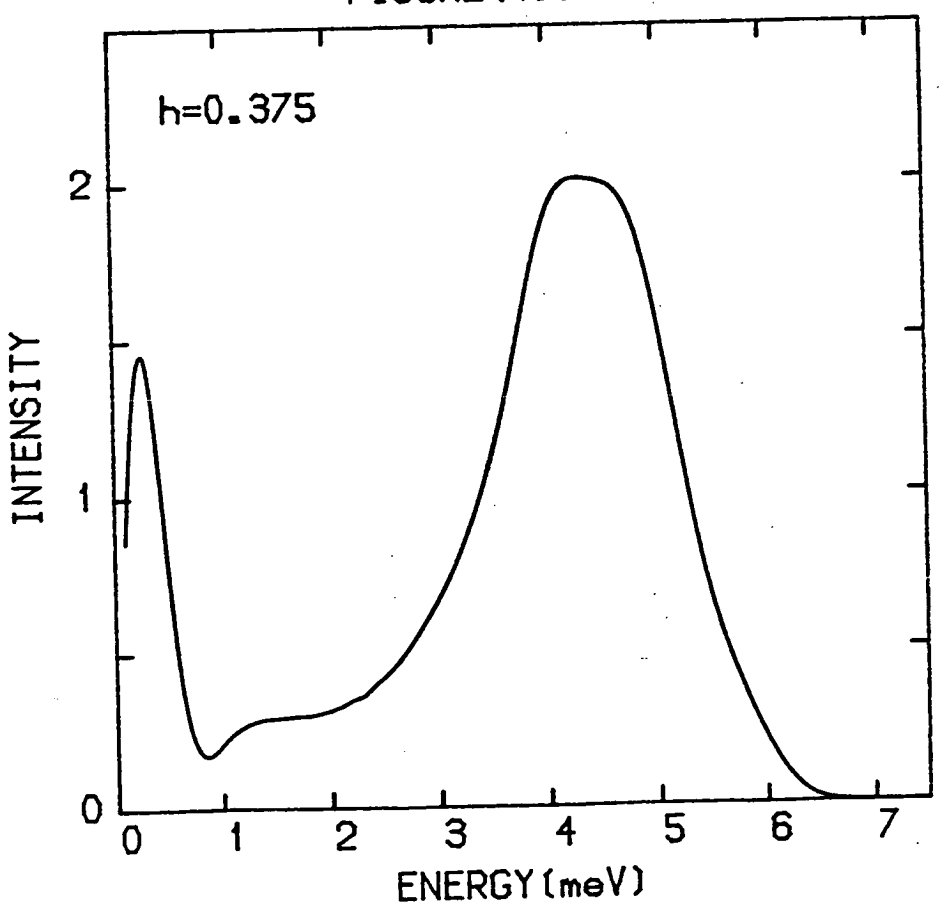

FIGURE(4.6.1e)

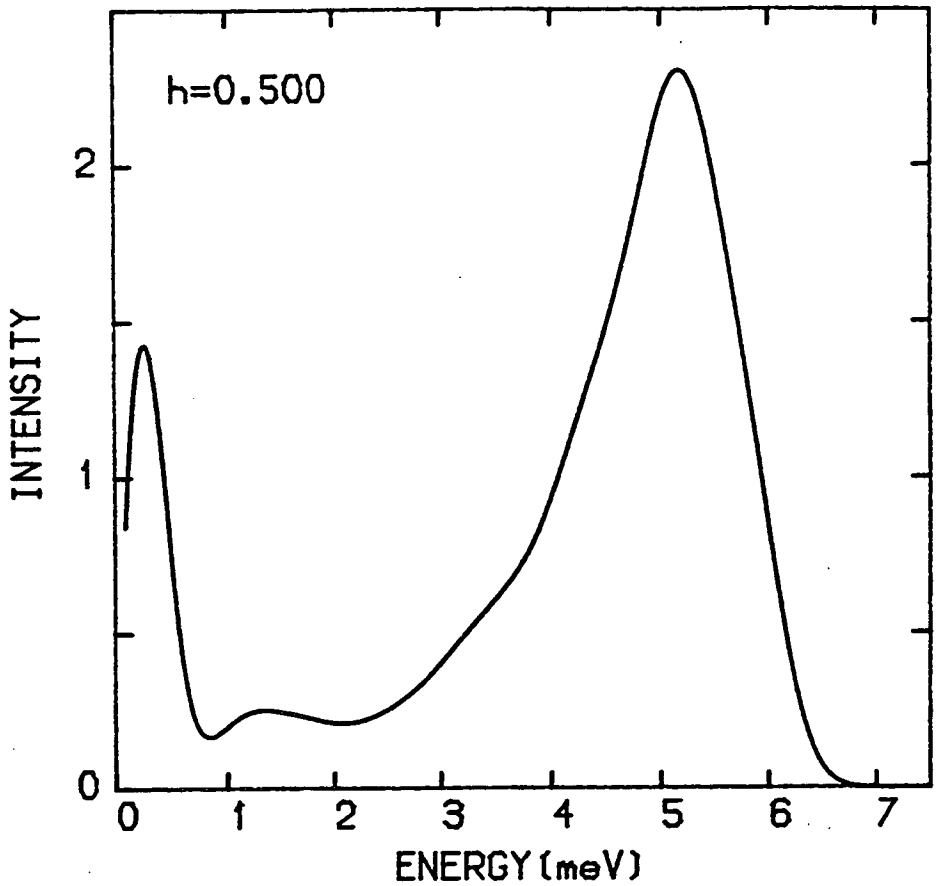

FIGURE(4.6.2)

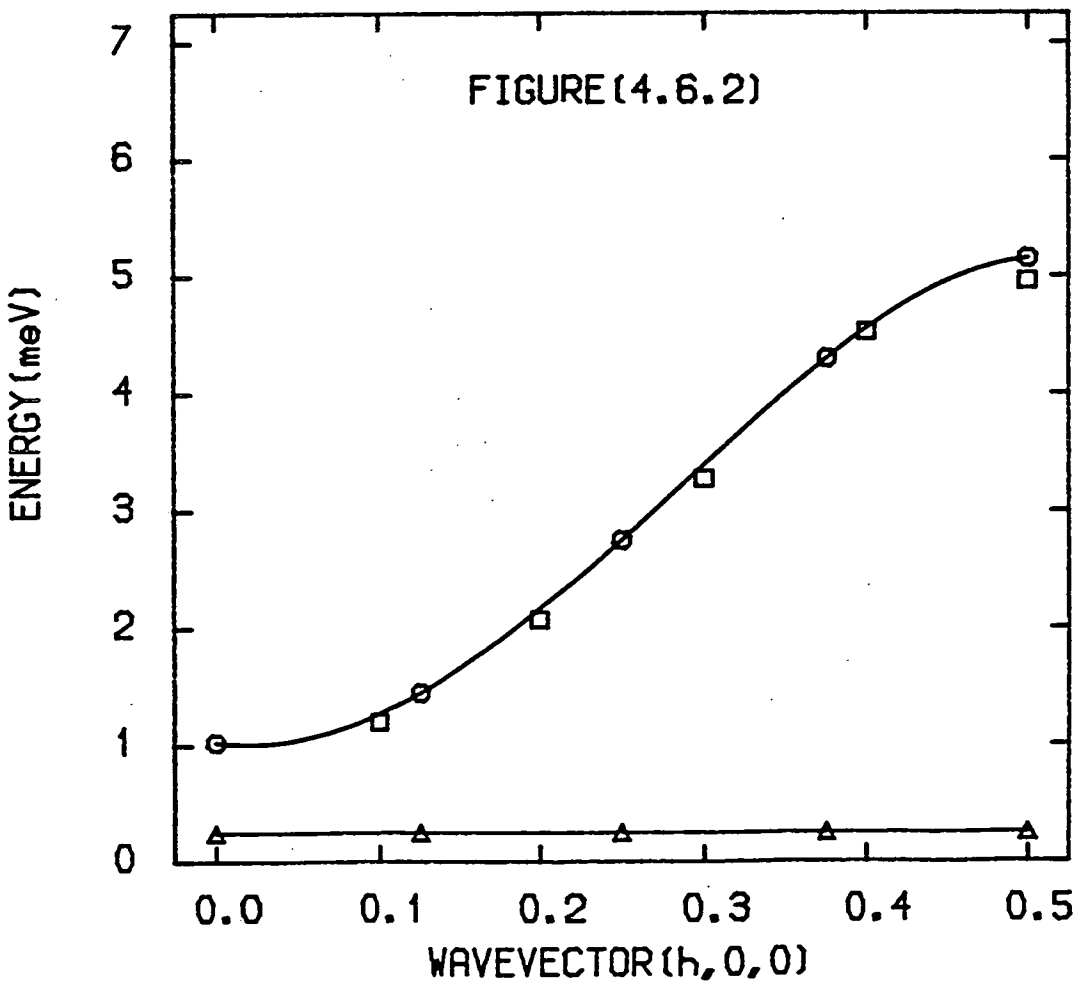

Unfortunately it is not possible to compare the lineshapes calculated with the results of Bertrand et al since the published paper did not contain detailed lineshapes or a value for the energy resolution of their spectrometer. However, this paper did contain a dispersion curve for the peak intensity in the lineshape. In figure (4.6.2) the positions of the measured peak intensities are indicated by squares and the calculated peak positions by circles. The solid line is a guide to the eye found by making a cubic interpolation through the calculated values. At the zone centre where the experimental and calculated values overlap only the calculated value has been plotted. The agreement between the calculated and measured dispersion curves is quite good.

CHAPTER FIVE

Spin Waves in the Random Anisotropy System $Fe_xCo_{1-x}Cl_2$

5.1 Introduction

In this chapter the results of computer simulations of, and inelastic neutron scattering measurements of the spin wave spectrum of a sample of $Fe_{0.85}Co_{0.15}Cl_2$ are presented. $Fe_xCo_{1-x}Cl_2$ is an example of a magnetic system which has random competing anisotropies. As discussed in section (2) of the previous chapter $FeCl_2$ is a layered antiferromagnet in which the ordered state of the spins is parallel to the c-axis. $COCl_2$ is also a layered antiferromagnet but one in which by contrast the spins in the ordered state point along the (1,2,0) direction in the hexagonal a - b plane.

The magnetic ordering of systems with random orthogonal anisotropies has been studied theoretically by a number of authors using different techniques. These theoretical studies have considered the properties of a Hamiltonian of the form:

$$\mathcal{H} = -\sum_{ij} I_{ij} S_i^z S_j^z + J_{ij}(S_i^x S_j^x + S_i^y S_j^y) \qquad (5.1.1)$$

where the sites i and j are randomly occupied by two species of magnetic ion of types A and B and where the exchange interactions satisfy the inequalities:

$$I_{AA} > J_{AA} \quad \text{and} \quad I_{BB} < J_{BB} \qquad (5.1.2)$$

The pure A material has uniaxial ordering and the pure B material has planar ordering. The exchange interactions I_{AB} and J_{AB} are non-zero so that the two species interact in the mixed system.

The phase diagram for the system described by the Hamiltonian in equation (5.1.1) is shown in figure (5.1.1). The form of the phase diagram has been studied by molecular field theory (Matsubara and Inawashiro (1977)), renormalisation group techniques (Fishman and Aharony (1978)) and Monte Carlo simulation (Inawashiro et al (1979)). These different techniques have all shown the existence of four phases all separated by second order continuous phase transitions whose phase lines meet at a tetracritical point. There are three ordered phases at low temperature. At the two ends of the concentration range there are phases in which only the spin components corresponding to the ordered components of the end members are ordered. In between these two phases however, there is a third phase in which the spins are arranged in such a way that both uniaxial and planar components of the spins are ordered. This phase has been termed the mixed phase (Fishman and Aharony (1978)).

The magnetic ordering of a number of materials which are believed to be examples of random anisotropy systems have been studied experimentally. A review of some of these studies is given in the article of Katsumata (1982). However, the material that has received the most comprehensive study of its magnetic ordering is $Fe_xCo_{1-x}Cl_2$ (Wong et al 1980, 1983). In section (2) the results of this work will be briefly reviewed.

It is, however, the low temperature spin wave spectrum of $Fe_xCO_{1-x}Cl_2$ that is of interest in this chapter. The effect of a random anisotropy adds a new problem to calculating the spin wave

Figure (5.1.1)

This figure shows the theoretical form for the phase diagram of a random anisotropy system.

FIGURE(5.1.1)

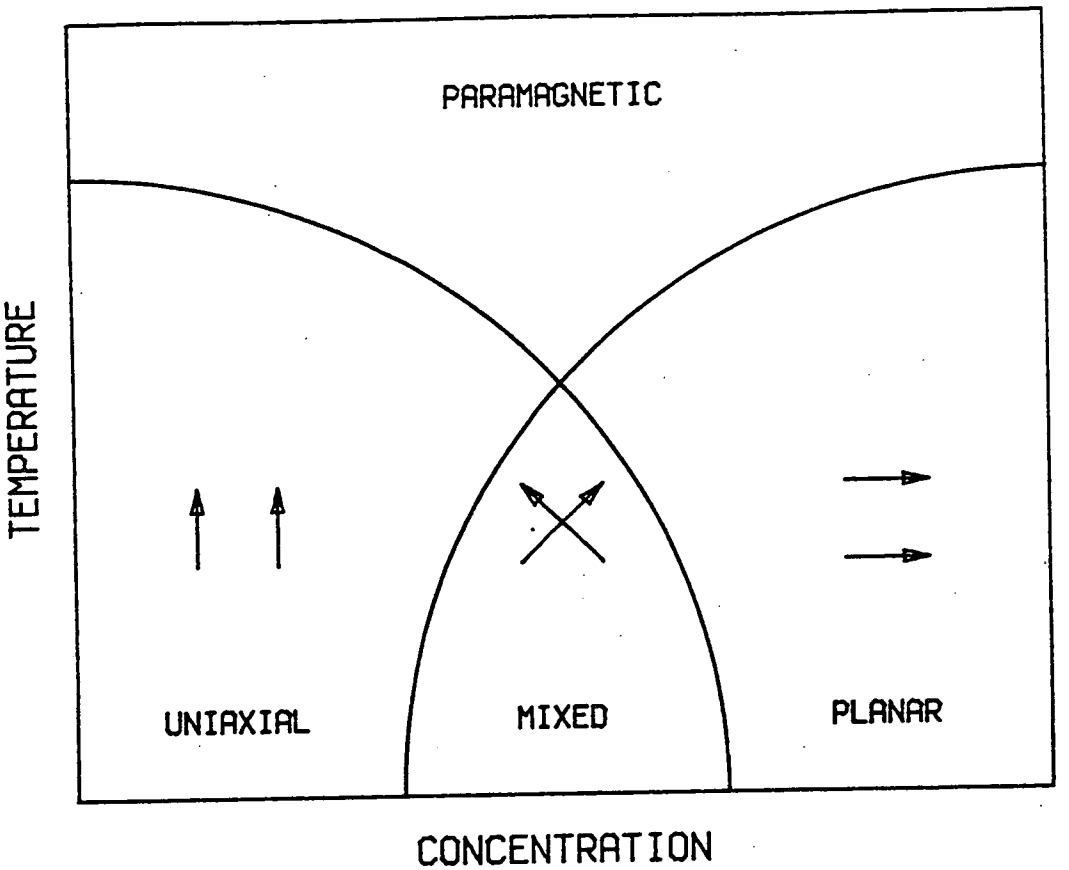
PARAMAGNETIC
TEMPERATURE
UNIAXIAL
MIXED
PLANAR
CONCENTRATION

spectrum of a mixed magnet, that of knowing the ground state of the system. As mentioned at the beginning of this section, in this chapter the results of inelastic neutron scattering measurements of the spin wave spectrum of a sample of $Fe_{0.85}Co_{0.15}Cl_2$ are presented. These results are compared with the results of an E.O.M. method calculation of the spin wave spectrum for a particular model of the ground state. Therefore the rest of this chapter is set out as follows. In section (2) the properties of $CoCl_2$ and the experimentally observed properties of the magnetic ordering in $Fe_xCo_{1-x}Cl_2$ are described. Also in this section, a discussion of the theoretical results for the ground state in the different phases is given. The model for the computer simulations is given in section (3). A description of the experimental arrangement of the spectrometer used for the inelastic neutron scattering measurements is contained in section (4). The results of the computer simulation and neutron scattering measurements are presented together in section (5) for comparison. A discussion of these results is given in section (6).

5.2 Properties of $CoCl_2$ and $Fe_xCo_{1-x}Cl_2$

This section is divided into three subsections. In the first the properties of $CoCl_2$ and its spin wave spectrum are described. The second subsection contains a brief description of the ordering properties of $Fe_xCo_{1-x}Cl_2$ known from experimental measurements. Finally, the third subsection contains a brief discussion of the theoretical models considered for the ordering in the zero temperature ground state of $Fe_xCo_{1-x}Cl_2$.

5.2 i) Properties of $CoCl_2$

$CoCl_2$ has the same rhombohedral $CdCl_2$ crystal structure (Wyckoff (1963) p. 272) as $FeCl_2$ and also like $FeCl_2$ is a layered antiferromagnet. Therefore $CoCl_2$ has the same hexagonal antiferromagnetic unit cell as $FeCl_2$ with lattice parameters a = 3.553 A and c = 34.718 A. However, unlike $FeCl_2$ the spins in $CoCl_2$ order along the (1,2,0) crystallographic direction (Wilkinson et al (1959)) below a Néel temperature of 24.9 K (Hutchings (1973)).

The Co^{2+} free ion has a ^4F ground state. Since $CoCl_2$ is structurally isomorphous to $FeCl_2$, the crystal field has the same symmetry as in $FeCl_2$. The strong cubic crystal field splits the ^4F level and makes a $^4T_{1g}$ triplet the lowest level. This triplet can be treated as an effective $\ell = 1$ level, i.e. a ^4P state, if the matrix elements of the total orbital angular momentum are replaced by $-\frac{3}{2}$ times the matrix elements of the effective orbital angular momentum (Lines (1963)). The trigonal crystal field, spin-orbit coupling and exchange interaction may therefore be written as:

$$\mathcal{H} = -\sum_i \left[\delta\left[(\ell_i^z)^2 - \frac{2}{3}\right] + \frac{3}{2}\lambda \underline{\ell}_i \cdot \underline{S}_i + \sum_j \mathcal{J}_{ij}\, \underline{S}_i \cdot \underline{S}_j\right] \qquad (5.2.1)$$

In figure (5.2.1) the various levels are shown when the trigonal crystal field and spin-orbit coupling are included. The energy levels indicated are those measured by Christie and Lockwood (1971) by Raman scattering at a temperature of 4.2 K. These energy levels cannot be reproduced by the trigonal crystal field and spin-orbit coupling terms alone (Christie and Lockwood (1971)). Also, it is

Figure (5.2.1)

This figure shows the various single ion levels of $CoCl_2$. The diagram is not to scale.

FIGURE(5.2.1)

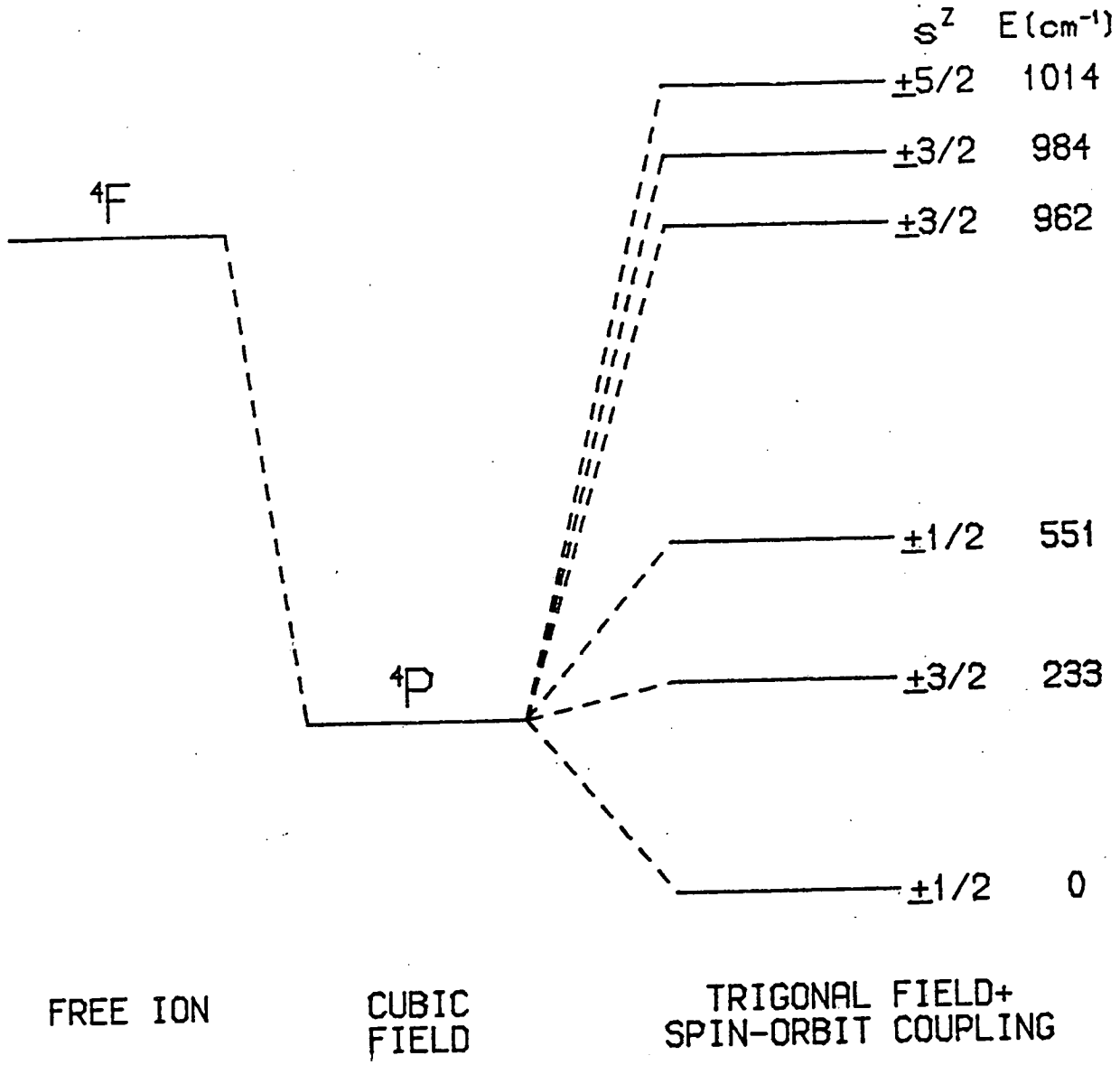
S^z E(cm^{-1})
±5/2 1014
±3/2 984
±3/2 962
^4F
±1/2 551
^4P
±3/2 233
±1/2 0
FREE ION
CUBIC FIELD
TRIGONAL FIELD+ SPIN-ORBIT COUPLING

not possible to obtain a value of $g^{\perp}$ for the lowest doublet which is in agreement with the measured value of $g^{\perp} = 6.0$ (Jacobs et al (1965)), only by including the trigonal field and spin orbit coupling. It was shown by Silverstein (1965) that the calculated value for $g^{\perp}$ could be improved by including the effect of the exchange interaction on the wavefunctions of the lowest doublet via a combination of perturbation theory and molecular field theory. More recently, Kardontchik et al (1977) have obtained the different energy levels by diagonalising the Hamiltonian in (5.2.1) in its entirety by including the exchange term in a molecular field approximation. Kardontchik et al have been able to explain fairly well all of the available experimental data using the parameters:

$$\delta = -405 \text{ cm}^{-1}, \quad \lambda = -159 \text{ cm}^{-1} \tag{5.2.2a}$$

$$\mathcal{J}_1 = 2.56 \text{ cm}^{-1}, \quad \mathcal{J}_2 = -0.18 \text{ cm}^{-1} \tag{5.2.2b}$$

where $\mathcal{J}_1$ and $\mathcal{J}_2$ are the isotropic exchange interactions between nearest neighbour Co^{2+} ions in the plane and next nearest neighbours out of the plane.

The lowest doublet shown in figure (5.2.1) may be treated as a pseudo-spin $S = \frac{1}{2}$ doublet. Then within this doublet the exchange Hamiltonian may be written as:

$$\mathcal{H} = -\sum_{ij} I_{ij} S_i^x S_j^x + J_{ij}(S_i^y S_j^y + S_i^z S_j^z) \tag{5.2.3}$$

where the x direction is along the crystallographic c axis and the z direction is along the (1,2,0) crystallographic direction. The spin wave excitation spectrum in the (h,0,0) direction for $CoCl_2$ has been measured by Hutchings (1973) using inelastic

neutron scattering. In table (5.2.1) the exchange parameters deduced from these measurements are given for the interactions between nearest neighbour in plane and next nearest neighbour, both interplanar and intraplanar, Co^{2+} ions. Of these exchange interactions the dominant interaction is the ferromagnetic nearest neighbour exchange. As a consequence, the excitation spectrum of $CoCl_2$ strongly resembles that of a two dimensional planar ferromagnet.

5.2 ii) Properties of $Fe_xCo_{1-x}Cl_2$

The magnetic ordering and phase transitions in $Fe_xCo_{1-x}Cl_2$ over the whole concentration range $0 < x < 1$ has been studied by Wong et al (1980, 1983) by neutron scattering and bulk susceptibility measurements. In figure (5.2.2) the results of Wong et al are summarised in a diagram showing the different regions observed as a function of concentration and temperature. At low temperature there are three regions which can be characterised. At the two ends of the concentration range there are phases in which only the uniaxial or the planar components of the spin are observed to order. In between these regions there is a third region in which peaks are observed at the Bragg positions which correspond to both the uniaxial and the planar components of the spin being ordered.

There is however a problem with classifying this central region as the mixed phase predicted by Fishman and Aharony (1978). The phase lines in figure (5.1.1) all corresponded to continuous second order phase transitions which were sharp and decoupled in the spin components. Measurements of the wavevector dependent susceptibility by Wong et al show that this is not the case for

Table (5.2.1)

In-plane (n.n.)	$2I_1 = 1.08$ meV,	$2J_1 = 2.46$ meV
Out of plane (n.n.n.)	$2I_2 = 0.09$ meV,	$2J_2 = -0.19$ meV

(After Hutchings (1973))

Figure (5.2.2)

This figure shows the measured 'phase diagram' of Wong et al (1980) for $Fe_xCo_{1-x}Cl_2$. The open circles are points determined by neutron diffraction and the closed circles by bulk susceptibility measurements.

FIGURE (5.2.2)

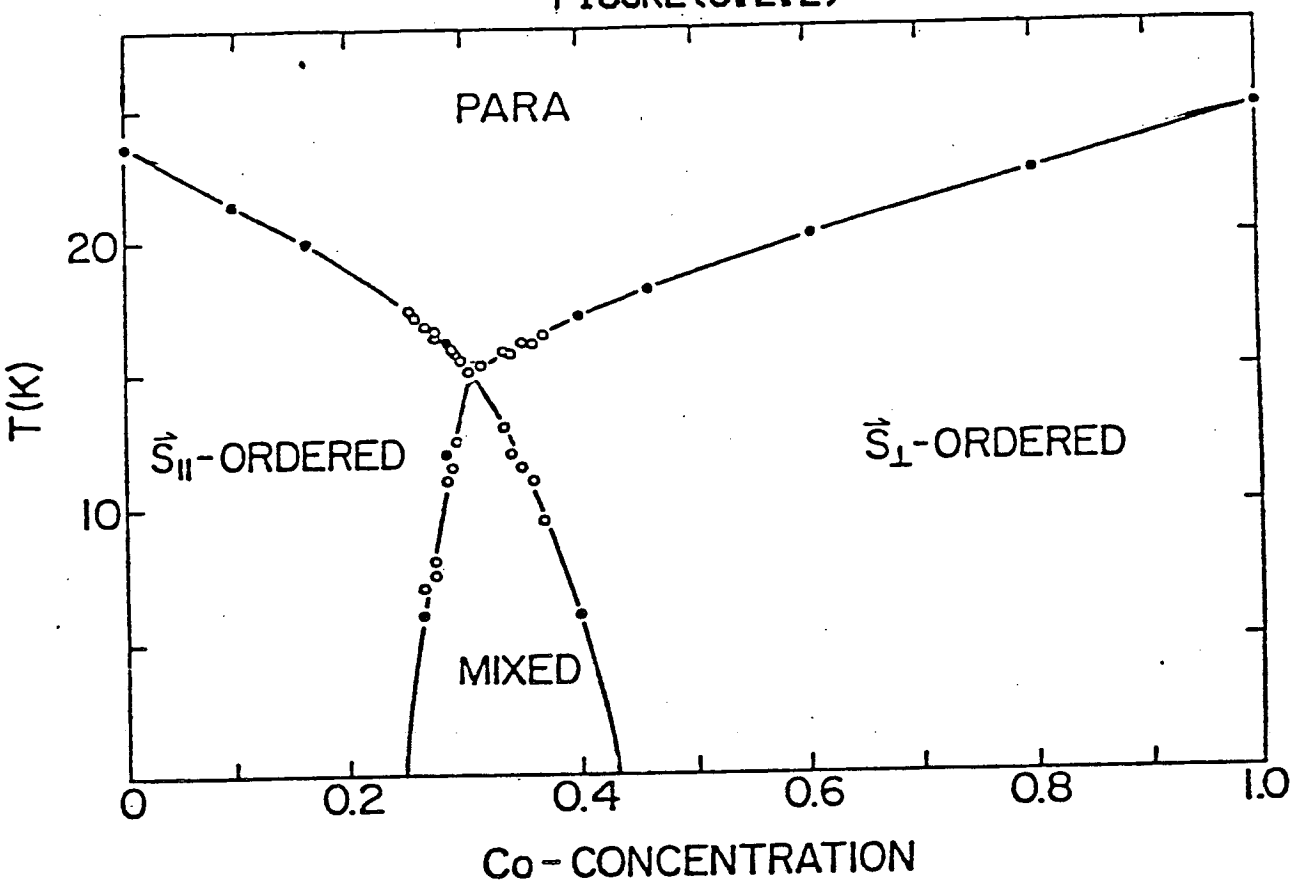
PARA
20
10
T(K)
$\vec{S}_{\parallel}$-ORDERED
$\vec{S}_{\perp}$-ORDERED
MIXED
0
0.2
0.4
0.6
0.8
1.0
Co-CONCENTRATION

$Fe_xCo_{1-x}Cl_2$. The "phase transitions" between the mixed phase and the other two low temperature phases are rounded and the ordering in the spin components is coupled. An explanation for this behaviour has recently been proposed by Wong et al (1983) and will be discussed in section (6). However, until then it will suffice to note that in the uniaxial phase only the uniaxial components of the spin are observed to order.

5.2 iii) Ground state of $Fe_xCo_{1-x}Cl_2$

The measurements briefly reviewed above do not answer the question of what is the ground state order in $Fe_xCo_{1-x}Cl_2$ at zero temperature. They do show that in the uniaxial phase, for example, the arrangement of the spins in the ground state must be such that the net value of the uniaxial component of the spin is non-zero while the net value of the planar component is zero. This restriction can, however, be achieved in different ways. For example, all the spins, both for the Fe^{2+} and Co^{2+} ions, could be aligned along the c-axis. Alternatively, the spins could be canted from the c-axis in such a way that the planar components are random in size and direction, or only have very short range order.

There is only one exact analytical solution for the ground state of a random anisotropy system. As is common in disordered systems this is the case of a single defect in an otherwise translationally invariant host. The case of a single Co^{2+} ion in $FeCl_2$ and a single Fe^{2+} in $CoCl_2$ has been studied by Oguchi and Ishikawa (1977). These authors modelled $FeCl_2$ and $CoCl_2$ as two dimensional ferromagnets with classical spins on a hexagonal lattice. Then, by exploiting the symmetry of the lattice sites surrounding the defect

Oguchi and Ishikawa constructed a difference equation for the cant angles of the spins, which minimised the Hamiltonian, at various equivalent distances from the defect. These authors then solved this equation using the cant angles of the defect and its nearest neighbours as initial conditions. Oguchi and Ishikawa calculated the exchange interaction between a Co^{2+} and Fe^{2+} ion by using the ansatz (Cowley and Buyers (1972)) that it was given by the geometric mean of the exchange interactions in the pure systems. Then using this value and the values of the exchange interactions in the pure systems, Oguchi and Ishikawa showed that the solution was only self consistent if the single defect aligned itself in the same direction as the host. That is to say, a single Co^{2+} spin in $FeCl_2$ would align itself along the c-axis and a single Fe^{2+} spin in $CoCl_2$ would align itself along the (1,2,0) direction in the a - b plane.

Therefore, for small concentrations of either Co^{2+} ions in $FeCl_2$ or Fe^{2+} ions in $CoCl_2$ the ground states are expected to be complete uniaxial and complete planar order respectively. When the concentration is not small, so that the single defect result is inapplicable, the situation is not so clear. Wiltshire (1981) has considered the stability of the ground states of complete uniaxial and complete planar order against the excitation of spin waves. This was done using the E.O.M. method described in the previous chapter. Essentially Wiltshire's method was to calculate $S^{\perp}(\underline{q} = 0, \omega)$ from the assumed ground state for various concentrations. The concentration at which a spin wave went to zero energy was then taken as the concentration at which there was a transition from the assumed groundstate, either all uniaxial or planar to the mixed phase.

Wiltshire reported that spin waves were found to go "soft", from the uniaxial ground state at a concentration x = 0.79 and from the planar ground state at a concentration x = 0.57. These are both in very good agreement with the results of Wong et al (1980).

It is, however, difficult to assess the accuracy of Wiltshire's calculations. The model of $Fe_xCo_{1-x}Cl_2$ used by Wiltshire was a three dimensional layered antiferromagnet with the nearest neighbour and next nearest neighbour exchange interactions calculated in the geometric mean ansatz. In the ground state with all the spins aligned uniaxially, Wiltshire took the value for the single ion energy D_i of the Fe^{2+} ions to be the same as in pure $FeCl_2$, but in the ground state with all the spins planar D_i was set to zero. The only details of the computational method published by Wiltshire were the size of the lattice (10 x 12 x 14) and the energy resolution which was 0.4 meV full width at half maximum. Further to this, Wiltshire did not publish any diagrams of the lineshape he obtained.

The use of the E.O.M. method to calculate spin wave energies in this context is questionable for two reasons. Firstly, since it is a $\underline{q} = 0$ mode which is calculated finite size effects will be at their greatest. Since the next nearest neighbour exchange interactions only have a small effect on the spin wave energies, there is little to be gained from constructing a three dimensional lattice. A consequence of this construction is that the size of the lattice in the a - b planes, within which the exchange interactions are strong, is small. Calculations of $S^{\perp}(q = 0, \omega)$ by the author on lattices as small as 10 x 10 have shown considerable finite size effects. Further to this, Wiltshire's energy resolution of 0.4 meV

means that to reduce the noise term to say 5% he would have had to iterate the equations of motion for $\sim$ 350 timesteps. This would have greatly accentuated any finite size effects. The second point that is questionable is that Wiltshire is attempting to calculate in the limit that ω is becoming very small. The response at very small energies is dependent on the long time behaviour of the equations of motion which is inherently the most inaccurate part of an E.O.M. method calculation.

5.3 Model for Calculations of $S^{\perp}(\underline{q},\omega)$ for $Fe_xCo_{1-x}Cl_2$

In order to use the E.O.M. method it is necessary to know the ground state of the system. The calculations presented in this chapter have been performed assuming that the groundstate in the uniaxial phase is one with all the spins aligned along the c-axis. $Fe_xCo_{1-x}Cl_2$ has been considered to be a two dimensional ferromagnet with nearest neighbour interactions only.

The lattice size used was one of 6400 spins distributed as described in the previous chapter. The value of the parameter λ (cf equation (4.3.15)) was chosen to be $\lambda = 0.8368$ (rads. THz)^2 which corresponds to an energy resolution of 2.0 meV full width at half maximum. A maximum energy for the spectrum of 12 meV was used for E_{max} along with a value n = 40 (cf equation (4.3.12)). The equations of motion were iterated for 230 timesteps and $S^{\perp}(\underline{q}, \omega)$ calculated for values of ω corresponding to the energy range 0 to 12 meV in intervals of 0.1 meV.

The values of the exchange energies, single ion energy and $g^{\perp}$'s used are given in table (5.3.1).

Table (5.3.1)

Exchange Parameters for $Fe_xCo_{1-x}Cl_2$ Simulation

$2 I_{FF} = 0.97$ meV, $2 J_{FF} = 0.68$ meV

$2 I_{CC} = 1.08$ meV, $2 J_{CC} = 2.46$ meV

$2 D_F(S_F - \frac{1}{2}) = 1.043$ meV

$g_F^{\perp} = 3.20$, $g_C^{\perp} = 6.00$

$S_F = 1.0$ $S_C = 0.5$

5.4 Experimental Technique

The spin wave spectrum of the sample of $Fe_{0.85}Co_{0.15}Cl_2$ was measured by inelastic neutron scattering using the Pluto triple axis spectrometer at A.E.R.E. Harwell. A schematic representation of the spectrometer layout is given in figure (5.4.1). The monochromator and analyser used were both pyrolytic graphite and neutrons were scattered from the (0,0,2) planes in both cases. A fixed final neutron wavevector of 2.67 A^{-1} was used throughout the measurements and a pyrolytic graphite filter was mounted between the sample and analyser to suppress contaminant neutrons that would be scattered by higher order planes in the analyser. The collimations used in the monochromator to sample, sample to analyser and analyser to detector positions were respectively 30', 30' and 60'. Scans were performed in the constant Q mode for neutron energy loss.

The sample of $Fe_{0.85}Co_{0.15}Cl_2$ was grown by Dr. T.E. Wood of the Inorganic Chemistry Laboratory, University of Oxford. The quoted concentration x = 0.85 corresponds to the concentrations of the constituents of the material at the start of the crystal growing method. The sample was aligned with its a* and c* hexagonal axes in the scattering plane and mounted in a standard CT-14 cryostat with liquid helium as the cryogen. Although the sample could be heated up from 5 K in the cryostat the temperature could not be measured accurately and it was not therefore possible to determine the concentration from the Néel temperature.

The reciprocal space diagram for the scattering plane was the same as that shown in figure (4.2.2) and the measurements were performed about the (1,0,7) Bragg peak. These measurements were made along the line (1-h, 0, 7) for h in the range 0.0 to 0.5.

Figure (5.4.1)

A schematic representation of the layout of Pluto triple axis spectrometer for the measurement of the spin wave spectrum of the $Fe_{0.85}Co_{0.15}Cl_2$ sample is shown.

FIGURE(5.4.1)

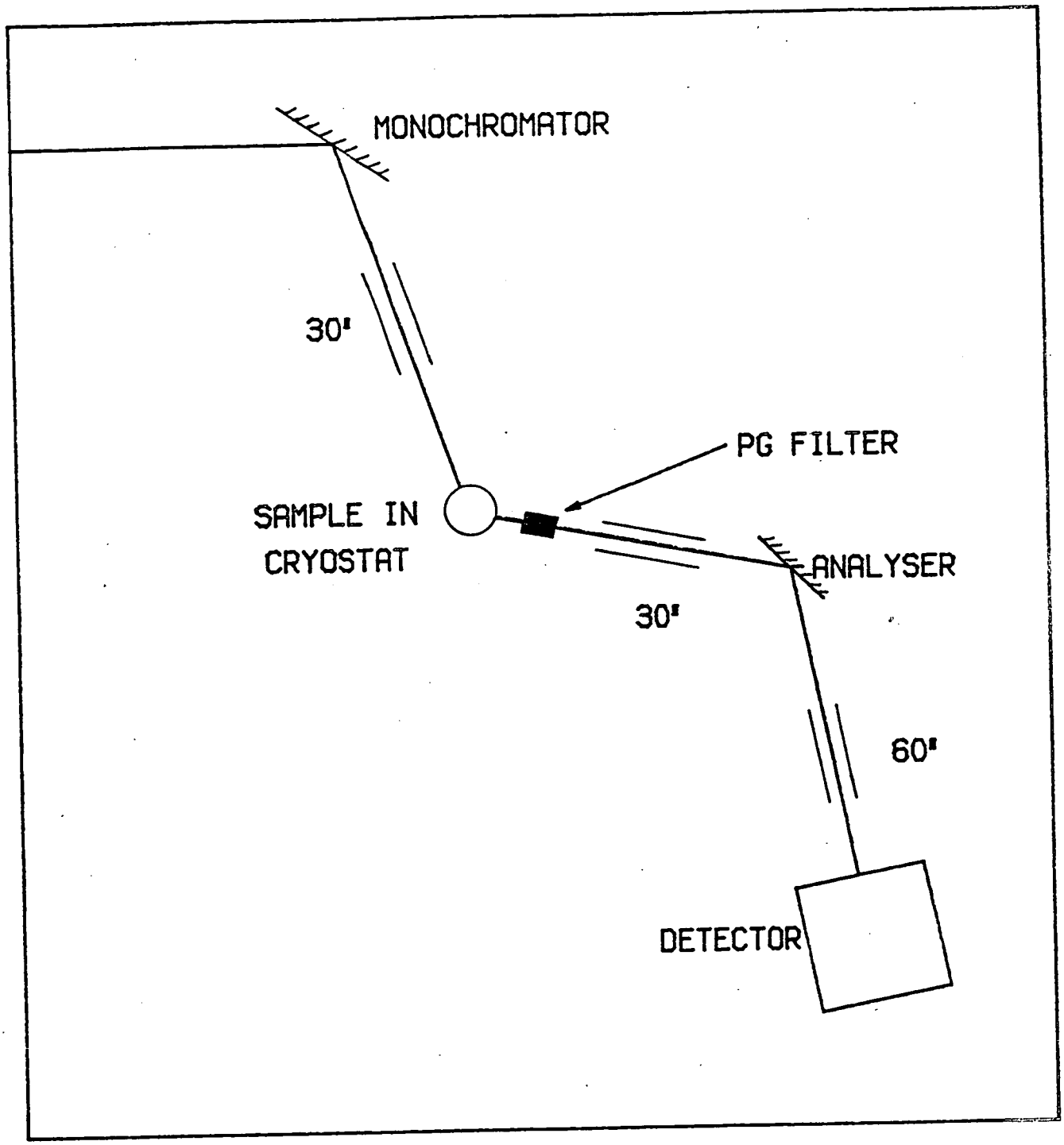
MONOCHROMATOR
30°
PG FILTER
SAMPLE IN
CRYOSTAT
ANALYSER
30°
60°
DETECTOR

Since Pluto triple axis spectrometer is a 'right-handed' spectrometer the reason for scanning in this direction was to focus the resolution function (Dolling (1975), p. 57)). The energy resolution of the spectrometer was estimated from a Vanadium scan to be 2.0 meV.

5.5 Results

In figures (5.5.1a - g) are shown the results of constant Q scans at 5 K along the direction (1-h, 0, 7) for the sample of $Fe_{0.85}Co_{0.15}Cl_2$. In these figures the solid lines are the results of the E.O.M. method simulations and the dotted lines represent the background and quasi-elastic scattering. The overall scales of the lineshapes from the simulations have been adjusted by eye to give a 'best fit' to the experimental data.

In figure (5.5.1a) which is at the zone boundary, the simulation result describes the observed spin wave very well, both in terms of the peak position and the lineshape. This is also true in figures (5.5.1b) and (5.5.1c) which are the lineshapes corresponding to values of h = 0.425 and 0.350 respectively. In figure (5.5.1d) the calculated lineshape although at about the right energy is not broad enough to fit the experimental data. Figure (5.5.1e) shows that at h = 0.20 the experimental lineshape has developed a double peak structure but the calculated lineshape only fits the lower peak and not the upper. In figure (5.5.1f) which corresponds to h = 0.10 the double peak structure has become clearly resolved. The lower peak however, is beginning to be submerged in the quasi elastic scattering. The position of the upper peak has increased in energy from that in figure (5.5.1e). Finally in figure (5.5.1g)

Figures (5.5.1a - g)

These figures show the measured inelastic lineshapes for the $Fe_{0.85}Co_{0.15}Cl_2$ sample at 5 K for various fixed wavevector transfers. The solid lines are the computed lineshapes using the Equation of Motion method, while the dotted lines represent the background level and the quasi-elastic scattering.

Figure (5.5.2)

A dispersion relation for the observed peak intensities in the inelastic spectrum of $Fe_{0.85}Co_{0.15}Cl_2$ is shown. The solid line is a cubic interpolation through the computed peak positions.

FIGURE(5.5.1a)

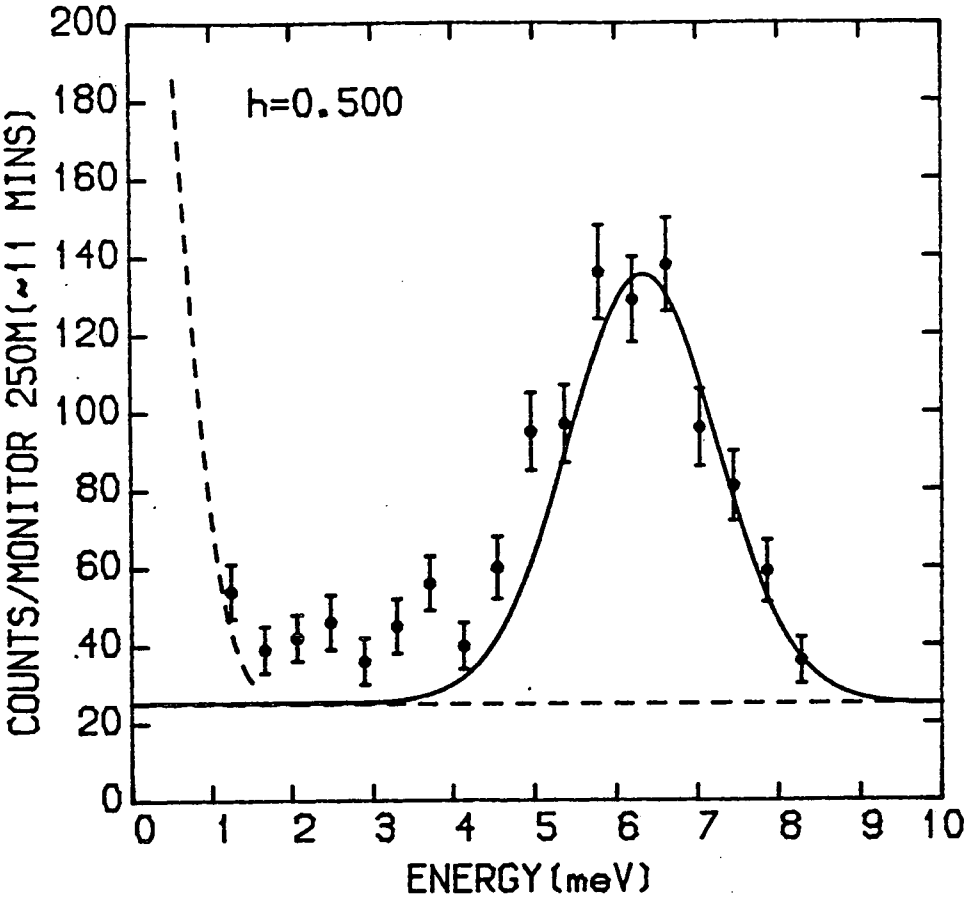

FIGURE(5.5.1b)

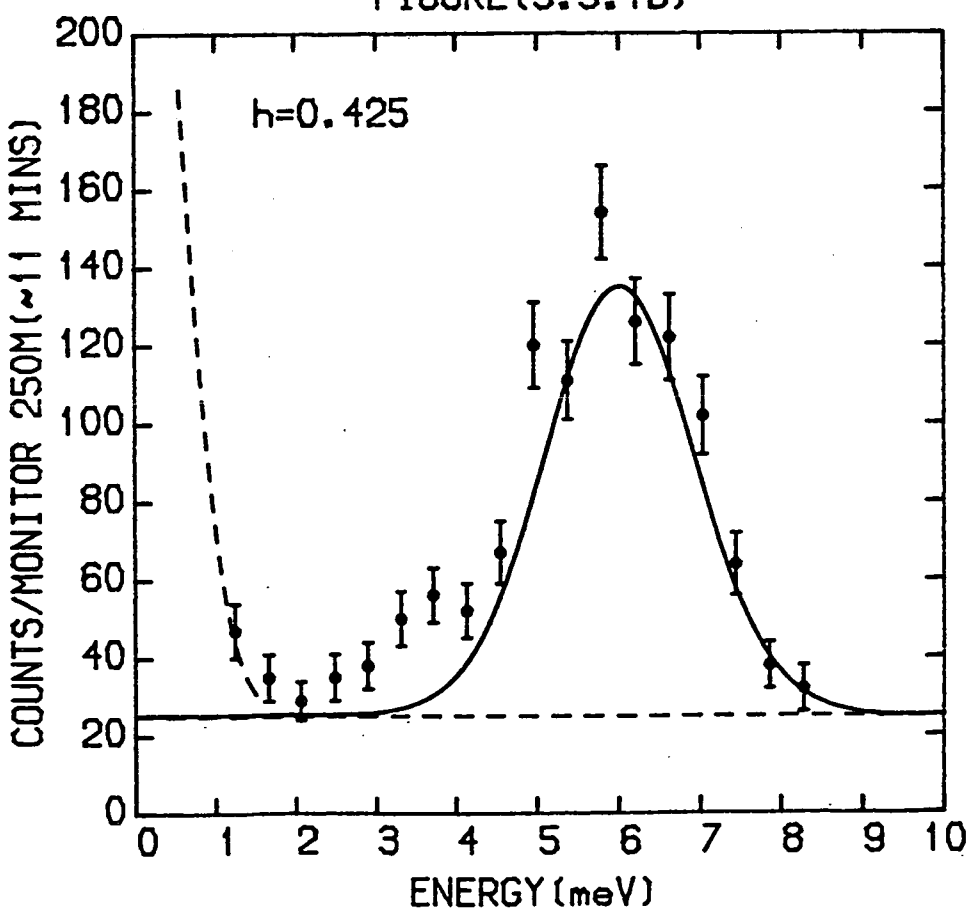

FIGURE(5.5.1c)

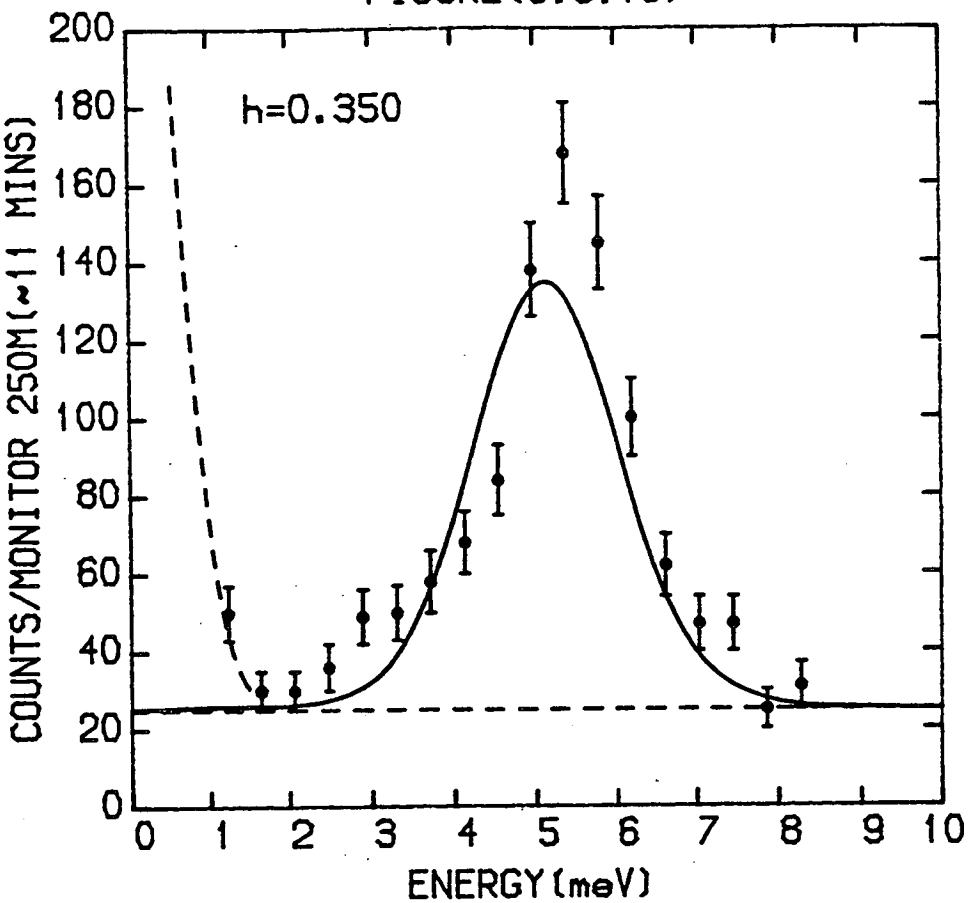

FIGURE(5.5.1d)

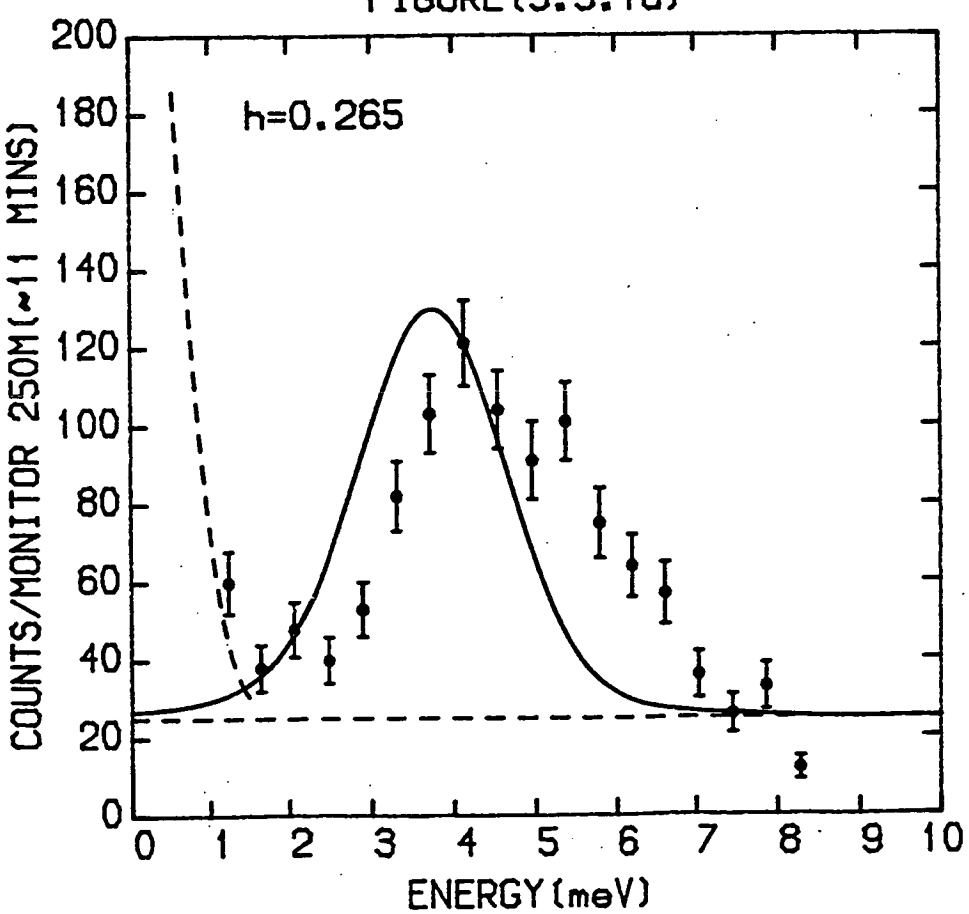

FIGURE(5.5.1e)

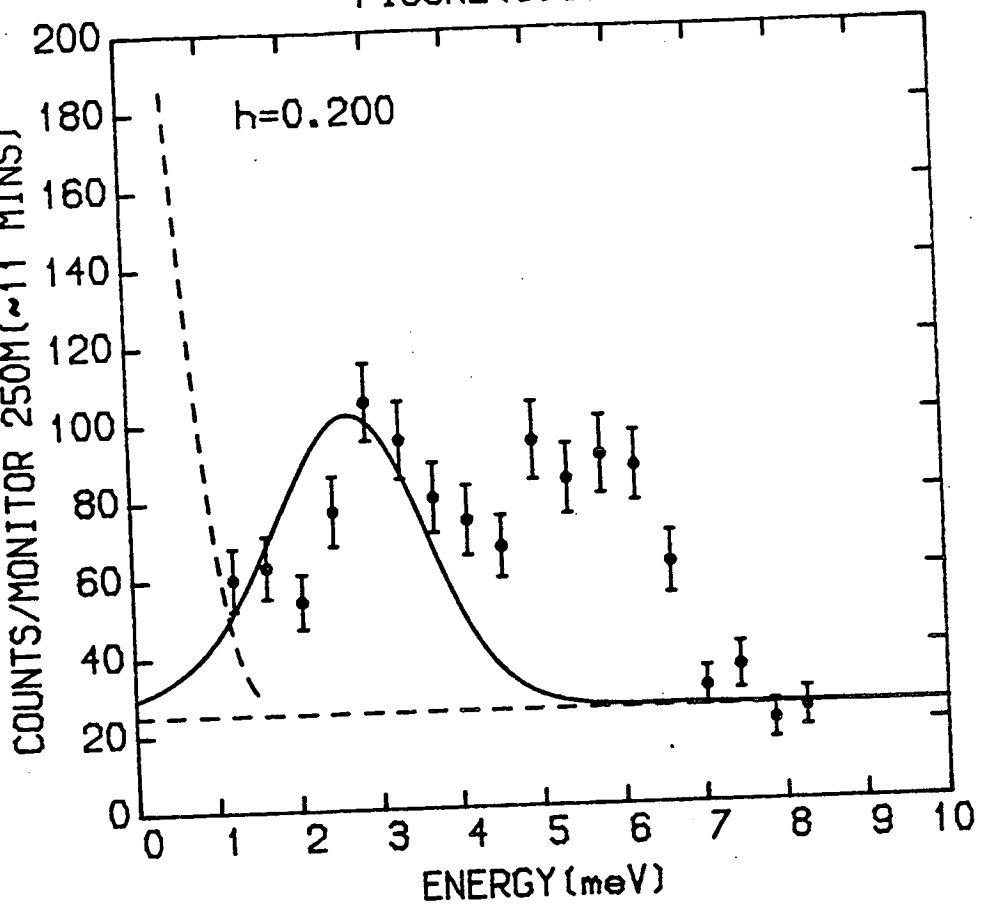

FIGURE(5.5.1f)

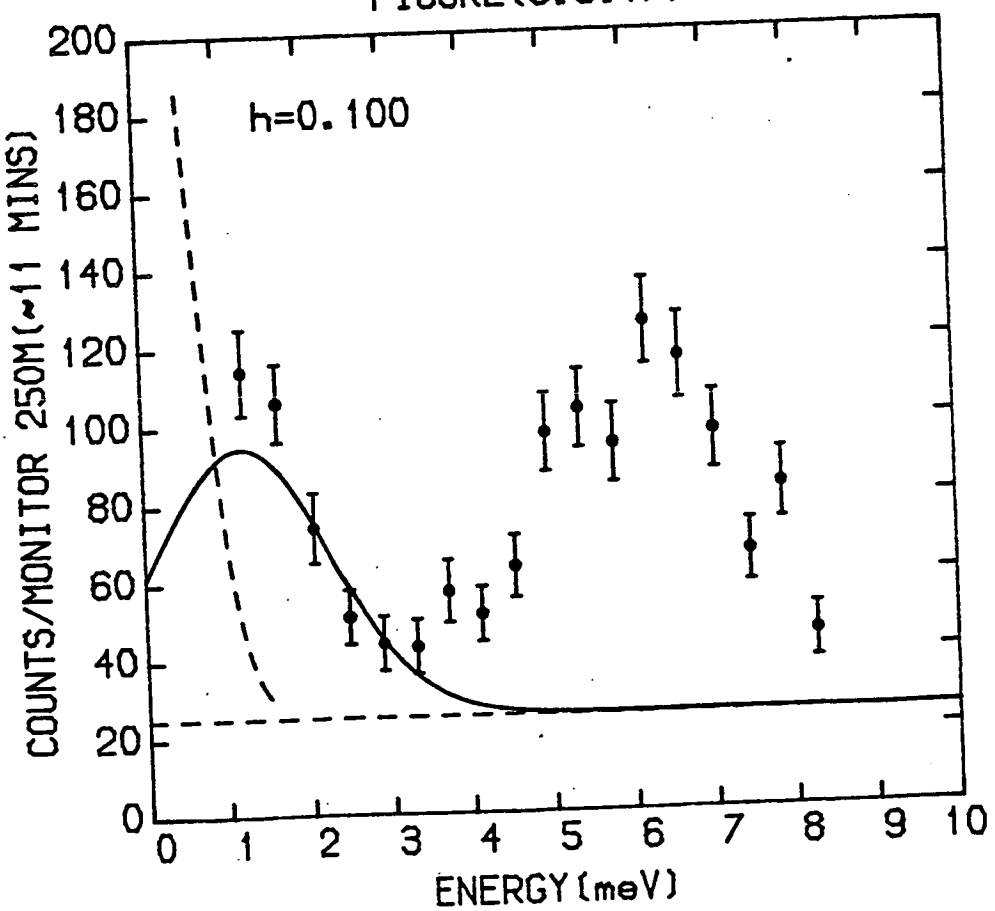

FIGURE(5.5.1g)

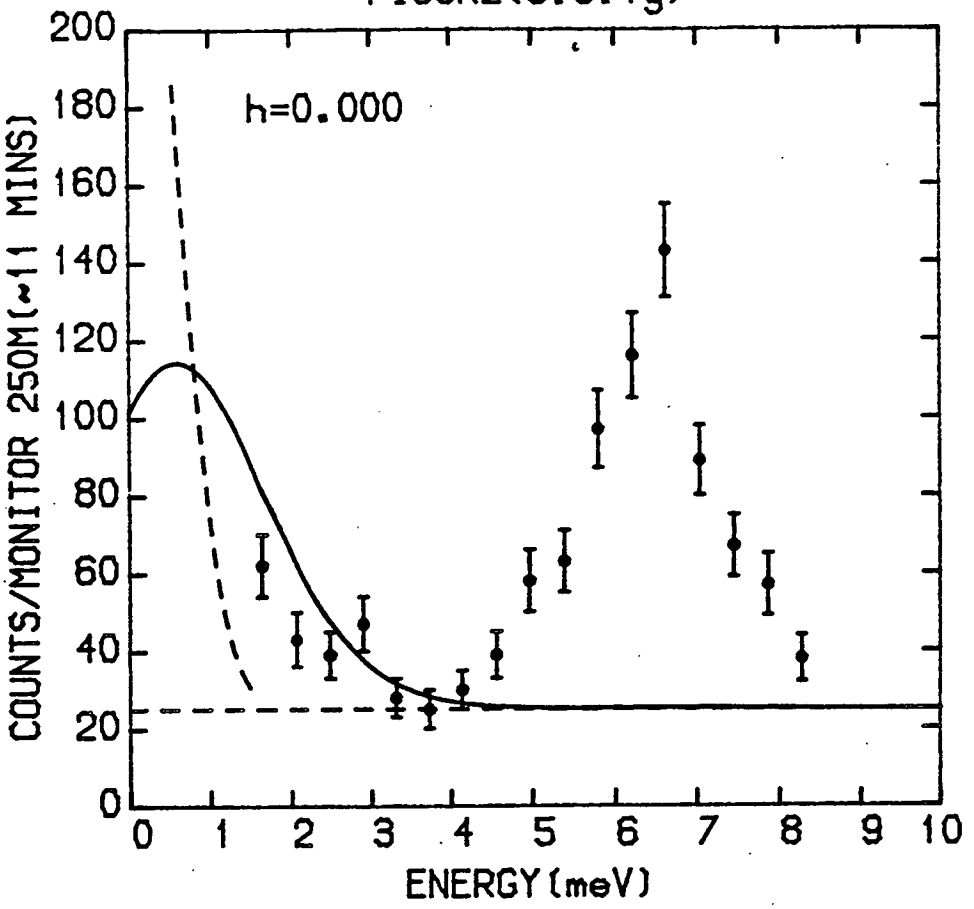

FIGURE(5.5.2)

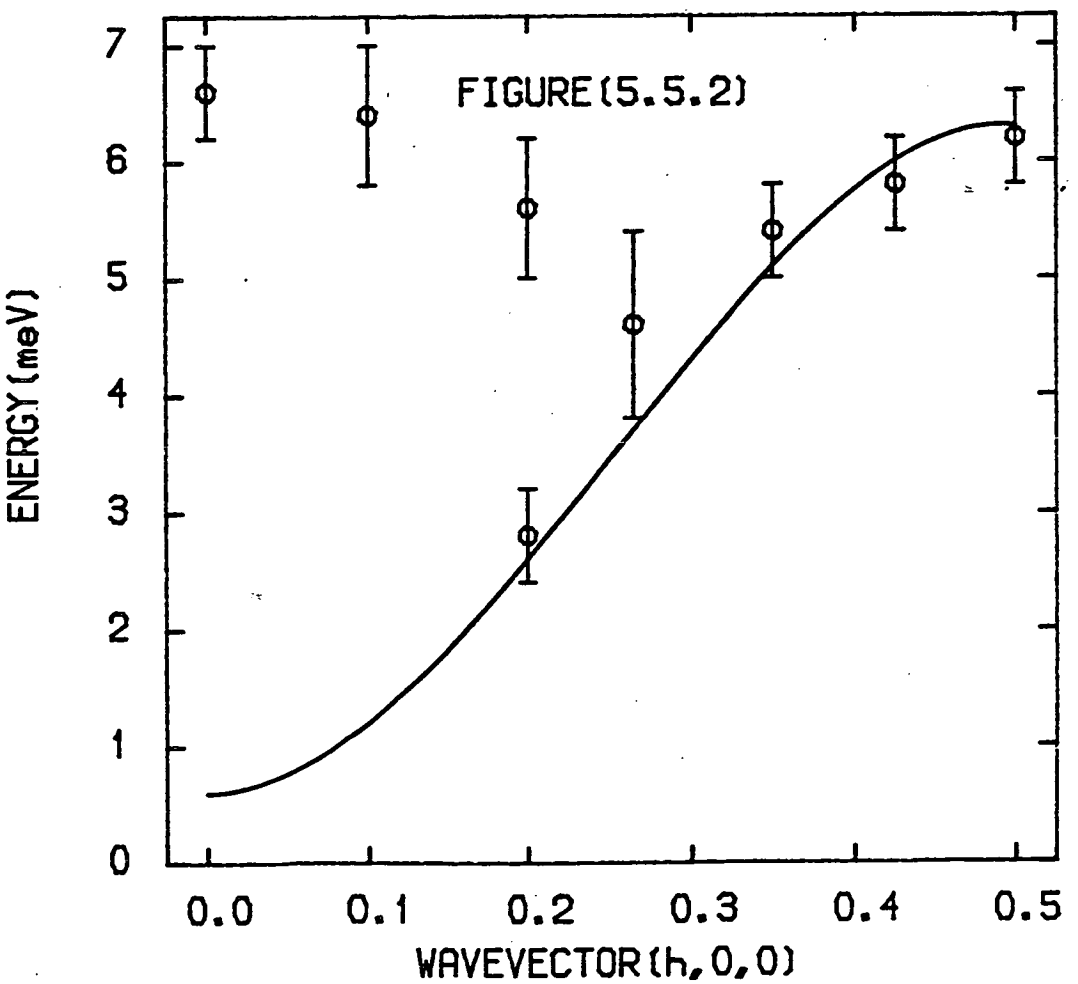

the zone centre scan is shown. The lower peak is now lost in the quasi-elastic scattering while the upper peak has continued to increase in energy. These results are summarised in a dispersion relation shown in figure (5.2.2). The solid line in figure (5.2.2) is drawn through the calculated points by cubic interpolation. From figures (5.5.1a - g) and (5.5.2) it can be seen that the simulation results model quite well the lower mode in the spectrum but do not show any indication of the upper mode.

A number of points should be made for the 'authenticity' of this upper mode as a magnetic excitation. As far as it could be, the sample was checked to make sure it was a single crystal. There was certainly no '60 twinning' about the c-axis, as is common in this crystal structure (see for example Hutchings (1973)). Also there was no evidence of any clustering of the Co^{2+} ions. This would have lead to an (0,0,9) magnetic Bragg peak which was explicitly absent.

The possibility that the upper mode was a phonon was also checked. This was done both by going to a larger wavevector transfer and by changing the temperature. The intensity of a phonon should increase if the wavevector transfer is increased while the intensity of a spin wave should decrease because of the magnetic form factor. A scan was performed at the (2,0,5) magnetic Bragg peak position. At this wavevector transfer an excitation was found at the same energy as that at (1,0,7) but with a peak intensity which was only half that at (1,0,7). Although the temperature of the sample could not be measured precisely, it was possible to determine when the sample was above the Néel temperature by observing the magnetic Bragg peak intensity. A constant Q scan was performed

at the (1,0,7) position at a temperature above the Néel temperature and the upper mode excitation was observed to have disappeared. A phonon would of course have still been present and would have increased in intensity because of the Bose population factor.

Apart from directly being a phonon there are two other ways in which phonons could have interfered with the measurements. Firstly, it is possible in $FeCl_2$ to have phonon-magnon hybridisation (Lovesey (1974)). This effect has been measured by Ziebeck and Houmanns (1976) but is very small and is therefore very unlikely to have affected the measured spin wave spectrum in such a large way. The second possibility is through magneto-vibrational scattering (Marshall and Lovesey (1971), p. 233). This is where a phonon mode can be observed through the elastic magnetic cross section because the magnetic spin is situated on a lattice site that is vibrating. Since the magnetic zone centre would then be a nuclear zone centre the upper mode would be an optic phonon. The number and symmetry of the zone centre optic phonons in $CdCl_2$ structure crystals has been calculated by Lockwood (1973). There are four optic phonons of which two are Raman active and two are infra-red active. The energies of the two Raman active optic phonons in $Fe_xCo_{1-x}Cl_2$ have been measured by Lockwood et al (1982) for x in the range 0 to 1. At x = 0.85 the lowest of these two modes is between 142 and 159 cm^{-1}, much too high in energy to be the upper mode in figure (5.2.2). This holds true for the whole range of x. The energies of the infra-red active optic phonons for pure $FeCl_2$ and $CoCl_2$ have been measured by Campbell and Vickers (1983). The energies of the lowest modes in these materials are respectively 201 and 213 cm^{-1}, again much too high in energy to be the upper mode in figure (5.2.2).

The upper mode in figure (5.2.2) can therefore only be interpreted as a magnetic spin wave excitation.

5.6 Discussion

A point not considered in section (5) which could have lead to a 'spurious' upper mode in figure (5.5.2) is the possibility of chemical ordering of the Fe^{2+} and Co^{2+} ions. This could not have been clustering of Co^{2+} ions as discussed in section (5) but might be an anticlustering of Co^{2+} ions. The existence of a two component structure to $Fe_xCo_{1-x}Cl_2$ should have led to new magnetic Bragg peaks. No new Bragg peaks were observed experimentally, although this could of course have been because the points where these peaks occurred were not checked out. In order to assess whether two component ordering could lead to an upper mode this possibility was simulated using the E.O.M. method. The lattice for the simulation was constructed in the computer so that the Co^{2+} ions could only occupy alternate sites on one of the rectangular sublattices. This meant that every Co^{2+} site was surrounded by 6 Fe^{2+} sites. These sites were occupied randomly and the spin wave spectra calculated as before. This two component ordering did not lead to a new mode and only slightly changed the calculated dispersion relation. Although it may be possible to think of other combinations of Co^{2+} and Fe^{2+} sites which lead to two component ordering it is not felt by the author that these would lead to significantly different results.

The upper mode in the spin wave spectrum of $Fe_xCo_{1-x}Cl_2$ cannot therefore be explained on the basis of a ground state in the uniaxial phase with all the spins aligned parallel to the c-axis.

Also intuitively it would not be expected that a small amount of canting of the spins would lead to such an upper mode. A small amount of canting would be expected only to lead to a renormalisation of the spin wave energies and an increase in the width of the lineshape. The existence of this upper mode in the spin wave spectrum of $Fe_xCo_{1-x}Cl_2$ therefore suggests that there is a considerable canting of the spins at a concentration x = 0.85, in the uniaxial phase.

As mentioned in section (2) Wong et al (1983) have recently proposed a new model for the Hamiltonian in $Fe_xCo_{1-x}Cl_2$ in order to explain their results on the magnetic ordering. It has so far been assumed that the exchange interaction between the magnetic ions could be adequately represented by equation (1.2.3). However, it is known that in systems where the orbital angular momentum is not quenched by the crystal field a more complicated interaction can arise (Elliott and Thorpe (1968)). The Fe^{2+} and Co^{2+} ions in $Fe_xCo_{1-x}Cl_2$ are of course examples of ions with unquenched orbital angular momentum. Therefore Wong et al (1983) have suggested that the Hamiltonian for $Fe_xCo_{1-x}Cl_2$ should include terms of the form

$$\Delta\mathcal{H} = - \sum_{ij} K_{ij} (\underline{r}_{ij} \cdot \underline{S}_i)(\underline{r}_{ij} \cdot \underline{S}_j) + G_{ij}\, \underline{r}_{ij} \cdot (\underline{S}_i \times \underline{S}_j) \qquad (5.6.1)$$

where $\underline{r}_{ij}$ is a unit vector pointing from site i to site j. In pure $FeCl_2$ or $CoCl_2$ these terms would be absent by symmetry but in $Fe_xCo_{1-x}Cl_2$ the local symmetry is broken by the site disorder. The effect on the phase diagram of $Fe_xCo_{1-x}Cl_2$ of including equation (5.6.1) in the Hamiltonian has been considered by Wong et al within the molecular field approximation. The terms in equation

(5.6.1) lead to random molecular fields which destroy the sharp second order phase transitions between the mixed phase and the uniaxial and planar phases. The effect of terms such as those in equation (5.6.1) on the spin wave spectrum is unknown. If these terms do exist in the Hamiltonian for $Fe_xCo_{1-x}Cl_2$ then the ground state can never be one of either complete uniaxial or complete planar order.

The future calculation of the spin wave spectrum for a random anisotropy system therefore requires the ground state to be determined first. If the spins in the system are treated as classical spins then it is possible to find the ground state of a finite size model on a computer using the method devised by Walker and Walstedt (1980). The spin wave spectrum may then be calculated in a qualitative manner by using the classical equations of motion. It should be possible from such a simulation to determine whether an upper mode in the spin wave spectrum of $Fe_xCo_{1-x}Cl_2$ can be generated either by a large canting of the spins or by including terms such as those in equation (5.6.1). It is hoped that it will be possible to carry out these simulations in the future.

APPENDIX A

Data Analysis Methods

i) Introduction

It is the purpose of this appendix to describe the methods referred to in Chapters Two and Three to analyse the experimental data collected. For the experiments described in Chapters Two and Three the aim of the data analysis was to vary the parameters governing the structure factor to find the 'best fit'. The 'best fit' is defined to be the set of parameters which minimise the function X^2 given by:

$$X^2 = \frac{1}{(N-k)} \sum_i \frac{(I_i^{obs} - I_i^{calc})^2}{\sigma_i^2} \qquad \text{(A.i.1)}$$

where i labels the data points in a scan, N is the number of data points, I_i^{obs} are the observed intensities which have standard deviations σ_i and I_i^{calc} is the calculated intensity which has k adjustable parameters. Estimating the values of the parameters by minimising X^2 is known as the Method of Least Squares (Frodesen et al (1979) p. 259). If the observed intensities I_i^{obs} are each distributed about their mean values with standard deviation σ_i by a Gaussian distribution function, then minimising X^2 is equivalent to maximising the likelihood (probability) of having observed the set of intensities I_i^{obs} (Frodesen et al (1979) p. 261). The definition of X^2 equation (A.i.1) is not in general equivalent to the usual statisticians definition of the chi-square variable (Hoel (1971) p. 228). However, in a number of limiting cases X^2 can be shown to be a chi-square variable (Frodesen et al (1979)

p. 285) and it is common in the literature to refer to the values of X^2 as the 'chi-square values'. In Chapters Two and Three reference to chi-square values, in fact referred to the values of X^2 as defined by equation (A.i.1).

The factor N - k in equation (A.i.1) is a normalisation factor. If the calculated intensity in equation (A.i.1) depends linearly on the adjustable parameters then the expectation value of equation (A.i.1) is one. When the calculated intensity depends non-linearly on the adjustable parameters the expectation value cannot be evaluated exactly. However, if the functional form of I_i^{calc} and the best fit estimate of the adjustable parameters provide a good description of the observed data then I_i^{calc} may be replaced by its tangent plane and the expectation value of equation (A.i.1) is then one as in the linear case. The value of X^2 has the physical interpretation that it measures the mean variance (normalised) of the observed values from the calculated values. The value of X^2 is therefore used as a goodness of fit test where, since the expectation value of X^2 is one, values of X^2 less than two are taken to indicate a good fit between theory and experiment. A value of X^2 less than 2 indicates that $\sim \frac{2}{3}$ of the observed values are less than 1.4 standard deviations from the respective calculated values.

Since the mechanics of minimising X^2 requires a large amount of numerical work, the process is carried out on a computer. In the following five sub-sections the methods underlying the computer programs that were written to do this in various circumstances are described. The methods for calculating the best fit parameters are contained in subsections (ii) to (iv) and the methods for calculating

the I_i^{calc} for Chapters Two and Three given in subsections (v) and (vi).

Subsection (ii) contains the method of solution for the situation where the I_i^{calc} depends linearly on the adjustable parameters. The results of this section were used in writing the programs LINFIT and ABFIT. In subsection (iii) Newton's method of solution for a set of non-linear equations is described. This method is used in subsection (iv) in the solution for the case where I^{calc} depends non-linearly on the adjustable parameters. In subsection (iv) the results of the previous two subsections are combined to describe the method of solution used when the calculated intensity depends non-linearly on the adjustable parameters. This was the method used in the program RB2FIT referred to in Chapter Two and the FITIT6 program referred to in Chapter Three.

The methods described in subsections (ii) to (iv) do not depend on the explicit form for I_i^{calc}, only on whether it depended linearly or non-linearly on the adjustable parameters. The calculation of the I_i^{calc} from a given form for the structure factor therefore takes place in a separate subroutine in the fitting programs. This calculation is not, however, as simple as it might seem since the observed intensity is the convolution of the structure factor with the resolution function. This means that the calculated intensity applicable to Chapters Two and Three is given by the convolution integral:

$$I^{calc}(\underline{Q}_i) = \int d^3\tau \; R(\underline{Q}_i, \tau) \; S(\underline{Q}_i + \underline{\tau}) \qquad \text{(A.i.2)}$$

where $\underline{Q}_i$ is the wavevector transfer for the i^{th} data point,

$R(\underline{Q}_i, \underline{\tau})$ is the resolution function and $S(\underline{Q}_i + \underline{\tau})$ is the structure factor. It is common in general fitting programs, available at such institutions as the I.L.L. for example, to perform the integrals in equation (A.i.2) numerically by summing over a three dimensional mesh. There are two problems with performing the integrals applicable to Chapters Two and Three in this way, (1) it would take an exceptionally large amount of computer time (prohibitively so) and (2) if the mesh size is compromised to account for (1) systematic errors will be introduced into the estimated parameters. In subsection (v) and (vi) the methods for performing the integrals in equation (A,i.2) for the structure factors used in Chapters Two and Three are described. These methods overcome problems (1) and (2) by performing some of the integrals analytically and hence only summing over a reduced mesh. Subsection (v) is applicable to both chapters and describes how the integration over the vertical component of the resolution function can be done. This result is extended in subsection (vi) to show how, in a certain limit, the integration over the longitudinal component of the resolution function may also be done analytically. Subsection (vi) is only applicable to some of the results in Chapter Three.

ii) Linear Regression

If the form for the calculated intensity is such that it can be written as:

$$I_i^{calc} = \sum_{m=1}^{k} p_m x_{im} \qquad \text{(A.ii.1)}$$

where x_{im} is the m^{th} independent variable for data point i and p_m is an adjustable parameter, then equation (A,i.1) can be minimised exactly in one step. The set of calculated values

corresponding to the observed values can be written in the matrix notation:

$$\tilde{I}^{calc} = \tilde{x}\ \tilde{p} \qquad \text{(A.ii.2)}$$

where $\tilde{I}^{calc}$ is an (N x 1) matrix containing the calculated values, $\tilde{p}$ is a (k x 1) matrix containing the adjustable parameters and $\tilde{x}$ is an (N x k) matrix containing the independent variables. Then, with the definition of two more matrices, $\tilde{I}^{obs}$ an (N x 1) matrix containing the observed values and $\tilde{V}$ an (N x N) diagonal matrix holding the variances of the observed values, then equation (A.i.1) can be written as:

$$X^2 = \frac{1}{N - k} (\tilde{I}^{obs} - \tilde{I}^{calc})^T \tilde{V}^{-1} (\tilde{I}^{obs} - \tilde{I}^{calc}) \qquad \text{(A.ii.3)}$$

Then the set of parameters which minimise X^2 will be the solutions to the equations

$$dX^2 = \sum_{m=1}^{k} \left(\frac{\partial X^2}{\partial p_m}\right) dp_m = 0 \qquad \text{(A.ii.4)}$$

If equation (A.ii.2) is substituted into equation (A.ii.3) then the set of equations (A,ii,4) can be written as:

$$-2(\tilde{x}^T \tilde{V}^{-1}\ \tilde{I}^{obs} - \tilde{x}^T \tilde{V}^{-1}\ \tilde{x}\ \tilde{p}) = \tilde{0} \qquad \text{(A.ii.5)}$$

where $\tilde{0}$ is a (k x 1) matrix of zeroes. The solution to equation (A.ii.5) is then:

$$\tilde{p} = (\tilde{x}^T \tilde{V}^{-1}\ \tilde{x})^{-1}\ \tilde{x}\ \tilde{V}^{-1}\ \tilde{I}^{obs} \qquad \text{(A.ii.6)}$$

This solution minimises the value of X^2 as can be shown from the values of the second partial derivatives of X^2 with respect to the adjustable parameters:

$$\left(\frac{\partial^2 X^2}{\partial p_m^2}\right) = 2 \sum_i \frac{(x_{im})^2}{\sigma_i^2} > 0 \text{ for all } m \qquad \text{(A.ii.7)}$$

Since there exist uncertainties in the observed values there will be correspondingly uncertainties in the estimated parameters given by equation (A.ii.6). In order to calculate the effect of the uncertainties in the observed values, which are denoted by δI_i^{obs}, on the estimated parameters a Taylor expansion is performed about the values of the estimated parameters such that:

$$p_m = \hat{p}_m + \sum_i \frac{\partial p_m}{\partial I_i^{obs}} \Bigg|_{\tilde{\hat{p}}} \delta I_i^{obs} + \text{higher order terms} \qquad \text{(A.ii.8)}$$

where the $\hat{p}_m$ are the estimated parameters given by equation (A.ii.6). In this case where the dependence is linear the higher order derivatives are zero. The next step is to consider the co-variance between the parameters p_m and p_n which forms the $(m,n)^{th}$ element of the co-variance matrix V(p), The element $V_{mn}(\tilde{p})$ is given by:

$$V_{mn}(\tilde{p}) = E\left[(p_m - \hat{p}_m)(p_n - \hat{p}_n)\right] = \sum_i \left(\frac{\partial p_m}{\partial I_i^{obs}}\right) \sigma_i^2 \left(\frac{\partial p_n}{\partial I_i^{obs}}\right) \qquad \text{(A.ii.9)}$$

where E [ ] denotes an expectation value and the result for uncorrelated data that $E\left[\delta I_i^{obs} . \delta I_j^{obs}\right] = \sigma_i^2 \delta_{ij}$. The derivatives in equation (A.ii.9) can be performed by noting from equation (A.ii.6) that $\left(\frac{\partial p_m}{\partial I_i^{obs}}\right)$ is the $(m,i)^{th}$ element of the matrix $\tilde{S}$ =

$(\tilde{x}^T \tilde{V}^{-1} \tilde{x})^{-1} \tilde{x} \tilde{V}^{-1}$. Equation (A.ii.9) may therefore be written in the matrix form:

$$\tilde{V}(\tilde{p}) = \tilde{S} \tilde{V} \tilde{S}^T = (\tilde{x}^T \tilde{V}^{-1} \tilde{x})^{-1} \qquad \text{(A.ii.10)}$$

The uncertainties in the estimated parameters are calculated from the matrix $\tilde{V}(\tilde{p})$ by taking the square roots of the diagonal elements. This last step can be given a more physical interpretation by noting from equation (A.ii.9) that the square roots of the diagonal elements of $\tilde{V}(\tilde{p})$ are given by:

$$\delta p_m = \sqrt{V_{mm}(\tilde{p})} = \sqrt{\sum_i \left(\frac{\partial p_m}{\partial I_i^{obs}}\right)^2 \sigma_i^2} \qquad \text{(A.ii.11)}$$

which is the result that would have been obtained by considering the p_m as functions of the variables I_i^{obs} and using the method of small changes (Squires (1976) p. 37).

The results of this subsection have been used in writing the computer programs LINFIT and ABFIT. The LINFIT program performed a straight line fit whereby the I_i^{obs} and I_i^{calc} were replaced by the general dependent variables y_i^{obs} and y_i^{calc}. All the straight line fits that were reported in the earlier chapters were done using this program.

In subsection (vi) when the evaluation of the I_i^{calc} for the $Mn_{0.65}Zn_{0.35}F_2$ data described in Chapter Three is discussed, it will be shown that the I_i^{calc} in this case depends linearly on two adjustable parameters A and B and non-linearly on two others κ and q_o. The ABFIT program performed a fit to some of the $Mn_{0.65}Zn_{0.35}F_2$ data in a special limit where κ was fixed to zero and q_o determined independently. In this situation the I_i^{calc} is only linearly

dependent on the remaining adjustable parameters and the above results can be applied. The two independent variables in this case were functions of the reduced wavevector transfer of the i^{th} data point in the scan.

iii) Newton's solution for non-linear equations

This subsection deals with the method of solving a set of n non-linear equations which depend on n-variables. The solution of such a set of equations is necessary for minimising X^2 when I_i^{calc} depends non-linearly on the adjustable parameters. The equations are written in the form:

$$f_m(a_1,\ldots,a_n) = 0, \text{ for } m = 1 \text{ to } n \qquad \text{(A.iii.1)}$$

where the f_m are the n nonlinear equations and the a's are the n variables. Then assuming that an approximate set of solutions exist which are 'close' to solving equations (A.iii.1) then the values of the functions for nearby values of the variables can be found from a Taylor expansion:

$$f_m(a_1',\ldots,a_n') = f_m(a_1,\ldots a_n) + \sum_{i=1}^{n} \left(\frac{\partial f_m}{\partial a_i}\right)(a_i' - a_i) + \text{higher order terms} \qquad \text{(A.iii.2)}$$

If the Taylor expansion is truncated above the linear terms, then these equations can be written in a matrix formalism:

$$\tilde{F}(\tilde{a}') = \tilde{F}(\tilde{a}) + \tilde{D}(\tilde{a}' - \tilde{a}) \qquad \text{(A.iii.3)}$$

where $\tilde{F}$ is an (n x 1) matrix with the values of its elements given by the functions $f_m(a_1,\ldots,a_n)$, $\tilde{a}$ is an (n x 1) matrix with its

elements given by the values of the variables and $\tilde{D}$ is an (n x n) matrix with its elements D_{mi} given by derivatives $(\frac{\partial f_m}{\partial a_i})$. The equations (A.iii.3) are an approximation to the equations (A.iii.1) which can be solved exactly. The solution is

$$\tilde{a}' = \tilde{a} - \tilde{D}^{-1} \tilde{F}(\tilde{a}) \qquad \text{(A.iii.4)}$$

Since equations (A.iii.3) were only an approximation to (A.iii.1) the solutions given in equation (A.iii.4) are only an approximate solution to the equation (A.iii.1). However, if the conditions are right, the $\tilde{a}'$ are a better approximation than the $\tilde{a}$ and the solutions to equations (A.iii.1) can be found by successive approximation. This is done by turning equation (A.iii.4) into an iteration formula

$$\tilde{a}^{\nu+1} = \tilde{a}^{\nu} - \tilde{D}^{-1} (\tilde{a}^{\nu}) \tilde{F} (\tilde{a}^{\nu}) \qquad \text{(A.iii.5)}$$

where ν labels the iteration. The iteration stops when the variables satisfy equations (A.iii.1) up to some preset numerical accuracy.

The convergence of equation (A.iii.5) to the solution of equations (A.iii.1) is unfortunately not guaranteed. There are a number of problems that can arise, (1) there could be a number of solutions to the equations (A.iii.1) or, (2) there could be a maximum, minimum or saddle point of the functions between the starting values and the solutions. There is not a general method for overcoming these problems except for finding a set of starting values that is sufficiently close to the solutions that problems (1) and (2) do not matter. The choice of the starting values therefore relies heavily on a knowledge of the Physics behind the equations (A.iii.1).

iv) Non linear regression

The set of parameters which minimise X^2 as given in equation (A.i.1) are the solutions to the equations (A.ii.4). If the dependence of I_i^{calc} on the adjustable parameters is non-linear then the equations resulting from (A.ii.4) will be a set of coupled non-linear equations given by:

$$\left(\frac{\partial X^2}{\partial p_m}\right) = -2 \sum_i \frac{(I_i^{obs} - I_i^{calc})}{\sigma_i^2} \left(\frac{\partial I_i^{calc}}{\partial p_m}\right) = 0 \qquad \text{(A.iv.1)}$$

If the identification $f_m(p_1,\ldots,p_k) = \left(\frac{\partial X^2}{\partial p_m}\right)$ is made then the method of solution for equation (A.iv.1) was that given in sub-section (iii). The solution is found by iteratively solving the equation:

$$\tilde{p}' = \tilde{p} - \tilde{D}^{-1}(\tilde{p})\,\tilde{F}(\tilde{p}) \qquad \text{(A.iv.2)}$$

where the elements of the matrix $\tilde{D}$ are given by

$$D_{mn}(\tilde{p}) = \left(\frac{\partial^2 X^2}{\partial p_m \partial p_n}\right) = \sum_i \frac{1}{\sigma_i^2}\left(\frac{\partial I_i^{calc}}{\partial p_m}\right)\left(\frac{\partial I_i^{calc}}{\partial p_n}\right) - \frac{(I_i^{obs} - I_i^{calc})}{\sigma_i^2}\left(\frac{\partial^2 I_i^{calc}}{\partial p_m \partial p_n}\right) \qquad \text{(A.iv.3)}$$

and the elements of the matrix $\tilde{F}$ are given by:

$$F_m(\tilde{p}) = \sum_i \frac{(I_i^{obs} - I_i^{calc})}{\sigma_i^2}\left(\frac{\partial I_i^{calc}}{\partial p_m}\right) \qquad \text{(A.iv.4)}$$

The solution given by equation (A.iv.2) will minimise X^2 if the matrix $\tilde{D}$ is positive definite as can be seen from equation (A.iv.3).

There is a further approximation that is made which greatly simplifies the implementation of the solution. The second derivatives in equation (A.iv.3) are weighed by the residual values which

should, on average, be small. Consequently, the second derivatives in equation (A.iv.3) are therefore dropped leaving only the need to calculate the first derivatives of the calculated intensity to obtain the elements of F and D. This is known as the Gauss approximation (Bard (1974) p. 96). The Gauss approximation has a physical interpretation which is very useful in evaluating the uncertainties in the estimated parameters. In dropping the second derivatives in equation (A.iv.3) the function I_i^{calc} has effectively been replaced by its Taylor expansion truncated after the linear terms, i.e.

$$I_i^{calc}(\tilde{p}') \simeq I_i^{calc}(\tilde{p}) + \sum_{m=1}^{k} (p_m' - p_m) \left.\frac{\partial I_i^{calc}}{\partial p_m}\right|_{\tilde{p}} \qquad \text{(A.iv.5)}$$

If this is substituted into equation (A.i.1) and the identifications $(I_i^{obs} - I_i^{calc}(\tilde{p})) \rightarrow I_i^{obs}$, $(\frac{\partial I_i^{calc}}{\partial p_m}) \rightarrow x_{im}$ and $(p_m' - p_m) \rightarrow p_m$ are made then the result is the linear regression problem of subsection (ii). However, since equation (A.iv.5) is an approximation so the solution to this equivalent linear problem will only be an approximate solution which must be iterated to find the non-linear solution. The solution of the non-linear regression problem using the Gauss approximation can therefore be considered as a multiple linear regression (Bard (1974) p. 99). The identification of the non-linear problem at each stage of the iteration with a linear problem means that the identification

$$\tilde{x}^T \tilde{V}^{-1} \tilde{x} = \tilde{D} \qquad \text{(A.iv.6)}$$

can be made. Therefore the uncertainties in the estimated parameters is found from equations (A.ii.9), (A.ii.10) and (A.iv.6) to be the square roots of the diagonal elements of the covariance matrix given by:

$$\tilde{V}(p) = \tilde{D}^{-1} \qquad \text{(A.iv.7)}$$

when the iteration has converged to the non-linear solution.

v) Evaluating the calculated intensities

The previous subsections have described how given a set of calculated intensities which depended on a set of adjustable parameters the best fit parameters could be found. This subsection and the following one deal with the evaluation of the calculated intensity from equation (A;i.2) for the structure factors considered in Chapters Two and Three. In Chapter Two the structure factor was given by:

$$S(\underline{q}) = \frac{A}{(\underline{q} - \underline{q}_o)^2 + \kappa^2} \qquad \text{(A.v.1)}$$

where $\underline{q}$ is a two dimensional reduced wavevector and the adjustable parameters are $\underline{q}_o$, κ and A. The structure factor considered in Chapter Three was given by:

$$S(\underline{q}) = \frac{A}{(\underline{q} - \underline{q}_o)^2 + \kappa^2} + \frac{B}{\left[(\underline{q} - \underline{q}_o)^2 + \kappa^2\right]^2} \qquad \text{(A.v.2)}$$

which differs from equation (A.v.1) because the reduced wavevector is now three dimensional and the Lorentzian squared term has been added with an adjustable parameter B. The Lorentzian squared term can be written as the derivative of the Lorentzian with respect to κ, in the form:

$$\frac{1}{\left[(\underline{q} - \underline{q}_o)^2 + \kappa^2\right]^2} = -\frac{1}{2\kappa}\frac{\partial}{\partial\kappa}\frac{1}{(\underline{q} - \underline{q}_o)^2 + \kappa^2} \qquad \text{(A.v.3)}$$

and therefore, in principle, if the integration of the Lorentzian over the resolution function can be performed then so too can the integration of the Lorentzian squared by differentiation under the integral sign.

The calculation of equation (A.i.2) depends on the form of the resolution function as well as the structure factor. The complete forms for the resolution functions are given for each case in Chapters Two and Three. However, it will suffice for this subsection to note that the resolution functions can be written in the form:

$$R(\tau_x, \tau_y, \tau_z) = R_p(\tau_x, \tau_y) \cdot R_v(\tau_z) \qquad \text{(A.v.4)}$$

where τ_x, τ_y are the in-plane and τ_z the out of plane components of the wavevector, and then to assume a functional form for $R_v(\tau_z)$. The decoupling of the vertical component of the resolution function $R_v(\tau_z)$ from the in-plane component $R_p(\tau_x, \tau_y)$ is a well known result (Cooper and Nathans (1967)). Therefore equation (A.i.2) becomes:

$$I^{calc}(\underline{q}_i) = \int d\tau_x\, d\tau_y\, d\tau_z\, R_p(\tau_x, \tau_y)\, R_v(\tau_z)\, S(\underline{q}_{xi} - q_o + \tau_x, \tau_y, \tau_z) \qquad \text{(A.v.5)}$$

where the direction in which the scan is performed is arbitrarily labelled x.

In a general fitting program equation (A.v.5) would be evaluated numerically as a summation over a three-dimensional mesh with the result that:

$$I^{calc}(\underline{q}) \simeq dx\, dy\, dz \sum_{r=-n_x}^{n_x} \sum_{s=-n_y}^{n_y} \sum_{t=-n_z}^{n_z} R_p(rdx, sdy) \cdot R_v(tdz)\, S(q_{xi} - q_o + r\,dx, s\,dy, t\,dz) \qquad \text{(A.v.6)}$$

where dx, dy, dz are the finite step sizes for the mesh and the limits of the integration are $\pm\ n_x dx$, $\pm\ n_y dy$ and $\pm\ n_z dz$. The derivatives of $I^{calc}(\underline{q}_i)$ with respect to the adjustable parameters $\tilde{p} \equiv (\kappa, \underline{q}_o, A, B)$ are then usually evaluated by finite differences using the approximation

$$\frac{\partial I^{calc}}{\partial p_j}(\underline{q}_i, p_j) \simeq \frac{I^{calc}(\underline{q}_i, p_j + \delta p_j) - I^{calc}(\underline{q}_i, p_j - \delta p_j)}{2\,\delta p_j} + O(\delta p_j^2) \quad \text{(A.v.7)}$$

and equation (A.v.6) to evaluate the I^{calc} on the right hand side of equation (A.v.7). A general fitting program using the results of subsection (iv) and equations (A.v.6) and (A.v.7) is therefore almost oblivious to the functional forms of the resolution function and structure factor since these are calculated in function subroutines which contain only a few lines of computer program. The price that is paid for this general applicability is the relatively large amount of computer time required. The requirement that the time taken by the fitting program should not be too great is perhaps more important than it would seem. As pointed out in subsection (iii) and (iv), the starting values for the adjustable parameters should be reasonably close to the best fit values to ensure convergence. The choice of starting parameters therefore requires a degree of human judgment based on the values obtained from the data analysis of previous scans. It is consequently not possible to simply 'load up' the computer with batch jobs and leave it to get on with them. Thus, a relatively fast 'turn round' of batch jobs is required. A general fitting program which takes of the order of an hour to run would have a turn round time of many days on the presently overcrowded

ERCC ICL 2900 computers. The need to reduce the amount of computer time the fitting program takes to run to the level of a few minutes is therefore of great importance.

The rest of this subsection shows how from a knowledge of the functional forms for $R_v(\tau_z)$ and $S(\underline{q})$ equation (A.v.5) may in part be integrated analytically and how the derivatives with respect to the adjustable parameters may also be done analytically. The first step is to write equation (A.v.5) as:

$$I^{calc}(q_i) \simeq \sum_{r=n_x} \sum_{s=n_y} dx.\, dy.\, R_p(r\,dx, s\,dy))\; I_v(\phi) \qquad \text{(A.v.8)}$$

where

$$I_v(\phi) = \int R_v(\tau_z)\; S(\phi, \tau_z) d\tau_z \qquad \text{(A.v.9)}$$

and $\phi = \sqrt{(q_{xi} - q_o + r\,dx)^2 + \kappa^2}$ for $S(\underline{q})$ given by equation (A.v.1) and $\phi = \sqrt{(q_{xi} - q_o + r\,dx)^2 + (s\,dy)^2 + \kappa^2}$ for $S(\underline{q})$ given by equation (A.v.2). The integral $I_v(\phi)$ can be done exactly for the structure factors given in equations (A.v.1) and (A.v.2) and the functional forms for $R_v(\tau_z)$ given in Chapters Two and Three. Equation (A.v.8) therefore only requires a summation over a two-dimensional rather than a three dimensional mesh and reduces the number of summations (computer time) by $\sim 2n_z$.

The structure factor applicable to Chapter Two is equation (A.v.1) and the functional form for $R_v(\tau_z)$ is a Gaussian given by

$$R_v(\tau_z) = \frac{1}{\sqrt{2\pi}\,\sigma} \exp\left(-\frac{\tau_z^2}{\sigma^2}\right) \qquad \text{(A.v.10)}$$

where σ is the standard deviation, which is 0.425 of the full width at half maximum. Therefore, in this case, equation (A.v.9) is given by (Abramowitz and Stegun (1964) p. 302),

$$I_v(\phi) = \frac{A}{\sqrt{2\pi}\,\sigma} \int_{-\infty}^{\infty} \frac{e^{-\tau_z^2/2\sigma^2}}{\tau_z^2 + \phi^2}\, d\tau_z = \frac{A}{\sigma}\cdot\sqrt{\frac{\pi}{2}}\cdot\frac{1}{\phi}\cdot e^{\frac{\phi^2}{2\sigma^2}}\cdot \operatorname{erfc}\left(\frac{\phi}{\sqrt{2}\sigma}\right) \qquad \text{(A.v.11)}$$

The appearance of three functions in equation (A.v.11), the exponential, the complementary error function and the square root in evaluating ϕ, does not slow down the program by as much as removing the z summation speeds it up. A comparison of the use of equations (A.v.6) with $n_z = 10$ and equation (A.v.8) using equation (A.v.11) in the fitting program RB2FIT showed a reduction by a factor of ~ 5 in the computer time taken. The next step is to calculate the derivatives of I_i^{calc} with respect to the adjustable parameters which are in this case, A, κ and q_o. Since these parameters are all contained in equation (A.v.11) it suffices to find the derivatives of (A.v.11) with respect to A, κ and q_o and then the sum of these over the x - y mesh as in equation (A.v.8). The derivative of (A.v.11) with respect to A is very simple because of the linear dependence of $I_v(\phi)$ on A and hence,

$$\frac{\partial I_v}{\partial A}(\phi) = \sqrt{\frac{\pi}{2}}\,\frac{1}{\phi,\sigma}\, e^{\phi^2/2\sigma^2}\, \operatorname{erfc}\left(\frac{\phi}{\sqrt{2}\sigma}\right) \qquad \text{(A.v.12a)}$$

The dependence of $I_v(\phi)$ on κ and q_o is through its dependence on ϕ and the derivatives of $I_v(\phi)$ with respect to κ and q_o can be obtained from the equations:

$$\frac{\partial I_v}{\partial \kappa}(\phi) = \frac{\kappa}{\phi} \frac{\partial I_v}{\partial \phi}(\phi) \text{ and } \frac{\partial I_v}{\partial \phi}(\phi) = - \frac{(q_{xi} - q_o + rdx)}{\phi} \frac{\partial I_v}{\partial \phi}(\phi)$$

(A.v.12b)

and

$$\frac{\partial I_v}{\partial \phi}(\phi) = \frac{A}{\sigma} \left[\frac{1}{\sigma\phi} + \sqrt{\frac{\pi}{2}} \left(\frac{1}{\phi^2} - \frac{1}{\sigma^2} \right) e^{\phi^2/2\sigma^2} \operatorname{erfc}\left(\frac{\phi}{\sqrt{2}\sigma} \right) \right] \quad \text{(A.v.12c)}$$

The effect of calculating these derivatives analytically and summing them over the x - y mesh in equation (A.v.8) at the same time as $I_v(\phi)$ reduces the computer time taken by a factor of ~ 7.

In Chapter Three the structure factor used was equation (A.v.2) and as a consequence the integral $I_v(\phi)$ is written as:

$$I_v(\phi) = A. \; I_L(\phi) - \frac{B}{2\kappa} \frac{\partial}{\partial \kappa} (I_L(\phi)) \quad \text{(A.v.13)}$$

where the integral $I_L(\phi)$ is given by:

$$I_L(\phi) = \int \frac{R_v(\tau_z)}{\tau_z^2 + \phi^2} \, d\tau_z \quad \text{(A.v.14)}$$

with $\phi = \sqrt{(q_{xi} - q_o + r\,dx)^2 + (s\,dy)^2 + \kappa^2}$ and use has been made of equation (A.v.3) in incorporating the Lorentzian squared into equation (A.v.13). The functional form of $R_v(\tau_z)$ in Chapter Three is that of a triangle given by:

$$R_v(\tau_z) = \begin{cases} \frac{1}{Q_v} \left(1 - \frac{|\tau_z|}{Q_v}\right) & |\tau_z| < Q_v \\ 0 & |\tau_z| > Q_v \end{cases} \quad \text{(A.v.15)}$$

where Q_v is the full width at half maximum of the triangle.

Hence, the integral $I_L(\phi)$ is given by:

$$I_L(\phi) = \frac{2}{Q_v} \int_0^{Q_v} \frac{1 - (\tau_z/Q_v)}{(\tau_z^2 + \phi^2)} \, d\tau_z = \frac{2}{\phi} \text{Tan}^{-1}\left(\frac{Q_v}{\phi}\right) - \frac{1}{Q_v} \text{Log}_e\left(1 + \left(\frac{Q_v}{\phi}\right)^2\right) \tag{A.v.16}$$

The derivative of $I_L(\phi)$ with respect to κ can be done using the chain rule such that:

$$\frac{\partial I_L}{\partial \kappa}(\phi) = \frac{\kappa}{\phi} \frac{\partial I_L}{\partial \phi}(\phi) = -\frac{2\kappa}{\phi^3} \text{Tan}^{-1}\left(\frac{Q_v}{\phi}\right) \tag{A.v.17}$$

and therefore equation (A.v.13) for $I_v(\phi)$ can be evaluated as:

$$I_v(\phi) = \left(2A + \frac{B}{\phi^2}\right)\left(\frac{1}{\phi} \text{Tan}^{-1}\left(\frac{Q_v}{\phi}\right)\right) - A \, \text{Log}_e\left(1 + \left(\frac{Q_v}{\phi}\right)^2\right) \tag{A.v.18}$$

The derivatives of $I_v(\phi)$ with respect to A and B are therefore given by:

$$\frac{\partial I_v}{\partial A}(\phi) = \frac{2}{\phi} \text{Tan}^{-1}\left(\frac{Q_v}{\phi}\right) - \frac{1}{Q_v} \text{Log}_e\left(1 + \left(\frac{Q_v}{\phi}\right)^2\right) \tag{A.v.19a}$$

$$\frac{\partial I_v}{\partial B}(\phi) = \frac{1}{\phi^3} \text{Tan}^{-1}\left(\frac{Q_v}{\phi}\right) \tag{A.v.19b}$$

and the derivatives with respect to κ and q_o given by equations (A.v.12b) and:

$$\frac{\partial I_v}{\partial \phi}(\phi) = -\left(2A + \frac{3B}{\phi^2}\right)\left(\frac{1}{\phi^2} \text{Tan}^{-1}\left(\frac{Q_v}{\phi}\right)\right) - \left(\frac{B}{\phi^3}\right)\left(\frac{Q_v}{Q_v^2 + \phi^2}\right) \tag{A.v.19c}$$

(vi) Evaluating both vertical and longitudinal convolutions analytically

In the experiments described in Chapter Three, the resolution function $R(\tau_x, \tau_y, \tau_z)$ decouples to an even greater extent than equation (A.v.4) and can be written as,

$$R(\tau_x, \tau_y, \tau_z) = R_T(\tau_x) . R_L(\tau_y) . R_v(\tau_z) \qquad \text{(A.vi.1)}$$

where the labels T and L refer to the transverse and longitudinal directions discussed in Chapter Three. This subsection shows how, given equation (A.vi.1) and a triangular form for $R_L(\tau_y)$ that equation (A.v.8) may be further integrated analytically to give the result:

$$I^{calc}(\underline{q}_i) = \sum_{r=-n_x}^{n_x} dx . R_T(r\, dx)\ I_L(\psi) \qquad \text{(A.vi.2)}$$

where

$$I_L(\psi) = \int R_L(\tau_y)\ I_v(\phi)\ d\tau_y \qquad \text{(A.vi.3)}$$

with $I_v(\phi)$ given by equation (A.v.18) and $\phi^2 = \tau_y^2 + \psi^2$ whereby $\psi = \sqrt{(q_{xi} - q_o + r\, dx)^2 + \kappa^2}$. In order to perform the integral $I_L(\psi)$ some of the terms in the integrand are replaced by a power series expansion which is integrated term by term. The radius of convergence for this expansion sets a limit to the use of equation (A.vi.2) rather than equation (A.v.8). It will be shown later that the series converges if $\psi < \sqrt{Q_v^2 - Q_L^2}$, where Q_v and Q_L are the full width half maxima of the vertical and longitudinal components of the resolution function. However, in practical terms the use of equation (A.vi.2) ceases to be

advantageous if $\psi > 0.6\sqrt{Q_v^2 - Q_L^2}$ because of the large number of terms that must be included in the power series. Equation (A.vi.2) is therefore very useful if κ is small, since the range over which an experimental scan is appreciably different from the background level will satisfy this condition. The advantage in using equation (A.vi.2) in such circumstances lies not just in time saving, but also in a greatly improved accuracy. Since with the vertical and longitudinal integrations done analytically the step size for the numerical integration in the transverse direction can be considerably reduced.

Therefore if the longitudinal component of the resolution function is given by:

$$R_L(\tau_y) = \begin{cases} \frac{1}{Q_L}(1 - \frac{|\tau_y|}{Q_L}) & |\tau_y| < Q_L \\ 0 & |\tau_y| > Q_L \end{cases} \qquad \text{(A.vi.4)}$$

then the integral $I_L(\psi)$ given in equation (A.vi.3) is:

$$I_L(\psi) = \frac{2A}{Q_L}\int_0^{Q_L} d\tau_y(1 - \frac{\tau_y}{Q_L})\left[\frac{2}{\sqrt{\tau_y^2 + \psi^2}}\,\mathrm{Tan}^{-1}\left(\frac{Q_v}{\sqrt{\tau_y^2 + \psi^2}}\right) - \frac{1}{Q_v}\,\mathrm{Log}_e(Q_v^2 + \psi^2 + \tau_y^2) - \frac{1}{Q_v}\,\mathrm{Log}_e(\tau_y^2 + \psi^2)\right] +$$

$$\frac{2B}{Q_L}\int_0^{Q_L} d\tau_y(1 - \frac{\tau_y}{Q_L})\left[\frac{1}{(\tau_y^2 + \psi^2)^{3/2}}\,\mathrm{Tan}^{-1}\left(\frac{Q_v}{\sqrt{\tau_y^2 + \psi^2}}\right)\right] \qquad \text{(A.vi.5)}$$

The evaluation of equation (A.vi.5) requires a total of ten integrals to be performed, of which eight can be done analytically

and two must be done by power series expansion. These integrals are labelled with a notation I_{MN} which refers to equation (A.vi.5), where M = L or LS for an integral which contributes to the Lorentzian or Lorentzian squared components of equation (A.vi.5) and N numbers the respective integrals from left to right in equation (A.vi.5).

The integrals which contribute to the Lorentzian component are considered first. The integral I_{L3} is given by:

$$I_{L3} = \frac{1}{Q_v}\int_o^{QL}(1 - \frac{\tau_y}{Q_L})\ \mathrm{Log}_e(\tau_y^2 + \psi^2)\,d\tau_y \qquad \text{(A.vi.6a)}$$

$$= \frac{1}{Q_v}\int_o^{Q_L}\mathrm{Log}_e\left[1 + (\frac{\tau_y}{\psi})^2\right]d\tau_y - \frac{1}{Q_v}\int_o^{Q_L}\tau_y\ \mathrm{Log}_e\left[1 + (\frac{\tau_y}{\psi})^2\right]d\tau_y -$$

$$\frac{2}{Q_v}\ \mathrm{Log}_e(\psi)\int_o^{Q_L}(1 - \frac{\tau_y}{Q_L})\,d\tau_y \qquad \text{(A.vi.6b)}$$

$$= \frac{\psi}{Q_v}\left[(\frac{Q_L}{\psi})\ (\mathrm{Log}_e\left[1+(\frac{Q_L}{\psi})^2\right]-2) + 2\ \mathrm{Tan}^{-1}(\frac{Q_L}{\psi})\right] - \frac{\psi^2}{2Q_v\ Q_L}$$

$$\left[(1 + (\frac{Q_L}{\psi})^2)\ (\mathrm{Log}_e\left[1 + (\frac{Q_L}{\psi})^2\right] - 1) + 1\right] - \frac{Q_L}{Q_v}\mathrm{Log}_e(\psi) \qquad \text{(A.vi.6c)}$$

where the results

$$\int_a^b \mathrm{Log}_e(1 + x^2)\,dx = \frac{1}{2}\int_{1+a^2}^{1+b^2}\frac{\mathrm{Log}_e(z)}{\sqrt{z-1}}\,dz = \left[\sqrt{z-1}(\mathrm{Log}_e(z) - 2) +\right.$$

$$\left. 2\ \mathrm{Tan}^{-1}(\sqrt{z-1})\right]_{1+a^2}^{1+b^2} \qquad \text{(A.vi.7a)}$$

which is given on page 204 of Gradsteyn and Ryzhik (1965) and,

$$\int_a^b x \, \mathrm{Log}_e (1 + x^2) dx = \frac{1}{2} \left[(1 + x^2)(\mathrm{Log}_e(1 \quad x^2) - 1) \right]_a^b \qquad \text{(A.vi.7b)}$$

have been used. The integral I_{L2} is the same as I_{L1} but with ψ replaced by $\sqrt{Q_v^2 + \psi^2}$ and therefore I_{L2} is given by:

$$I_{L2} = \frac{1}{Q_v} \int_o^{Q_L} (1 - \frac{\tau_y}{Q_L}) \, \mathrm{Log}_e(\tau_y^2 + Q_v^2 + \psi^2) d\tau_y \qquad \text{(A.vi.8a)}$$

$$= \frac{\sqrt{Q_v^2 + \psi^2}}{Q_v} \left[(\frac{Q_v}{\sqrt{Q_v^2 + \psi^2}}) (\mathrm{Log}_e \left[1 + \frac{Q_L^2}{(Q_v^2 + \psi^2)} \right] - 2) + 2. \right.$$

$$\left. \mathrm{Tan}^{-1} (\frac{Q_L}{\sqrt{Q_v^2 + \psi^2}}) \right] - \frac{(Q_v^2 + \psi^2)}{2 Q_v Q_L} \left[(1 + \frac{Q_L^2}{Q_v^2 + \psi^2}) (\mathrm{Log}_e \right.$$

$$\left. \left[1 + \frac{Q_L^2}{(Q_v^2 + \psi^2)} \right] - 1) + 1 \right] - \frac{Q_L}{Q_v} \mathrm{Log}_e (\sqrt{Q_v^2 + \psi^2}) \qquad \text{(A.vi.8b)}$$

The integral I_{L1} given by:

$$I_{L1} = 2 \int_o^{Q_L} (1 - \frac{\tau_y}{Q_L}) \, \mathrm{Tan}^{-1} (\frac{Q_v}{\sqrt{\tau_y^2 + \psi^2}}) \frac{1}{\sqrt{\tau_y^2 + \psi^2}} d\tau_y \qquad \text{(A.vi.9)}$$

must be split into two parts $I_{L1}^{(1)}$ and $I_{L1}^{(2)}$ which separate the terms in the triangle. Thus, the integral $I_{L1}^{(2)}$ is given by

$$I_{L1}^{(2)} = 2 \int_o^{Q_L} (\frac{\tau_y}{Q_L}) \, \mathrm{Tan}^{-1} (\frac{Q_v}{\sqrt{\tau_y^2 + \psi^2}}) \frac{1}{\sqrt{\tau_y^2 + \psi^2}} d\tau_y \qquad \text{(A.vi.10a)}$$

$$= - \frac{2 Q_v}{Q_L} \int_{Q_v/\psi}^{Q_v/\sqrt{Q_L^2 + \psi^2}} \frac{\mathrm{Tan}^{-1}(z)}{z^2} dz \qquad \text{(A.vi.10b)}$$

$$= \frac{2 Q_v}{Q_L} \left[\frac{\mathrm{Tan}^{-1}(z)}{z} + \frac{1}{2} \mathrm{Log}_e (\frac{1 + z^2}{z^2}) \right]_{Q_v/\psi}^{Q_v/\sqrt{Q_L^2 + \psi^2}} \qquad \text{(A.vi.10c)}$$

where in going from equation (A.vi.10a) to (A.vi.10b) the substitution $z = Q_v/\sqrt{\tau_y^2 + \psi^2}$ was used and the integral (A.vi.10b) is given on page 210 of Gradsteyn and Ryzhik (1965). The remaining integral for the Lorentzian component is $I_{L1}^{(1)}$ and it is given by:

$$I_{L1}^{(1)} = 2\int_0^{Q_L} \frac{1}{\sqrt{\tau_y^2 + \psi^2}} \, \mathrm{Tan}^{-1}\left(\frac{Q_v}{\sqrt{\tau_y^2 + \psi^2}}\right) d\tau_y \qquad \text{(A.vi.11a)}$$

$$= \pi\int_0^{Q_L} \frac{d\tau_y}{\sqrt{\tau_y^2 + \psi^2}} - 2\int_0^{Q_L} \frac{\mathrm{Tan}^{-1}\left(\tau_y^2 + \psi^2/Q_v\right)}{\sqrt{\tau_y^2 + \psi^2}} d\tau_y \qquad \text{(A.vi.11b)}$$

where the result $\mathrm{Tan}^{-1}(1/x) = \pi/2 - \mathrm{Tan}^{-1}(x)$ has been used in going from (A.vi.11a) to (A.vi.11b). The first integral on the right hand side of equation (A.vi.11b) can be done using the substitution $\tau_y = \psi\mathrm{Sinh}\theta$. However, the second integral on the right hand side of equation (A.vi.11b) cannot be done in closed form and therefore it is necessary to expand the inverse tangent as a power series and integrate term by term. The Taylor series for $\mathrm{Tan}^{-1}(x)$ can be written as:

$$\mathrm{Tan}^{-1}(x) = \int \frac{dx}{1 + x^2} = \sum_{m=0}^{\infty} (-1)^m \int x^{2m}\, dx = \sum_{m=0}^{\infty} \frac{(-1)^m x^{2m+1}}{2m + 1}, \quad |x|<1 \qquad \text{(A.vi.12)}$$

where the term by term integration is allowed for $|x|<1$ since the binomial expansion of the integrand satisfies the condition for uniform convergence (Arfken (1970) p. 256). In equation (A.vi.11b) it is the power series expansion for $\mathrm{Tan}^{-1}(x)/x$ that is used, which can be shown to be uniformly convergent for $|x|<1$. Hence, if

equation (A.vi.12) is substituted into equation (A.vi.11b) the series may be integrated term by term, which if the substitution $y = \psi . \tau_y$ is made gives:

$$I_{L1}^{(1)} = \pi \, \mathrm{Sinh}^{-1}\left(\frac{Q_L}{\psi}\right) - 2 \sum_{m=o}^{\infty} \frac{(-1)^m}{2m+1} \left(\frac{\psi}{Q_v}\right)^{2m+1} \int_o^{Q_L/\psi} (1+y^2)^m \, dy \qquad \text{(A.vi.13a)}$$

$$= \pi \, \mathrm{Sinh}^{-1}\left(\frac{Q_L}{\psi}\right) - \left(\frac{2\,Q_L}{Q_v}\right) \sum_{m=o}^{\infty} \frac{(-1)^m}{(2m+1)} \left(\frac{\psi}{Q_v}\right)^{2m} \sum_{n=o}^{\infty} \frac{{}^{m}C_n}{(2n+1)} \left(\frac{Q_L}{\psi}\right)^{2n} \qquad \text{(A.vi.13b)}$$

where ${}^{m}C_n$ is the binomial coefficient $\frac{m!}{(m-n)!\,n!}$.

The convergence properties of the summation on the right hand side of equation (A.vi.13b) need to be considered since they determine the usefulness of this result. If the m^{th} term in the summation over m is denoted as S_m then the magnitude of S_m is such that:

$$|S_m| < \frac{1}{2m+1} \left(\frac{\psi^2 + Q_L^2}{Q_L^2}\right)^m \qquad \text{(A.vi.14)}$$

Since the summation over m is an alternating series, the series converges by the Leibnitz criterion (Arfken, (1970) p. 250) if $\psi < \sqrt{Q_v^2 - Q_L^2}$. The range of ψ for which the series result is useful in practice is limited by the number of terms that need to be taken in the summation to obtain a given numerical precision. The summation from m = o to ∞ in equation (A.vi.13b) is therefore replaced by a sum S(u) given by:

$$S(u) = \sum_{m=o}^{u} \left(\frac{Q_L}{Q_v}\right) \frac{(-1)^m}{(2m+1)} \left(\frac{\psi}{Q_v}\right)^{2m} \sum_{n=o}^{m} \frac{{}^{m}C_n}{(2n+1)} \left(\frac{Q_L}{\psi}\right)^{2n} \qquad \text{(A.vi.15)}$$

Since the series is alternating and $|S_{m+1}| < |S_m|$ it is guaranteed that the sum from u to ∞ will be less than the difference $|S(u) - S(u-1)|$ and the summation may be truncated when the difference between successive terms is less than some prescribed value. In figure (A.vi.1) the value of u as a function of ψ^2 is plotted, where the value of u was found by evaluating equation (A.vi.15) until u satisfied the condition $|S(u) - S(u-1)| < 0.0001\ S(u)$. The values $Q_v = 0.0517$ and $Q_L = 0.00765$ were used which are applicable to the results for the $Mn_{0.65}Zn_{0.35}F_2$ data reported in Chapter Three. The best fit straight line shown in figure (A.vi.1) gives the empirical relation $U = \exp((0.96 \pm 0.11) + (1032 \pm 63)\psi^2)$.

The choice of a percentage cut off rather than an absolute cut off to the summation is easily justified. Since, in equation (A.i.1) the difference between the observed and calculated values is compared to the error in the observed value the effect that the percentage truncation has can be found by comparing the error introduced in the calculated value to the error in the observed value. The error in the calculated value will be $0.02n_x$ per cent which for $n_x = 50$, the value used in Chapter Three, is insignificant compared to the error in the observed value. However, the advantage of a percentage cut off is that it requires fewer terms to be summed when ψ is 'large'. The amount of time taken to evaluate S(u) is expected to go as the number of terms that need to be summed, which is $\frac{1}{2}(u^2 + u)$. If the empirical formula for u is substituted into this relation, then it can be seen that the amount of computer time taken to evaluate S(u) varies rapidly with

Figure (A.vi.1)

This figure shows the variation of the upper limit U of the sum in equation (A.vi.15) for which convergence was obtained as a function of ψ^2. The solid line is the best straight line fit.

FIGURE(A.vi.1)

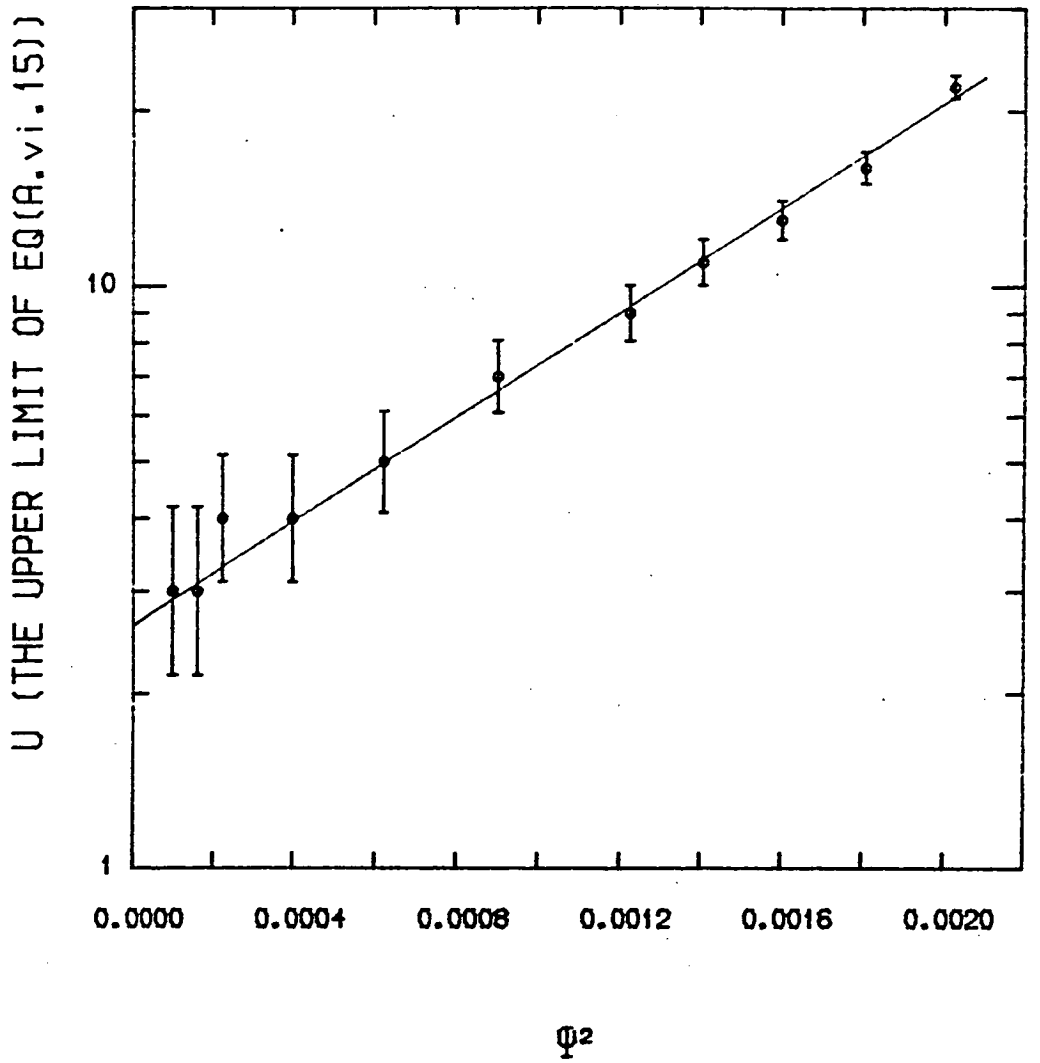
U (THE UPPER LIMIT OF EQ(A.vi.15))
10
1
0.0000
0.0004
0.0008
0.0012
0.0016
0.0020
Φ²

ψ. For the values of the resolution function for the $Mn_{0.65}Zn_{0.35}F_2$ measurements in Chapter Three, a practical limit on the computer time used meant that only values of $\psi < 0.6\sqrt{Q_v^2 - Q_L^2}$ could be calculated.

The integration for the Lorentzian squared component is done in a similar way to that for the Lorentzian. The integral I_{LS1} is given by:

$$I_{LS1} = \int_0^{Q_L} (1 - \frac{\tau_y}{Q_L}) \frac{1}{(\tau_y^2 + \psi^2)^{3/2}} \text{Tan}^{-1}(\frac{Q_v}{\sqrt{\tau_y^2 + \psi^2}}) d\tau_y \qquad \text{(A.vi.16)}$$

This integral is broken up into two parts so that $I_{LS1}^{(2)}$ is given by,

$$I_{LS1}^{(2)} = \int_0^{Q_L} (\frac{\tau_y}{Q_L}) \frac{1}{(\tau_y^2 + \psi^2)^{3/2}} \text{Tan}^{-1}(\frac{Q_v}{\tau_y^2 + \psi^2}) d\tau_y \qquad \text{(A.vi.17a)}$$

$$= \frac{1}{Q_L Q_v} \int_{Q_v/\sqrt{Q_L^2+\psi^2}}^{Q_v/\psi} \text{Tan}^{-1}(z)\, dz \qquad \text{(A.vi.17b)}$$

$$= \left[\frac{1}{Q_L Q_v} (z \text{Tan}^{-1}(z) - \frac{1}{2}\text{Log}_e(1 + z^2))\right]_{Q_v/\sqrt{Q_L^2+\psi^2}}^{Q_v/\psi}$$

where in going from equation (A.vi.17a) to (A.vi.17b) the substitution $z = Q_v/\sqrt{\tau_y^2 + \psi^2}$ was used and the integral (A.vi.17b) is given on page 82 of Abramowitz and Stegun (1964). The integral $I_{LS1}^{(1)}$ is given by:

$$I_{LS1}^{(1)} = \int_0^{Q_L} \frac{1}{(\tau_y^2 + \psi^2)^{3/2}} \text{Tan}^{-1}(\frac{Q_v}{\sqrt{\tau_y^2 + \psi^2}}) d\tau_y \qquad \text{(A.vi.18a)}$$

$$= \frac{\pi}{2}\int_o^{Q_L} \frac{d\tau_y}{(\tau_y^2 + \psi^2)^{3/2}} - \int_o^{Q_L} \frac{1}{(\tau^2 + \psi^2)^{3/2}} \; \mathrm{Tan}^{-1}\left(\frac{\sqrt{\tau_y^2 + \psi^2}}{Q_v}\right) d\tau_y \qquad \text{(A.vi.18b)}$$

where the result $\mathrm{Tan}^{-1}\left(\frac{1}{x}\right) = \frac{\pi}{2} - \mathrm{Tan}^{-1}(x)$ has been used. The first integral on the right hand side of equation (A.vi.18b) can be done by using the substitution $\tau_y = \psi \mathrm{Sinh}\theta$, and the result is:

$$\frac{\pi}{2}\int_o^{Q_L} \frac{d\tau_y}{(\tau_y^2 + \psi^2)^{3/2}} = \frac{\pi}{2\psi^2} \mathrm{Tanh}\left[\mathrm{Sinh}^{-1}\left(\frac{Q_L}{\psi}\right)\right] = \frac{\pi\, Q_L}{2\psi^2\sqrt{Q_L^2 + \psi^2}} \qquad \text{(A.vi.19)}$$

The second integral on the right hand side of equation (A.vi.18b) must be done by expanding the inverse tangent using equation (A.vi.12). The result is that:

$$\int_o^{Q_L} \frac{1}{(\tau_y^2 + \psi^2)^{3/2}} \mathrm{Tan}^{-1}\left(\frac{\tau_y^2 + \psi^2}{Q_v}\right) d\tau_y = \frac{1}{\psi^2} \sum_{m=o}^{\infty} \frac{(-1)^m}{(2m+1)} \left(\frac{\psi}{Q_v}\right)^{2m+1} x$$

$$\int_o^{Q_L/\psi} (1 + y^2)^{m-1}\, dy \qquad \text{(A.vi.20a)}$$

$$= \frac{1}{\psi Q_v}\int_o^{Q_L/\psi} \frac{dy}{(1+y^2)} - \frac{1}{Q_v^2} \sum_{m=o}^{\infty} \frac{(-1)^m}{(2m+3)} \left(\frac{\psi}{Q_v}\right)^{2m+1} \int_o^{Q_L/\psi} (1+y^2)^m\, dy \qquad \text{(A.vi.20b)}$$

$$= \frac{1}{\psi Q_v} \mathrm{Tan}^{-1}\left(\frac{Q_L}{\psi}\right) - \frac{Q_L}{Q_v^3} \sum_{m=o}^{\infty} \frac{(-1)^m}{(2m+3)} \left(\frac{\psi}{Q_v}\right)^{2m} \sum_{n=o}^{m} {}^{m}C_n \frac{1}{(2n+1)} \left(\frac{Q_L}{\psi}\right)^{2n} \qquad \text{(A.vi.20c)}$$

Hence, the integral $I_{LS1}^{(1)}$ is:

$$I_{LS1}^{(1)} = \frac{\pi\, Q_L}{2\psi^2\sqrt{Q_L^2 + \psi^2}} - \frac{1}{\psi Q_v} \mathrm{Tan}^{-1}\left(\frac{Q_L}{\psi}\right) + \frac{Q_L}{Q_v^3} \sum_{m=o}^{\infty} \frac{(-1)m}{(2m+3)} \left(\frac{\psi}{Q_v}\right)^{2m} x$$

$$\sum_{n=o}^{m} {}^{m}C_n \frac{1}{(2n+1)} \left(\frac{Q_L}{\psi}\right)^{2n} \qquad \text{(A.vi.21)}$$

The summation on the right hand side of equation (A.vi.21) differs from the summation in equation (A.vi.18b) only through having a factor of (2m + 3) rather than (2m + 1) in the denominator. It is therefore clear that the convergence properties for this summation will be the same as those for the summation discussed earlier.

Therefore $I_L(\psi)$ can be written in terms of the various integrals as:

$$I_L(\psi) = \frac{2A}{Q_L}\left(I_{L1}^{(1)} - I_{L1}^{(2)} - I_{L2} - I_{L3}\right) + \frac{2B}{Q_L}\left(I_{LS1}^{(1)} - I_{LS1}^{(2)}\right) \qquad \text{(A.vi.22)}$$

The evaluation of the right hand side of equation (A.vi.22) may seem to require the evaluation of a large number of inverse tangents and logarithms. However, the functions that occur in the integrals contributing to equation (A.vi.22) occur many times and it is possible to write equation (A.vi.22) in terms of what is a reasonably limited set of quantities. These are

$$a_1 = Q_L^2 + \psi^2 \quad , \quad r_1 = \sqrt{a_1}$$

$$a_2 = Q_v^2 + \psi^2 \quad , \quad r_2 = \sqrt{a_2}$$

$$a_3 = Q_v^2 + Q_L^2 + \psi^2 \quad , \qquad \text{(A.vi.23)}$$

$$S_1 = {}^{1}/_{Q_v Q_L} \quad , \quad S_2 = {}^{Q_L}/_{Q_v}$$

$$z_1 = \frac{Q_L}{\psi} \quad , \quad z_2 = \frac{Q_v}{\psi} \quad , \quad z_3 = \frac{Q_v}{r_1}, \quad z_4 = \frac{Q_L}{r_2}$$

$$t_1 = \mathrm{Tan}^{-1}(z_1), \; t_2 = \mathrm{Tan}^{-1}(z_2), \; t_3 = \mathrm{Tan}^{-1}(z_3), \; t_4 - \mathrm{Tan}^{-1}(z_4)$$

$$\ell_1 = \mathrm{Log}_e(a_1), \; \ell_2 = \mathrm{Log}_e(a_2), \; \mu_3 = \mathrm{Log}_e(a_3), \; \ell_4 = \mathrm{Log}_e(\psi^2)$$

$$F(L) = \left(\frac{Q_L}{Q_v}\right) \sum_{m=o}^{u} \frac{1}{(2m+L)} \left(\frac{-1}{z_2^2}\right)^m \sum_{n=o}^{m} \frac{{}^{m}C_n}{(2n+1)} (z_2^2)^n$$

Then equation (A.vi.22) is given in terms of the quantities in equation (A.vi.23) as:

$$I_L(\psi) = \frac{A}{Q_L}\left[2\pi\ \mathrm{Sinh}^{-1}(z_1) - 4F(1) - \frac{4}{S_2}\left(\frac{t_3}{z_3} - \frac{t_2}{z_2}\right) - \frac{2}{S_2}(\ell_3 - \ell_2)\right.$$

$$+ S_2\left[\left[\left(1-\frac{1}{z_1^2}\right)\ell_1 - \left(1 - \frac{1}{z_4^2}\right)\ell_3\right] + \left[\frac{\ell_4}{z_1^2} - \frac{\ell_2}{z_4^2}\right] + 4\left[\frac{t_1}{z_1} - \frac{t_4}{z_1}\right]\right]\Bigg]$$

$$+ \frac{B}{Q_L}\left[\frac{\pi\ z_1}{\psi\ r_1}\ 2S_1(z_1t_1 + z_2t_2 - z_3t_3) + S_1(\ell_1 + \ell_2 - \ell_3 - \ell_4)\right.$$

$$\left. + 2F(3)\right] \qquad \text{(A.vi.24)}$$

The derivatives of $I_L(\psi)$ with respect to A and B can still be done analytically because of the linear dependence. The dependence of $I_L(\psi)$ on the parameters κ and q_o has, however, become very involved and as a result the derivatives of $I_L(\psi)$ with respect to these parameters was done by finite differences.

References

Abramowitz M. and Stegun I. (1964) 'Handbook of Mathematical Functions', Dover Press, New York.

Aharony A. (1978) Phys. Rev. B, 18, 3328.

Aharony A. (1982) J. Mag. Magn. Mat., 31 - 34, 1432.

Aharony A. (1983) Lecture notes of the school on 'Multicritical Phenomena', Geilo, Norway.

Aharony A,, Imry Y. and Ma S.K. (1976), Phys. Rev. Lett., 37, 1364.

Alben R. (1969) J. Phys. Soc. Jpn., 26, 261.

Alben R., Kirkpatrick S. and Beeman D. (1977) Phys. Rev. B, 15,346.

Alben R. and Thorpe M.F. (1975) J. Phys. C, 8, L275.

Als-Nielsen J., Birgeneau R.J. Guggenheim H.J. and Shirane G. (1975) Phys. Rev. B, 12, 4963.

Amit D.J. (1974) J Phys. C, 7, 3369.

Amit D.J. (1978) 'Field Theory, the Renormalisation Group and Critical Phenomena', McGraw Hill, London.

Arfken G. (1970) 'Mathematical Methods for Physicists', Academic Press, London.

Bacon G.E. 'Neutron Diffraction', 3rd ed., Clarendon Press, Oxford.

Bard Y. (1974) 'Nonlinear Parameter Estimation', Academic Press, London

Belanger D.P., King A.R. and Jaccarino V. (1982) Phys. Rev. Lett., 48, 1050.

Bertrand D., Petitgrand D., Hennion B. and Legrand S. (1981) J. Phys. C, 14, 1975.

Bervillier C (1976) Phys. Rev. B, 14, 4964.

Binder K., Imry Y. and Pytte E. (1981) Phys. Rev. B, 24, 6736.

Birgeneau R.J., Guggenheim H.J. and Shirane G. (1970) Phys. Rev. B, 1, 2211.

Birgeneau R.J., Yelon W.B., Cohen E. and Makovsky J. (1972) Phys. Rev. B, 5, 2607.

Birgeneau R.J., Cowley R.A., Shirane G., Tarvin J.A. and Guggenheim H.J. (1980) Phys. Rev. B, 21, 317.

Birgeneau R.J., Cowley R.A., Shirane G., Yoshizawa H., Belanger D.P., King A.R. and Jaccarino V. (1983a) Phys. Rev. B, 27, 6747.

Birgeneau R.J., Yoshizawa H., Cowley R.A., Shirane G. and Ikeda H. (1983b) Phys. Rev. B, 28, 1438.

Brady-Moreira F.G., Fittipaldi I.R., Rezende S.M., Tahir-Kheli R.A., and Zeks B. (1977) Phys. Status Solidi B, 80, 385.

Breed D.J., Gillijamse K. and Miedema A.R. (1969) Physica, 45, 205.

Bruce A.D. (1981) J. Phys. C, 14, 193.

Bruce A.D. (1982) in 'Nonlinear Phenomena at Phase Transitions and Instabilities', ed. T. Riste, Plenum, New York.

Buyers W.J.L., Holden T.M., Svensson E.C., Cowley R.A. and Hutchings M.T. (1971) J. Phys. C, 4, 2139.

Buyers W.J.L., Pepper D.E. and Elliott R.J. (1972) J. Phys. C, 5, 2611.

Campbell J.A. and Vickers R.E.M. (1983) J. Phys. C, 16, 999.

Cardy J. (1983). Unpublished, U.C.S.B. preprint no. TH-55.

Chesser N.J. and Axe J.D. (1973) Acta Cryst A, 29, 160.

Coniglio A. (1983) Lecture notes of the school on 'Magnetic Phase Transitions', Erice, Sicily, Italy.

Coombs G.J. and Cowley R.A. (1975) J. Phys. C, 8, 1889.

Coombs G.J., Cowley R.A., Buyers W.J.L., Svensson E.C., Holden T.M. and Jones D.A. (1976) J. Phys. C, 9, 2167.

Cooper M.J. And Nathans R. (1967) Acta Cryst, 23, 357.

Cowley R.A. (1980) Phil. Trans.R . Soc. Lond. B, 290, 583.

Cowley R.A. (1982) in 'Excitations in Disordered Systems', ed. M.F. Thorpe, Plenum, New York.

Cowley R.A., Birgeneau R.J. and Shirane G. (1980a) in 'Ordering in Strongly Fluctuating Condensed Matter Systems', ed. T. Riste, Plenum, New York.

Cowley R.A., Birgeneau R.J., Shirane G., Guggenheim H.J. and Ikeda H. (1980d) Phys. Rev. B, 21, 4038.

Cowley R.A., Birgeneau R.J., Shirane G. and Yoshizawa H. (1983b) Lecture notes of the school on 'Multicritical Phenomena', Geilo, Norway.

Cowley R.A. and Buyers W.J.L (1972) Rev. Mod. Phys., 44, 406.

Cowley R.A. and Buyers W.J.L. (1982) J. Phys. C, 15, L1209.

Cowley R.A., Buyers W.J.L., Martel P. and Stevenson R.W.H. (1973) J. Phys. C, 6, 2997.

Cowley R.A. and Carneiro K. (1980) J. Phys. C, 13, 3281.

Cowley R.A., Hagan M., Yoshizawa H. and Shirane G. (1983a). Unpublished.

Cowley R.A., Shirane G., Birgeneau R.J. and Guggenheim H.J. (1977) Phys. Rev. B, 15, 4292.

Cowley R.A., Shirane G., Birgeneau R.J., Svensson E.C. and Guggenheim H.J. (1980b) Phys. Rev. B, 22, 4412.

Cowley R.A., Yoshizawa H., Shirane G., Birgeneau R.J., Belanger D.P., King A.R. and Jaccarino V. (1983c). Unpublished.

Dolling G. (1975) in 'Dynamical Properties of Solids', Vol. 1, ed. G.K. Horton and A.A. Maradudin, North Holland, Amsterdam.

Elliott R.J. (1982) in 'Excitations in Disordered Systems', ed. M. Thorpe, Plenum, New York.

Elliott R.J. and Thorpe M.F. (1968) J. Appl. Phys., 39, 802.

Fähnle M. (1983) Phys. Rev. B, 27, 2851.

Fisher M.E. (1964) J. Math. Phys., 5, 944.

Fisher M.E. and Aharony A. (1974) Phys. Rev. B, 10, 2818.

Fisher M.E. and Burford R.J. (1967) Phys. Rev., 156, 583.

Fishman S. and Aharony A. (1978) Phys. Rev. B, 18, 3507.

Fishman S. and Aharony A. (1979) J. Phys. C, 12, L729.

Frodesen A.G., Skjeggstad O. and Tøfte H. (1979) 'Probability and Statistics for Particle Physics', Universitetforlaget, Oslo.

Fyne P. and Hutchings M.T. (1982) private communication.

Gehring G. (1977) J. Phys. C, 10, 531.

de Gennes P.G. (1976). J. de Physique Lett., 37, L1.

Gradsteyn I.S. and Ryzhik I.M. (1965) 'Tables of Integrals, Series and Products', Academic Press, London.

Grant M. and Gunton J.D. (1983). Unpublished.

Grinstein G. (1976) Phys. Rev. Lett., 37, 944.

Grinstein G. and Ma S.K. (1982) Phys. Rev. Lett., 49, 685.

Grinstein G. and Mukamel D. (1983) Phys. Rev. B, 27, 4503.

Halley J.W. and Holcomb W.K. (1978) J. Phys. C, 11, 753.

Harris A.B. (1974) J. Phys. C, 7, 1671.

Hoel P.G. (1971) 'Introduction to Mathematical Statistics', 4th ed., Wiley, New York.

Hohenberg P.C., Aharony A., Halperin B.I. and Siggia E.D. (1976) Phys. Rev. B, 13, 2986.

Hutchings M.T. (1964) Solid State Phys., 16, 227.

Hutchings M.T., Ikeda H. and Janke E. (1982) Phys. Rev. Lett., 49, 386.

Hutchings M.T., Rainford B.D. and Guggenheim H.J. (1970) J. Phys. C, 3, 307.

Hutchings M.T., Schulhof M.P. and Guggenheim H.J. (1972) Phys. Rev. B, 5, 154.

Ikeda H. (1981) J. Phys. Soc. Jpn., 50, 3215.

Ikeda H. and Hirakawa K. (1974) Solid State Commun., 14, 529.

Ikeda H. and Hutchings M.T. (1978) J. Phys. C, 11, L529.

Ikeda H., Suzuki M. and Hutchings M.T. (1979) J. Phys. Soc. Jpn., 46, 1153.

Imry Y., (1983) private communcation.

Imry Y. and Ma S.K. (1975) Phys. Rev. Lett., 35, 1399.

Inawashiro S., Togawa T. and Kurosaka R. (1979) J. Phys. C, 12, 2351.

Jacobs I.S., Roberts S. and Lawrence P.E. (1965) J. Appl. Phys., 36, 1197.

Kadanoff L.P. (1966) Physica, 2, 263.

Kardontchik J.E., Cohen E. and Makovsky J. (1977) Phys. Rev. B, 16, 508.

Katsumata K. (1983) J. Mag. Magn. Mat., 31 - 34, 1435.

Keffer F. (1966) Handbuch der Physik, XVIII/2, 1.

Kirkpatrick S. (1973) Rev. Mod. Phys., 45, 574.

Kirkpatrick S. and Harris A.B. (1975) Phys. Rev. B, 12, 4980.

Kittel C. (1976) 'Introduction to Solid State Physics', 5th ed., Wiley, New York.

Kogon H.S. and Wallace D.J. (1981) J. Phys. A, 14, L527.

Kogut J.B. (1979) Rev. Mod. Phys., 51, 659.

Lockwood D.J. (1973) J. Opt. Soc. America, 63, 374.

Lockwood D.J., Mischler G., Zwick A., Johnstone I.W., Psaltakis G.C., Cottam M.G., Legrand S. and Leotin J. (1982) J. Phys. C, 15, 2973.

Lovesey S.W. (1974) J. Phys. C, 7, 2049.

Mackenzie N.J. (1983) private communication.

Majkrzak C.F., Axe J.D. and Bruce A.D. (1980) Phys. Rev. B, 22, 5278.

Maletta H. (1982) in 'Excitations in Disordered Systems', ed. M.F. Thorpe, Plenum, New York.

Martel P., Cowley R.A. and Stevenson R.W.H. (1968) Can. J. Phys., 46, 1355.

Marshall W. and Lovesey S.W. (1971) 'Theory of Thermal Neutron Scattering', Oxford University Press, Oxford.

Matsubara F. (1981) J. Phys. Soc. Jpn., 50, 1469.

Matsubara F. and Inawashiro S. (1977) J. Phys. Soc. Jpn., 42 1529.

Mattis D.C. (1965) 'The Theory of Magnetism', Harper and Row, New York.

Meyer G.M. and Dietrich O.W. (1978) J. Phys. C, 11, 1451.

NAGFLIB (1977) 'Numerical Algorithms Group Fortran Library', Mk. 6, Vol. 5.

Nikotin O., Lingard P.A. and Dietrich O.W. (1969) J. Phys. C, 2, 1168.

Oguchi T. and Ishikawa T. (1977) J. Phys. Soc. Jpn., 42, 1513.

Onsager L. (1944) Phys. Rev., 65, 117.

Parisi G. and Sourlas N. (1979) Phys. Rev. Lett., 43, 744.

Pynn R. and Passell L. (1974) B.N.L. research memo no. G-19.

Pytte E., Imry Y. and Mukamel D. (1981) Phys. Rev. Lett., 46, 1173.

Rhynne J.J. (1983) Lecture notes of the school on 'Magnetic Phase Transitions', Erice, Sicily, Italy.

Samuelsen E.J. (1974) J. Phys. Chem. Solids, 35, 785.

Schulhof M.P., Nathans R., Heller P. and Linz A., (1971) Phys. Rev. B, 4, 2254.

Shapira Y. and Foner S. (1970). Phys. Rev. B, 1, 3083.

Shapira Y. and Oliveira N.F. (1983) Phys. Rev. B, 27, 4336.

Shapiro S.M. and Chesser N.J. (1972) Nucl. Instrumen. Meth., 101, 183.

Silverstein S.D. (1965) Phys. Rev. Lett., 5, 140.

Squires G.L. (1976) 'Practical Physics', 2nd ed., McGraw-Hill, London.

Stanley H.E. (1971 'Introduction to Phase Transitions and Critical Phenomena', Oxford University Press, Oxford.

Stauffer D., Ferrer M. and Wortis M. (1972) Phys. Rev. Lett., 29, 345.

Stephenson G. (1973) 'Mathematical Methods for Science Students', 2nd ed, Longmann, London.

Tarko H.B. and Fisher M.E. (1975) Phys. Rev. B, 11, 1217.

Thorpe M.F. and Alben R. (1976) J. Phys. C, 9, 2555.

Tonegawa T. (1974) Prog. Theor. Phys., 51, 1293.

Tracy C.A. and McCoy B.M. (1975) Phys. Rev. B, 12, 368.

Tuchendler J., Margarino J., Bertrand D. and Fert A.R. (1980) J. Phys. C, 13, 233.

Walker L.R. and Walstedt R.E. (1980) Phys. Rev. B, 22, 3816.

Wallace D.J. and Zia R.K.P. (1979) Phys. Rev. Lett., 43, 808.

Watson R.E. and Freemen A.J. (1961) Acta Cryst., 14, 27.

Werner S.A. and Pynn R. (1971) J. Appl. Phys., 42, 4736.

Wilkinson M., Cable J.W. Wollan E.O. and Koehler W.C. (1959) Phys. Rev. 113, 497.

Wiltshire M.C.K. (1981) Solid State Commun., 38, 803.

Wong P.Z., Horn P.M., Birgeneau R.J., Safinya C.R. and Shirane G. (1980) Phys. Rev. Lett., 45, 1974.

Wong P.Z., Horn P.M., Birgeneau R.J. and Shirane G. (1983) Phys. Rev. B, 27, 428.

Wong P.Z., von Molnar S. and Dimon P. (1982) J. Appl. Phys. 53, 7954.

Wyckoff R.W.G. (1963) 'Crystal Structures', Vol. 1, Wiley, New York.

Yasuoka H., Magon J. and Jaccarino V. (1982) J. Phys. Soc. Jpn., 51, 1039.

Yelon W.B. and Birgeneau R.J. (1972) Phys. Rev. B, 5, 2615.

Yoshizawa H., Cowley R.A., Shirane G., Birgeneau R.J., Guggenheim H.J. and Ikeda H. (1982). Phys. Rev. Lett, 48, 438.

Young A.P. (1977) J. Phys. C, 10, L257.

Zeiger H.J. and Pratt G.W. (1973) 'Magnetic Interactions in Solids', Clarendon Press, Oxford.

Ziebeck K. and Houmanns J. (1976) in 'Proceedings of the Conference on Neutron Scattering', Vol. II, 840., ed. R. Moon, Gatlinburg, U.S.A.

Ziman J.M. (1971) 'Principles of the Theory of Solids', 2nd ed, Cambridge University Press, Cambridge.

Ziman J.M. (1979) 'Models of Disorder', Cambridge University Press, Cambridge.

Random fields and three-dimensional Ising models: $Co_xZn_{1-x}F_2$

M. Hagen and R. A. Cowley
Department of Physics, University of Edinburgh, Mayfield Road, Edinburgh EH9 3JZ, Scotland, United Kingdom

S. K. Satija, H. Yoshizawa, and G. Shirane
Brookhaven National Laboratory, Upton, New York 11973

R. J. Birgeneau
Department of Physics, Massachusetts Institute of Technology, Cambridge, Massachusetts 02139

H. J. Guggenheim
Bell Laboratories, Murray Hill, New Jersey 07974

(Received 28 March 1983)

The phase transition and ordering of the $d=3$ diluted Ising antiferromagnet $Co_xZn_{1-x}F_2$ has been studied using two-axis neutron diffraction for the cases (i) where x is close to the percolation threshold, in zero applied magnetic field, and (ii) as a function of applied magnetic field for samples with $x=0.26$ and 0.35. The results of the percolation study show complicated behavior, probably due to concentration gradient problems. Nevertheless, there is strong evidence that the inverse correlation length decreases to zero at the onset of long-range order. The results of the magnetic field study are compared with the theoretical predictions for the $d=3$ Ising model in a random field. It is found that when the samples are cooled in even the smallest (nonzero) fields the long-range magnetic order is destroyed and that the structure factor is well described by the Lorentzian plus Lorentzian squared form. The inverse correlation length is found to have a power-law dependence on the applied magnetic field at low temperature with exponents $\nu_H=2.17\pm0.3$ for the $x=0.26$ sample and $\nu_H=3.63\pm0.3$ for the $x=0.35$ sample. This result is not consistent with the current theoretical predictions for the field dependence of the inverse correlation length in the $d=3$ Ising model in a random field. The measurements also show that the system is frozen at low temperatures and this freezing may be responsible for the discrepancy between theory and experiment.

I. INTRODUCTION

The effect of a random field on the ordering of Ising models has been studied theoretically in several recent papers. Imry and Ma[1] showed by comparing the random-field energy to the energy needed to produce a smooth domain wall that an Ising model is unstable against the breakup into domains for all dimensionalities less than $d_c=2$. In contrast, there have been ϵ-expansion[2,3] and supersymmetry arguments[4] which suggest that in the presence of random fields the behavior of a system is similar to that of the pure system in two less dimensions. Since $d_c=1$ for the Ising model this would suggest that $d_c=3$ in the presence of a random field.

It was the existence of these two results that led us to begin an experimental study of the effect of a random field on a three-dimensional Ising model. Fishman and Aharony[5] first pointed out that a uniform field applied to a random antiferromagnet produced a randomly directed staggered field. They initially considered a random bond antiferromagnet when the random field is proportional to the ferromagnetic susceptibility and the applied uniform field. In practice, site random antiferromagnets are more readily available, and then the random staggered field has two components: a part proportional to the ferromagnetic susceptibility as discussed by Fishman and Aharony; and another part, which is probably dominant in practice due to the randomness in the dipole moment from site to site. The strength of this latter term is directly proportional to the applied field and is independent of temperature. Our experiments were performed on the antiferromagnet CoF_2 diluted with the nonmagnetic material ZnF_2. CoF_2 is an antiferromagnet with exchange interactions between nearest and next-nearest neighbors; due to the crystal-field effects the exchange is very anisotropic.[6] CoF_2 and ZnF_2 form mixed crystals in which there is no tendency toward short-range chemical order of the Co and Zn. Both the excitations[7] and the phase transitions[8] of this system have been measured, so that it is quite well characterized.

When this work was begun we intended to study the phase transitions and the onset of long-range order close to the percolation threshold. This was intended to complement earlier work[9–11] on the percolation problem, by providing more reliable measurements of the thermal exponents for a three-dimensional Ising system and further information about the ordering of three-dimensional systems. In three-dimensional systems with close to Heisenberg interactions,[11] the inverse correlation length κ is not zero at the onset of long-range order and in a $KMn_xZn_{1-x}F_3$ crystal the long-range order was found

to decrease below 6.0 K. Experiments on a three-dimensional Ising system would clarify whether these unexpected features result from unexpected aspects of three dimensions or are present only in the systems with nearly Heisenberg-type interactions.

Our experiments were performed using neutron scattering techniques at the Brookhaven National Laboratory High Flux Beam Reactor and are described in detail in Sec. II. The results of the percolation experiments are described only briefly in the Appendix because they were not wholly successful. The effect of applying a uniform field to these samples is described in Sec. III, and these experiments yielded many interesting new results which are analyzed in Sec. IV; some of these have already been briefly described.[12]

Since we first began this experimental work there have been several theoretical papers on the effect of random fields on Ising models. Pytte *et al.*[13] have extended the work of Wallace and Zia[14] on capillary waves to systems with a random field. The model proposed by Pytte *et al.* included in the Hamiltonian the lowest-order analytic term introduced by the random field and then used the replica technique to perform the averaging over the disorder. In this model Pytte *et al.* found that, as a result of the critical dimension for the roughening transition being shifted from $d_R=3$ to 5 by the random field, the lower critical dimension for the model was 3 and not 2. A physical interpretation of this result, given by Binder *et al.*,[15] was that the shift in d_R meant that in $d=3$ the width of a domain wall increased at the same rate as the domain size and that the interface must be considered as rough on all length scales. In a recent paper, however, Grinstein and Ma[16] have argued that the random field introduces a non-analytic term into the Hamiltonian, rather than an analytic one. Their renormalization-group calculations with this Hamiltonian show that, although d_R shifts from 3 to 5, the variation of the domain wall width in $d=3$ is not as fast as the domain size, and as a consequence for large length scales the domain walls are effectively smooth. They then argue that $d_c=2$ as given by Imry and Ma. Similar results have been obtained by Villian.[17]

An alternative approach was used by Kogen and Wallace.[18] They extended the supersymmetry argument of Parisi and Sourlas[4] and showed within this framework that capillary waves destroyed the long-range order for $d<d_c=3$. In a recent paper Cardy[19] has argued that this is an exact result for $T=0$ and similar arguments have been given by Niemi.[19]

Clearly, in view of this theoretical controversy and activity, experiments must be performed to test these theories. As we shall describe in detail in the conclusion, a cursory glance at our experimental results suggests that all these theories are incorrect, but a more circumspect analysis suggests caution. There is no doubt that although aspects of these theories are correct, much work needs to be done before they will provide a complete description of our results.

Specifically, the theories described above are all for a ferromagnet with uniform interactions in the presence of a random field. Our experiments, on the other hand, are for an antiferromagnet *with vacancies* in a uniform applied field. It is believed that near six dimensions[16] these problems are equivalent. However, it is not at all obvious that the vacancies do not become relevant in $d=3$; certainly domain walls will preferentially be located near the vacancies and this could affect the scaling of the domain-wall width with length thus altering d_c.

II. EXPERIMENTAL TECHNIQUES

Crystals of $Co_xZn_{1-x}F_2$ were grown from very pure CoF_2 and ZnF_2 by using the Czochralski method of growth. The samples had a volume of several cm^3 and consisted of several large single-crystal grains. These crystals were cleaved to obtain single crystals with a volume of about 1 cm^3. Several of these crystals with x nominally 0.25 and hence close to the percolation concentration were studied in detail as a function of temperature in the hope of elucidating the percolation properties of this three-dimensional Ising system. The results are reported in the Appendix.

One of these crystals and another with a nominal concentration of $x=0.35$ were selected for studying in an applied magnetic field. It is unfortunately very difficult to determine accurately the concentrations, x, in these samples. Approximate values of x for these two samples can be obtained from the measured Néel temperatures of 6.70 ± 0.05 and 13.25 ± 0.01 K, respectively. As a rough estimate, if we assume that the Néel temperature is proportional to the number of spins in the infinitely connected network, and that the fraction of spins in the infinitely connected network is taken from the work of Kirkpatrick,[20] then the concentrations x are 0.26 and 0.35, respectively. The former concentration is very close to the percolation concentration of 0.24 for a bcc lattice.[21]

The neutron-diffraction measurements were performed at the Brookhaven National Laboratory High Flux Beam Reactor using a two-axis spectrometer. An incident neutron wave vector of 2.67 $Å^{-1}$ was obtained by reflection from the (002) planes of a pyrolitic graphite monochromator. In order to suppress neutrons reflected from higher-order planes two pyrolitic graphite filters were used. In the percolation experiments the samples were mounted with the [010] axis vertical in a variable temperature cryostat. The collimation used was 20′ before the monochromator, 20′ between the monochromator and sample, and 20′ between the sample and detector. The resolution function was then measured at the (100) reflection to be 0.015 $Å^{-1}$ full width at half maximum (FWHM) parallel to the wave-vector transfer and 0.005 $Å^{-1}$ perpendicular to the wave-vector transfer.

In order to perform the random-field experiments the samples were aligned with the [001] axis vertical and placed in the variable temperature insert of a superconducting magnet which produced a vertical magnetic field of up to 7.5 T. The measurements on the $x=0.26$ sample were performed with the same collimations as the zero-field experiments. However, for the measurements on the $x=0.35$ sample the 20′ collimators were replaced by 10′ collimators throughout. The resolution function in the scattering plane was then measured as 0.009 $Å^{-1}$

(FWHM) parallel to the wave-vector transfer and 0.0024 Å^{-1} perpendicular to the wave-vector transfer.

III. EXPERIMENTAL RESULTS

As discussed in the Introduction a uniform field applied to a random antiferromagnet produces a randomly directed staggered field. We have therefore performed experiments by applying a uniform field to the $Co_xZn_{1-x}F_2$ system. In the sample for which $x=0.26$ x is close to the percolation point, and the applied field is relatively large so that the results are undoubtedly strongly influenced by the proximity of the percolation threshold. Consequently, we also performed experiments on a more concentrated system with $x=0.35$.

One of the difficulties of working with Ising systems at low temperatures is the problem of ensuring that the relaxation times for the establishment of thermodynamic equilibrium are always shorter than the time of the experiment. Because of this problem the experiments were mostly performed by changing the magnetic field while the sample was at a temperature above T_N, and then cooling the sample while keeping the magnetic field fixed. Although there is no guarantee that this procedure gives the low-temperature ground state, it is accepted as giving the best approximation to the ground state in spin-glasses. We measured the scattering in the neighborhood of the (1,0,0) lattice point for several different magnetic fields as shown in Fig. 1 for $x=0.26$ and in Fig. 2 for $x=0.35$. In the former case the peak intensity at the (1,0,0) lattice point monotonically decreased with increasing field as also shown in more detail in Fig. 3. This decrease is similar to that observed for the scattering in the absence of a field as a function of temperature (see Fig. 16, sample *A*) suggesting that there might be a phase transition at about 1.0 T. The behavior is, however, quite different as can be seen

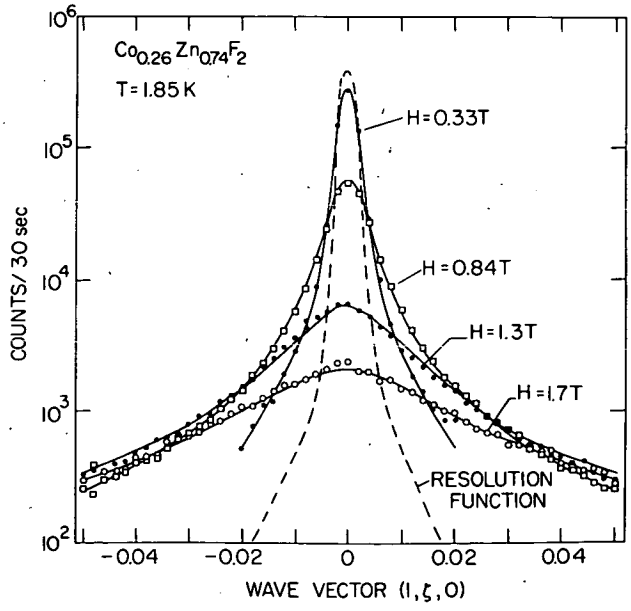

FIG. 1. Scattering for wave-vector transfers along [1ζ0] at 1.85 K from $Co_{0.26}Zn_{0.74}F_2$. The lines are fits to the sum of a Lorentzian and a Lorentzian squared as detailed in the text.

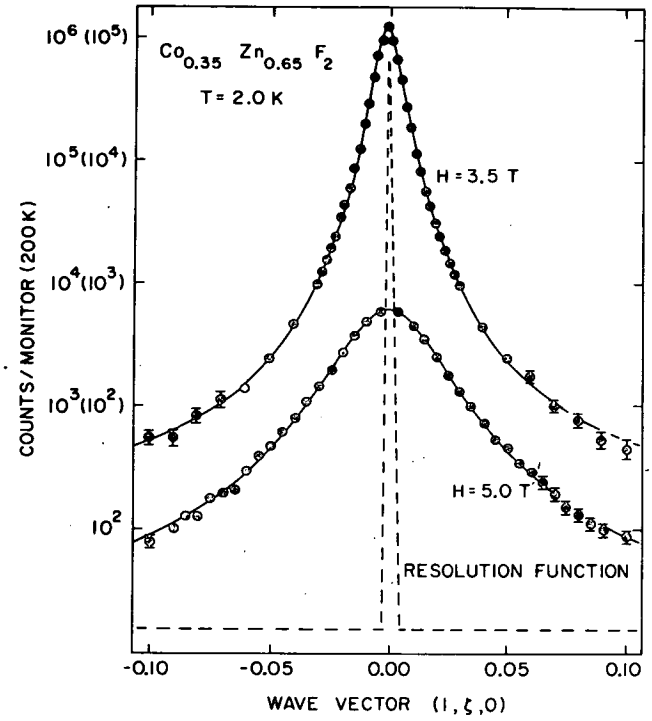

FIG. 2. Scattering for wave-vector transfers along [1ζ0] at 2.0 K from $Co_{0.35}Zn_{0.65}F_2$. The solid lines are fits to the sum of a Lorentzian and a Lorentzian squared as described in the text.

from inspection of Figs. 1 and 2. The width of the scattering as a function of the wave vector is steadily increasing with increasing magnetic field, unlike the case of decreasing temperature. Since the width of the (2,0,0) nuclear Bragg peak is unchanged on applying the field, this increase in the width means that the long-range antiferromagnetic order has been destroyed for magnetic fields much less than 1.0 T. The behavior of the width in the sample with $x=0.35$ is very similar, as shown in Fig. 2, although the increase in the width is much smaller for a given magnetic field strength than in the more dilute sample. The peak intensity in the $x=0.35$ sample initially increases as a function of magnetic field; the peak intensity is a maximum for a field of about 1.5 T, and at larger

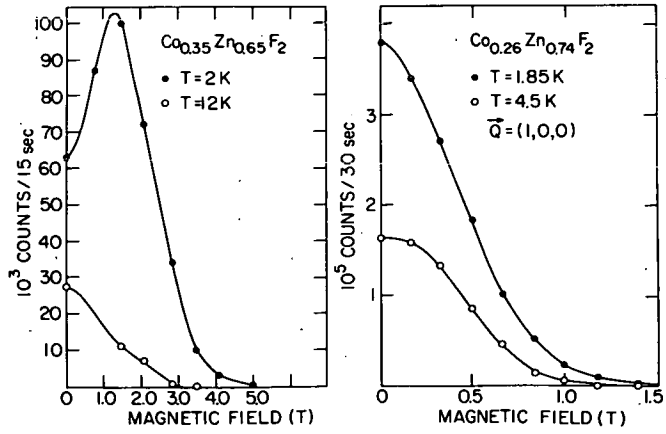

FIG. 3. Peak intensity of the scattering with $\vec{Q}=(1,0,0)$ in $Co_xZn_{1-x}F_2$ as a function of magnetic field.

fields the peak intensity falls uniformly as a function of magnetic field in a similar way to that for $x=0.26$. We believe that this "anomalous" increase for small fields can be explained by considering the effect of extinction. This crystal, even though it is site disordered, has a sufficiently small mosaic spread so that in the zero field the intensity of the (1,0,0) reflection is *extinction limited.* When the sample is cooled in an applied field the magnetic order within the mosaic blocks is broken up into domains by the random-field effect, and as a consequence the Darwin angle of the magnetic domains within the mosaic block will be increased allowing a greater proportion of the incident beam to be scattered. The effect of the random field on the peak intensity is thus manifested in two ways; one reduces the scattering power of a magnetic domain by the destruction of long-range order while the other increases the proportion of the beam that each mosaic block is able to scatter. The initial effect of a random field might therefore increase the magnetic peak intensity by lifting the extinction present in the (1,0,0) reflection. This behavior makes it very difficult to make precise statements about the small field measurements in this sample. It should be emphasized that this behavior occurs only for the magnetic scattering and that the nuclear Bragg peaks are unaffected.

The behavior of the scattering as a function of temperature at fixed field is illustrated in Fig. 4 for $x=0.26$ and in Fig. 5 for $x=0.35$. At low temperatures the width of the scattering is almost independent of temperature but then increases with increasing temperature, while the intensity generally decreases with increasing temperature.

At the beginning of this section we discussed the difficulty of knowing whether the system is in the thermodynamic equilibrium state at low temperatures. In both samples the state of the system is frozen at low temperatures below about 4.0 K but in the case of $x=0.26$ only for fields below 1.2 T. This is illustrated in Fig. 6 where we compare the scattering observed when the system is cooled in zero field, with that resulting from cooling in a

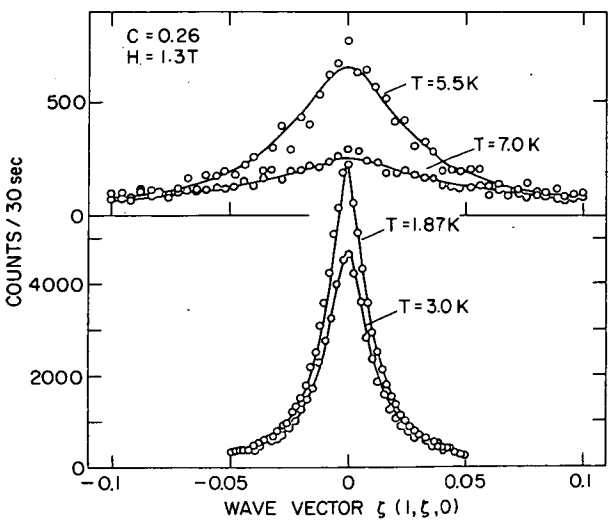

FIG. 4. Scattering for wave-vector transfers $\vec{Q}=(1,\zeta,0)$ with $H=1.3$ T at various temperatures for $Co_{0.26}Zn_{0.74}F_2$. The solid lines are Lorentzian fits to the measurements.

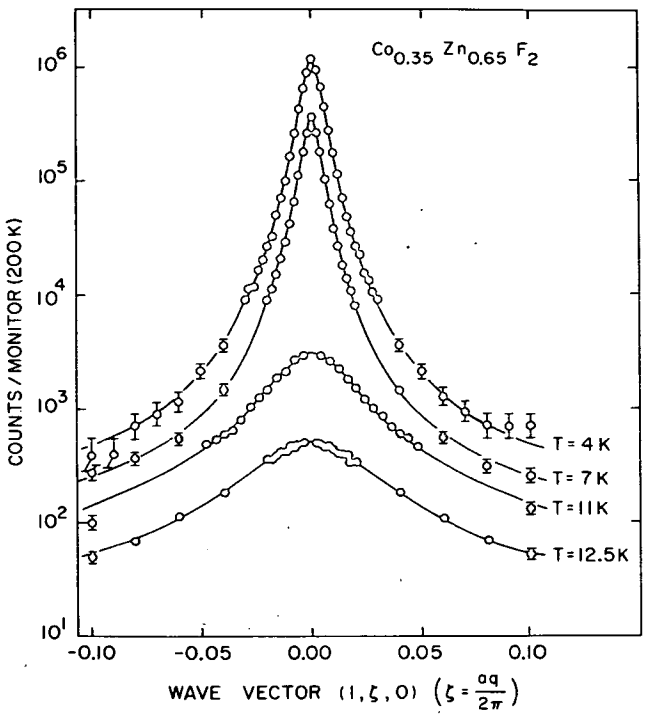

FIG. 5. Scattering for wave-vector transfers $\vec{Q}=(1,\zeta,0)$ with $H=3.5$ T at various temperatures for $Co_{0.35}Zn_{0.65}F_2$. The solid lines are Lorentzian plus Lorentzian-squared fits to the measurements for temperatures below 11 K and Lorentzian fits for 11 K and 12.5 K.

field of 2.5 T and then reducing the field to zero. In the latter case the scattering is fairly similar to that observed when the sample is cooled in a field of 0.8 T. We do not understand the origin of the small shift in peak position in Fig. 6, especially as the nuclear Bragg reflections were not changed. Clearly one expects strong magnetoelastic effects accompanying the domain wall formation and such effects presumably account for the distortions evidenced in Fig. 6. This result demonstrates that at low temperatures and fields the scattering is dependent on the immediate prior history of the sample. Similar results were obtained even at the largest fields used in the $x=0.35$ sample. We cannot therefore be certain that the results obtained by cooling in a field, shown in Figs. 1–5 and discussed in the rest of this paper, are characteristic of the thermodynamic equilibrium state at low temperatures. They are characteristic of the state obtained by cooling in a field and the scattering is then constant over periods of several days.

IV. ANALYSIS OF THE RESULTS

The scattering, shown in Figs. 1 and 2, was initially analyzed by fitting it to a Lorentzian profile, which has proved to be so successful at describing the scattering observed in many other circumstances. The intensity was fitted to the form

$$I(\vec{Q})=|f(\vec{Q})|^2\frac{A}{\kappa^2+(\vec{q}^{\,*})^2}\,, \tag{1}$$

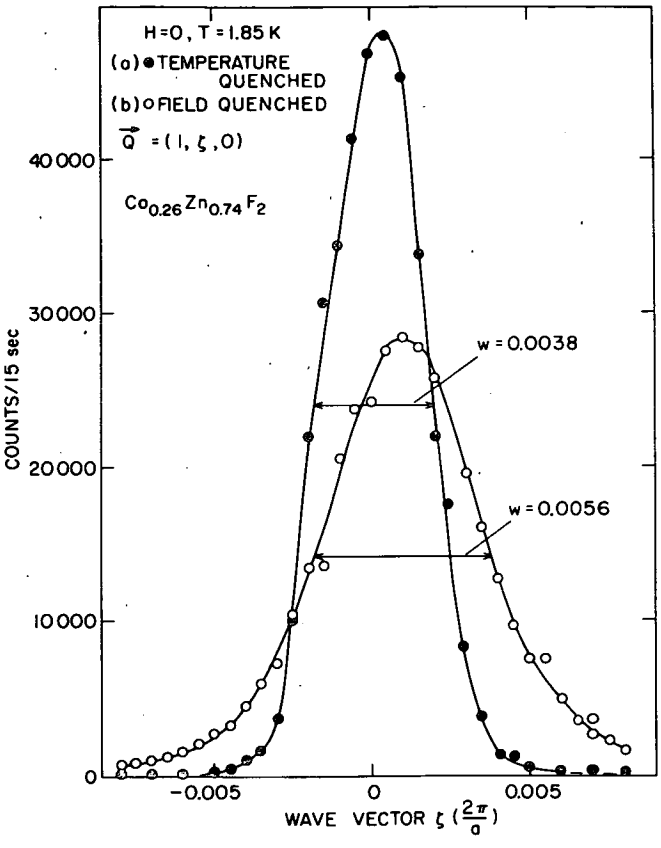

FIG. 6. Scattering observed for wave vectors along the direction $[1\zeta 0]$ at 1.85 K and $H=0$ obtained by cooling the sample when $H=0$ and in a field of 2.5 T and then reducing the field. The difference in the results show that the spins are frozen at low temperatures and fields.

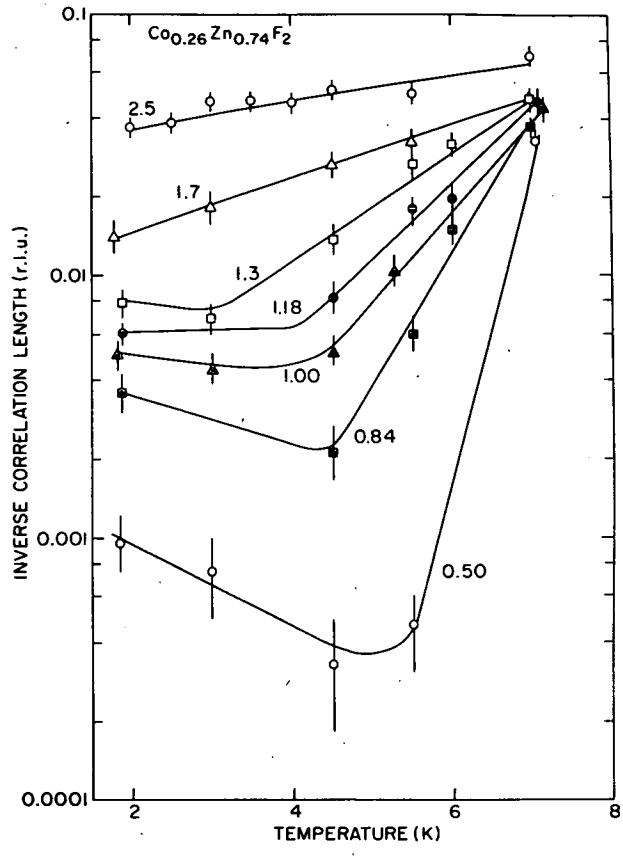

FIG. 7. Inverse correlation length κ (reciprocal-lattice units) deduced for $Co_{0.26}Zn_{0.74}F_2$ as a function of temperature for various applied fields. The solid lines are guides to the eye.

where $f(\vec{Q})$ is the form factor of the Co^{2+} ion[22] and $\vec{q}^*$ is the difference between $\vec{Q}$ and the reciprocal-lattice vector (1,0,0) expressed in reciprocal-lattice units. The analysis was performed by convoluting Eq. (1) with the measured experimental resolution and fitting the parameters A and κ to the experimental results. Equation (1) gave a good description of the experimental results for temperatures above T_N and in the $x=0.26$ sample for fields above 1.2 T. At lower temperatures and fields, the results could not be described by Eq. (1). We attempted to fit these results by the Lorentzian form [Eq. (1)], and an additional central Gaussian to represent an increased mosaic spread for the magnetic structure. This combination of functions failed to describe many of these results, because the scattering falls off more slowly than a Gaussian for small q^*, but more rapidly than a Lorentzian in the wings.

Several different functional forms have been tried to describe the results for low temperatures. Before the recent theoretical advances described in the Introduction, fits to the $x=0.26$ data were made assuming that

$$I(\vec{Q})=|f(\vec{Q})|^2\frac{A}{|\vec{q}^*|^{2-\eta}}\ . \qquad (2)$$

This form gives a good description[12] of the $x=0.26$ experimental results when convoluted with the experimental resolution function. The exponent η is close to zero for

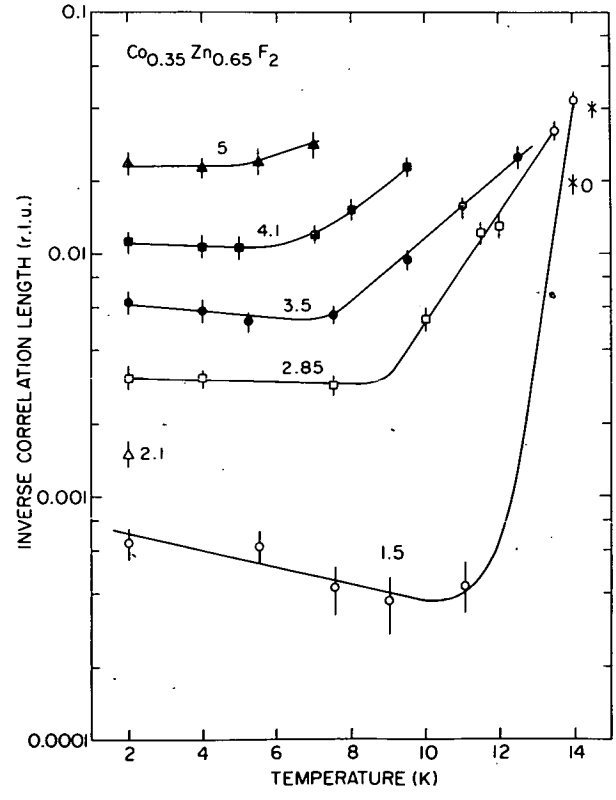

FIG. 8. Inverse correlation length κ deduced for $Co_{0.35}Zn_{0.65}F_2$ as a function of temperature for various applied fields.

$H=1.2$ T and at a temperature of 2.0 K and then steadily decreases with decreasing field and approaches -1 when $H=0$. The exponent is given approximately by $\eta=-1+(H/H_c)^2$ when $H_c\approx 1.1$ T, and the amplitude A depends at least approximately on the applied field such as H^{-2}.

Although this form gives a reasonably accurate description of the experimental results, recent theoretical work[13,18] suggests that a more appropriate form is

$$I(\vec{Q})=|f(\vec{Q})|^2\left[\frac{A}{\kappa^2+|\vec{q}^{\,\alpha}|^2}+\frac{B}{(\kappa^2+|\vec{q}^{\,\alpha}|^2)^2}\right]. \tag{3}$$

As discussed in the paper[23] on $Rb_2Co_xMg_{1-x}F_4$, the Lorentzian-squared term continuously evolves into a Bragg peak as $H\rightarrow 0$, provided that $B\sim\langle S_z\rangle^2\kappa^{4-d}$, where d is the dimensionality of the system. We find that Eq. (3) does give a very satisfactory description of the results, so that the results can be described either by Eqs. (2) or (3). A similar conclusion was found[23] in the two-dimensional system $Rb_2Co_xMg_{1-x}F_4$. However, since current theory strongly favors the Lorentzian plus Lorentzian-squared form, most of our efforts have concentrated on fitting the parameters in Eq. (3), A, B, and κ, to the experimental results.

As shown in Figs. 1, 2, 4, and 5, Eq. (3) gives a good description of our experimental results. The results for the temperature dependence of the inverse correlation length κ for various different fields are shown in Fig. 7 for $x=0.26$ and in Fig. 8 for $x=0.35$. In both cases, on cooling from high temperatures κ sharply decreases with decreasing temperature and is then constant or even slightly increases on further cooling.

As noted previously, the random staggered field contains both a direct Zeeman contribution due to the randomness in the moment and an induced contribution due to the randomness in the interaction. The former, which is dominant, is temperature independent whereas the latter peaks near T_N. These two fields both are generated by the dilution and further they *oppose* each other locally. The diminution of the bond-randomness term with decreasing temperature below T_N may account for the observed decrease in the correlation length as $T\rightarrow 0$.

In Fig. 9 we show the low-temperature behavior of B/κ and A as a function of field for the two samples. For $x=0.35$ B/κ is nearly constant except at the lowest fields where the effect of the extinction is to reduce its value. For $x=0.26$ B/κ decreases to zero at about 1.2 T. The amplitude of the Lorentzian A is almost constant for fields above 1.2 T in the $x=0.26$ sample and decreases as the field is reduced. In the $x=0.35$ sample the amplitude A increases with increasing field in a similar way to the $x=0.26$ sample, but does not become constant even at the highest fields. These results are, we believe, characteristic of both high- and low-field behavior respectively. At low fields $A\rightarrow 0$ and the scattering is almost purely Lorentzian squared with B/κ a constant. The scattering then develops smoothly into a Bragg peak as $\kappa\rightarrow 0$. At relatively large fields the amplitude of the Lorentzian squared decreases and the system becomes a normal paramagnet.

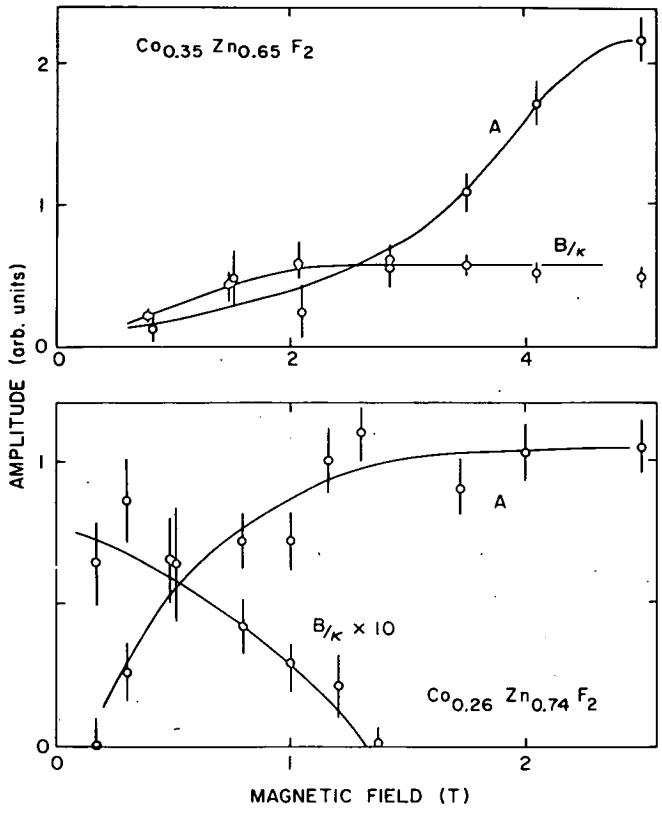

FIG. 9. Amplitude of the Lorentzian A and Lorentzian squared B divided by κ deduced for $Co_{0.26}Zn_{0.74}F_2$ at 1.85 K and $Co_{0.35}Zn_{0.65}F_2$ at 2.0 K.

The behavior of B/κ is very similar to that of the square of an order parameter. In Fig. 10 we show its behavior as a function of temperature for various fields and the data collapses, at least approximately, to a single curve which is very similar to that of the Bragg peak intensity (see Fig. 16, sample A). The behavior is more complex in the $x=0.26$ sample because the amplitude of the Lorentzian-squared term is nonzero only within a circle described approximately by

$$\left[\frac{T}{T_c}\right]^2+\left[\frac{H}{H_c}\right]^2=R^2=1,$$

where $T_c=6.7$ K and $H_c=1.2$ T. In Fig. 11 we have therefore shown B/κ plotted against R. Although the errors are considerable the behavior is not inconsistent with that of the order parameter (see Fig. 16, sample A). This behavior is thus consistent with our heuristic prediction that $B\sim\langle S_z\rangle^2\kappa$ in three dimensions.

As described in the Introduction there is considerable interest in the behavior of the three-dimensional Ising model in small random fields and at low temperatures. Our results show that the scattering is broader than a Bragg peak and evolves smoothly into a Bragg peak as the field is reduced. Although we cannot determine κ with any accuracy at the smallest fields, there is a marked increase in the intensity of the wings of the Bragg peak for fields as small as 0.17 T for $x=0.26$ and 0.8 T for

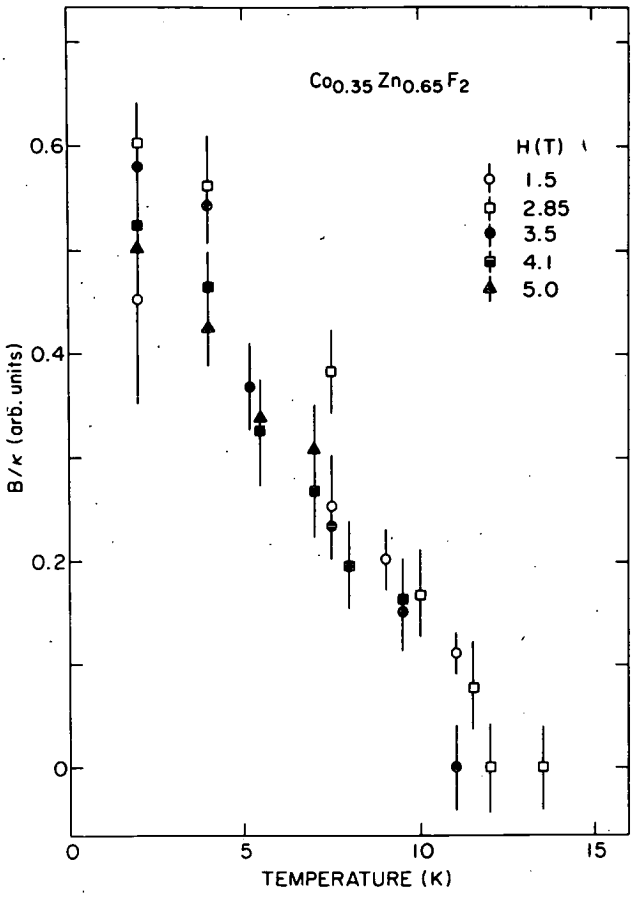

FIG. 10. Amplitude of the Lorentzian squared plotted against temperature for $Co_{0.35}Zn_{0.65}F_2$ for various fields.

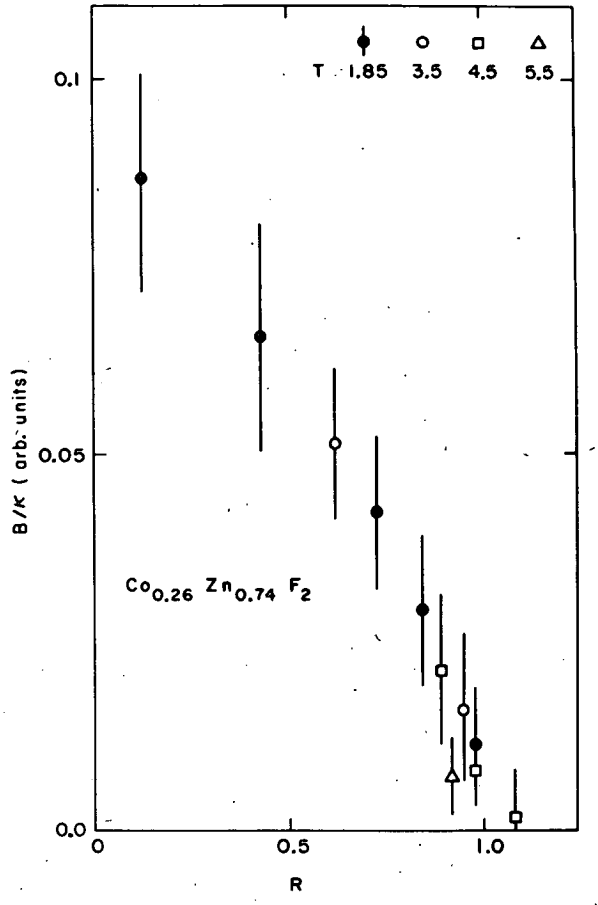

FIG. 11. Amplitude of the Lorentzian squared B/κ plotted against $R=[(T/T_c)^2+(H/H_c)^2]^{1/2}$ for $Co_{0.26}Zn_{0.74}F_2$.

$x=0.35$. These fields correspond to temperatures $g\mu_B H/k_B$ of 0.48 and 2.3 K, respectively, which are much smaller than the transition temperatures of 6.7 and 13.7 K and of the energy needed to turn one Co^{2+} ion in the presence of only one of its antiferromagnet neighbors: 11.1 K.[6,7] These results show that cooling the samples in these fields which are considerably smaller than the other fields in the system results in the crystals being in a magnetic state with no long-range order at low temperatures. If $d_c=3$ then it would be expected[13,18] that at low temperatures $\kappa \propto \exp[-(H_0/H)^2]$, where H_0 is some constant. In Fig. 12 we show $\ln\kappa$ plotted against $1/H^2$ for the $x=0.35$ sample, and the results clearly do not give a straight line. We also test a power-law description in Fig. 13 and this gives a much better description of the results apart from the result at lowest fields which may be influenced by the extinction problem discussed above. A least-squares fit omitting this point gives

$$\kappa=\kappa_0 H^{\nu_H}$$

with $\nu_H=3.63\pm0.12$, $\kappa_0=0.000\,069\pm0.000\,012$, and χ^2 is 2.62, where κ is in reciprocal-lattice units and the magnetic fields in tesla. A similar analysis has been performed on the results for the $x=0.25$ sample and gives $\nu_H=2.17\pm0.16$ while $\kappa_0=0.0047\pm0.0004$, while χ^2 is 1.12; the fit is shown in Fig. 14. It is not too surprising

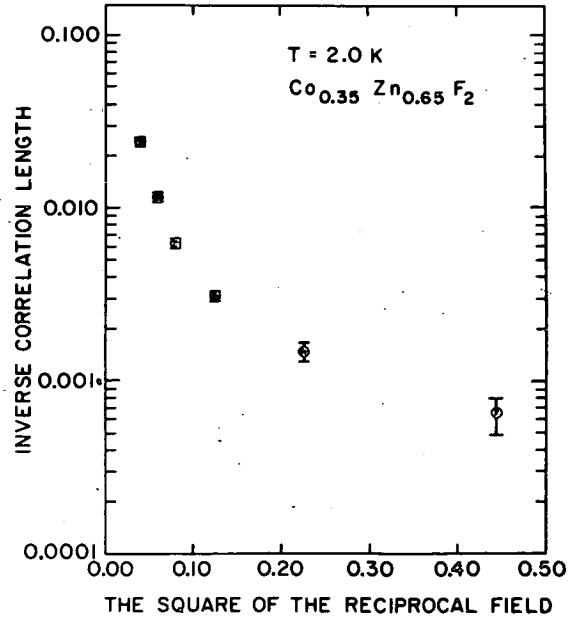

FIG. 12. Logarithm of κ at 2.0 K plotted against $1/H^2$. A straight line is to be expected if the lower critical dimension is 3.

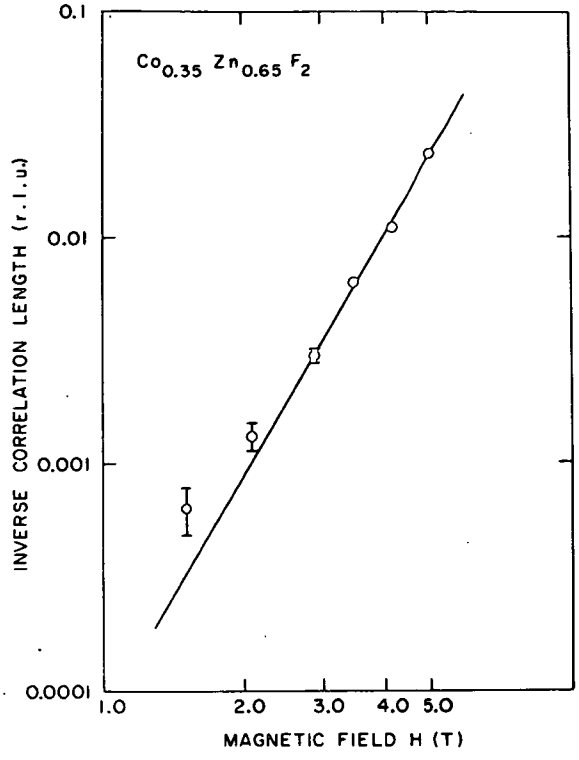

FIG. 13. κ at 2.0 K plotted against the applied field for $Co_{0.35}Zn_{0.65}F_2$. The straight line is a fit which gives the exponent.

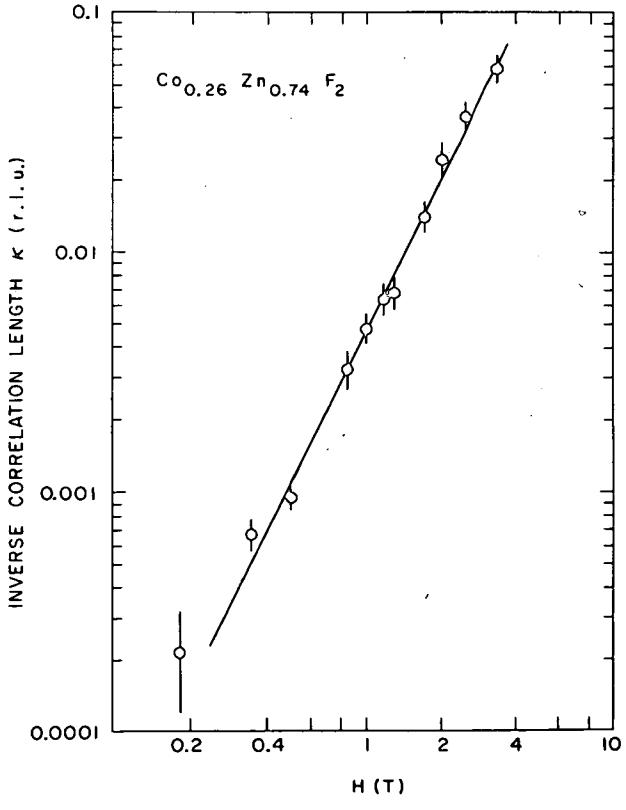

FIG. 14. κ at 1.85 K for $Co_{0.26}Zn_{0.74}F_2$ plotted against H. The straight line is a fit to the results.

that the results for ν_H for the two concentrations are different because all the results are in the Lorentzian-squared quasiordered phase for the $x=0.35$ sample whereas for $x=0.26$ the fit was performed over the whole range of H. It is more likely therefore that $\nu_H=3.63$ is the appropriate "random-field exponent" for this system. There is also a very large difference in the values of κ_0 by nearly 2 orders of magnitude. Such a large change cannot be accounted for by statistical factors such as x or $1-x$. The effect of the random field must increase very rapidly as the percolation point is approached. As discussed by Fähnle,[24] this probably reflects the highly ramified and hence quasi-one-dimensional nature of the infinite network near percolation.

Finally in Fig. 15 we show the low-temperature structure factor $I(1,0,0)$; that is, the intensity for $\vec{Q}=(1,0,0)$ corrected for the finite experimental resolution as a function of magnetic field for both systems. The results for $x=0.35$ are approximately linear apart from the point at the lowest fields. When this is omitted a least-squares fit to the form

$$I=I_0H^{-\gamma_H}$$

gives $\gamma_H=10.9\pm0.6$. In the case of $x=0.26$ the three points at the largest fields clearly are not part of the same straight line and omitting these points gives $\gamma_H=8.0\pm0.6$.

V. DISCUSSION AND CONCLUSIONS

The main conclusion of the experiment is that the application of a magnetic field whose energy is much smaller than the exchange energy or kT_N has a drastic effect upon

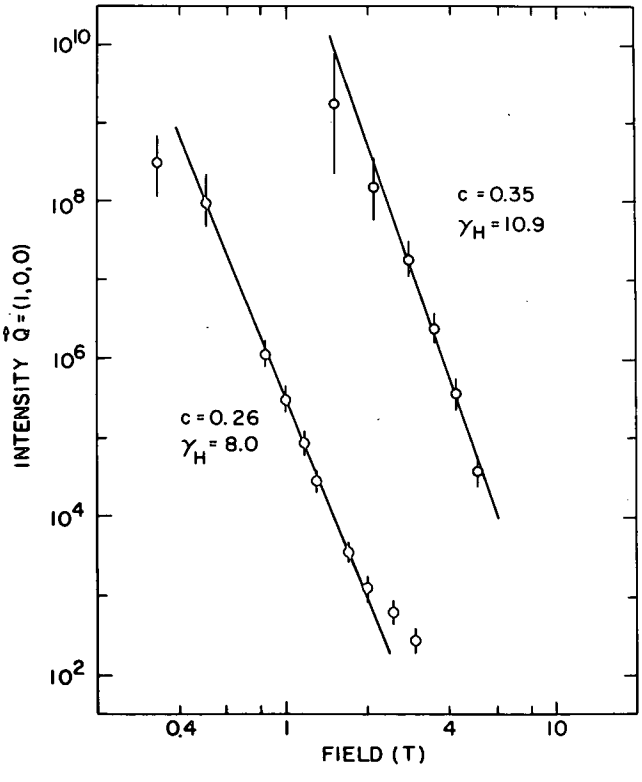

FIG. 15. Scattering for wave vector $\vec{Q}=(1,0,0)$ corrected for the resolution as a function of the magnetic field.

the phase transition and ordering of $Co_xZn_{1-x}F_2$. When the system is cooled in a uniform magnetic field, the state reached at low temperatures is not one of long-range antiferromagnetic order. The scattering at low fields is dominated by a Lorentzian squared with a width which increases with increasing field. This Lorentzian-squared term represents, we believe, a quasiordered random-field state. Firstly, this is because the intensity of the scattering at low fields is the same as that of the Bragg reflection describing the long-range order in the absence of a magnetic field. This result holds not only at low temperatures but at all temperatures below T_N. Secondly, at large fields, 1.2 T when $x=0.26$, the intensity of the Lorentzian-squared term decreases and the system becomes a normal paramagnet. This critical field corresponds to a single-site field energy of only about $\frac{1}{2}T_N$ or 0.31 of the nearest-neighbor exchange energy.

The detailed behavior of the inverse correlation length as a function of field is undoubtedly complex. In the $x=0.35$ sample $\kappa \propto H^{\nu_H}$ with $\nu_H=3.63\pm0.12$, at low temperatures. A different power 2.17 ± 0.16 was obtained for the $x=0.26$ sample, but this latter result is dominated by the results in the high-field paramagnetic region, $H>1.2$ T, and the results at low fields were of insufficient accuracy to determine the limiting low-field behavior.

These results appear to be inconsistent with current theories of the $d=3$ Ising model in a random field. Those theories for which $d_c=2$ predict long-range order at low temperatures while the theories which give $d_c=3$ suggest that $\kappa \sim \exp[-(H_0/H)^2]$. Our results, if simply interpreted, would suggest that $d_c>3$.

There may be several reasons for the discrepancy other than errors in the theories or the experiments. As mentioned in the Introduction, it may be that a uniform field applied to a random antiferromagnet does not give the same behavior as a random field applied to a uniform ferromagnet. The physics of random-field systems has been found to be unexpectedly subtle and the effect of the random exchange interactions and, specifically, vacancies which provide a soft path for the domain walls may be more severe than currently thought.

Another difficulty may arise because of the difficulty of establishing the thermodynamic ground state at low temperatures. We know that this system is frozen at 2.0 K and so, if long-range order is the equilibrium state only for temperatures somewhat below the freezing temperature, then this state could not be sampled in the experiment. The theories might then be correct but, so far as experimental work is concerned, they are irrelevant to the behavior in real experiments.

Birefringence measurements[25] show a sharp peak at low fields for these three-dimensional antiferromagnets. Indeed the peak in $d(\Delta n)/dT$, which is proportional to the heat capacity, appears to be sharper in a field than for $H=0$, reflecting a crossover in the heat-capacity exponent α from -0.09 to ~ 0.0. In addition, the temperature of the peak as a function of field follows the theoretically predicted changes in T_N ($\Delta T_N \sim H^{2/\gamma}$) quite well. In $Fe_xZn_{1-x}F_2$ a comparison of the neutron scattering results with the birefringence results shows that the peak occurs at a temperature just above that at which κ reaches its minimum value. Our results indicate that the peak is not associated with the development of true long-range antiferromagnetic order. Current theories describe the breakup of long-range order in a random field as due to the presence of domains walls. Most likely these walls are sufficiently far apart in the region probed by the birefringence measurements that the ordering within the antiferromagnetic domains gives a peak in the heat capacity with negligible rounding. The change in α suggests that new critical behavior is being observed but, presumably, this critical behavior is cut off by entry into the domain-wall state. Extension of the birefringence measurements to higher fields, especially in more dilute samples, would test this latter idea.

Clearly these experiments show that random fields drastically change the properties of systems close to phase transitions and prevent the establishment of long-range order. The random fields may have an energy which is very much less than kT_N and yet produce a very large effect. Since impurities in crystals can frequently produce random fields, their effects may be more important than hitherto considered.

Finally, these experiments present a challenge to theory. The theory should be extended to include the effect of temperature when our experiments show unambiguously that large effects occur close to T_N for the $d=3$ Ising model. The theory should then be extended to consider the establishment of the thermodynamic equilibrium state at lower temperatures. Random fields produce large and dramatic effects on the ordering and phase transitions of $d=3$ Ising models and we hope this paper will lead to further experimental and theoretical work on this difficult problem.

ACKNOWLEDGMENTS

We have benefited from helpful discussions with A. Aharony, A. N. Berker, K. Da'Bell, P. M. Horn, Y. Imry, D. Mukamel, E. Pytte, G. Grinstein, and D. J. Wallace. The work at Brookhaven National Laboratory was supported by the Division of Basic Energy Sciences, U. S. Department of Energy, under Contract No. DE-AC02-76CH0016, the work at Massachusetts Institute of Technology was supported by the National Science Foundation Low Temperature Physics Program under Contract No. DMR-79-23203, and the work at Edinburgh was supported by the Science and Engineering Research Council. One of us (M.H.) acknowledges the financial support of United Kingdom Science and Engineering Research Council studentship.

APPENDIX: PERCOLATION IN $Co_xZn_{1-x}F_2$

1. Experimental results

The neutron scattering from the magnetic fluctuations in $Co_xZn_{1-x}F_2$ was studied for six samples with x nominally equal to 0.25. In two of these samples the magnetic scattering observed for wave vectors close to the (1,0,0) lattice point was weak and only slowly varying with the

wave vector even at 1.2 K. This presumably meant that the concentrations of these samples were so much less than the percolation threshold that all the magnetic spins were in relatively small independent clusters.

In each of the other four samples the results were qualitatively similar although different in detail and so we describe the results for only two of the samples labeled *A* and *B*. In each of these samples there was intense magnetic scattering at the (1,0,0) reciprocal-lattice point at low temperatures, the width of which was determined by the experimental resolution. This scattering is indicative of long-range order at low temperatures and its temperature dependence is shown in Fig. 16. The intensity of the scattering is closely proportional to $T_N - T$ for each sample except that close to T_N, where there is evidence of rounding, presumably due to concentration fluctuations. The onset of long-range order occurred at a similar temperature between 5.5 and 7.0 K in each sample.

The diffuse scattering observed for a wave-vector transfer $\vec{Q}=(1,0,-0.008)$ is shown in Fig. 17 for samples *A* and *B*. It increases rapidly as the phase transition is approached and has a maximum at a temperature somewhat below the onset of long-range order. On further cooling the amplitude of the critical scattering decreases slightly for sample *A* but at temperatures below 2.5 K increases again. This increase in the critical scattering intensity at low temperatures is unexpected. It also occurs in the $x=0.35$ sample in the applied magnetic field. This suggests that the low-temperature behavior for sample *A* may arise from random fields possibly arising from impurities or from dipolar interactions.

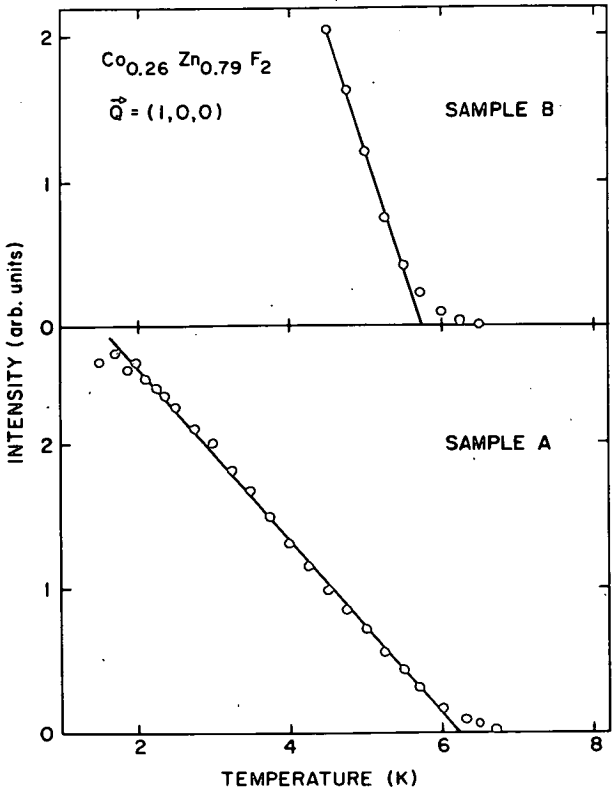

FIG. 16. Integrated Bragg intensity of the (100) magnetic lattice point for two samples of $Co_xZn_{1-x}F_2$ with $x \approx 0.26$.

The diffuse scattering was measured in detail using scans with wave vectors along the direction $[\zeta 00]$ and $[00\eta]$ through the (1,0,0) lattice point. The diffuse scattering was then analyzed assuming that it could be described by a Lorentzian profile, Eq. (1). The results are displayed in Figs. 18 and 19. The inverse correlation length decreased as the temperature was reduced from 10 K and would appear to be heading towards zero at T_N. Somewhat above T_N the inverse correlation length ceases to decrease and is then almost independent of temperature until possibly at low temperatures, below 2 K, when it decreases again. The amplitude *A* decreases with decreasing temperature.

2. Discussion of results

As mentioned in the Introduction the initial objective of these experiments was to perform a detailed study of the percolation in a three-dimensional Ising system similar to that performed for other systems. Unfortunately, the crystal-growth problems made a detailed study impossible. The results described above and shown in Figs. 16—19 are in some respects unexpected but can probably be understood if there is a considerable spread in T_N in different parts of the crystal. Indeed, in an Ising system it is expected that the transition temperature increases very rapidly with concentration close to the percolation point, because the temperature is determined by the one-

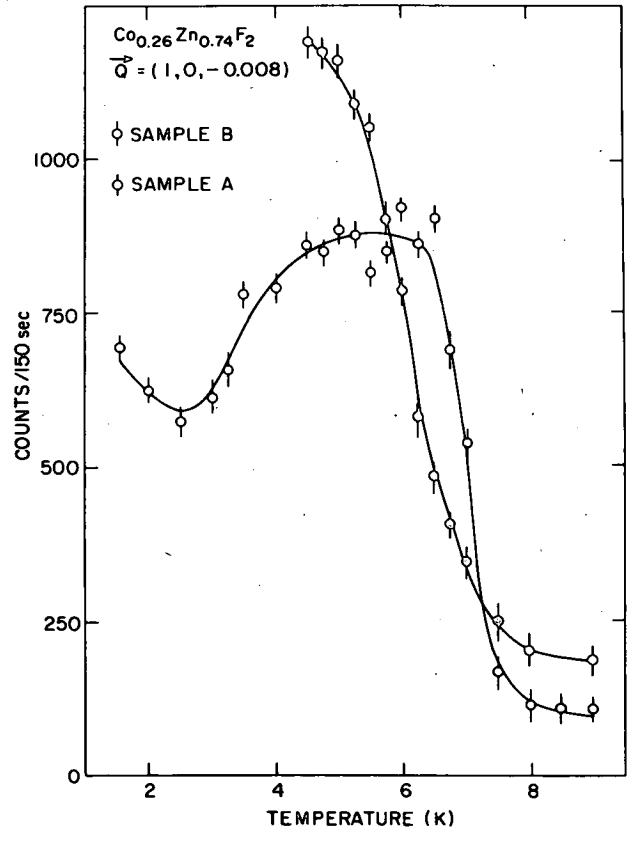

FIG. 17. Scattering observed for a wave-vector transfer of $\vec{Q}=(1,0,-0.008)$ from two samples of $Co_xZn_{1-x}F_2$. The wave-vector transfer was chosen to be close to the (1,0,0) reciprocal-lattice point but not so close that the scattering was contaminated by the Bragg reflection.

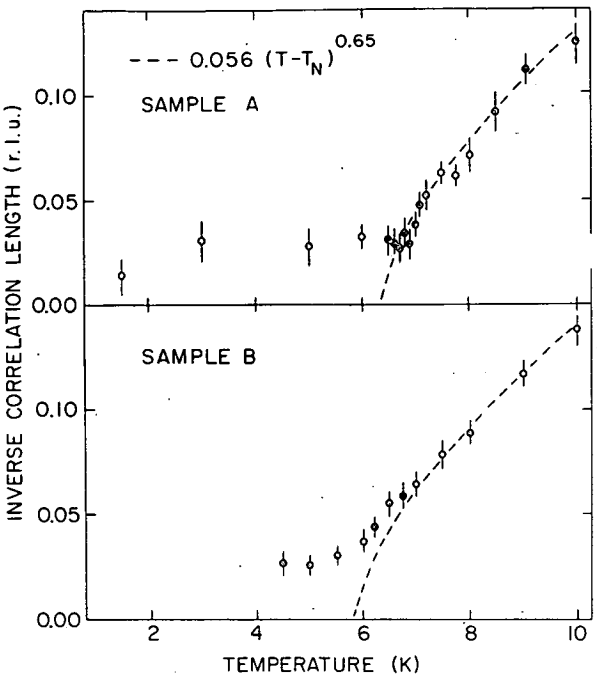

FIG. 18. Inverse correlation length κ as a function of temperature for two samples of $Co_xZn_{1-x}F_2$ with $x \approx 0.26$.

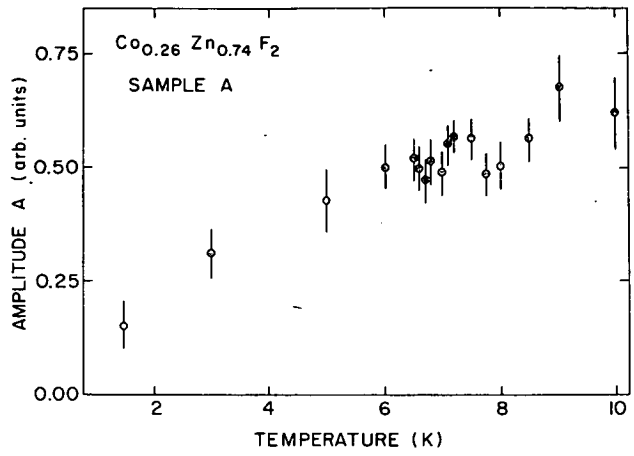

FIG. 19. Amplitude A of the Lorentzian critical scattering for $Co_xZn_{1-x}F_2$ with $x \approx 0.26$.

dimensional weak links[26] which order as $\exp(-J/k_BT)$. Specifically then $T_N \sim \ln(c-c_p)$ so that a small spread in concentration will produce a very broad distribution of Néel temperatures; it is interesting to note that because of the singular dependence of T_N on concentrations the peak in the T_N distribution will come near the temperature appropriate to the large concentration limit. This may explain why all samples which ordered had similar apparent Néel temperatures. For a system with a distribution of Néel temperatures it is known that an analysis of the critical scattering, such as that described above, gives a nonzero value of κ at T_N as we indeed observe. The mean-field-like behavior of the intensity at the (1,0,0) reflection has two possible origins. First, the spread in Néel temperatures tends to linearize the behavior near the mean T_N. Second, for systems near the percolation threshold the infinite network is highly ramified with many dangling ends connected by one-dimensional links. These dangling ends will come into registry with the backbone only gradually with decreasing temperature. This could produce the observed linear behavior. As shown in Fig. 18, between 10 and 7 K the inverse correlation length exhibits behavior consistent with that expected[27] for a three-dimensional Ising model. We have argued above that κ does not go to zero at $\langle T_N \rangle \sim 6.4$ K because of the distribution of Néel temperatures. The diffuse scattering below $\langle T_N \rangle$ presumably arises from scattering from each of finite clusters, dangling ends on the infinite network, and critical fluctuations in regions with a reduced T_N.

In conclusion, we believe that these results strongly suggest that the inverse correlation length would decrease to zero at T_N in a homogeneous Ising system, unlike the behavior found in three-dimensional Heisenberg systems.[11] We believe that the unusual results found in the Heisenberg systems are a consequence of the importance of dipolar forces in these systems.

[1]Y. Imry and S.-k. Ma, Phys. Rev. Lett. 35, 1399 (1975).
[2]G. Grinstein, Phys. Rev. Lett. 37, 944 (1976).
[3]A. Aharony, Y. Imry, and S.-k. Ma, Phys. Rev. Lett. 37, 1364 (1976).
[4]G. Parisi and N. Sourlas, Phys. Rev. Lett. 43, 744 (1979).
[5]S. Fishman and A. Aharony, J. Phys. C 12, L729 (1979).
[6]P. Martel, R. A. Cowley, and R. W. H. Stevenson, Can. J. Phys. 46, 1355 (1968).
[7]R. A. Cowley, O. W. Dietrich, and D. A. Jones, J. Phys. C 8, 3023 (1975).
[8]R. A. Cowley and K. Carneiro, J. Phys. C. 13, 3281 (1980).
[9]R. J. Birgeneau, R. A. Cowley, G. Shirane, and H. J. Guggenheim, Phys. Rev. Lett. 37, 940 (1976); R. J. Birgeneau, R. A. Cowley, G. Shirane, J. A. Tarvin, and H. J. Guggenheim, Phys. Rev. B 21, 317 (1980).
[10]R. A. Cowley, R. J. Birgeneau, G. Shirane, H. J. Guggenheim, and H. Ikeda, Phys. Rev. B 21, 4038 (1980).
[11]R. A. Cowley, G. Shirane, R. J. Birgeneau, and E. C. Svensson, Phys. Rev. Lett. 39, 894 (1977); R. A. Cowley, G. Shirane, R. J. Birgeneau, E. C. Svensson, and H. J. Guggenheim, Phys. Rev. B 22, 4412 (1980).
[12]H. Yoshizawa, R. A. Cowley, G. Shirane, R. J. Birgeneau, H. J. Guggenheim, and H. Ikeda, Phys. Rev. Lett. 48, 438 (1982).
[13]E. Pytte, Y. Imry, and D. Mukamel, Phys. Rev. Lett. 46, 1173 (1981).
[14]D. J. Wallace and R. K. P. Zia, Phys. Rev. Lett. 43, 808 (1979).
[15]K. Binder, Y. Imry, and E. Pytte, Phys. Rev. B 24, 6736 (1981).
[16]G. Grinstein and S.-k. Ma, Phys. Rev. Lett. 49, 685 (1982).
[17]J. Villain, J. Phys. (Paris) 43, L551 (1982).
[18]H. S. Kogon and D. J. Wallace, J. Phys. A 14, L527 (1981).
[19]J. Cardy (unpublished); A. Niemi, Phys. Rev. Lett. 49, 1808 (1982).
[20]S. Kirkpatrick, Rev. Mod. Phys. 45, 574 (1973).

[21]V. K. S. Shante and S. Kirkpatrick, Adv. Phys. 20, 352 (1971).
[22]R. E. Watson and A. J. Freeman, Acta Crystallogr. 14, 27 (1961).
[23]R. J. Birgeneau, H. Yoshizawa, R. A. Cowley, G. Shirane, and H. Ikeda (unpublished).
[24]M. Fähnle, Phys. Rev. B 27, 5821 (1983).
[25]D. P. Belanger, A. R. King, and V. Jaccarino, Phys. Rev. Lett. 48, 1050 (1982).
[26]H. E. Stanley, R. J. Birgeneau, P. J. Reynolds, and J. F. Nicoll, J. Phys. C 9, L553 (1976); D. Stauffer, Z. Phys. B 22, 161 (1976).
[27]H. E. Stanley, *Introduction to Phase Transitions and Critical Phenomena* (Oxford University Press, New York, 1971).